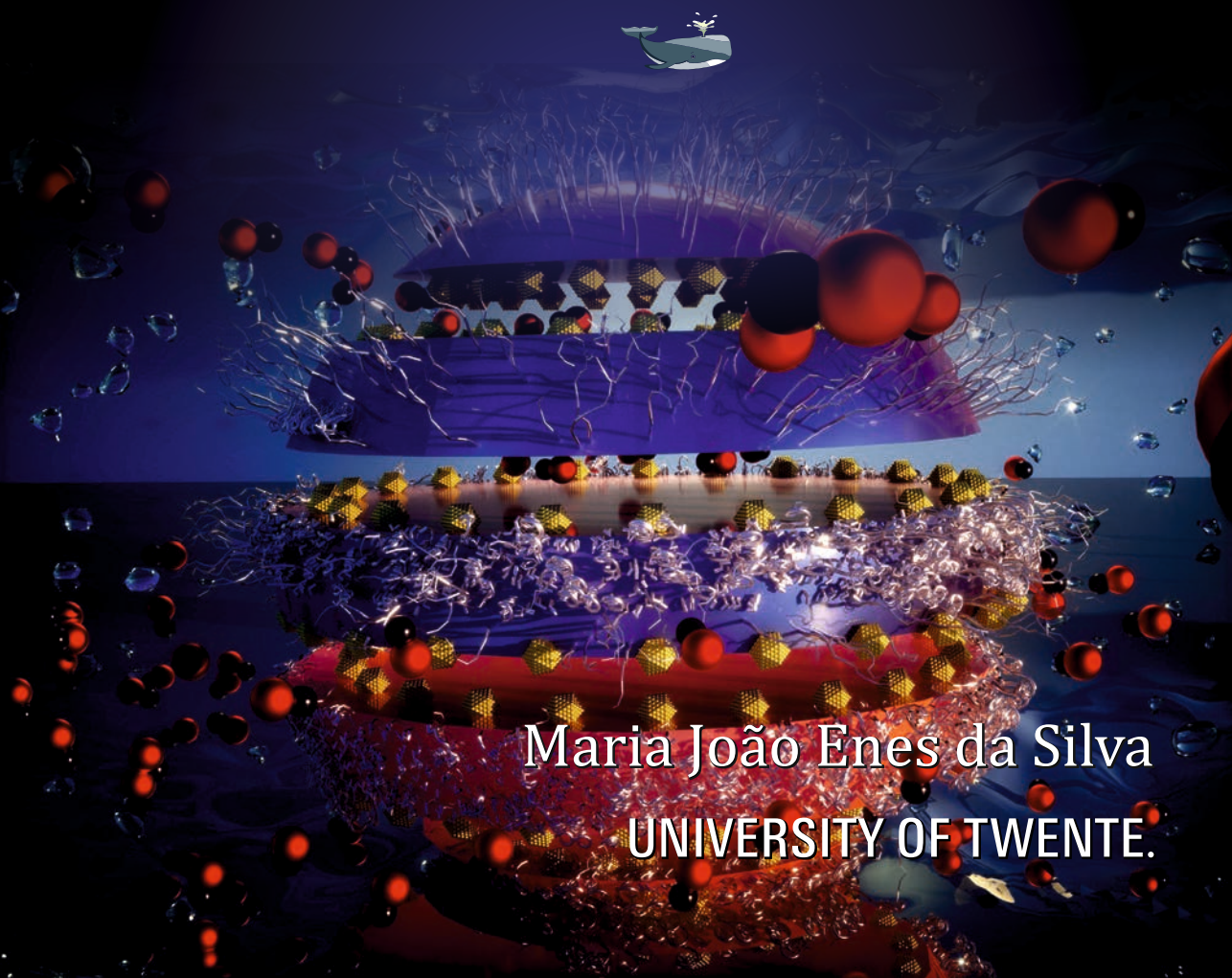# UTILIZATION OF P-NIPAM POLYMERIC BRUSHES IN THE DEVELOPMENT OF THERMO-RESPONSIVE CATALYTIC SYSTEMS

A Study of the Effects of Self-Regulating Polymers on Molecular Transport and Reaction Kinetics

Maria João Enes da Silva

UNIVERSITY OF TWENTE.

UTILIZATION OF P-NIPAM POLYMERIC BRUSHES IN THE DEVELOPMENT OF THERMO-RESPONSIVE CATALYTIC SYSTEMS

A STUDY OF THE EFFECTS OF SELF-REGULATING POLYMERS ON MOLECULAR TRANSPORT AND REACTION KINETICS

Maria João Enes da Silva

UTILIZATION OF P-NIPAM POLYMERIC BRUSHES IN THE DEVELOPMENT OF THERMO-RESPONSIVE CATALYTIC SYSTEMS

A STUDY OF THE EFFECTS OF SELF-REGULATING POLYMERS ON MOLECULAR TRANSPORT AND REACTION KINETICS

DISSERTATION

to obtain the degree of doctor at University of Twente,
on the authority of the rector magnificus,
prof. dr. ir. A. Veldkamp,
on the account of the decision of the Doctorate Board,
to be publicly defended
on Thursday 1 December 2022 at 16:45 hours

by

Maria João Enes da Silva
born on 30th of January 1994
in Viana do Castelo, Portugal

This dissertation has been approved by:

Supervisor
 prof. dr. ir. L. Lefferts

Co-supervisor
 dr. J.A. Faria Albanese

Graduation Committee:

Chair/secretary: prof.dr. J.L. Herek

Supervisor: prof.dr.ir. L. Lefferts
Universiteit Twente, TNW,
Catalytic Processes and Materials

Co-Supervisor: dr. J.A. Faria Albanese
Univerisiteit Twente, TNW
Catalytic Processes and Mateirals

Committee members: dr. S.J.A. de Beer
Universiteit Twente, TNW
Sustainable Polymer Chemistry

prof.dr.ir. W.M. de Vos
Universiteit Twente, TNW
Membrane Science & Technology

prof.dr. J.G.E. Gardeniers
Universiteit Twente, TNW
Mesoscale Chemical Systems

prof.dr. A. Urakawa
Delft University of Technology
Faculty of Applied Sciences

prof.dr. P.C.A. Bruijnincx
Utrecht Univeristy
Faculty of Science

Contents

Chapter 1

Introduction

1.1 Motivation

Industrial processes involving highly exothermic reactions, such as -selective- oxidations and hydrogenations, cause a significant adiabatic temperature rise. The heat release during the reaction can cause an increase in temperature in the catalyst if it is not removed adequately. [1] The temperature rise will cause the reaction rate to increase, leading to even more significant heat production. In the presence of unreacted products, the reaction will continue to accelerate in this positive feedback loop leading to a runaway reaction. The increased reaction temperature generally favours the formation of undesired by-products and thus yield losses as well as catalyst deactivation. In the worst case, a run-away reaction can even lead to a melt-down or explosion of the reactor. [2] Heat removal, from these processes is therefore essential since the rate of heat generation increases exponentially with temperature, while the removed heat increases only linearly with temperature. Consequently, these processes are generally operated at overall mild temperature and low conversion, thus mitigating the risk of a run-away and hotspot formation.[3] The risk of a run-away event is more prominent in gas phase reactions, due to the lower heat capacity of gasses and higher diffusion coefficients compared to liquids. Nevertheless, temperature control in liquid phase reactions could be challenging in highly exothermic reactions due to larger thermal inertia of the system. Nowadays, there are no conventional means to control the reaction rate and consequently the temperature at the catalyst particle level. Instead, the reaction temperature of the bulk is controlled by an external control loop based on the reactor temperature, feed composition, and pressure, that uses active quenching in the reactor.[4] In this approach, the temperature increments at the catalyst particle typically exceed the measurable temperature in the bulk of the reactor.

To tackle this issue, the flow pattern inside the reactor can be manipulated to obtain a turbulent behaviour and, in this way, maximise thermal mixing. Or to increase the heat exchange capacity, shell and tube reactors are implemented. Here, the physico-chemical properties of the catalyst also play an important role on the heat removal efficiency. This has led to the development of catalysts with high thermal conductivity and optimized geometric structures, such as monoliths (e.g. aluminium foam) that can favour isothermal operation. [5] The present thesis proposes a way to control the reaction rate based on the temperature at the individual catalyst particles, theoretically yielding intrinsically safer and atom-efficient operation. This will consequently alleviate the need of using these external measures since the reaction rate will be intrinsically manipulated. Even though run-away behaviour is more prominent in gas phase reactions, there are currently no

materials available that can operate at the high temperatures required in gas phase reactions. A more feasible approach for the first steps of developing a catalyst capable of self-regulating the reaction rate is to perform experiments in the liquid phase. Here, the lower operating temperatures facilitate the use of organic-based functionalities that can act as regulating valves, in the same manner that biological systems do, without major deactivation issues. In this line, this thesis lays down the foundation for creating a self-regulating catalyst.

1.2   Adaptive catalysis

To achieve a catalyst with intrinsic reaction control or self-regulation, one proposal is to render a conventional catalyst with "nano-valves" that adjust the molecular diffusion in a dynamic fashion to control the reaction rate, maintaining the reaction conditions in the desired temperature range. This concept implies a discontinuous behaviour, where the catalytic activity can be switched ON and OFF above or below a certain threshold value of the trigging variable (e.g. temperature).[6] The catalyst activity could be regulated by exposing or blocking the access to a metal active site by autonomously adapting to small changes in the reaction medium. In this way, the catalysts could locally change from active to inactive in response to an internal stimulus and thus self-regulate the reaction-rate.

1.3   Stimulus-responsive materials on the catalyst surface

A potential candidate for controlling the molecular diffusion and thus tune catalyst selectivity are stimulus-responsive polymers. The development of these bio-inspired materials have become relevant due to their ability to reversibly undergo conformational changes in response to small environmental stimulus (e.g., temperature, pH, ionic change, light radiation, electric field).[7–10] These polymers, hydrogels, and gels can undergo large conformational transitions from swollen to collapsed states upon reaching a specific critical solubility point.[11,12] For instance, if one considers a thermo-responsive polymer as the temperature starts to increase, due to the release of reaction heat, the polymer responds to this perturbation via the conformational collapse onto the pore entrance, creating a barrier for the molecular transport towards the active site (see Figure 1.1).
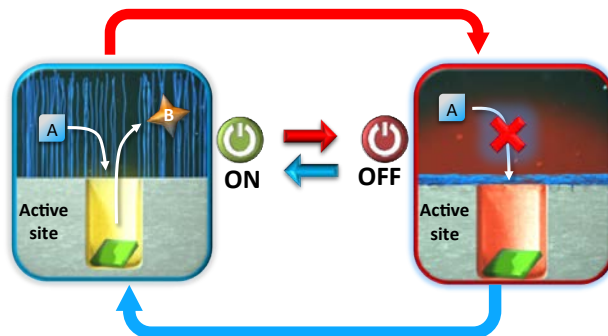
Figure 1.1: Schematic illustration of a negative feedback loop in which the collapse of the polymer coating leads to a mass transport limitation that switches OFF the catalyst.

Achieving a dynamic behaviour where the activity can be switched "ON" and "OFF" is rather challenging because it requires similar time scales for the heat released from the reaction occurring at the catalyst surface and the response of the stimulus-responsive polymer. So far, no one has demonstrated this self-regulating mechanism in heterogeneous catalysis. Only the group of Prof. J. Aizenberg has reported self-regulating behaviour on macroscopic devices.[13,14] The macro device consists of a hydrogel pillars with a catalyst on the tips that reversible actuate as the gel swells or contracts in response to a chemical stimulus (C) (see Figure 1.2a). To control the reaction activity the system is immersed in a liquid bilayer, where the hydrogel moves in or out of the top layer containing the reaction solution. As shown in Figure 1.2b, upon an increase of the temperature generated during hydrogen peroxide decomposition, the hydrogel contracts causing the reaction to slowdown. This mechanical action (M) stops the heat generation from the exothermic reaction, causing the gel to reversibly swell again. This experiment demonstrates that stimulus-responsive polymers have a reversible and relatively fast change in conformation.
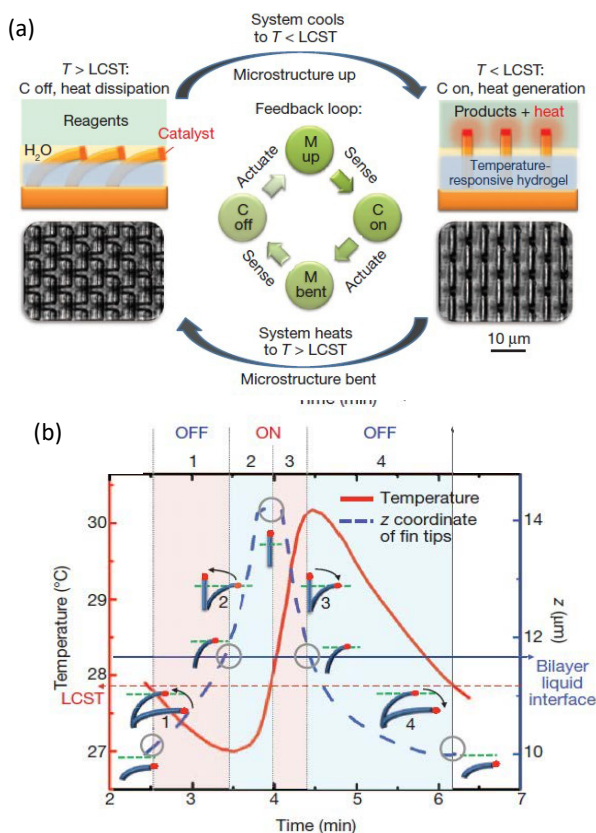
Figure 1.2: Schematic of the temperature-regulating device showing a chemomechanical (C→M) and mechanochemical (M←C) feedback loop, in which mechanical action of temperature-responsive gel is coupled with an exothermic reaction (hydrogen peroxide decomposition). The side view schematic and top view microscope images depict ON/OFF states of the reaction in the top layer (a), temperature evolution for a control sample with catalyst-functionalized microstructure tips with a gel where the Low Critical Solution Temperature (LCST) was 27 °C (b).[13]

This self-regulation mechanism has never been demonstrated for heterogeneous catalysts. Therefore, the focus of this thesis is to understand the interplay between polymeric brushes, molecular transport, solvation effects, catalytic activity, and selectivity in aqueous phase. This knowledge will be crucial to develop designing rules to achieve a catalyst with

self-regulating behaviour, which is crucial for practical application in industrial catalysis. The next sections describe all the key techniques and concepts that are involved in the synthesis, characterization of mass transfer, kinetics and modelling studies that are required to stablish fundamentally relevant polymer-catalyst-performance relationships. This is followed by a non-exhaustive literature review on the key developments on adaptive catalysts.

1.4 Synthesis of polymeric brushes

Polymer brushes belong to the class of surface tethered polymers, which can be anchored on a flat or curved surface by covalent chemical bonds. Chemical grafting can be done by "grafting to", where the pre-synthesized polymeric brush is immobilized on the surface or by "grafting from", where the polymer chain grows from polymerization initiating sites on the substrate.[15,16] The properties of the polymeric brushes anchored to the surface can be tuned depending on the physical and chemical properties of the immobilized polymer, the number of anchoring points, grafting density, topology, chemical composition, and functionality.[17] There are several polymerization techniques such as reversible addition-fragmentation chain transfer (RAFT), nitroxide-mediated polymerization (NMP), living anionic polymerization, and atom transfer radical polymerization (ATRP). Here, ATRP ensures a well-controlled growth of the polymeric chain[18] due to an equilibrium between active and dormant states of a growing polymeric chain, which is regulated by a reversible activation-deactivation mechanism (see Eq.1.1). [19] The reversible redox process is catalysed by a transition metal complex (L/Mt^n-X, where X is the counterion (Cl, Br), Mt^n the transition metal complex (Cu, Ru) and L the ligand). The transfer of a halide (X) occurs between the dormant chain (P$_n$-X) and the transition metal complex, which results in a radical (P$_n$*) for propagation by addition of a new monomer and the transition metal complex in a different oxidation state (X-Mt^{n+1}-Y/Ligand).[18,19] The uniform growth of the polymer brushes is guaranteed due to the fast rate constant of activation (k$_a$) together with a rapid reversible deactivation. To manipulate the thickness of polymeric brushes the time of the polymerization can be varied as longer polymerization times lead to larger polymeric brushes.

$$P_n-\mathsf{X} \ + \ \mathsf{L}/\boldsymbol{M}\boldsymbol{t}^n \ \underset{\boldsymbol{k_d}}{\overset{\boldsymbol{k_a}}{\rightleftharpoons}} \ P_n^* \ + \ L/\boldsymbol{M}\boldsymbol{t}^{n+1}-\mathsf{X}$$

Eq. 1.1
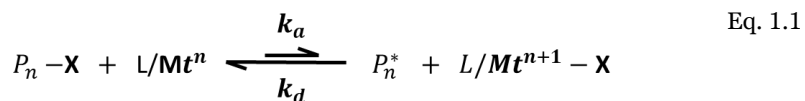
1.5   Properties of stimulus-responsive polymers

When using these materials to control the reaction activity it is important to determine the polymer swelling and deswelling characteristics. The polymeric chain mobility/swelling is dependent on the brush grafting density (σ, grafted chains per unit of surface) and polymer thickness (H).[20,21] Figure 1.3 shows the mushroom-to-brush transition, where higher grafting density leads to stretching of the polymeric brushes (brush regime). The stretch of the polymeric brush results from increasing the osmotic pressure among the chains, due to increasing the steric hindrance between individual polymer chains. In this situation the thickness of the swollen polymer brush layer is larger than the radius of gyration (R_g) of the swollen free polymer chain and of the polymer chain in the mushroom regime. In the mushroom regime, the polymer chains maximize the contact between the polymer segments. while keeping chain stretching to a minimum.[22]
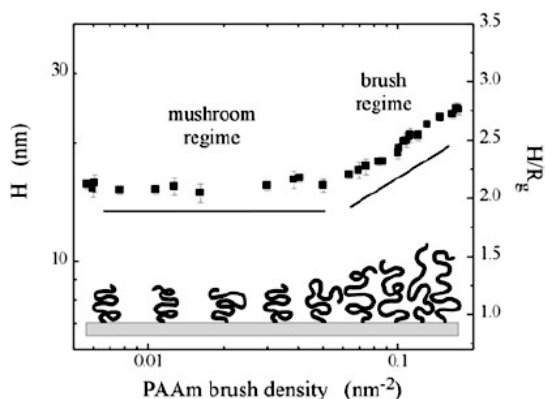

Figure 1.3: Schematic of brush wet thickness (H) and grafting density (σ) on a polymeric brush polymerized on a surface, where D represents the distance between grafting sites, ν is dependent of solvent quality (good solvent $\nu \approx 1/3$ and in a poor solvent ≈ 0.5) and R_g radius of gyration. [23]

1.6 Conformational changes in stimulus-responsive polymers

Stimulus-responsive polymers can respond to different external or internal triggers such as chemical (e.g. pH and ionic strength) and physical (e.g. temperature, light and pressure) triggers thanks to the vast possibilities of chemical functionalities. One of the most studied thermo-responsive polymers is Poly(n-isopropylacrylamide) (p-NIPAM) with an abrupt conformational transition at its lower critical solution Temperature (LCST), which in water is around 32 °C (see Figure 1.4). The LCST depends on the functional groups (type of polymer) on the polymeric chain, molecular weight, concentration in the solution, and composition of the liquid phase. Therefore, the type of polymer can be adjusted depending on the transition temperature desired. For instance, poly(2-isopropyl-2-oxazoline) (PIOZ) is another thermo-responsive polymer with a LCST of around 48 °C.[24] These conformational changes are caused by a change in solubility of the polymeric chain, where below the LCST, the Gibbs free energy of the polymer in liquid water is primarily dominated by the H-bonding between the -NH motive in the polymer chains and water molecules (i.e. enthalpic contributions dominate).[25] As temperature increases above the LCST, the hydrogen bonds are destabilized and Van der Waals forces between polymer-chains drive the Gibbs free energy of the system (i.e. entropic contributions dominate), leading to the collapse of the polymer brushes.[25,26] The stretching of the polymeric chain and LCST can change in the presence of salts and different solvents by disrupting the water-polymer bonds.[27] Humphreys et al. [26] reported the effect of anions on the LCST of p-NIPAM brushes, where concentrations higher than 10 mM of potassium thiocyanate lowered p-NIPAM LCST with a maximum decrease of ~ 6 °C with a concentration of 250 mM). Y. Yu et al.[28] reported the effect of ethanol concentration in water-ethanol mixtures on a p-NIPAM brushes swelling, where by the presence of 30% ethanol/water the swelling ratio decreased from 4 to 1. These examples show the complexity of combining stimulus-responsive polymers to different environmental conditions, highlighting the importance of characterizing these materials under reaction conditions.
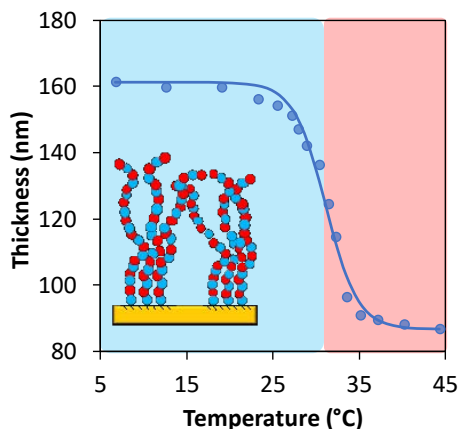
Figure 1.4: Equilibrium thermo-responsive behaviour of p-NIPAM brushes in water as a function of temperature monitored by ellipsometry on a silicon wafer, adapted from [26]. Blue represents temperatures below LCST and red above LCST.

1.7 Application on catalysis

1.7.1 Transport effects

The majority of the research into the application of this approach in heterogeneous catalysis has been focussed on using an external stimulus to trigger the polymer conformation change to alter the molecular transport towards the catalyst.[29–34] Combining catalytic materials with polymers that respond to external stimulus has been demonstrated as a powerful tool for precise control of selectivity, stability, and recyclability in liquid environments.[6,35–37] Z. Chen et al.[32] reported that in the presence of a thermo-responsive core-shell nano-reactor the conversion of 4-nitrophenol was reduced upon an increase of temperature due to the collapse of the polymeric chains, as shown in Figure 1.5. The catalyst consists of a p-NIPAM hydrogel coated on the external pore mouth of mesoporous silica hollow spheres with gold nanoparticles inside the silica spheres. By separating the polymeric chain and the metal nanoparticles it was possible to avoid any interaction of the p-NIPAM brushes on the active site. While it was clear that the functionalized catalyst had a tremendous effect on the reaction at high temperatures, the results using a catalyst without a p-NIPAM coating were not included in this study. Essentially, the authors assumed no significant effect on the reaction rate by the polymer

addition at temperatures below the LCST (32 °C) in comparison to an un-functionalized catalyst.
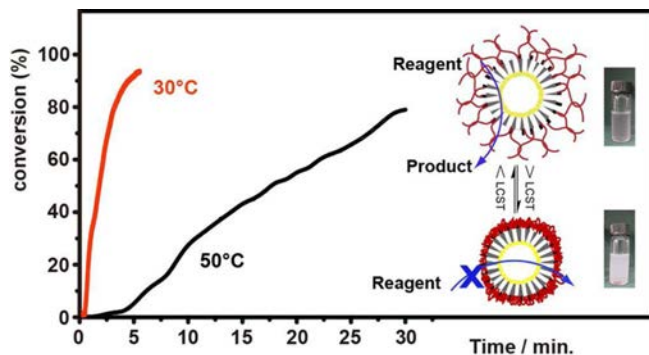
Figure 1.5: Conversion of 4-nitrophnol runs at 30 °C and 50 °C obtained by UV-vis adsorption spectrum of p-NIPAM/Au@meso-SiO$_2$ with 250 nm particle size catalyst and a schematic illustration of p-NIPAM coated on a core-shell catalyst, that consist of a core of Au nanoparticles loaded onto carbon nanospheres to form Au/C and the shell consists of mesoporous silica with 40 nm thickness. The stimuli-responsive polymer is coated into the outside surface of the shell.[32]

M. Ballauff and J. Dzubiella reported yolk-shell nano-reactors consisting of gold nanoparticles surrounded by a p-NIPAM hydrogel.[33,38–41] Figure 1.6 shows the effect of temperature on the reaction kinetics by these nano-reactors on the conversion of 4-nitrophenol. Where at low and high temperatures the curve follows Arrhenius-like behaviour, i.e. the temperature enhances the reaction rate. However, in the transition regime where the polymer shifts from a swollen to a collapsed state there is a drop in the activity, implying non-Arrhenius behaviour. These results agree with the trend observed by Z. Chen et al.[32], as shown in Figure 1.5, where the polymer collapse caused a drop in the reaction rate.

The authors made a theoretical description of the polymer-controlled reaction, to explain the non-Arrhenius behaviour of this system, where the inverse of the apparent kinetic constant (k_{app}^{-1}) of the nano-reactor is defined as the summation of the inverse of the

kinetics of mass transport (k_d) and surface reaction (k_r). The intrinsic catalytic activity of the catalyst (k_r) is assumed to be the same as that observed on a non-coated catalyst. Here, the transport constant (k_d) was assumed to follow a Debye-Smoluchowski permeability-dependent diffusion, where the transport depends on both the effective diffusion of the reactants in the polymeric matrix and the Gibbs free energy change of solvation (ΔG_{sol}) between reactant-polymer and reactant-solvent. This demonstrates that transport through a polymeric matrix cannot be explained by simple diffusion coefficient theory.
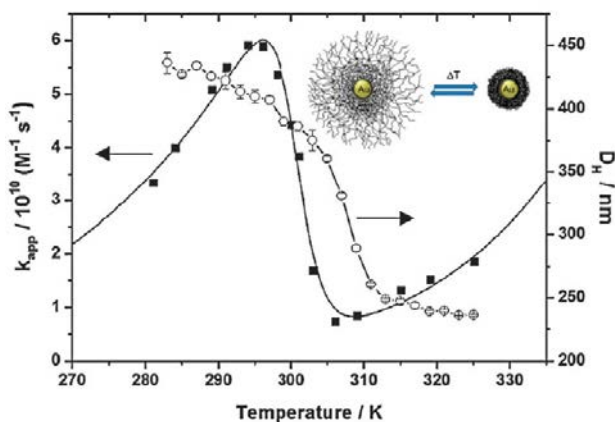
Figure 1.6: Influence of temperature on the pseudo-first order rate constant, k_{obs} (filled squares) measured in the presence of Au@p-NIPAM particles, compared with the corresponding hydrodynamic diameters (DH) (open circles). The solid line shows the fitting of the kinetic data.[42]

1.7.2 Solvation effects

Catalytic reactions depend on the atomic structure and electronic properties of the active site, as well as the chemical environment surrounding the active site. These surrounding molecules interact with the bare active site as well as with adsorbed reactants, intermediates, and products, influencing the catalytic performance by altering the energy landscape of the catalytic reaction. Recently, major research has been developed to understand the effect of solvents on catalyst activity and selectivity.[43–47] Solvents can influence reactant solubility and transport, enhance protons transfer, compete with the reactant for adsorption sites, and change the binding and reactivity of surface species.[48]

H. Zhao et al.[49] showed the influence of polar solvents on furfural hydrogenation selectivity towards furfuryl alcohol (FOL) on a palladium catalyst, where selectivity is dictated by the adsorption configuration of furfural. The authors obtained different reaction orders in hydrogen for furfural hydrogenation in water and cyclohexane due to changes in the rate determining step. Similar effects were observed by N. Singh et al.[50] during phenol hydrogenation, where decreasing the pH increased the hydrogenation rate. The authors argue that, when H-insertion is the rate determining step (RDS) the pH effect is determined by the Hydrogen Binding Energy (HBE). At high coverage of hydrogen, the hydrogen adsorption strength increased with increasing pH. Consequently, the reaction rate decreased due to a higher activation energy barrier caused by stabilization of hydrogen chemisorbed at the metal surface. Using molecular dynamic (MD) simulations, the authors showed that the adsorption/desorption of hydrogen is significantly influenced by both the presence of ions (OH$^-$, H$^+$) and the corresponding orientation of water molecules at the metal surface. In addition, pH variations altered the electrochemical potential at the metal surfaces influencing the H-insertion rate.

In this context, the addition of stimulus-responsive polymers might also influence catalyst activity and selectivity due to so called "solvation effects", where the energy landscape of the catalytic reaction can be modified by the presence of functional groups on the polymeric chain, similar to the effects observed in enzymes. Even though the literature on the solvation effects caused by stimulus-responsive polymers is rather scarce, some reports on polymer-hybrid catalysts are available. For instance, A. R. Riscoe et al.[51] showed that on polymer-palladium nanocrystal hybrid catalysts the activity for CO oxidation increased due to the presence of microporous cavities near the metal site. CO has a strong interaction with palladium and competes for open sites with molecular oxygen, making CO desorption and dissociative adsorption of oxygen the rate determining step. Authors argue that the nitrogen lone electron pairs on the amino groups of the polymer interacts with the metal surface affecting the transition state enthalpy and entropy for the rate limiting step.

1.8   Transport studies using ATR-IR spectroscopy in aqueous phase

In-situ Attenuated Total Reflection Infrared (ATR-IR) spectroscopy is often implemented to gain insights into reaction kinetics and catalytic mechanisms on gas and liquid-phase reactions.[52–54] This technique allows the monitoring of the molecular vibrations at the solid-liquid interface in a time-resolved mode to obtain structure-activity relationships.[55–57] In this technique, a thin catalyst layer is coated on the top surface of an optical element (typically ZnSe trapezoidal prism) where the infrared light is propagated by multiple internal reflections (see Figure 1.7a-b).[58] At the reflection points, an evanescent wave is formed at the interface between the optical element and the solid. The penetration depth (d_p) of the evanescent wave is defined as the distance required for the amplitude of the electric field to fall to e^{-1} compared to the surface. As shown in Eq.1.2, the penetration depth depends on the optical constants, where n_1 and n_2 denote the refractive index of the sample and IRE, respectively, θ the angle of incidence and λ the wavelength.[59]

$$d_p = \frac{\lambda}{2\pi n_1 \sqrt{(sin^2\theta - (\frac{n_2}{n_1})^2)}}$$

Eq.1.2

The refractive index of the samples (n_1) of a porous layer of e.g. Al_2O_3 is calculated based on Eq.1.3, where φ is the relative porosity and n_c and n_d are the refractive index of the phases c (dense solid alumina) and d (medium filling the pores, e.g. air or water), respectively.[60]

$$n_1 = \sqrt{(1 - \Phi)n_c^2 + \Phi n_d^2}$$

Eq.1.3

By restricting the evanescence wave to the catalyst surface, limiting the penetration depth (d_p) to only a few microns, the absorption contribution of liquid solvents as well as dissolved molecules is minimized.[59,61] This allows facile probing of chemisorbed reaction intermediates with sufficient intensity allowing the study of reaction kinetics.
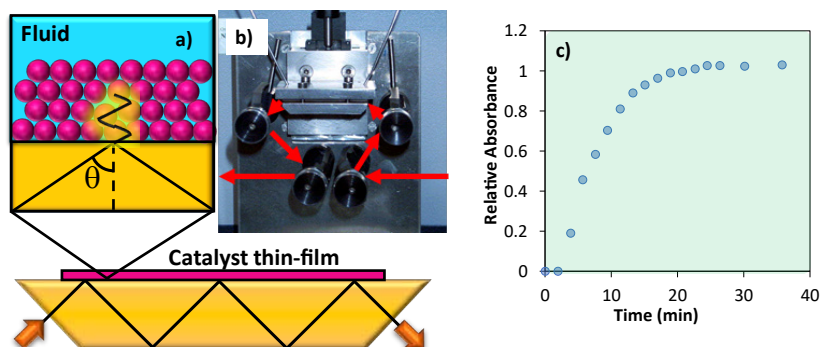
Figure 1.7: Schematic representation of an IRE used on ATR-IR spectroscopy, (a) evanescent wave formed at the catalyst layer, (b) flow-through cell employed for ATR-IR spectroscopy, where the arrows represent the direction of the IR light and (c) relative absorbance of chemisorbed species.

By measuring the IR absorbance of chemisorbed species as a function of time of exposure to a solvent containing molecules that chemisorb on the catalyst, it is possible to obtain the saturation curve, where the curve profile depends on the catalyst properties, ATR-IR cell fluid dynamics, and reaction kinetics. Figure 1.7c shows a typical saturation curve in the presence of CO bonding to the palladium surface, where the plateau indicates the time at which all the palladium surface was saturated with CO. Considering this analogy, ATR-IR spectroscopy could be used as a tool to study the effect on mass transfer created by the addition of stimulus-responsive polymers. To avoid any kinetic effect on the reaction the polymeric brushes should be decoupled from the metal active site. This can be achieved by employing a model catalyst on the ATR crystal with polymeric brushes that are physically separated from the catalyst. For these reasons, ATR-IR is a powerful technique to study both kinetics and well as transport in idealized catalytic systems. Since this technique is at the core of the herein presented thesis, the following sub-sections describe in detailed the fundamental background and potential uses of ATR-IR spectroscopy.

1.8.1 Fundamentals

By measuring the IR absorbance of chemisorbed species as a function of time of exposure to a solvent containing molecules that chemisorb on the catalyst, it is possible to obtain the saturation curve, where the curve profile depends on the catalyst properties, ATR-IR cell fluid dynamics, and reaction kinetics. Figure 1.7c shows a typical saturation curve in the presence of CO bonding to the palladium surface, where the plateau indicates the time at which all the palladium surface was saturated with CO. Considering this analogy, ATR-IR spectroscopy could be used as a tool to study the effect on mass transfer created by the addition of stimulus-responsive polymers. To avoid any kinetic effect on the reaction the polymeric brushes should be decoupled from the metal active site. This can be achieved by employing a model catalyst on the ATR crystal with polymeric brushes that are physically separated from the catalyst. For these reasons, ATR-IR is a powerful technique to study both kinetics and well as transport in idealized catalytic systems. Since this technique is at the core of the herein presented thesis, the following sub-sections describe in detailed the fundamental background and potential uses of ATR-IR spectroscopy.

For a molecule to absorb IR light, the energy of the photons of the incident radiation must be equal to that of the molecular vibration in the sample under analysis. In ATR these molecular vibrations are probed by the evanescent waves generated upon reflection of the light within the IRE.[62] The spectrum of molecules in gas phase is characterized with a series of vibrational and rotational transitions, due to the rotational freedom these molecules. Figure 8a shows the infrared absorption spectra of carbon monoxide (CO) in the gas phase, where the purely vibration transition is at 2143 cm^{-1}.[63] The overall intensity of the spectral lines is proportional to the change in the dipole moment. Therefore, species with polar bonds, such as CO, exhibit strong infrared bands, in contrast, less polar covalent bonds, such as C-C bonds, absorb infrared light only weakly.[63] Moreover, molecules with no dipole moment, such as di-hydrogen, di-nitrogen and di-oxygen, cannot be detected by IR light.

When a CO molecule forms a chemical bond with a metal surface, such as a Pd metal cluster, only the vibrational transitions are observed due to the loss in rotational freedom. In addition, in liquid phase molecular rotations are partially blocked by interactions with solvent molecules. Figure 1.8a shows the effect of chemisorption on metal surface on the CO infrared adsorption bands, observing a shift to lower frequency compared to CO in the

gas phase. For the adsorption to occur on Pd, the CO donates σ electrons to the empty states of the d-band of the metal and the metal donates electrons to the anti-bonding molecular orbitals ($2\pi^*$) of CO.[64] This electron-transfer strengthens the metal-carbon bond and weakens the C-O bond due to electron back-donation, explaining the shifts observed in the CO spectrum. The extent of weakening of the CO bond depends on the extent of back donation from the metal and other surrounding molecules.[65] Molecules bind to specific sites at the metal surface in geometries that correspond to a minimum energy configuration, either by binding to a single surface atom or group of atoms.[66] The typical *in-situ* CO-chemisorption spectrum consists of three main adsorption bands, corresponding to linear (2000-2130 cm^{-1}), bridge (1880-2000 cm^{-1}) and multi (1800-1880 cm^{-1}) bonded CO (see Figure 1.8a-b). Ebbesen et at.[67] performed CO adsorption in gas phase and aqueous phase to study the effect of the solvent on the CO infrared adsorption bands (see Figure 1.8a), using the same catalyst layer for both measurements. Here, major changes can be observed in the presence of the solvent, including a red shift (i.e. to lower energy and lower wave number) for all adsorption bands, an increase of the signal intensity and a decrease of the linear-to-bridge ratio when compared to chemisorption in gas phase. This phenomenon is attributed to increased π-back donation from the metal and a direct effect of water on the dipole moment of adsorbed CO.[67,68]
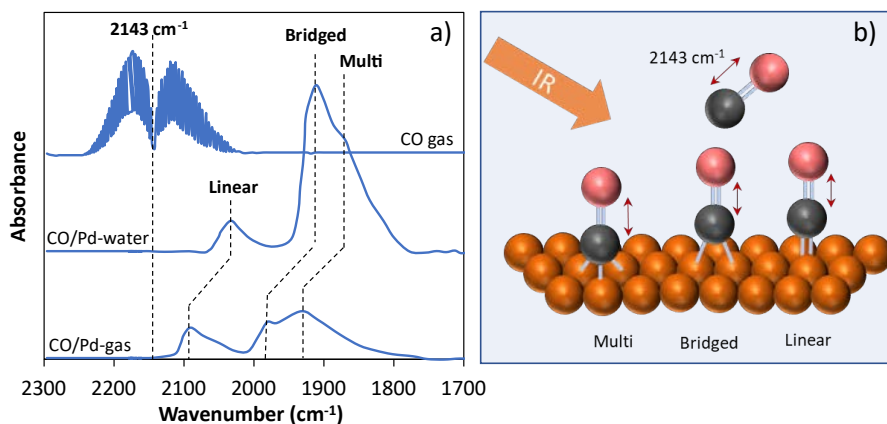
Figure 1.8: Infrared absorption spectrum for different systems: (1) vibration-rotation line spectrum of CO in gas phase [63], and (2) *in-situ* ATR-IR spectra at full CO coverage (saturation) on pre-reduced Pd/Al$_2$O$_3$ catalyst containing 5 wt. % Pd at 25 °C on a 5 μm catalyst layer for dry CO (1 % CO/Ar) and CO dissolved in water 1.4x10^{-6} mol l^{-1} (pH=7), for comparison of bands intensities the spectra in dry gas and in CO-saturated in water

were measured on the same catalyst layer to ensure that the same amount of palladium sites is available for adsorption, reproduced from [67] with permission from the Royal Society of Chemistry (a). Schematic representation of the CO free in gas phase and CO adsorbing into a metal surface where three coordinates are identified linear, multi and bridged (b).

1.8.2 Practical aspects for the study of solid-liquid interfaces via ATR-IR spectroscopy

Experimental results of *in-situ* and *operando* ATR-IR experiments are determined by both chemical reaction steps at the surface (e.g. adsorption, surface reaction, and desorption) as well as mass transfer processes (e.g. convective flow and molecular diffusion) determining the concentration of species in liquid phase close to the active sites. In this section, we will review key practical issues that must be considered, including quality of the spectrum, cell design, deposition and stability of the catalyst layer, and decoupling of mass transfer effects and surface chemistry dynamics using experiments and theoretical modelling.

1.8.2.1 Practical aspects for the study of solid-liquid interfaces via ATR-IR spectroscopy

Performing ATR-IR experiments with powder catalysts can be rather challenging as the quality of the IR spectra is affected by the chemistry of the liquid phase, the optical properties of the IRE, and catalyst coating. For instance, Ebbesen et al.[60] reported that water is a problematic IR light absorber with two intense bands over the full mid infrared region, at 3500 cm^{-1} and 1635 cm^{-1} caused by OH-stretching and O-H-O scissors bending. Consequently, this region may not be used for analysis of species unless proper water subtraction is performed during data processing. In addition, homonuclear diatomic molecules, like hydrogen, nitrogen and oxygen, cannot be detected by IR light.[63] When these are inert (e.g. N_2) it is possible to conduct ATR-IR spectroscopy without major complications. The challenge arises when these molecules are part of the reaction under study as direct observation is not feasible. Furthermore, spectra collected at the solid-liquid interface comprises signals from all molecules that possess a polarizable bond. Therefore, the presence of both solvated and adsorbed species (e.g. reactants, reaction

intermediates, products and spectators at the metal surface or support) can lead to a complex IR spectrum [69], complicating reliable identification of the reactive species. Consequently, extra experiments or computational modelling are needed to discriminate between the different species. Coupling the outlet flow of an ATR-IR cell with analytical techniques, such as UV-Vis spectroscopy or gas- and liquid- chromatography, can potentially be employed to conduct so-called *operando* experiments. Here, the reactant disappearance and product formation rates are coupled with the IR data to investigate the reaction mechanism. However, this can be challenging as ATR-IR experiments are usually performed with reactor cells with rather short residence time (high flow rates and small reactor volume) and with small amounts of catalyst, causing low conversion. Therefore, the changes in concentration in the outgoing flow are often below the detection limit of analytical techniques.

Achieving high signal to noise ratio for adsorbed species in the liquid-solid systems can also be a major issue of the technique. A way to improve the spectrum intensity is to optimize the material of the internal reflection element (IRE) as the spectra depend on refractive index of the IRE and samples (see Eq.1.2 and Eq.1.3). For total reflection to occur, the refractive index of the IRE needs to be higher than that of coated sample. An IRE with low refractive index, like zinc selenide (R.E. of 2.4) compared to germanium (R.E. of 4), will lead to larger penetration depth of the evanescence wave and consequently increases the signal to noise ratio of surface species when the catalyst layer is sufficiently thick.[70]

1.8.2.2 Design of ATR-IR cells

The ATR-IR cell designs vary depending on the shape of the optical element and the conditions required to study the reaction of interest.[70] For batch reactor experiments, immersed ATR probes with fiber optics are available to monitor concentrations of dissolved species in the liquid.[71,72] However, information on adsorbed species is usually not obtained. In contrast, horizontal cell reactors are used to study thin films or porous catalyst layers.[67,73–75] The optimal size and number of reflections of the IRE depend on the strength of absorption of IR light. Metal layers, such as Pt, Pd or Au strongly absorb IR light, so that single-bounce elements can be used, especially when using ATR surface enhanced infrared absorption spectroscopy (ATR-SEIRAS).[76] Multi-bounce

elements improve signal to noise ratio in case of weakly adsorbing samples, since absorption of IR light takes place at every point of total reflection. These elements are suitable for studying adsorbed species on metal particles dispersed on a porous support layer such as alumina or silica, which are weak IR absorbers. The high surface area of such supports allows significant metal loading and dispersion, improving the signal-to-noise ratio of adsorbed species. A possible disadvantage is that increasing the metal loading in the supports usually comes at the expense of the metal dispersion (i.e. larger metal clusters are formed during catalyst synthesis), which is not desired in the case of structure-sensitive reactions.[77] Furthermore, when considering multi bounce elements, the IR spectrum is an average of IR absorption at all individual points of total reflection. If the catalyst layer is not homogeneous, i.e. that sections of the IRE surface are exposed directly to the liquid phase, then IR absorption of the solvent might dominate the spectra. In addition, concentration gradients along the ATR-IR cell and within the catalyst layer may develop due to the catalytic reaction. In such cases, hydrodynamic and molecular diffusion studies are needed for proper interpretation of results of ATR-IR experiments.

1.8.2.3 Catalyst deposition

Thin metal coatings, e. g. Pt or Pd [78,79], can be deposited on the ATR-IR crystal by physical vapor deposition methods. This technique can be carried out in vacuum (e.g. 1.5×10^{-5} mbar for Pt) and the thickness of the film is can be measured by a sputtering quartz crystal sensor.[79] As a typical example, Moradzaman et al.[80] reported the formation of a copper (Cu) film with a thickness of 12 nm by magnetron sputtering. Alternatively, metal can be deposited by evaporating a solution containing the metal precursor on an IRE surface, e.g. obtaining platinum clusters up to 30 nm as reported by Ebbesen et al.[81]. Removing such coatings from the IRE surface can be challenging. Reutilizing the IRE requires polishing with e.g. diamond paste, decreasing the longevity of the IRE.[79] In addition, proper quantification of the number of metal active sites available is rather difficult.

In contrast to metal coatings, thin layers of catalysts on a porous support, can be characterized in detail by characterizing the original catalyst in powder form, prior to deposition on the IRE. Consequently, the structure of the catalyst, i.e. metal loading, dispersion, porosity, can be systematically varied and the influence of structure on the

ATR-IR results can be determined. Furthermore, the deposited catalyst layers can be easily removed from the IRE by rinsing the surface with organic solvents, facilitating reuse of the expensive ATR-IR crystals.

In a typical preparation procedure, the supported catalyst particles are dispersed in a solvent (e.g. isopropanol or acetone) followed by ultra-sonication or ball milling to obtain very small catalyst particles. The slurry containing the catalyst particles is then wet-coated on the surface of the crystal and dried at room temperature for 24h.[82–84] Another alternative is to deposit the catalyst via spray coating, where the IRE is placed on a heating element and spray coated until reaching the desired loading.[85–88] The layer thickness is preferably similar or slightly larger than the penetration depth to minimize the contribution of the liquid to the IR spectra. In addition, a solvent with low boiling point (b.p.) is preferred, such as isopropanol (b.p. 82.6 °C), as fast evaporation of the solvent will facilitate the formation of a homogeneous coating.

1.8.2.4 Catalyst stability

Obtaining quantitative and reproducible experimental data with ATR-IR requires stable catalyst layers on the IRE. Therefore, easy removal of the layer as discussed above can also be a disadvantage. Essentially, any catalyst losses during the experiment will decrease the signal of absorbed species in the infrared spectrum, possibly causing misinterpretation. Unfortunately, avoiding metal loss during dynamic experiments has been proven to be rather challenging.[89] To mitigate these effects on porous catalyst layers, immobilization strategies haven been developed using colloidal particles that can act as binders during spray coating onto the IRE crystals.[81] The resulting layers are sufficiently stable to allow multiple experiments with one sample. This is required when studying surface intermediates at different reactant concentrations or temperatures, keeping the catalyst properties unchanged during the experiments. Additional thermal treatment can be done to densify the layer as well as to remove excess solvent and/or contaminants from the pores in the catalyst layer. This step is often conducted at temperatures ranging from 250 to 270 °C, below the upper operational limit of most common IRE, e.g. 300 °C for zinc-selenide as well as silicon.[90]

In addition, heterogeneity in the thickness of the catalyst layer will lead to differences in the dynamic behavior caused by molecular diffusion across the catalyst layer, influencing the time required to achieve a steady state. For this reason, a homogeneous distribution of the catalyst layer is required. This is key, particularly, when molecular transport is the step controlling the catalyst behavior.

For catalytic materials that are temperature sensitive, e.g. polymer-coated inorganic catalysts, the maximum temperature of any thermal treatment is obviously limited. To solve this issue, one can use a porous membrane placed on top of the catalyst layer to ensure the layer stability by mechanical immobilization, as shown in Figure 1.9. In this case, a 12 µm thick membrane had pores with a diameter of 200 nm preventing catalyst detachment, while allowing fast diffusion of reactants. The main challenge with this approach is to achieve complete removal of bubbles in the membrane pores, as bubbles would block diffusion of molecules to the catalysts layer. Fortunately, this can be prevented by pre-wetting the membrane with a solvent with low-surface tension, e.g. isopropanol or ethanol.[91] Afterwards, the ethanol is slowly removed by placing the membrane in a large volume of water with slow agitation for several hours. Brittle ceramic membranes (e.g. silicon membranes) are less suitable for this approach because of mechanical failure during assembly of the cell. Notably, the membrane has no effect on the ATR-IR spectra as it is located above the catalyst layer beyond the penetration depth of the evanescent waves (see Figure 1.9b).
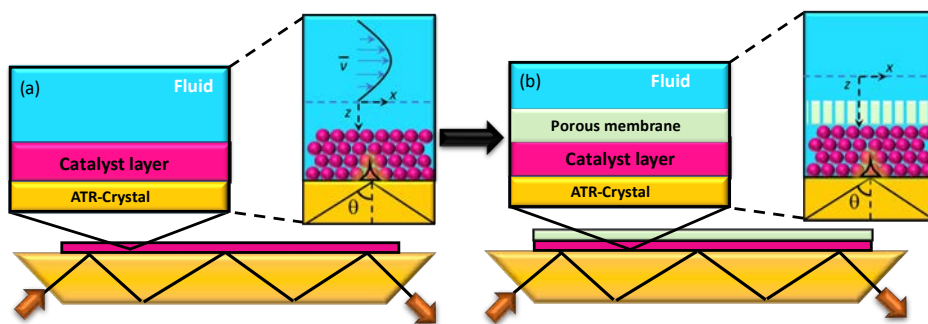

Figure 1.9: Schematic representation of the ATR-IR assembly in the case of catalyst layer (a), catalyst layer with a membrane on top (b).

1.8.2.5 Mass transfer effects on ATR-IR cells

The transport in a flow-through ATR-IR cell involves convection and diffusion processes. Choosing the proper cell architecture and operating conditions is essential to decouple transport effects from the dynamic behavior of the surface chemistry during the catalytic reaction. The external mass transfer (convection and diffusion) is defined as the transport of the reactants from the bulk of the liquid fed to the cell to the catalyst surface.[57] Therefore, to minimize the presence of mass transfer limitations, experiments are preferably conducted at high flow rates in small volumes of analysis, i.e. small ATR-IR cells. The internal mass transfer process, on the other hand, is related to the diffusion of the reactants inside the porous catalytic layer.[57,92] To minimize the diffusion limitations in the catalyst layer, the layer thickness is usually below 10 μm. External mass transfer limitations become relevant when multiple internal reflection elements with high geometrical surface areas are used in the ATR-IR experiments, possibly causing concentration gradients along the length of the flowthrough cell. A concentration gradient inside the ATR cell can be misleading in dynamic experiments as the evolution of the IR peaks of key surface reaction intermediates can be dictated by the rate of transfer rather than the intrinsic reaction kinetics.

Design of experiments can be improved based on basic numerical calculations to determine if the system is under mass transfer limitations.[92–94] For instance, the Sherwood number (see Eq. 1.4) describes the ratio between convective mass transfer and mass transfer by diffusion. The mass transfer coefficient (k_l) can be obtained by Eq. 1.4 when Sh is known from correlations between the Reynolds number and Schmidt number, to estimate the stagnant layer thickness (δ) of the liquid on top of the catalyst layer according $\delta = D_a / k_l$. This information is key when determining the possible impact of increasing the flowrate of the liquid phase in the flow through cell. Similarly, the Peclet number (Pe) (see Eq. 1.5) determines the ratio of the convection rate and diffusion rate in the liquid in the cell. When Pe is larger than unity one can assume that transport in the ATR-IR cell is dominated by molecular diffusion. Furthermore, the Thiele modulus (φ) number (see Eq. 1.6) is defined as the ratio between the rate of reaction and the rate of transport by diffusion inside the porous catalyst layer. In this case, for values of φ significantly lower than unity, internal mass transfer limitations can be neglected.

$$Sh = \frac{mass\ transport\ rate}{diffusion\ rate} = \frac{k_l b}{D_a} \qquad \text{Eq.1.4}$$

$$Pe = \frac{convection\ rate}{diffusion\ rate} = \frac{h\ v}{D_a} \qquad \text{Eq.1.5}$$

$$\varphi = \frac{reaction\ rate}{diffusion\ rate} = b\sqrt{\frac{k_a}{D_{eff,a}}\left(\frac{n+1}{2}\right)C_a^{n-1}} \qquad \text{Eq.1.6}$$

$$D_{eff,a} = D_a\frac{\varepsilon}{\tau} \qquad \text{Eq.1.7}$$

Here, the Sherwood number is Sh, the Peclet number is Pe, the Thiele modulus for an irreversible n^{th} order reaction is φ, the external mass transfer coefficient is k_l, the catalyst height is denoted as b, $D_{eff,a}$ is the effective diffusion coefficient of the specie a in the porous catalyst layer (see Eq. 1.7), D_a is the diffusion coefficient of the specie a, ε is the catalyst porosity obtained from N_2 physisorption, τ is the catalyst tortuosity, v the local flow velocity, h is the height of the ATR-IR cell, k_a is the intrinsic reaction rate constant of specie a, C_a is the initial concentration of the specie a and n^{th} the reaction order.

In addition, experimental tests can be done to determine the extent of mass transfer limitations. For instance, if the flowrate of the liquid phase reactant does not affect the rate of IR signal saturation it is safe to assume that external mass transfer limitations are negligible. Similarly, internal mass transfer limitations in the catalyst coating on the IRE is ruled out when increasing the catalyst layer thickness has no effect on the time needed to reach saturation of the IR peak(s). Finally, varying the particle size of the catalyst and/or pore-size probes intraparticle diffusion limitations.

To obtain more accurate information about the dynamics of the ATR cell, one can employ finite element analysis of the flow through system. The fluid dynamic modelling allows us to determine the interplay between geometry, volumes, flowrates, liquid properties (e.g. viscosity, surface tension, solubility of gaseous species) and the evolution of IR peaks as a

function of time and stimuli employed in the ATR-IR experiment (e.g. temperature, pH, concentrations or pressure).

The timescales of the mass transfer processes depend on the geometry of the cell. A flow through cell with a cylindrical shape has usually higher reactor volumes compared to a flat cell (see Figure 1.10). As a result, the space velocity achieved in the cylindrical systems is lower, which negatively affects the convective transport of the molecules inside the ATR-IR cell. For instance, the geometric volume of a flat cell is c.a. 0.06 mL, while in the case of the cylindrical one this volume is c.a. 2 mL, resulting residence times of 1.6 and 59 s, respectively, for a flow rate of ~ 2 mL min^{-1} (see Table 1.1). Here, one can immediately recognize that selecting a flat cell will be preferred for the study of relatively fast reaction processes. This choice comes at the expense of more complex sealing of the reaction cell and thus operate at milder temperature and pressures, when compared to the cylindrical ones.
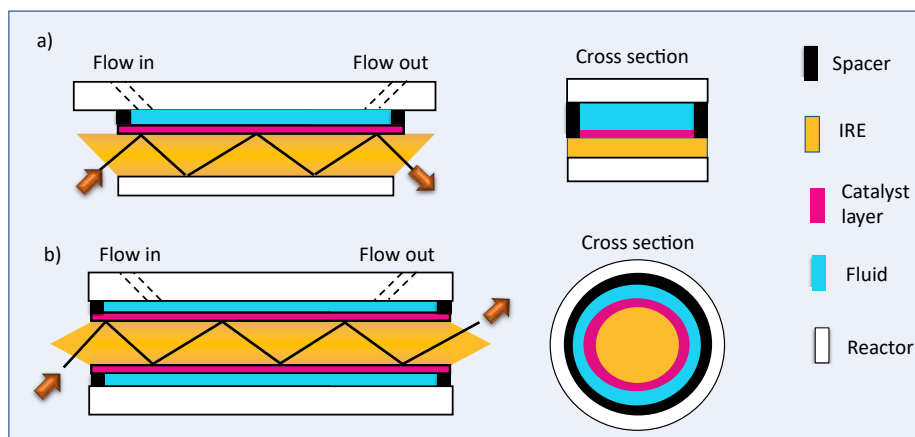
Figure 1.10: Scheme of a flat cell (a) with a ZnSe IRE with the dimensions of 5 cm length and 2 cm width where catalyst is deposited on top surface of the crystal, a cylindrical cell (b) with a ZnSe IRE with the dimensions of 8.25 cm length and diameter of 0.63 cm with catalyst coated on the cylindrical surface of the IRE. The pink layer represents the catalyst layer and the arrows the IR light going in and out of the IRE. The blue layer represents the fluid inside the cell.

The transport phenomena inside an ATR-IR cell can be monitored by following the IR signals of a probe molecule in the bulk of the liquid solution on changing the composition of the feed. As can be noticed in Figure 1.11b, the observed time to reach full saturation (steady state) in the ATR-IR was 14 s and 180 s for flat and cylindrical cells, respectively (see Table 1.1). The large difference is mostly due to the difference in residence time. Note that in these experiments no catalyst layer is present. Adding the porous catalyst to the IRE interface will add an extra delay in the saturation curve as molecules have to travel inside the pores of the catalyst particles to reach the active sites.

Table 1.1: Comparison between flow rate, volume of reactor, residence time, time to reach full saturation of the ATR-IR cell switching from water to a new solution on a flat IRE switching from water to a triton X-100 solution (0.086 mol L^{-1}) [94] and a cylindrical IRE switching from water to a 2.5 wt.% acetone solution [95]. The time to saturate the cell is defined as the time at which the IR signal reaches 99% the maximum intensity.

	Flat IRE	Cylindrical IRE
Flow rate (mL min^{-1})	2.2	2
Cell volume (mL)	0.06	2
Residence time (s)	1.6	59
Time saturation cell (s)	14	180

The concentration profile inside the ATR-IR cell can be calculated assuming that mass transfer is governed by convection and diffusion.[96,97] Note that in this model the diffusion of molecules varies in the x (longitudinal) and z (distance between the surface of the reactor and the IRE) direction (see profile in Figure 1.11aii). Here, one assumes that the system can be described with Fick's first and second laws of diffusion. This essentially limits the approach to ideal systems in which diffusion coefficients can be approximated to those at infinite dilution. In more complex cases involving concentrated multi-component diffusion the Maxwell–Stefan diffusion model should be employed.

Here, the saturation curve can be modelled by averaging the concentrations across the length of the IRE surface, as the absorption of IR light in the evanescent wave at each point of total reflection contributes. As shown in Figure 1.11b, both calculated curves for flat and cylindrical cells agree well with the experimental data. Since this model is based on first principles, it is allowed predict the behavior of the system at higher flowrates, temperatures, and concentrations to optimize cell design and operating conditions for studying catalysts under reactive conditions. For instance, Aguire et al.[94] reported that the time to reach steady state is associated to the solute properties, demonstrating that the steady state can be reached earlier when the probe molecule has a higher diffusion coefficient. The authors observed that switching from water to an aqueous solution of triton X-100 (0.086 mol L^{-1} and diffusion coefficient of $5.5x10^{-7}$ cm^2 s^{-1}) or switching from water to isopropanol (0.65 mol L^{-1} and diffusion coefficient of $0.8x10^{-5}$ cm^2 s^{-1}), the saturation time is shortened from 18 to 8 seconds. Similar observations are reported by Urakawa et al.[97] for experiments in a flat cell with 0.077 mL and a residence time of 3 s (flow rate of 1.9 mL min^{-1}). Using the same flow rate, the authors showed that a compound with higher diffusion coefficient (acetonitrile) filled the reactor faster when compared to a compound with lower diffusion coefficient (hemogoblin). Therefore, a convection-diffusion model is needed to describe the transport inside the ATR-IR cell.
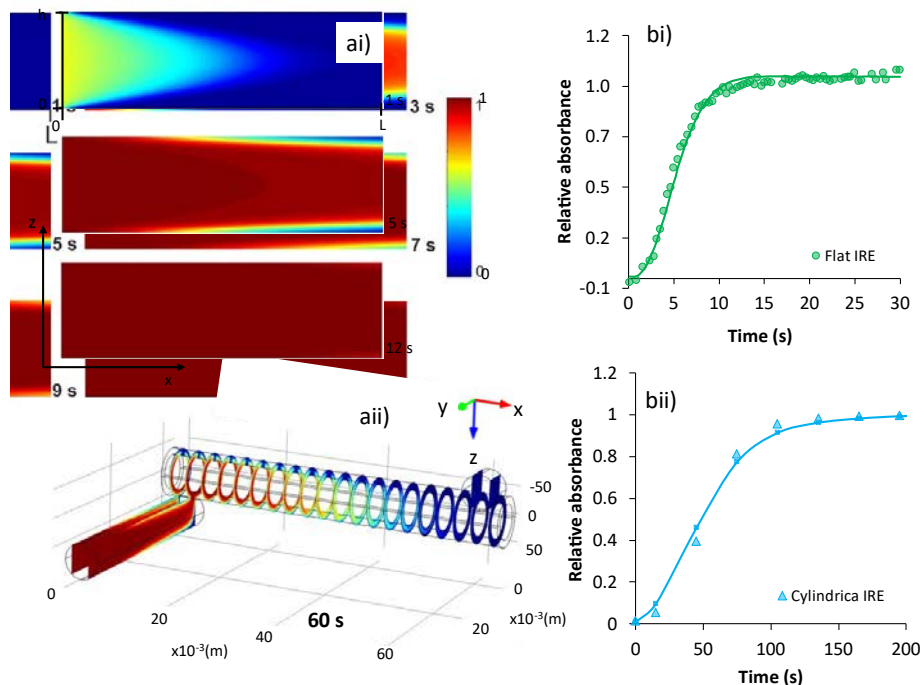
Figure 1.11: (a) Time solved snapshots of the convention-diffusion model after switching from water to triton X-100 solution (0.086 mol L^{-1}) at 25 °C in a flat flow-through ATR-IR cell (ai) [94], and from water to 2.5 wt. % acetone solution at 25 °C and 1 bar after 60 s in a cylindrical flow-through ATR-IR cell. [95] (bi) normalized IR signal as a function of time for Triton x solution (peak at 1097 cm^{-1}) and (bii) normalized peak areas over time (peaks between 1150-950 cm^{-1}) switching from water to 9.2 wt. % glycerol at 25 °C and 1 bar. A similar saturation curve was obtained switching from water to acetone and switching from water to glycerol. The authors used the glycerol solution to compare the model results with the experimental data instead of in the presence of the acetone solution, shown in Figure 1.11ii. The Lines are predictions based on the convection-diffusion model. Details of the experimental conditions see Table 1.1.

1.8.3 Application of ATR-IR in heterogeneous catalysis in liquid phase

One of the challenges in developing fundamentally meaningful models of catalytic reactions is the identification of reaction intermediates, determining kinetics and performance of the catalyst. Rate expressions based on macro-kinetics, typically

represented in terms of power law expressions, provide a coarse but effective way to predict the rate of reaction required for reactor design and operation. Such models, however, do not include details of the reaction mechanism, i.e. identification of intermediate species on the surface and the degree of rate control of specific elementary steps involved in the catalytic reaction, preventing utilization of these models for operating the system outside the window of experimental conditions. Also, the empirical nature of power-law kinetics restricts the development of property-structure-performance relationships that can help to develop improved catalysts.[98,99] In this context, ATR-IR can help in deducing the reaction mechanism by detecting interactions of reactants and reaction intermediates with catalytic surfaces in liquid phase. On one hand, the peak intensity of the surface specie provides a semi-quantitative measure of their relative abundance on the catalyst surface. On the other hand, experiments conducted using *operando* ATR-IR, analyzing the effluent in real-time, can provide kinetic information simultaneously. Such information can be extracted using three modes of operation of ATR-IR spectroscopy, including steady state, transient, and modulation or step response. Here, it is important to be cautious with the interpretation of the data as the surface coverage and thus chemistry varies with the concentration of the reactants and products in the direct vicinity of the active sites. For this reason, it is key to determine the extent of possible effects of mass transfer on the local concentrations.

In the following section we briefly discuss these methods and their application in heterogeneous catalysis. Firstly, steady state operation mode is discussed, i.e. performing a reaction at the catalytic surface by feeding all reactants to the ATR cell. Next, transient mode will be described, in which the surface is first exposed to one reactant followed by exposure to the second reactant. The adsorption and formation of new species is studied by observing the IR peaks over the time.

1.8.3.1 Steady state

In case of steady state operation, the catalytic performance does not change with time by applying constant processing conditions, provided that the catalyst does not undergo deactivation. This implies that reaction rates and, if present, concentration profiles across the reactor or within the catalyst layer do also not change over time. Obviously, measurements require that the system has reached the steady state. The information that

can be obtained from these experiments is limited to detection of reaction intermediates as well as spectator species and, when their extinction coefficients are available, their concentration at the catalyst surface.

For instance, Ebbesen et al.[100] performed *in situ* ATR-IR experiments of nitrite hydrogenation over Pd/Al$_2$O$_3$. In this system, nitrite (NO$_2^-$) reacts with hydrogen (H$_2$) on a metal surface forming nitrogen (N$_2$) and ammonia (NH$_4^+$) (see Eq. 1.8 and 1.9 with Gibbs free energy values at 25 °C).[101]
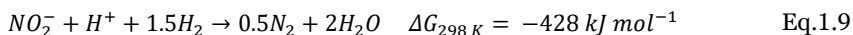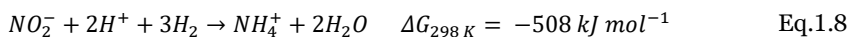
$$NO_2^- + 2H^+ + 3H_2 \rightarrow NH_4^+ + 2H_2O \quad \Delta G_{298\,K} = -508\,kJ\,mol^{-1} \qquad \text{Eq.1.8}$$

$$NO_2^- + H^+ + 1.5H_2 \rightarrow 0.5N_2 + 2H_2O \quad \Delta G_{298\,K} = -428\,kJ\,mol^{-1} \qquad \text{Eq.1.9}$$

Figure 1.12 shows the IR spectra and the saturation curve obtained during reaction between NO$_2^-$ and H$_2$ over a pre-reduced Pd/A$_2$O$_3$ catalyst layer (H-Pd/Al$_2$O$_3$) at two different hydrogen concentrations, approaching the steady state in typically 10 minutes. Note that the profiles observed in the first 10 minutes represent a typical transient experiment, which will be discussed in the next section. Here, four peaks can be observed at 1235, 1450, 1510 and 1720 cm^{-1} in the steady state obtained after 10 minutes. Molecular nitrogen cannot be detected by IR spectroscopy, while in case of NH$_4^+$, although being IR active, adsorbed ammonia cannot be distinct from ammonia in bulk water, complicating data interpretation.[68] The latter issue, i.e. NH$_4^+$ detection, is addressed by conducting experiments where no metal is present to discern between surface and bulk species**.** From this experiment it was determined that the peak located at frequency 1450 cm^{-1} belongs to NH$_4^+$.

The peaks at 1510 and 1720 cm^{-1} were assigned to NO$_{(ads)}$ and NH$_{2(ads)}$, respectively, which are believed to be key intermediate species in the reaction. In the so-called steady state region (after 10 min), it can be observed that, under these experimental conditions, the NH$_{2(ads)}$ had higher peak intensity in comparison to NO$_{(ads)}$. This could be associated to higher metal surface coverage of NH$_{2(ads)}$ compared to NO$_{(ads)}$. The peak at 1235 cm^{-1} was attributed to NO$_2^-$ in solution since it appeared in the same spectral region as in bare ZnSe

IRE (Figure 1.12b-d). One can notice that none of the peaks could be attributed to adsorbed NO_2^- on palladium, indicating that in the presence of hydrogen on the palladium surface NO_2^- is rapidly converted. Furthermore, it is clear that lower amounts of surface intermediates $NO_{(ads)}$, $NH_{2(ads)}$ and NH_4^+ are observed upon decreasing the hydrogen concentration (Figure 1.12b-d). These results suggest slower reaction of the intermediate surface species when decreasing the hydrogen concentration. It should be noted that the assignment of the 1720 cm^{-1} signal to $NH_{2(ads)}$ is still under debate as results of experiments with $^{15}NO_2^-$ and D_2 gave inconsistent results. Therefore, the peak is probably better assigned to a $NH_xO_{y(ads)}$ species with x and y both equal to or larger than 1.[102,103]
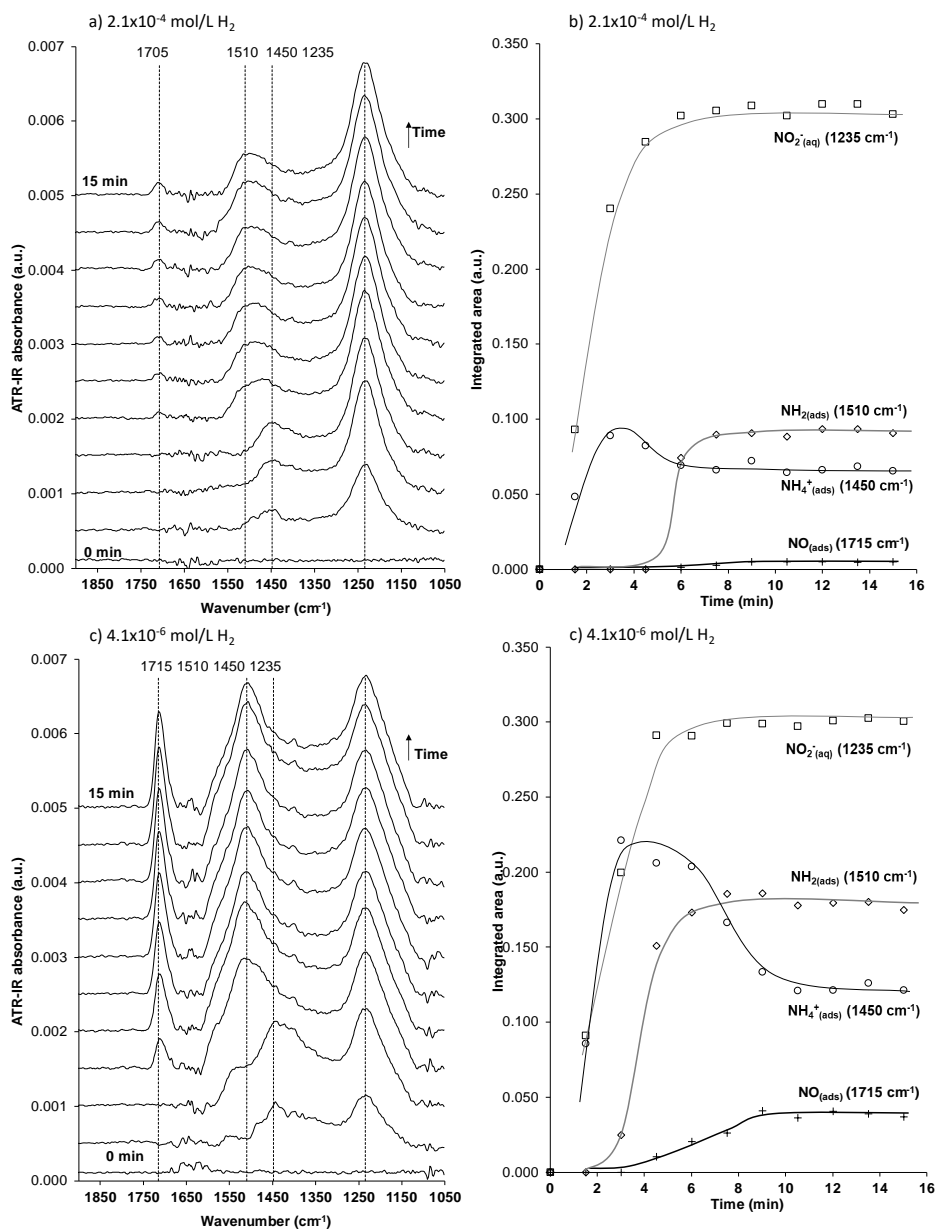
Figure 1.12: Water corrected ATR-IR spectrum from 1900 to 1050 cm^{-1} (a, c) and integrated peak areas (b, d) under steady state experiments of nitrite hydrogenation with a NO$_2^-$ concentration of 4.3x10^{-4} mol L^{-1} and H$_2$ concentration of 2.1x10^{-5} mol L^{-1} (a, b) and 4.1x10^{-4} mol L^{-1} (c,d) at pH 7 over a H-Pd/Al$_2$O$_3$ catalyst containing 5 wt. % Pd and Al$_2$O$_3$ on a 5 µm catalyst layer coated on a ZnSe IRE.[100]

1.8.3.2 Transient state

In transient operation the surface is first exposed to one of the reactants until equilibrium coverage of the adsorbed species is reached. Afterwards, the feed is switched to the second reactant and the evolution of the surface chemistry is followed until a new final state of the spectra is reached. By varying the composition of the feed, it is possible to identify the possible surface reaction intermediates in the catalytic process. The observed rate of conversion can be used to distinguish between kinetically relevant intermediates from any spectator species.

For a transient experiment, the authors performed the adsorption of NO_2^- on a reduced palladium catalyst (H-Pd/Al$_2$O$_3$) containing chemisorbed hydrogen, in absence of hydrogen in the feed. Figure 1.13 shows the observed IR spectra and the saturation curves, observing the same peaks as in the steady state experiments (see Figure 12) at frequencies 1450, 1720, 1510, and 1235 cm^{-1}. In the first 10 minutes, a peak at 1450 cm^{-1} dominated the spectrum in comparison to the peaks at 1720, 1510, and 1235 cm^{-1}. Formation of NH_4^+ on pre-reduced palladium could be associated to the reduction of NO_2^- with hydrogen in the catalyst in the form of palladium hydride and/or chemisorbed hydrogen (H-Pd), as there is no other source of hydrogen available in this system. This observation is in agreement with experimental results in a batch reactor, where excess of hydrogen increased the NH_4^+ formation.[104] Furthermore, while the peak of NH_4^+ continuously decreased, the intensity of the $NH_{2(ads)}$ peak increased, stabilizing when formation of ammonia essentially stopped, as the ammonia concentration became insignificant after 6 minutes by washing out the produced ammonia while flowing through the ATR cell. At that point, chemisorbed hydrogen becomes scarce because the reaction of NO_2^- to NH_4^+ requires a lot of hydrogen. The amount of $NH_{2(ads)}$ saturates, indicating that $NH_{2(ads)}$ formation stopped. In contrast, $NO_{(ads)}$ formation continued for longer time, indicating this reaction pathway is still significant when the surface is poor in chemisorbed hydrogen.
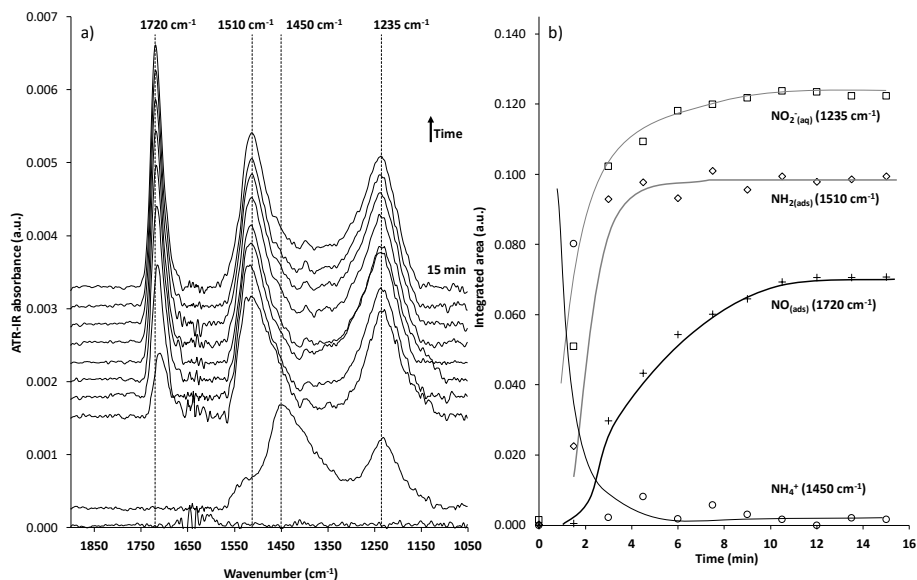
Figure 1.13: (a) water corrected ATR-IR spectra while flowing a solution of $NO_2^-{}_{(aq)}$ (4.3×10^{-4} mol L^{-1}) over H-Pd/Al$_2$O$_3$ at pH 7, (b) integrated peak areas of observed species during NO_2^-(aq) flow over Pd/Al$_2$O$_3$ catalyst containing 5 wt. % Pd and Al$_2$O$_3$.[100]

To study the reactivity of the reaction intermediates after NO_2^- adsorption with hydrogen, the surface at the end of the experiment discussed above was exposed to H$_2$ dissolved in water. As shown in Figure 1.14, NO$_{(ads)}$ was immediately consumed, while the NH$_{2(ads)}$ peak remained constant and NH$_4^+$ is not formed during the first 12 min. This shows that NO$_{(ads)}$ is highly reactive with hydrogen and converts selectively to N$_2$. The authors excluded the hypothesis of NO desorption from the palladium surface because of the strong interaction of NO with the metal site. When the surface is depleted from NO$_{(ads)}$ after typically 15 minutes, conversion of NH$_{2(ads)}$ to NH$_4^+$ is observed. The NH$_4^+$ peak disappeared at the end of the experiment, indicating that NH$_4^+$ binds weakly to the palladium and is again flushed out.
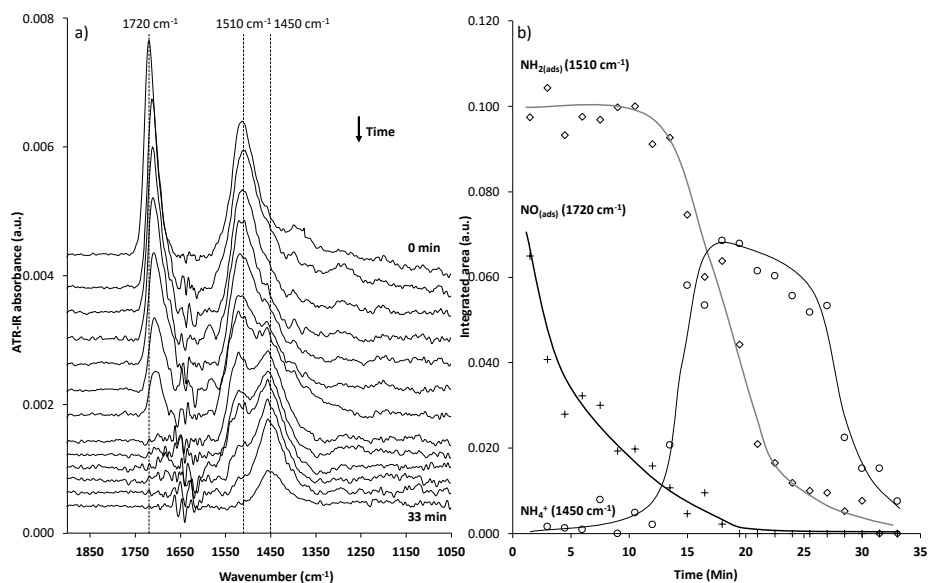
Figure 1.14: (a) water corrected ATR-IR spectra and (b) Integrated peak area during the flow of H_2/H_2O (4.1×10^{-6} mol L^{-1} H_2) over Pd/Al_2O_3 with $NO_{(ads)}$ and $NH_{2(ads)}$ previously formed during the adsorption of NO_2^- on reduced palladium.[100]

Figure 1.15 shows a schematic representation of the catalyst surface during both transient experiments, where adsorption of NO_2^- on $H-Pd/Al_2O_3$ forms $NO_{(ads)}$, NH_4^+ and $NH_{2(ads)}$. The addition of H_2 to the covered surface leads to two independent parallel reactions, where NO yields to N_2 formation and $NH_{2(ads)}$ forms NH_4^+. In this showcase, it becomes clear how powerful ATR-IR spectroscopy under transient conditions can be in unraveling mechanisms of catalytic reaction in aqueous phase.

However, it should also be noted that complementary techniques as well as kinetic studies are also essential as observations are limited to those species that are detectable with IR. A recent rigorous kinetic study on the same catalytic system revealed that the rate determining step depends strongly on the concentrations of the reactants and suggested that N_2 formation proceeds via a dimerization reaction of a partly hydrogenated NOH_x species.[102] Furthermore, kinetic isotope experiments and DFT calculations revealed that the formation reactions of HNO and HNOH on the catalyst surface are co-limiting

and that H transfer proceeds via protons in surrounding water molecules.[103] Such insights obviously cannot be obtained based on ATR-IR only.
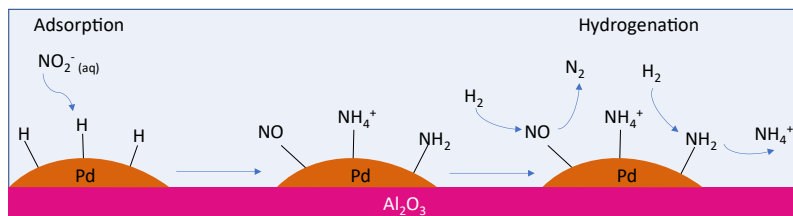
Figure 1.15: Schematic representation of adsorption of NO_2^- and hydrogenation in a palladium alumina catalyst after steady state and transient state experiments on ATR-IR spectroscopy.[105]

1.9 Nitrite hydrogenation as probe for transport and reaction kinetics

In general, agriculture relies on two sources of nitrogen compounds mainly nitrates or ammonium salts. These essential plant fertilizers are produced naturally by either thunderstorms, that can split the bonds between atmospheric nitrogen or by nitrogen fixing soil bacteria (diazotroph). Historically, agriculture has been limited by deficits in nitrogen available to plants in the form of nitrate or ammonium. Nowadays, however, c.a. 80 % of the ammonia produced via the Haber-Bosch (HB) process is used for synthetic nitrogen fertilizer production, which is estimated to feed nearly 70 % of the world population. The annual production of ammonia increased from 16 million tons per year in 1961 to c.a. 160 million tons per year in 2020s.[106–108] The consequence of this huge production of synthetic nitrogen-based fertilizers is the uncontrolled release of nitrates into the groundwater, causing an impact on the biodiversity (eutrophication of water bodies), global warming (e.g. N_2O) and consequences for the human health (e.g. Liver damage).[101,109]

There are various methods to remove nitrates from groundwater sources the easiest among this is biological denitrification, which uses aerobic bacteria to convert the nitrates into nitrogen.[110–112] The drawback of this process are the slow reaction rates, large

volumes of reactor required, and the requirement of the addition of nutrients to feed the bacteria. Other methods for removing nitrates from drinking water includes membrane operations or ion exchange.[113] However, these processes are generally not selective and also remove other beneficial ions from the drinking water. In addition, it will resolve in a concentrated nitrate stream which will need to be treated downstream. Thus, catalytic hydrogenation is the process of choice due to its fast reaction rates and a high selectivity from nitrates to nitrogen. The first step in the process is the reduction of nitrates (NO_3^-) to nitrite (NO_2^-) over a bi-metallic catalyst, i.e. Cu/Pd.[114] The conversion of nitrites to nitrogen is, however, scientifically more challenging due to the undesired co-production of ammonia (see Eq. 1.8 and 1.9).[115,116]

The hydrogenation of nitrites (NO_2^-) is a fast reaction where the catalytic activity and selectivity are dependent on the reaction temperature and concentration profile inside the catalyst particles, making it ideal to study the effect of thermo-responsive polymeric brushes. In consequence, this reaction was selected as a probe reaction to study the effect of polymeric brushes on catalytic systems, where transport and kinetics effects can be coupled. In this way, we can demonstrate if the addition of thermo-responsive polymers can affect transport and the micro-environment near the metal surface.

1.10 Scope and outline

This thesis provides key insights in how to achieve the aforementioned self-regulating mechanism based on temperature by combining diffusion studies, rigorous reaction kinetics, *in-situ* ATR-IR spectroscopy, and detailed molecular transport-reaction modelling.

Chapter 2 is intended to gain more insights on the effect of thermo-responsive polymers in the molecular transport. For this, an idealized catalyst was developed intended to mimic a core-shell nanoparticle (see Figure 1.16 (left side)). In this system, the metal active sites were placed in a porous alumina support, mimicking the core, and the thermo-responsive polymers were coated on a porous membrane with straight channels, mimicking the shell of the catalyst (see Figure 1.16 (right side)). In this way, the polymer has a physical separation from the metal active site avoiding any kinetic effect. The transport was studied under *in-situ* ATR-IR spectroscopy, a technique that allows us to study the polymers behaviour on a dynamic system, which is extremely relevant when considering catalytic reactions.
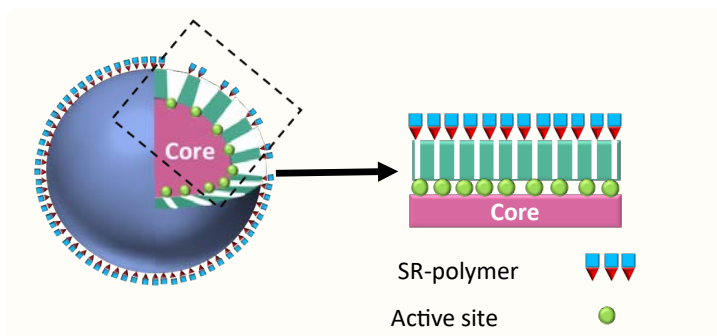
Figure 1.16: (Left side) Schematic representation of a model catalyst made to study the molecular transport in the ATR-IR spectroscopy mimicking the structure of a polymer coated nanoparticle (core-shell). (Right side) System applied on the ATR-IR spectroscopy experiments where the core represents a palladium supported on alumina catalyst and the shell a porous membrane (dark green) polymerized with a thermo responsive polymer.

Next, we applied these thermo-responsive polymers on a more practical system, where the stimulus-responsive polymers are directly coated on a heterogeneous catalyst. **Chapter 3** aims to gain insights into the effect of adding polymeric brushes to a palladium alumina catalyst on the performance in the nitrite hydrogenation reaction. This chapter mainly focuses on solvation effects induced by the addition of polymers in the kinetic regime, i.e. free of any mass transfer limitations.

Chapter 4 aims to unravel the transport effects caused by the conformational changes of the thermo-responsive polymers in the nitrite hydrogenation reaction. A similar catalytic system was used as described in **Chapter 3**, but with larger support particles sizes to induce internal mass transfer limitations.

Chapter 5 summarizes the previous chapters and provides insights on future research directions on thermo-responsive catalyst and their ability to control reaction rates.

1.11 References

[1]   A. Kummer, T. Varga, Feeding trajectory optimization in fed-batch reactor with highly exothermic reactions, Comput. Chem. Eng. 98 (2017) 1–11. https://doi.org/10.1016/j.compchemeng.2016.12.008.

[2]   A. Kummer, T. Varga, What do we know already about reactor runaway? – A review, Process Saf. Environ. Prot. 147 (2021) 460–476. https://doi.org/10.1016/j.psep.2020.09.059.

[3]   V. Hoof, Structural changes in ethylene epoxidation catalysts investigated by transmission electron microscopy Structural changes in Ethylene Epoxidation catalysts investigated by, Eindhoven University of Technology, 2019.

[4]   D. Rebsdat, S; Mayer, Ethylene Oxide, in: Ullmann's Encycl. Ind. Chem., Wiley-VCH Verlag GmbH & Co., 2001: pp. 547–568. https://doi.org/10.1002/14356007.a10_117.

[5]   L. Fratalocchi, C.G. Visconti, G. Groppi, L. Lietti, E. Tronconi, Intensifying heat transfer in Fischer-Tropsch tubular reactors through the adoption of conductive packed foams, Chem. Eng. J. 349 (2018) 829–837. https://doi.org/10.1016/j.cej.2018.05.108.

[6]   G. Prieto, H. Tüysüz, N. Duyckaerts, J. Knossalla, G.H. Wang, F. Schüth, Hollow Nano- and Microstructures as Catalysts, Chem. Rev. 116 (2016) 14056–14119. https://doi.org/10.1021/acs.chemrev.6b00374.

[7]   A. Grinthal, J. Aizenberg, Adaptive all the way down: Building responsive materials from hierarchies of chemomechanical feedback, Chem. Soc. Rev. 42 (2013) 7072–7085. https://doi.org/10.1039/c3cs60045a.

[8]   R. Eelkema, J.H. Van Esch, Catalytic control over the formation of supramolecular materials, Org. Biomol. Chem. 12 (2014) 6292–6296. https://doi.org/10.1039/c4ob01108b.

[9]   F. Xia, L. Jiang, Bio-inspired, smart, multiscale interfacial materials, Adv. Mater. 20 (2008) 2842–2858. https://doi.org/10.1002/adma.200800836.

[10]   X. Liu, Y. Yang, M.W. Urban, Stimuli-Responsive Polymeric Nanoparticles, Macromol. Rapid Commun. 201700030 (2017) 1–20. https://doi.org/10.1002/marc.201700030.

[11]   M. a C. Stuart, W.T.S. Huck, J. Genzer, M. Müller, C. Ober, M. Stamm, G.B. Sukhorukov, I. Szleifer, V. V Tsukruk, M. Urban, F. Winnik, S. Zauscher, I. Luzinov, S. Minko, Emerging applications of stimuli-responsive polymer materials., Nat. Mater. 9 (2010) 101–113. https://doi.org/10.1038/nmat2614.

[12]   T. Chen, R. Ferris, J. Zhang, R. Ducker, S. Zauscher, Stimulus-responsive polymer brushes on surfaces: Transduction mechanisms and applications, Prog. Polym. Sci. 35 (2010) 94–112. https://doi.org/10.1016/j.progpolymsci.2009.11.004.

[13]   X. He, M. Aizenberg, O. Kuksenok, L.D. Zarzar, A. Shastri, A.C. Balazs, J. Aizenberg, Synthetic homeostatic materials with chemo-mechano-chemical self-regulation, Nature. 487 (2012) 214–218. https://doi.org/10.1038/nature11223.

[14]   A. Grinthal, J. Aizenberg, Adaptive all the way down: building responsive materials from hierarchies of chemomechanical feedback., Chem. Soc. Rev. 42 (2013) 7072–85. https://doi.org/10.1039/c3cs60045a.

[15]   B. Zdyrko, I. Luzinov, Polymer Surfaces and Interfaces, 2008.

[16]   B. Zdyrko, I. Luzinov, Polymer brushes by the 'grafting to' method, Macromol. Rapid Commun. 32 (2011) 859–869. https://doi.org/10.1002/marc.201100162.

[17]   F. Liu, M.W. Urban, Recent advances and challenges in designing stimuli-responsive polymers, Prog. Polym. Sci. 35 (2010) 3–23. https://doi.org/10.1016/j.progpolymsci.2009.10.002.

[18]   K. Matyjaszewski, Atom Transfer Radical Polymerization (ATRP): Current Status and Future Perspectives, Macromolecules. 45 (2012) 4015–4039. https://doi.org/10.1021/ma3001719.

[19]   T.G. Ribelli, F. Lorandi, M. Fantin, K. Matyjaszewski, Atom Transfer Radical Polymerization: Billion Times More Active Catalysts and New Initiation Systems, Macromol. Rapid Commun. 40 (2019) 1–44. https://doi.org/10.1002/marc.201800616.

[20]   C.J. Galvin, J. Genzer, Applications of surface-grafted macromolecules derived from post-polymerization modification reactions, Prog. Polym. Sci. 37 (2012) 871–906. https://doi.org/10.1016/j.progpolymsci.2011.12.001.

[21]   T. Wu, K. Efimenko, J. Genzer, Combinatorial study of the mushroom-to-brush crossover in surface anchored polyacrylamide, J. Am. Chem. Soc. 124 (2002) 9394–9395. https://doi.org/10.1021/ja027412n.

[22]   R. Barbey, L. Lavanant, D. Paripovic, N. Schüwer, C. Sugnaux, S. Tugulu, H.A. Klok, Polymer brushes via surface-initiated controlled radical polymerization: synthesis, characterization, properties, and applications, Chem. Rev. 109 (2009) 5437–5527. https://doi.org/10.1021/cr900045a.

[23]   W. De Groot, Smart polymer brushes in nanopores: Towards controlled molecular transport through pore-spanning biomembranes, 2013. https://ris.utwente.nl/ws/files/6059188/thesis_G_de_Groot.pdf.

[24]   P.F. Cao, J.D. Mangadlao, R.C. Advincula, Stimuli-Responsive Polymers and their Potential Applications in Oil-Gas Industry, Polym. Rev. 55 (2015) 706–733. https://doi.org/10.1080/15583724.2015.1040553.

[25]   M.H. Futscher, M. Philipp, P. Müller-Buschbaum, A. Schulte, The Role of Backbone Hydration of Poly(N-isopropyl acrylamide) Across the Volume Phase Transition Compared to its Monomer, Sci. Rep. 7 (2017) 1–10. https://doi.org/10.1038/s41598-017-17272-7.

[26]   B.A. Humphreys, J.D. Willott, T.J. Murdoch, G.B. Webber, E.J. Wanless, Specific ion modulated thermoresponse of poly(N-isopropylacrylamide) brushes, Phys.Chem.Chem.Phys. 18 (2016) 6037–6046. https://doi.org/10.1039/C5CP07468A.

[27]   T.J. Murdoch, B.A. Humphreys, E.C. Johnson, G.B. Webber, E.J. Wanless, Specific ion effects on thermoresponsive polymer brushes: Comparison to other architectures, J. Colloid Interface Sci. 526 (2018) 429–450. https://doi.org/10.1016/j.jcis.2018.04.086.

[28]   Y. Yu, M. Cirelli, B.D. Kieviet, E.S. Kooij, G.J. Vancso, S. de Beer, Tunable friction by employment of co-non-solvency of PNIPAM brushes, Polymer (Guildf). 102 (2016) 372–378. https://doi.org/10.1016/j.polymer.2016.08.029.

[29]   H.C. Lee, T. Heil, J.K. Sun, B.V.K.J. Schmidt, Dispersed nano-MOFs via a stimuli-responsive biohybrid-system with enhanced photocatalytic performance, Mater. Horizons. 6 (2019) 802–809. https://doi.org/10.1039/c8mh01342j.

[30]   X. Mao, W. Tian, J. Wu, G.C. Rutledge, T.A. Hatton, Electrochemically responsive heterogeneous catalysis for controlling reaction kinetics, J. Am. Chem. Soc. 137 (2015) 1348–1355. https://doi.org/10.1021/ja512224g.

[31]   Y. You, K.K. Kalebaila, S.L. Brock, D. Oupicky, Temperature-Controlled Uptake

and Release in PNIPAM-Modified Porous Silica Nanoparticles, Chem. Mater. (2008) 3354–3359. https://doi.org/10.1021/cm703363w.

[32]   Z. Chen, Z. Cui, C. Cao, W. He, L. Jiang, W. Song, Temperature-Responsive Smart Nanoreactors : Poly(N-isopropylacrylamide)-Coated Au@Mesoporous-SiO2 Hollow Nanospheres, Langmuir. 28 (2012) 13452–13458. https://doi.org/10.1021/la3022535.

[33]   S. Wu, J. Dzubiella, J. Kaiser, M. Drechsler, X. Guo, M. Ballauff, Y. Lu, Thermosensitive Au-PNIPA Yolk-Shell Nanoparticles with Tunable Selectivity for Catalysis, Angew. Chemie Int. Ed. 51 (2012) 2229–2233. https://doi.org/10.1002/anie.201106515.

[34]   H. Jia, R. Roa, S. Angioletti-Uberti, K. Henzler, A. Ott, X. Lin, J. Möser, Z. Kochovski, A. Schnegg, J. Dzubiella, M. Ballauff, Y. Lu, Thermosensitive Cu2O-PNIPAM core-shell nanoreactors with tunable photocatalytic activity, J. Mater. Chem. A. 4 (2016) 9677–9684. https://doi.org/10.1039/c6ta03528k.

[35]   L.D. Zarzar, J. Aizenberg, Stimuli-responsive chemomechanical actuation: A hybrid materials approach, Acc. Chem. Res. 47 (2014) 530–539. https://doi.org/10.1021/ar4001923.

[36]   J. Zhang, M. Zhang, K. Tang, F. Verpoort, T. Sun, Polymer-based stimuli-responsive recyclable catalytic systems for organic synthesis, Small. 10 (2014) 32–46. https://doi.org/10.1002/smll.201300287.

[37]   D. Diaz Diaz, D. Kuhbeck, R.J. Koopmans, Stimuli-responsive gels as reaction vessels and reusable catalysts, Chem. Soc. Rev. (2011) 427–448. https://doi.org/10.1039/c005401c.

[38]   R. Roa, W.K. Kim, M. Kanduč, J. Dzubiella, S. Angioletti-Uberti, Catalyzed Bimolecular Reactions in Responsive Nanoreactors, ACS Catal. 7 (2017) 5604–5611. https://doi.org/10.1021/acscatal.7b01701.

[39]   Y. Lu, Y. Mei, M. Drechsler, M. Ballauff, Thermosensitive core-shell particles as carriers for Ag nanoparticles: Modulating the catalytic activity by a phase transition in networks, Angew. Chemie - Int. Ed. 45 (2006) 813–816. https://doi.org/10.1002/anie.200502731.

[40]   M. Kanduč, W.K. Kim, R. Roa, J. Dzubiella, Modeling of stimuli-responsive nanoreactors: Rational rate control towards the design of colloidal enzymes, Mol.

Syst. Des. Eng. 5 (2020) 602–619. https://doi.org/10.1039/c9me00106a.

[41]   S. Angioletti-Uberti, Y. Lu, M. Ballauff, J. Dzubiella, Theory of Solvation-Controlled Reactions in Stimuli-Responsive Nanoreactors, J. Phys. Chem. C. 119 (2015) 15723–15730. https://doi.org/10.1021/acs.jpcc.5b03830.

[42]   P. Hervés, M. Pérez-Lorenzo, L.M. Liz-Marzán, J. Dzubiella, Y. Lub, M. Ballauff, Catalysis by metallic nanoparticles in aqueous solution: Model reactions, Chem. Soc. Rev. 41 (2012) 5577–5587. https://doi.org/10.1039/c2cs35029g.

[43]   D.T. Bregante, A.M. Johnson, A.Y. Patel, E.Z. Ayla, M.J. Cordon, B.C. Bukowski, J. Greeley, R. Gounder, D.W. Flaherty, Cooperative effects between hydrophilic pores and solvents: Catalytic consequences of hydrogen bonding on alkene epoxidation in zeolites, J. Am. Chem. Soc. 141 (2019) 7302–7319. https://doi.org/10.1021/jacs.8b12861.

[44]   N.S. Gould, S. Li, H.J. Cho, H. Landfield, S. Caratzoulas, D. Vlachos, P. Bai, B. Xu, Understanding solvent effects on adsorption and protonation in porous catalysts, Nat. Commun. 11 (2020) 1–13. https://doi.org/10.1038/s41467-020-14860-6.

[45]   S. Mukherjee, M.A. Vannice, Solvent effects in liquid-phase reactions. I. Activity and selectivity during citral hydrogenation on Pt/SiO2 and evaluation of mass transfer effects, J. Catal. 243 (2006) 108–130. https://doi.org/10.1016/j.jcat.2006.06.021.

[46]   M.A. Mellmer, C. Sener, J.M.R. Gallo, J.S. Luterbacher, D.M. Alonso, J.A. Dumesic, Solvent Effects in Acid-Catalyzed Biomass Conversion Reactions, Angew. Chemie - Int. Ed. 1 (2014) 11872–11875. https://doi.org/10.1002/anie.201408359.

[47]   D. Sicinska, D.G. Truhlar, P. Paneth, Solvent-dependent transition states for decarboxylations, J. Am. Chem. Soc. 123 (2001) 7683–7686. https://doi.org/10.1021/ja010791k.

[48]   G. Li, B. Wang, D.E. Resasco, Solvent effects on catalytic reactions and related phenomena at liquid-solid interfaces, Surf. Sci. Rep. (2021) 100541. https://doi.org/10.1016/j.surfrep.2021.100541.

[49]   Z. Zhao, R. Bababrik, W. Xue, Y. Li, N.M. Briggs, D.T. Nguyen, U. Nguyen, S.P. Crossley, S. Wang, B. Wang, D.E. Resasco, Solvent-mediated charge separation drives alternative hydrogenation path of furanics in liquid water, Nat. Catal. 2

(2019) 431–436. https://doi.org/10.1038/s41929-019-0257-z.

[50]   N. Singh, M.S. Lee, S.A. Akhade, G. Cheng, D.M. Camaioni, O.Y. Gutiérrez, V.A. Glezakou, R. Rousseau, J.A. Lercher, C.T. Campbell, Impact of pH on Aqueous-Phase Phenol Hydrogenation Catalyzed by Carbon-Supported Pt and Rh, ACS Catal. 9 (2019) 1120–1128. https://doi.org/10.1021/acscatal.8b04039.

[51]   A.R. Riscoe, C.J. Wrasman, A.A. Herzing, A.S. Hoffman, A. Menon, A. Boubnov, M. Vargas, S.R. Bare, M. Cargnello, Transition state and product diffusion control by polymer–nanocrystal hybrid catalysts, Nat. Catal. 2 (2019) 852–863. https://doi.org/10.1038/s41929-019-0322-7.

[52]   S.D. Ebbesen, B.L. Mojet, L. Lefferts, In situ ATR-IR study of nitrite hydrogenation over Pd/Al2O3, J. Catal. 256 (2008) 15–23. https://doi.org/10.1016/j.jcat.2008.02.013.

[53]   H. Topsøe, Developments in operando studies and in situ characterization of heterogeneous catalysts, J. Catal. 216 (2003) 155–164. https://doi.org/10.1016/S0021-9517(02)00133-1.

[54]   J.-M. Andenason, A. Baiker, In-situ characterization of heterogeneous catalysts themed issue, Chem. Soc. Rev. (2010). https://doi.org/10.1039/b919544k.

[55]   J.M. Dreimann, E. Kohls, H.F.W. Warmeling, M. Stein, L.F. Guo, M. Garland, T.N. Dinh, A.J. Vorholt, In Situ Infrared Spectroscopy as a Tool for Monitoring Molecular Catalyst for Hydroformylation in Continuous Processes, ACS Catal. 9 (2019) 4308–4319. https://doi.org/10.1021/acscatal.8b05066.

[56]   A. Aguirre, C.L.A. Berli, S.E. Collins, ATR-FTIR spectrokinetic analysis of the CO adsorption and oxidation at water/platinum interface, Catal. Today. 283 (2017) 127–133. https://doi.org/10.1016/j.cattod.2016.03.042.

[57]   L. Rodríguez-García, R. Walker, E. Spier, K. Hungerbühler, F. Meemken, Mass transfer considerations for monitoring catalytic solid-liquid interfaces under operating conditions, React. Chem. Eng. 3 (2018) 55–67. https://doi.org/10.1039/c7re00179g.

[58]   B.L. Mojet, S.D. Ebbesen, L. Lefferts, Light at the interface: The potential of attenuated total reflection infrared spectroscopy for understanding heterogeneous catalysis in water, Chem. Soc. Rev. 39 (2010) 4643–4655. https://doi.org/10.1039/c0cs00014k.

[59]   A. Götz, R. Nikzad-Langerodi, Y. Staedler, A. Bellaire, J. Saukel, Apparent penetration depth in attenuated total reflection Fourier-transform infrared (ATR-FTIR) spectroscopy of Allium cepa L. epidermis and cuticle, Spectrochim. Acta - Part   A   Mol.   Biomol.   Spectrosc.   224   (2020)   1–6. https://doi.org/10.1016/j.saa.2019.117460.

[60]   B.L. Mojet, S.D. Ebbesen, L. Lefferts, Light at the interface: the potential of attenuated total reflection infrared spectroscopy for understanding heterogeneous catalysis   in   water,   Chem.   Soc.   Rev.   39   (2010)   4643. https://doi.org/10.1039/c0cs00014k.

[61]   K. Koichumanova, K. Koichumanova, In situ Infrared Spectroscopy under Hydrothermal Conditions application for aqueous phase reforming, 2015. https://doi.org/10.3990/1.9789036539630.

[62]   B. Schrader, Infrared and Raman Spectroscopy, Method and Applications, 1996. https://doi.org/10.1016/0924-2031(00)00065-5.

[63]   J. W. Niemantsverdriet, Spectroscopy in catalysis, 2007.

[64]   G. Blyholder, Molecular orbital view of chemisorbed carbon monoxide, J. Phys. Chem. 68 (1964) 2772–2778. https://doi.org/10.1021/j100792a006.

[65]   M.C.J. Bradford, M.A. Vannice, Estimation of CO heats of adsorption on metal surfaces from vibrational spectra, Ind. Eng. Chem. Res. 35 (1996) 3171–3178. https://doi.org/10.1021/ie960016r.

[66]   U. Hanefeld, L. Lefferts, Catalysis: an integrated textbook for student, 2018.

[67]   S.D. Ebbesen, B.L. Mojet, L. Lefferts, The influence of water and pH on adsorption and oxidation of CO on Pd/Al2O3--an investigation by attenuated total reflection infrared spectroscopy., Phys. Chem. Chem. Phys. 11 (2009) 641–649. https://doi.org/10.1039/b814605e.

[68]   S.D. Ebbesen, B.L. Mojet, L. Lefferts, A. No, N.H. Oh, P. Al, P. Al O, In Situ Attenuated Total Reflection Infrared (ATR-IR) Study of the Adsorption of NO , NH OH , and NH on Pd / Al O and Pt / Al O In Situ Attenuated Total Reflection Infrared (ATR-IR) Study of the, (2008) 869–879.

[69]   J.-M. Andanson, A. Baiker, Exploring catalytic solid/liquid interfaces by in situ attenuated total reflection infrared spectroscopy, Chem. Soc. Rev. 39 (2010) 4571. https://doi.org/10.1039/b919544k.

[70]   T. Bürgi, A. Baiker, Attenuated Total Reflection Infrared Spectroscopy of Solid Catalysts Functioning in the Presence of Liquid-Phase Reactants, Adv. Catal. 50 (2006) 227–283. https://doi.org/10.1016/S0360-0564(06)50005-7.

[71]   G. Mul, G.M. Hamminga, J.A. Moulijn, Operando ATR-FTIR analysis of liquid-phase catalytic reactions: Can heterogeneous catalysts be observed?, Vib. Spectrosc. 34 (2004) 109–121. https://doi.org/10.1016/j.vibspec.2003.07.004.

[72]   J. Zakzeski, R.J.H. Grisel, A.T. Smit, B.M. Weckhuysen, Solid acid-catalyzed cellulose hydrolysis monitored by in situ Atr-Ir spectroscopy, ChemSusChem. 5 (2012) 430–437. https://doi.org/10.1002/cssc.201100631.

[73]   D. Ferri, T. Bürgi, A. Baiker, In situ ATR-IR study of the adsorption of cinchonidine on Pd/Al2O3: Differences and similarities with adsorption on Pt/Al2O3, J. Catal. 210 (2002) 160–170. https://doi.org/10.1006/jcat.2002.3660.

[74]   N.S. Gould, B. Xu, Catalyst characterization in the presence of solvent: Development of liquid phase structure-activity relationships, Chem. Sci. 9 (2018) 281–287. https://doi.org/10.1039/c7sc03728g.

[75]   C.J. Baranowski, T. Fovanna, M. Roger, M. Signorile, J. McCaig, A.M. Bahmanpour, D. Ferri, O. Kröcher, Water Inhibition of Oxymethylene Dimethyl Ether Synthesis over Zeolite H-Beta: A Combined Kinetic and in Situ ATR-IR Study, ACS Catal. 10 (2020) 8106–8119. https://doi.org/10.1021/acscatal.0c01805.

[76]   I.R. Andvaag, T.A. Morhart, O.J.R. Clarke, I.J. Burgess, Hybrid Gold-Conductive Metal Oxide Films for Attenuated Total Reflectance Surface Enhanced Infrared Absorption Spectroscopy, ACS Appl. Nano Mater. 2 (2019) 1274–1284. https://doi.org/10.1021/acsanm.8b02155.

[77]   R.A. van Santen, Insensitive Catalytic Relationships, Acc. Chem. Res. 42 (2009) 57–66.

[78]   D. Ferri, T. Bürgi, An in situ attenuated total reflection infrared study of a chiral catalytic solid-liquid interface: Cinchonidine adsorption on Pt, J. Am. Chem. Soc. 123 (2001) 12074–12084. https://doi.org/10.1021/ja011769u.

[79]   D. Ferri, T. Biirgi, A. Baiker, Pt and Pt/Al2O3 thin films for investigation of catalytic solid-liquid interfaces by ATR-IR spectroscopy: CO adsorption, ha-

induced reconstruction and surface-enhanced absorption, J. Phys. Chem. B. 105 (2001) 3187–3195. https://doi.org/10.1021/jp002268i.

[80]   M. Moradzaman, G. Mul, Infrared Analysis of Interfacial Phenomena during Electrochemical Reduction of CO2over Polycrystalline Copper Electrodes, ACS Catal. 10 (2020) 8049–8057. https://doi.org/10.1021/acscatal.0c02130.

[81]   S.D. Ebbesen, Spectroscopy under the surface, In-Situ ATR-IR studies of Hetergeneous Catalysis in Water, 2007.

[82]   N. Maeda, S. Sano, T. Mallat, K. Hungerbühler, A. Baiker, Heterogeneous asymmetric hydrogenation of activated ketones: Mechanistic insight into the role of alcohol products by in situ modulation-excitation IR spectroscopy, J. Phys. Chem. C. 116 (2012) 4182–4188. https://doi.org/10.1021/jp210939d.

[83]   S.D. Ebbesen, B.L. Mojet, L. Lefferts, Effect of pH on the Nitrite Hydrogenation Mechanism over Pd/Al2O3 and Pt/Al2O3: Details Obtained with ATR-IR Spectroscopy, J. Phys. Chem. C. (2011) 1186–1194. https://doi.org/10.1021/jp106521t.

[84]   C. Keresszegi, D. Ferri, T. Mallat, A. Baiker, Unraveling the surface reactions during liquid-phase oxidation of benzyl alcohol on Pd/Al2O3: An in situ ATR-IR study, J. Phys. Chem. B. 109 (2005) 958–967. https://doi.org/10.1021/jp0459864.

[85]   K. Koichumanova, K.B. Sai Sankar Gupta, L. Lefferts, B.L. Mojet, K. Seshan, An in situ ATR-IR spectroscopy study of aluminas under aqueous phase reforming conditions, Phys. Chem. Chem. Phys. 17 (2015) 23795–23804. https://doi.org/10.1039/C5CP02168E.

[86]   K. Koichumanova, A.K.K. Vikla, R. Cortese, F. Ferrante, K. Seshan, D. Duca, L. Lefferts, In situ ATR-IR studies in aqueous phase reforming of hydroxyacetone on Pt/ZrO2 and Pt/AlO(OH) catalysts: The role of aldol condensation, Appl. Catal. B Environ. 232 (2018) 454–463. https://doi.org/10.1016/j.apcatb.2018.03.090.

[87]   M.J. Enes da Silva, A. Banerjee, L. Lefferts, J.A.F. Albanese, In-situ ATR-IR Spectroscopy Reveals Complex Absorption-Diffusion Dynamics in Model Polymer-Membrane-Catalyst Assemblies (PCMA), ChemCatChem. (2022). https://doi.org/10.1002/cctc.202101835.

[88]   M.J.E. da Silva, L. Lefferts, J.A. Faria Albanese, N-isopropylacrylamide polymer

brushes alter the micro-solvation environment during aqueous nitrite hydrogenation on Pd/Al2O3 catalyst, J. Catal. 402 (2021) 114–124. https://doi.org/10.1016/j.jcat.2021.08.003.

[89]   Y.X. Chen, A. Miki, S. Ye, H. Sakai, M. Osawa, Formate, an active intermediate for direct oxidation of methanol on Pt electrode, J. Am. Chem. Soc. 125 (2003) 3680–3681. https://doi.org/10.1021/ja029044t.

[90]   UV-VIS-IR Optical Materials, Https://Harricksci.Com/Optics/Windows/. (n.d.).

[91]   J. Guan, K.L. Fujimoto, M.S. Sacks, W.R. Wagner, Preparation and characterization of highly porous, biodegradable polyurethane scaffolds for soft tissue applications, Biomaterials. 26 (2005) 3961–3971. https://doi.org/10.1016/j.biomaterials.2004.10.018.

[92]   R. Hansen, H. Bruus, T.H. Callisen, O. Hassager, Transient Convection, Diffusion, and Adsorption in Surface-Based Biosensors, Langmuir. (2012) 7557–7563. https://doi.org/10.1021/la3000763.

[93]   A. Aguirre, C.L.A. Berli, S.E. Collins, ATR-FTIR spectrokinetic analysis of the CO adsorption and oxidation at water/platinum interface, Catal. Today. 283 (2017) 127–133. https://doi.org/10.1016/j.cattod.2016.03.042.

[94]   A. Aguirre, P.A. Kler, C.L.A. Berli, S.E. Collins, Design and operational limits of an ATR-FTIR spectroscopic microreactor for investigating reactions at liquid-solid interface, Chem. Eng. J. 243 (2014) 197–206. https://doi.org/10.1016/j.cej.2014.01.001.

[95]   K. Koichumanova, A. Visan, B. Geerdink, R.G.H. Lammertink, B.L. Mojet, K. Seshan, L. Lefferts, ATR-IR spectroscopic cell for in situ studies at solid-liquid interface at elevated temperatures and pressures, Catal. Today. 283 (2017) 185–194. https://doi.org/10.1016/j.cattod.2016.06.034.

[96]   R.B. Bird, W.E. Stewart, E.N. Lightfoot, Transport Phenoma, John Wiley & Sons, 2006.

[97]   A. Urakawa, R. Wirz, T. Bürgi, A. Baiker, ATR-IR Flow-Through Cell for Concentration Modulation Excitation Spectroscopy: Diffusion Experiments and Simulations, J. Phys. Chem. B. 107 (2003) 13061–13068. https://doi.org/10.1021/jp0359889.

[98]   M.A. Bañares, Operando methodology: Combination of in situ spectroscopy and

simultaneous activity measurements under catalytic reaction conditions, Catal. Today. 100 (2005) 71–77. https://doi.org/10.1016/j.cattod.2004.12.017.

[99]   F.C. Meunier, The design and testing of kinetically-appropriate operando spectroscopic cells for investigating heterogeneous catalytic reactions, Chem. Soc. Rev. 39 (2010) 4602. https://doi.org/10.1039/b919705m.

[100]   S.D. Ebbesen, B.L. Mojet, L. Lefferts, In situ ATR-IR study of nitrite hydrogenation over Pd/Al2O3, J. Catal. 256 (2008) 15–23. https://doi.org/10.1016/j.jcat.2008.02.013.

[101]   C.A. Clark, C.P. Reddy, H. Xu, K.N. Heck, G. Luo, T.P. Senftle, M.S. Wong, Mechanistic insights into ph-controlled nitrite reduction to ammonia and hydrazine over rhodium, ACS Catal. 10 (2020) 494–509. https://doi.org/10.1021/acscatal.9b03239.

[102]   P. Xu, S. Agarwal, L. Lefferts, Mechanism of nitrite hydrogenation over Pd/γ-Al2O3 according a rigorous kinetic study, J. Catal. 383 (2020) 124–134. https://doi.org/10.1016/j.jcat.2020.01.003.

[103]   P. Huang, Y. Yan, A. Banerjee, L. Lefferts, B. Wang, J.A. Faria Albanese, Proton Shuttling Flattens the Energy Landscape of Nitrite Catalytic Reduction, (2022) 1–30. https://doi.org/10.2139/ssrn.4056131.

[104]   P. Xu, S. Agarwal, L. Lefferts, Mechanism of nitrite hydrogenation over Pd/γ-Al2O3 according a rigorous kinetic study, J. Catal. 383 (2020) 124–134. https://doi.org/10.1016/j.jcat.2020.01.003.

[105]   S.D. Ebbesen, In-Situ ATR-IR studies of Hetergeneous Catalysis in Water, 2007.

[106]   C. Smith, A.K. Hill, L. Torrente-Murciano, Current and future role of Haber-Bosch ammonia in a carbon-free energy landscape, Energy Environ. Sci. 13 (2020) 331–344. https://doi.org/10.1039/c9ee02873k.

[107]   J.N. Galloway, A.R. Townsend, J.W. Erisman, M. Bekunda, Z. Cai, J.R. Freney, L.A. Martinelli, S.P. Seitzinger, M.A. Sutton, Transformation of the Nitrogen Cycle : Recent Trends, Questions, and Potential Solutions, Science (80-.). 320 (2008) 889–892.

[108]   J.A. Faria, Renaissance of ammonia synthesis for sustainable production of energy and fertilizers, Curr. Opin. Green Sustain. Chem. 29 (2021) 100466. https://doi.org/10.1016/j.cogsc.2021.100466.

[109]   K.N. Heck, S. Garcia-Segura, P. Westerhoff, M.S. Wong, Catalytic Converters for Water Treatment, Acc. Chem. Res. 52 (2019) 906–915. https://doi.org/10.1021/acs.accounts.8b00642.

[110]   W.G. Zumft, Cell biology and molecular basis of denitrification., Microbiol. Mol. Biol. Rev. 61 (1997) 533–616. https://doi.org/10.1128/.61.4.533-616.1997.

[111]   B. Krause, K.H. Nealson, Physiology and enzymology involved in denitrification by Shewanella putrefaciens, Appl. Environ. Microbiol. 63 (1997) 2613–2618. https://doi.org/10.1128/aem.63.7.2613-2618.1997.

[112]   F. Rezvani, M.H. Sarrafzadeh, S. Ebrahimi, H.M. Oh, Nitrate removal from drinking water with a focus on biological methods: a review, Environ. Sci. Pollut. Res. 26 (2019) 1124–1141. https://doi.org/10.1007/s11356-017-9185-0.

[113]   Archna, S.K. Sharma, R.C. Sobti, Nitrate removal from ground water: A review, E-Journal Chem. 9 (2012) 1667–1675. https://doi.org/10.1155/2012/154616.

[114]   Y. Sakamoto, Y. Kamiya, T. Okuhara, Selective hydrogenation of nitrate to nitrite in water over Cu-Pd bimetallic clusters supported on active carbon, J. Mol. Catal. A Chem. 250 (2006) 80–86. https://doi.org/10.1016/j.molcata.2006.01.041.

[115]   S. Hôrold, T. Tacke, K.D. Vorlop, Catalytical removal of nitrate and nitrite from drinking water: 1. screening for hydrogenation catalysts and influence of reaction conditions on activity and selectivity, Environ. Technol. (United Kingdom). 14 (1993) 931–939. https://doi.org/10.1080/09593339309385367.

[116]   A. Pintar, G. Berčič, J. Levec, Catalytic liquid-phase nitrite reduction: Kinetics and catalyst deactivation, AIChE J. 44 (1998) 2280–2292. https://doi.org/10.1002/aic.690441017.

Chapter 2

Leveraging *In-situ* ATR-IR spectroscopy to unravel the interplay between absorption and diffusion processes in model polymer-membrane-catalyst assembly (PCMA)

Abstract

Molecular transport in porous membranes plays an essential role in diverse range of applications (food, catalysis, separation processes, etc.). Here, we have studied a Polymer-Membrane-Catalyst Assembly (PCMA) system consisting of PET membranes with a well-defined pore structure coated with thermo-responsive polymer (p-NIPAM) coupled to an in-situ ATR-IR cell containing a detection layer based on palladium nanoparticles supported on Al_2O_3. This PCMA model is designed to mimic the structure of a core-shell porous particle coated externally with stimulus-responsive polymer. At low temperatures (< 32 ºC), where p-NIPAM is in its swollen state, the addition of polymer brushes (PCMA) caused a delay in CO chemisorption on Pd as observed with in-situ ATR-IR. Strikingly, when the polymer collapses due to an increase of temperature above the Lower Critical Solution Temperature (LCST) (>32 °C), we observed faster CO adsorption. Our multi-physics model of the CO transport and chemisorption on the PCMA suggests that the delay in the molecular transport is caused by the strong affinity of the CO molecules with the polymer brushes. When stimulus-responsive polymers are present, a complex interplay between diffusion and absorption determines the dynamic behaviour of the system. Furthermore, we demonstrate that this behaviour could be reversed by reducing the amount of the polymer inside the pores with respect to the surface, in which the delay observed is now above the LCST. This knowledge provides new insights on the dynamics of transport, absorption, and chemisorption processes occurring on the so-called nano-reactors, that consist of stimuli responsive polymers coated on nano particles, which can have great implications in the development of new self-regulating catalysts.

2.1 Introduction

Combining catalytic materials with responsive polymers to create so-called "nano-reactors" that respond to external stimulus, has been demonstrated as a powerful tool for precise control of selectivity, stability, and recyclability in liquid environments.[1] These soft coatings undergo fully reversible conformational transitions from solvated to aggregated states upon reaching a critical solubility limit, which is triggered by temperature, pH, magnetic field, and/or light.[2–4] In this context, thermo-responsive poly-n-isopropylacrylamide (p-NIPAM) is considered as the archetypal coating of stimulus-responsive catalysts. The first description of these catalytic materials was reported by the group of M. Ballauff using p-NIPAM brushes covalently attached to the surface of a polystyrene core decorated by silver nanoclusters for the reduction of 4-nitrophenol (NPh) by sodium boron hydride.[5] These p-NIPAM brushes have a lower critical solution temperature (LCST) of c.a. 32 °C. Below this temperature the water molecules solvate the polymer thanks to the enthalpic H-bonding interactions with the N-H and C=O motives of p-NIPAM. In the swollen state, the reduction of NPh could be conducted at similar rates as those observed over the uncoated catalyst. As the temperature increased, the entropic contributions to the Gibbs free energy of the system dominate, expelling the water from the polymer domains and triggering the polymer collapse into a globular-like structure.[6] At these conditions the reaction rate slowed down due to the lower effective diffusion coefficient of the reactants through the collapsed p-NIPAM layer around the catalyst. More recently, the authors reported a theoretical framework for describing this system in which the observed kinetic constant (k_{obs}) was defined as two resistances in series (i.e. $k_{obs}^{-1} = k_r^{-1} + k_d^{-1}$).[7] The model was limited to first order reaction rates and the kinetic constant (k_r) of the coated catalyst was assumed to be the same of that observed on the normal catalyst. The diffusion constant (k_d) was assumed to follow the Debye–Smoluchowski theory, which for an egg-shell catalyst can be simplified to $k_d = 4\pi c_0 R_g P$, where c_0 was the initial concentration of the limiting reactant, R_g was the thickness of the polymer layer, and P was the permeability as defined by $P = D_g exp\left(\frac{-\Delta G_{sol}}{k_b T}\right)$. Here, it became clear that to manipulate the reaction rates using these stimulus-responsive (SR) polymers in egg-shell catalysts, the system must be mass transfer limited in either the swollen or de-swollen states of the p-NIPAM (see Figure 2.1b – negative stimulus-responsive).[6] In turn, the observed kinetics in the mass transport limited regime were linearly affected by the effective diffusion of the reactant in the polymer matrix (D_g), while the Gibbs free energy change of solvation exponentially

influenced the rate. This definition of the observed kinetic constant properly described also the experiments in which the reaction rate of the hydrogenation reaction of hydrophobic substrates increased even when the polymer collapsed at temperatures above the LCST. Since the ΔG_{sol} was dependent on both the reactant-polymer and reactant-solvent interactions the "solvation" of the non-polar reactant increased in the hydrophobic polymer matrix. This elegant approach offered a theoretical basis for the study of more complex reaction systems demonstrating its robustness.[4,8–12]
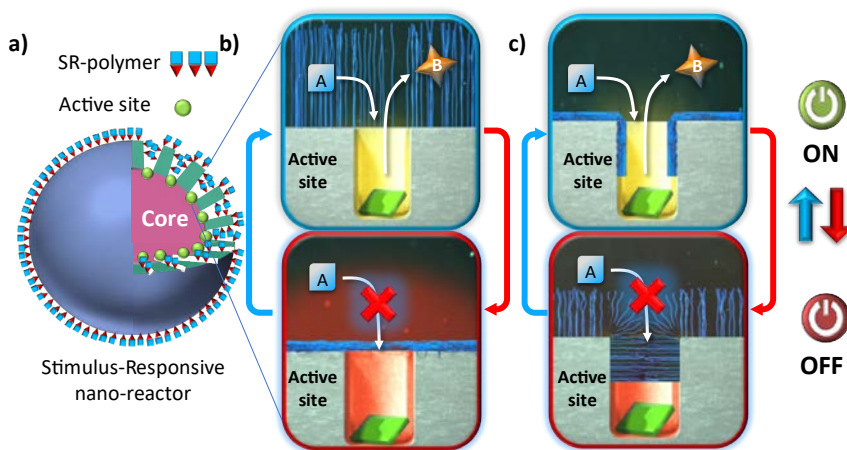
Figure 2.1: Schematic illustration of stimulus-responsive nano-reactor (a) operating under negative stimulus-response (b) in which the collapse of the polymer coatings leads to a mass transport limitation that switches OFF the catalyst, and with a positive stimulus-responsive (c) in which the opposite occurs.

Extrapolating the use of stimulus-responsive polymers to drug delivery, separation processes, wastewater treatment and bio-sensors applications has enabled precise regulation of the permeability and selectivity via flexible adjustment of pore sizes and surface properties.[13–15] In stark contrast to the responsive nano-reactor, in the case of polymer-coated membranes the molecular transport is hindered when the polymer is in the swollen state due to the reduction of the pore diameter (see Figure 2.1c – positive stimulus-responsive). This inverted effect has been employed to create so-called thermo-mechanical actuation of valves across different length-scales. For instance, Y. Park et

al.[16] reported a reversible self-actuated membrane based on thermo-responsive p-NIPAM gels. The smart membranes consisted of a body frame macroscopic p-NIPAM polymer confined in a polytetrafluoroethylene (PTFE) assembling. The confined p-NIPAM at low temperatures was swollen by water, which resulted in a complete closure of the millimetre pores. By increasing the temperature to 40 °C the polymer was dehydrated shrinking the p-NIPAM polymer and opening the pores. Z. B. Zhang et al.[17] reported a thermo- and pH-responsive nylon membrane prepared via consecutive surface-initiated atom transfer radical polymerizations (ATRPs) of N-isopropylacrylamide. In this case, the bare Nylon micro-filtration membranes with pore sizes of ~ 5 µm showed fluxes that varied from 3 to 3.1 mL cm^{-2} min^{-1} as temperature increased, while the p-NIPAM coated counterparts showed a temperature-dependent flux with values that decreased from 0.16 to 0.05 mL cm^{-2} min^{-1} at 45 and 25 °C, respectively. Notably, decreasing further the pore-size of the membrane greatly impacted the observed trends. H. Alem et al.[18] demonstrated that in p-NIPAM coated poly(ethyleneterephthalate) (PET) membranes with track-etched straight channels of 330 nm the permeability monotonically increased as temperature increased, while in the small pore membranes with 80 nm the opposite trend was observed. The authors argued that in the former system the diffusion was primarily controlled by the effective pore size, which at low temperatures was reduced by the swollen state of the polymer. In the latter, however, the diffusion was speculated to be limited by the transport through the polymer layer at the pore-mouth, resembling the observed trends in micro-gels.

While these results provide a broader view of the complexity of the transport processes occurring on stimulus-responsive membranes, very little is known about the dynamic behavior of these materials, which is essential when coupled to catalytic materials. The concept of stimuli responsive catalysts implies a discontinuous behaviour, where the catalytic activity can be switched 'ON' and 'OFF' above or below a certain threshold value of the triggering variable (e.g. temperature, pH, light, etc.).[19] By adjusting the molecular diffusion to the active site, the reaction rate can be regulated, consequently preventing the formation of by-products. In principle, one could conceive a mechanism in which the undesired reaction triggers the phase transition of the polymer, leading to the self-regulating mechanism. Even though this concept has been demonstrated on microscopic devices by the group of J. Aizenberg[20], no one has ever shown a self-regulated catalyst in heterogeneous catalysis with the dynamics of the reactions and response of the polymeric "valve". Clearly, to create self-regulating catalysts that use the desired output of

their own activity requires a fundamental understanding of the interplay between the polymer conformation and mass transport rates under dynamic conditions.

In-situ Attenuated Total Reflection Infrared (ATR-IR) spectroscopy of heterogeneous catalyst allows fast and accurate monitoring of the chemical identity of chemisorbed species, while capturing the transience of mass transport processes.[21] In this technique a thin-film catalyst layer is coated on an optical element that allows internal light reflection. The evanescent waves generated at the reflection interface interact with their environment as they propagate, allowing the monitoring of the molecular vibrations at the solid/liquid interface. This is due to the surface restrictions of the evanescent wave to the solid-liquid interface, limiting the penetration depth to only a few microns (c.a. 1-3 μm). Consequently, the liquid contribution, which has a strong infrared absorption, is minimized.[22] In heterogeneous catalysis, In-situ ATR-IR spectroscopy is used to study the surface intermediates under reaction conditions to unravel the reaction mechanism [23–25] and/or disentangle the solvent interplay on the reaction rate.[26] While there are a few studies on the transport characteristics inside flow cells of ATR-IR to generate so-called "spectro-kinetics" [21,27,28] as well as a few studies on polymer-solvent interactions determining swelling characteristics[29], there are no studies on mass transfer dynamics on polymeric systems in combination with kinetics on a model catalyst.

In this report, we study the transport dynamics through a Polymer-Membrane-Catalyst Assembly (PCMA) employing in-situ ATR-IR spectroscopy of chemisorbed carbon monoxide on Pd-Al$_2$O$_3$. This model PCMA mimics a core-shell catalyst, where the stimulus-responsive polymer brushes are decoupled from the catalytic active site. In this way, it is possible to determine the kinetics of the mass transfer process without the interference of the polymer on the solvating environment around the Pd surface. Because aqueous phase CO chemisorption on reduced Pd is a well-studied irreversible process with a known Pd-CO stoichiometry, it was possible to quantitatively measure the rates of diffusion through the nano-porous membranes containing polymers by correlating the saturation times of the CO-Pd vibrational frequencies with the Pd surface area loaded in the ATR-IR crystal. Furthermore, the PCMA consisted of membranes with straight channels made of poly(ethyltheralpthalate) (PET) with narrow pore-size distribution and well controlled thickness that can be functionalized with p-NIPAM coatings via atom-transfer radical polymerization (ATRP) in a reproducible manner. This allowed rigorous estimation of the transport processes in this system. By combining detailed ATR-IR CO

chemisorption data and multi-physics modelling of the transport and chemisorption processes, we demonstrate for the first time that in the transient mode the polymer content greatly influences the transport through the PCMA via strong molecule-polymer interactions (i.e. CO absorption in p-NIPAM) that leads to extended induction times, rather than the reduction of the diffusion coefficient (i.e. more tortuous and narrow pathways), as generally accepted.

2.2   Materials and methods

2.2.1   Materials and chemicals

The poly(ethyltheralpthalate) (PET) membrane with straight channels of 200 nm pore size diameter was obtained from it4iP on 4A sheets(https://www.it4ip-iontracktechnology.com). The final membranes were obtained by cutting sections of 2x5 cm that match with the ATR-IR crystal size. For the polymerization, N-isopropylacrylamide (NIPAM, 97 %, 2210-25-5), 3-aminopropyltriethoxysilane (APTES, 99 %, 919-30-2), trimethylamine (Eth$_3$N, 99%, 75-5-3), α-bromoisobutyrylbromide (BIBB, 98 %), 20769-85-1), copper (II) bromide (CuBr$_2$, 99 %, 7789-45-9), 1,1,4,7,10,10-Hexamethyltriethylenetetramine (HMTETA, 97 %, 3083-10-1), and L-ascorbic acid (99 %, 50-81-7) were obtained from Sigma-Aldrich. The solvents Tetrahydrofuran (THF, 109-99-9), methanol (67-56-1), ethanol (64-17-5) and n-hexane (99.4 %, 110-54-3) were obtained from Merck. The molecular sieves (4Å, 4-8 mesh, 70955-01-0) used to dry THF were obtained from Honeywell. For the catalyst synthesis gamma alumina support (γ-Al$_2$O$_3$) was obtained from BASF (Al 3992E 1/8"). Palladium precursor tetra-amine-palladium (II) nitrate solution (10 wt. % in H$_2$O, 1360-08-6), ammonium (25% v/v water, 1336-21-6), and sodium nitrite (99.99%, 7632-00-0) were obtained from Sigma-Aldrich. All the aqueous solutions were prepared using ultra purified water obtained from a water purification system (Millipore, synergy). The Internal Reflection Element (IRE) used was a zinc selenide (ZnSe) trapezoid prism (5x2x0.2 cm) with 45° incident angle and 20 000 – 650 cm^{-1} wavenumber range obtained from CRYSTRAN.

2.2.2   Catalyst preparation

Palladium alumina catalyst was prepared via wet impregnation following a synthesis method reported elsewhere.[30,31] The γ-Al$_2$O$_3$ powder with particle size below 38 μm

was dispersed in deionized (DI) H_2O. Then, the pH was adjusted to 9 by adding ammonia before incorporating the palladium precursor. The weight ratio used was 1/1.4/11.4/114 for $NH_3/Pd/\gamma-Al_2O_3/H_2O$, respectively to obtain a 3.5 wt. % Pd/Al_2O_3 catalyst. Afterwards, the water was removed in a rotary evaporator under vacuum at 70 °C. Palladium supported on alumina was calcined in air followed by reduction in hydrogen at 400 °C. Poly(N-isopropylacrylamide) (p-NIPAM), shown in Figure S2.1a, was directly coated at the catalyst surface via atom transfer radical polymerization (ATRP) method.[32] For more details please refer to **Chapter 3**.

2.2.3   Surface polymerization

P-NIPAM was synthesized with the ARGET ATRP (activators continuously regenerated by electron transfer atom transfer radical polymerization) method. For more details please refer to [33]. The "grafted from" radical polymerization started with N-isopropylacrylamide purification by recrystallization with hexane and stored below 4 °C before used. The membrane was first exposed to plasma (plasma cleaner Harrick) with oxygen for 10 min. The coupling agent used to bind the n-NIPAM to the membrane surface was 3-aminopropyl)triethoxysilane (APTES, 99 %), as shown in Figure S2.1b. The silanization was made by exposing the surface to APTES (10 drops) under vacuum for 30 min at room temperature before being annealed for further 30 min at 105 °C in air at atmospheric pressure. Subsequently, the APTES functionalized membrane was submersed into a sealed solution with THF (35 mL), BIBB (0.91 mL) and Eth3N (1.16 mL) in a glass reactor (see Figure S2.2) at room temperature. After 60 min, the bromine functionalized membrane was washed two times with THF, ethanol and water. Then, it was added to a sealed glass reactor and deoxygenated under continuous N_2 gas for 15 min (see Figure S2.2). A solution with 23.3 g water, 9.2 g methanol, 1.7 g NIPAM, 0.006 g $CuBr_2$ and 0.06 g HMTETA was stirred and deoxygenated under continuous N_2 atmosphere for 15 min at room temperature. The L-ascorbic acid (0.03 g) was added, and the solution was deoxygenated for further 15min, where the color changes from blue to yellow. The polymerization starts upon transferring the solution with a needle into the reactor containing the bromine functionalized membrane. Then, the polymerized membrane was washed with ethanol and water until the surface was clean.

2.2.4   Catalyst characterization

The active metal surface area was measured with CO chemisorption at room temperature (Chemisorb 2750, Micrometrics, gas phase). The palladium loading was measured with μ-XRF (Bruker Tiger S8). The support surface area was measured with N_2 adsorption at -196 °C (Micromeritics Tristar 3000 analyzer). The spatial palladium distribution was measured by Scanning Transmission Electron Microscope - High-Angle Annular Dark Field (STEM-HAADF) (Tecnai F30) in a Cs-probe corrected Titan (ThermoFischer Scientific, formerly FEI) with 300KV and coupled with a HAADF detector (Fischione). The polymer content on the catalyst surface was determined using elemental analysis (CHNS-0 Analyzer, Thermo Scientific) and thermo-gravimetrical analysis (TGA, Mettler Toledo). For more details related with catalyst characterization procedure see **Chapter 3**. Homogeneity and thickness of the catalyst layer on the Internal reflective element (IRE) was measured with Scanning Electron Microscopy (SEM JEOL- LA6010) using a mimic on a glass plate.

2.2.5   Polymeric membrane characterization

The PET membrane morphology (pore density, thickness and channel structure) was measured with Scanning Electron Microscopy (SEM JEOL LA6010). The morphology of p-NIPAM brushes grafted within nanopores was imaged by TEM (Tecnai F30) with a Scanning Transmission Electron Microscope - High-Angle Annular Dark Field (STEM-HAADF) in a Cs-probe corrected Titan (ThermoFischer Scientific, formerly FEI) with 300KV and coupled with a HAADF detector (Fischione). The membrane composition and distribution of carbon and nitrogen was measured with X-Ray Energy Dispersive spectroscopy (EDS) topography with an Ultim Max detector (Oxford Instruments). The polymer content at the membrane surface was determined using elemental analysis (CHNS-0 Analyzer, Thermo Scientific) and thermo-gravimetrical analysis (TGA, Mettler Toledo). For the TGA experiments, the sample was heated from 25 °C to 1000 °C at a ramp rate of 10 °C min^{-1} in 100 % synthetic air with 30 mL min^{-1} flow. Polymerization homogeneity at the surface was measured by Ellipsometry in a silicon wafer on the dry state (Mk-2000V ellipsometer from J.A. Woollam Co. Inc.) operating with a 75° incidence angle and a wavelength range of 370-1000 nm. Pore coverage by P-NIPAM brushes was measured by Atomic Force Microscopy (AFM) on a 2 μm pore size diameter membrane by Nanoscope V Dimension Icon Atomic Force Microscope (AFM) in Taping mode. AFM

probes consisted of sharped silicon tip with Au reflecting (Scanasyst fluid probes from Bruker). The temperature was induced using a Lakeshore 335 temperature controller.

2.2.6   ATR-IR experiments procedure

The CO diffusion was measured with Attenuated Total Reflection Infrared Spectroscopy (ATR-IR) in a customized flow cell, shown in Figure S2.3a. [22] The flow-through chamber had a thickness of 0.15 cm and a width/length of 4x1 cm, which was created by a spacer placed between the Internal Reflection Element (IRE) and the polished top plate. The cell was mounted within the sample compartment of an infrared spectrometer (Bruker Tensor 27) equipped with a Mercury Cadmium Telluride (MCT) detector refrigerated by liquid N_2. The infrared spectra were recorded by averaging 128 scans with a resolution of 4 cm^{-1}. The aqueous flows were pumped by a peristaltic pump downstream of the ATR-IR cell with a flow rate of 2 mL min^{-1}, resulting in a residence time of 12 s. The gases were saturated in DI water with 10 % CO/He (Praxair), He (Praxair), or H_2 (Praxair) at 1 bar with a total gas flow rate of 50 mL min^{-1}. CO concentration was 0.095 mol m^{-3} based on Henry's law (gases solubility in water at 1 atm). The temperature in the saturators was kept constant using a thermostatic bath. Experiments were measured at 25 °C and 40 °C controlled by a thermocouple placed near the liquid in the ATR cell, see supporting information Figure S2.4. To keep the temperature constant, a heating element was placed on top of the ATR cell and the inlet line. For all the experiments, before the flow-through-cell was assembled, the catalyst was first reduced by flushing with H_2/H_2O for 2 hours. Then, He/H_2O is flushed through the system for 30 min where water background was recorded. To start the chemisorption experiment, the CO/He dissolved in DI water was fed to the ATR-IR cell at 2 mL min^{-1}. In this moment, the IR spectra was recorded every 2 min until the peak intensity of the CO-bonded species on Pd surface reached a plateau. Then, the flow of CO was switched to He dissolved in DI water to remove the CO in the system and safely disassemble the cell. Every experiment was made with a new palladium surface. To prevent any effect of polymeric brushes on chemisorbed CO molecules, polymer brushes and Pd particles are physically separated by limiting the presence of polymer to the PET membrane (see Section S2.8.8. and Figure S2.3).

2.2.6.1 ATR-IR catalyst layer

For the ATR-IR experiments a catalyst layer was deposited on the top surface of the crystal. For that, a suspension of Pd/Al_2O_3 (0.12 g) in 2-propanol (20 mL) was sonicated in an ultrasonic processor (Fischer Scientific – 705) for 45 min. Then, internal reflective element surface was cleaned with ethanol and by plasma (plasma cleaner Harrick) with oxygen for 10 min before each coating. [23,34] The clean zinc-selenide (ZnSe) crystal was placed on a hot plate at 120 °C, where the catalyst solution was spray-coated until reaching the desired loading of c.a. 5 mg of catalyst. To obtain a stable layer on the crystal surface, the coated catalyst was calcined at 300 °C (1 °C min^{-1}) for 1 hour in N_2 at 20 mL min^{-1}. When p-NIPAM brushes are directly coated on the catalyst surface, the catalyst layer could not be calcined due to the polymer's thermal stability. Instead, a membrane (Whatman Nuclepore track etched polycarbonate membrane filters with a pore size of 0.2 μm) was placed between the catalyst layer and the rubber from the cell chamber to guarantee the layer stability (see Figure S2.3b). To ensure reproducibility of the results a new catalyst layer was used in every ATR experiment.

2.2.6.2 Data analysis

The ATR-IR correction of the spectra for CO adsorption was performed by subtraction of the water background as explained in detail in previous work.[22] To calculate the integrated peak area of each peak, a Gaussian line shape function was applied centred at the frequency ω_0 using equation Eq. 2.1.[35]

$$I(\omega) = \frac{A e^{\frac{-4\ln(2)(\omega-\omega_c)^2}{x^2}}}{x\sqrt{\frac{\pi}{4\ln(2)}}}$$

<div align="right">Eq. 2.1</div>

Where $I(\omega)$ is the absorbance (a.u.) at a given frequency (ω, wavenumber cm^{-1}), A is the integrated area (a.u.) and x is the full width at half maximum intensity. The total integrated peak area was calculated by the area summation of the CO peaks at the palladium surface.

2.3   Results and discussion

2.3.1   Characterization

Figure 2.2a shows a schematic representation of the Polymer Membrane Catalyst Assembly (PMCA) used on the ATR-IR experiments to study CO transport. Table S2.1 summarizes the characterization results of the prepared catalyst with a 1 wt. % and 3.5 wt. % Pd with a dispersion of 56 % and 36 %, respectively. The average particle size, obtained from dynamic CO chemisorption, was 2 and 3 nm for 1 and 3.5 wt. % Pd/Al_2O_3, respectively, assuming a uniform size distribution and hemisphere shape of the metal clusters. These results are in line with the palladium particle size distributions obtained from STEM-HAADF characterization with values of 1.6 ± 0.4 and 3.1 ± 0.5 nm for the 3.5 and 1 wt.% Pd/Al_2O_3 catalysts, respectively (see Figure 2.2g). Figure 2.2f shows the morphology of 3.5 wt. % Pd/Al_2O_3 where the palladium nanoparticles are well distributed on an Al_2O_3 support. Figures 2.2di and ii show a typical Pd/Al_2O_3 layer of 5 ± 0.5 μm on a glass plate, in which a homogeneous film without any surface cracks was obtained, similar to the results of Ebbesen et al. [22,34]. The membrane morphology consisted of straight pore-channels with a well-defined pore size (Figure 2.2bi-bii). The pore diameter obtained was 200 ± 40 nm (see Figure 2.2c) with a thickness of 12 μm (see Figure 2.2bii) and a pore density of $1x108$ cm^{-2}.
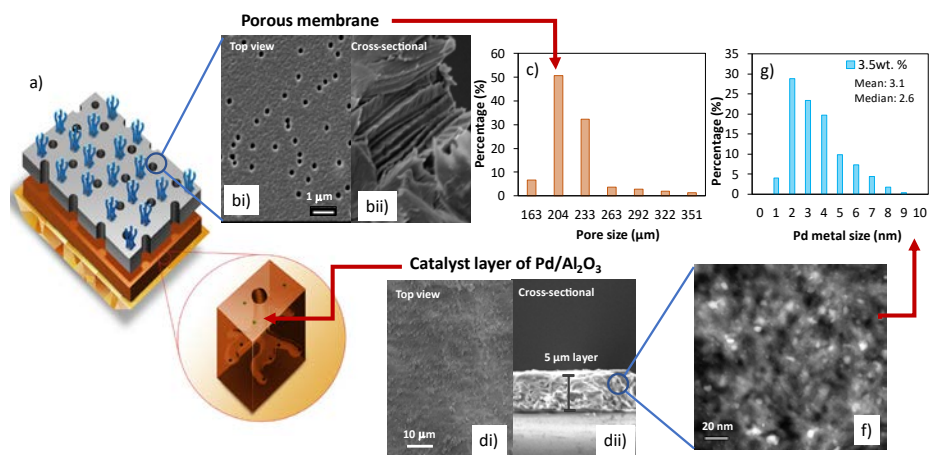
Figure 2.2: Schematic representation of polymer membrane catalyst assembly on the ATR-IR crystal (a), SEM images from the membrane with 200 nm pore size diameter (bi) Top view and (bii) cross-sectional, pore size distribution obtained from the SEM images (c), SEM images of the catalyst layer obtained on a glass plate for top view (di) and cross-sectional views (dii), STEM-HAADF characterization of 3.5 wt. % Pd/Al_2O_3 catalyst (f) and the corresponding metal particle size distribution (g) of pre-reduced catalyst.

The thermal stability of polymeric membranes was studied via thermal gravimetric analysis (TGA) (see Figure S2.5), where the decomposition of the membrane and p-NIPAM brushes occurred above 350 °C. To determine the polymer distribution, STEM-HAADF-EDS mapping characterization was conducted on the membranes after surface polymerization of P-NIPAM. Since nitrogen is one of the components in the chemical structure of p-NIPAM (see Figure S2.1a), we used it to determine the presence of polymer brushes on the external surface and inside the pores. As shown on Figure 2.3aii-ciii, the N was only detected on those samples coated by p-NIPAM brushes. These results agree with the elemental analysis (EA), where N was not detected on 0 min polymerization (see Table S2.2). Further evidence of the presence of the p-NIPAM polymer inside the pores was obtained from conducting cross-sectional characterization of the membranes using Focused Ionized Beam (FIB) SEM micro-processing followed by STEM-HAADF-SEM characterization. Here, we observed that N was homogeneously distributed along the membrane pore confirming full coverage of the wall of the pores in the membranes (see Figure S2.6 b-iii).
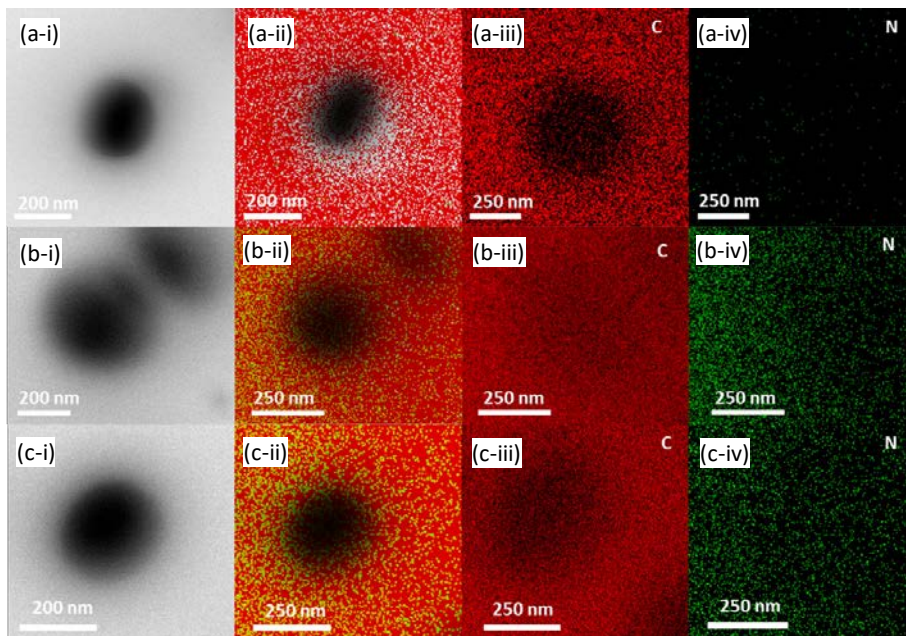
Figure 2.3: STEM-HAADF characterization (i) and EDS mapping for carbon (iii), nitrogen (iv) and both (ii) at the membrane pore containing 0 min, 5 min and 15 min polymerization time (a-c, respectively).

Since P-NIPAM is a thermo-responsive polymer, i.e. it displays a reversible phase transition from swollen to collapsed above its Lower Critical Solution Temperature (LCST), we conducted in-situ ellipsometry characterization to obtain its equilibrium hydration transition curve as a function of the polymer content in liquid water environment. Direct measurements on PET membranes, however, were not possible due to the strong light absorption of the material. To circumvent this issue, we conducted these measurements on a silicon wafer (Section S2.8.4.3) in which polymer brushes were grown via ATRP at conditions that lead to polymer loadings similar to those obtained in the membranes. As shown in Figure S2.8a the coatings obtained during ATRP on silicon wafer showed a LCST at 32 °C, typical for P-NIPAM. These observations agreed with the pore coverage results obtained via in-situ AFM characterization of PET membranes coated with P-NIPAM. As can be noticed in Figure S2.9 (see details Section S2.8.4.4.), the polymer brushes in the swollen state decreases the surface area available for diffusion compared

with the collapsed state. The effective pore diameter increased from 1.41 μm to 1.8 μm, resulting in a decrease in the fraction of the surface area of the pores blocked by the polymer from 30 % to 10 % (see Figure S2.10). These observations agree with previous reports on polymer coated membranes, where the swollen state creates a smaller effective pore diameter. [14,36] The AFM results agree with STEM-HAADF mapping where the polymer brushes can be observed in the internal walls of the membrane pore (see Figure S2.6). Similar observations were reported on PET membrane coated with p-NIPAM brushes, where brushes grew on both the surface and inside the pores. [18,37] The thickness of the polymer brushes below and above LCST on the silicon surface obtained at different polymerization times (e.g., 350 nm and 70 nm for the sample with 15 min of polymerization below and above the LCST, respectively, see Figure S2.8) suggests a high surface polymer density due to the high swelling ratio.

2.3.2 *In-situ* ATR-IR chemisorption of CO on Pd/Al$_2$O$_3$ films

To derive quantitative information about the molecular transport of probe molecules in thin films of porous heterogeneous catalysts using in-situ ATR-IR in liquid phase, it is essential to identify and quantify the speciation of chemisorbed molecules on the active sites, while minimizing the interference of the solvent environment. For this reason, we employed catalyst layers that were thicker than the light penetration depth (see Section S2.8.5). The typical in-situ CO-chemisorption spectra on Pd/Al$_2$O$_3$ catalyst is presented in Figure 2.4a-b. As expected, three main adsorption bands can be identified in this spectrum, corresponding to C-O bonded linear (CO(L)), bridge (CO(b)), and multi (CO(M)). The CO(L) peak was found at 2060 cm^{-1} wavenumbers and the overlapping peaks at 1931 and 1895 cm^{-1} can be attributed to CO(B) and CO(M), respectively. These results are in line with previous reports on pre-reduced 5 wt.% Pd/Al$_2$O$_3$ conducted on a ATR-IR spectroscopy at room temperature with 1 % CO dissolved in water.[24] The integrated peak area of each CO peak was determined by Eq. 2.1 (see Figure 2.4a). In order to eliminate the possible effect of convective transport inside the ATR chamber we calculated the Peclet number (Pe>>1) and measured the ATR-CO chemisorption profiles at different flowrates (1 and 2 mL min^{-1} see Section S2.8.11). This analysis indicated that the rate of CO is dominated by diffusion rather than convection.

By recording the relative absorbance of chemisorbed CO* as a function of time we could identify three distinct regions (see Figure 2.4c). Initially, there is a 2 min induction period

in which the derivative of the curve is zero (see Figure 2.4d), followed by a section with constant increase before reaching a plateau characteristic of Pd surface saturation with CO. Since CO can only be adsorbed onto the Pd surface and our catalyst is completely reduced before each experiment, the induction period is likely caused by chemisorption on the upper section of the catalyst layer as the penetration of the evanescent waves in the ATR-IR is limited to 0.87 ± 0.06 μm (see Section S2.8.5) out the 5 μm of catalyst layer. This would suggest that the kinetic constant of CO chemisorption on Pd is significantly higher than that of the diffusion, which leads to the formation of a moving front inside the layer that delays the ATR-IR signal (see Section S2.8.6). Notably, increasing the Pd metal surface area proportionally increased the induction time and thus also the total saturation time (see Table S2.1, Figure S2.13, and comparing Figure S2.14 to Figure 2.4b).
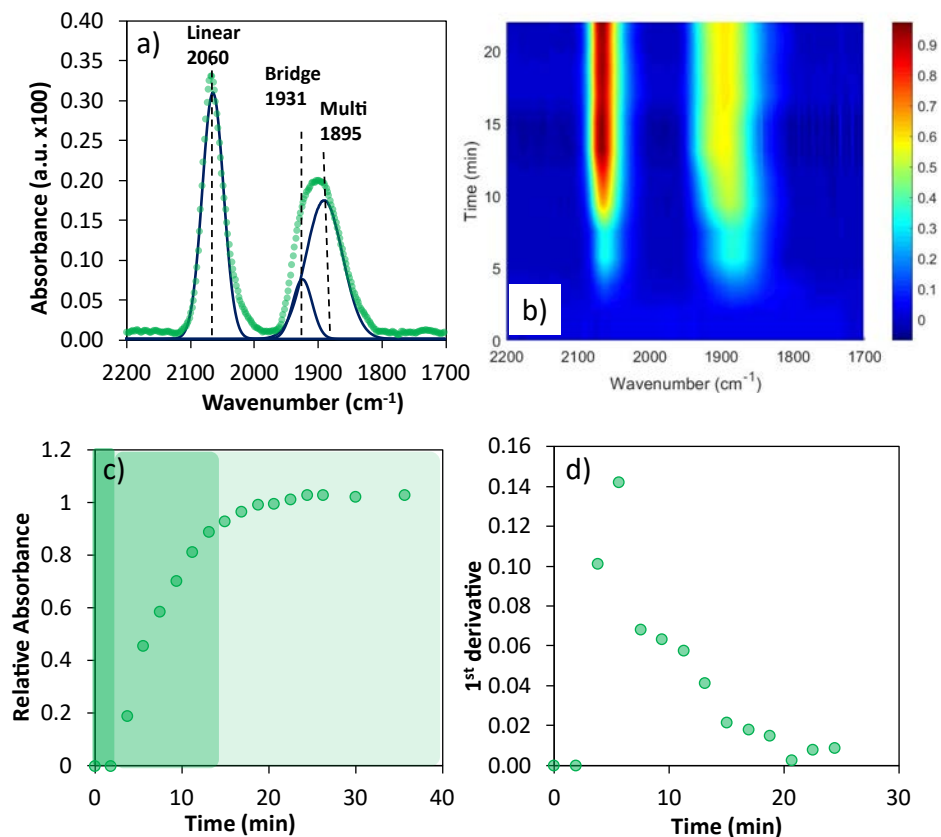

Figure 2.4: In situ ATR-IR spectra at full CO coverage (saturation) on Pd/Al$_2$O$_3$ catalyst containing 1wt. % Pd and the peak deconvolution obtained from Eq. 2.1 (a), ATR-IR spectra as a function of time of CO chemisorption (b), relative absorbance (normalized

integrated peak area of the three CO peaks at the palladium surface, linear (2060 cm^{-1}), bridge (1931 cm^{-1}) and multi (1895 cm^{-1})) (c) and 1st derivative of Figure 2b (d) on Pd/Al$_2$O$_3$ catalyst containing 1 wt. % Pd coated on a ZnSe crystal containing c.a. 5 mg conducted at 25 °C on a flow of 10% CO/Ar dissolved in water with a flow rate of 2 mL min^{-1}.

2.3.3 Effect of temperature on *In-situ* ATR-IR chemisorption of CO on Pd/Al$_2$O$_3$ films

Figure 2.5a shows the effect of temperature on CO transport, keeping the CO concentration constant by adjusting the CO/He ratio used in the liquid saturation vessels using Henry's law. This allowed us to compare the results obtained at different temperatures. As shown on Figure 2.5a, increasing the temperature from 25 to 40 °C had no significant effect on the ATR-IR CO chemisorption saturation curves on the 3.5 wt. % Pd/Al$_2$O$_3$ catalyst (see Figure S2.18a and Section S2.8.9.1) as the temperature increases. The negligible change in saturation time can be attributed to the low activation energy barriers for molecular diffusion of CO at infinite dilution in water (e.g. 10-15 kJ mol^{-1}).[39]

2.3.4 Membrane-Catalyst Assemblies (MCA)

To create the Membrane Catalyst Assembly, a nano-porous membrane with 12 μm thickness and 200 nm pore diameter was placed on top of the catalyst layer (See Figure S2.3b and Figure 2.2). Since the evanescent wave from ATR-IR is restricted to the catalyst/solid interface, there is no chemical interference of the PET polymer membrane on the CO IR spectrum. By keeping the palladium amount and CO concentration constant, any delay in the transport should be caused by the presence of an external resistance, i.e. the membrane. Notably, Figure 2.5b shows no significant delay caused by the addition of the membrane (see Figure S2.18b). This can be attributed to straight channels (τ=1) and demonstrates that the diffusion through the membrane is not the limiting step.
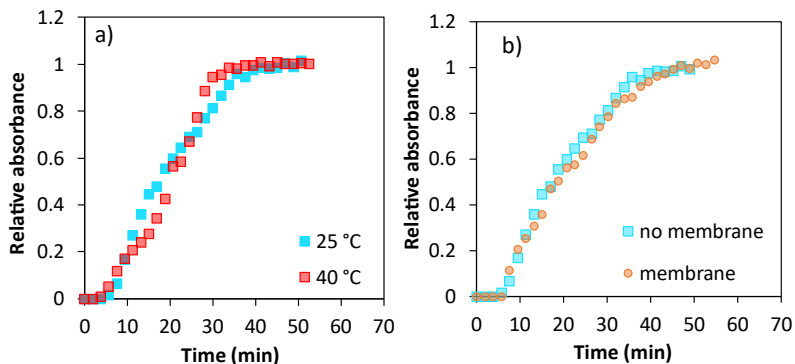
Figure 2.5: Relative absorbance (normalized integrated peak area of the three CO peaks at the palladium surface at different temperature (a) and membrane (b) on Pd/Al$_2$O$_3$ catalyst containing 3.5 wt. % Pd coated on a ZnSe crystal containing c.a. 5 mg conducted on a flow of 10% CO/Ar dissolved in water with a flow rate of 2 mL min^{-1}.

2.3.5   Polymer-Membrane-Catalyst Assemblies (PMCA)

To investigate the interplay between molecular transport and the polymer brushes, we prepared PET membranes with increasing p-NIPAM polymer content by changing the ATRP polymerization time (see Section S2.8.10). As shown in Figure 2.6a, longer polymerization times increased the initial induction period from 2 minutes, in the case of non-coated membranes, to 15 and 35 minutes in the p-NIPAM functionalized membranes with polymerization times of 5 and 15 minutes, respectively. This shift in the CO saturation curve, however, did not change the rate of CO adsorption significantly as indicated by the similar slopes observed in the linear region of the saturation curve. The net effect of this delay in the process is a significantly longer saturation time for the PMCA systems at 25 °C, i.e. at temperatures below LCST of p-NIPAM. Upon increasing the temperature above 32 °C, the polymer brushes conformation changes from swollen to collapsed state. It appears that under these conditions the diffusion process was accelerated, leading to saturation curves similar to those obtained with bare membranes when 5 minutes polymerization was used (Figure 2.6b). This result would suggest that the swollen polymer suppresses diffusion more than the collapsed polymer.

While it is tempting to rationalize these results exclusively in terms of changes in the effective pore diameter and tortuosity of the membranes coated with p-NIPAM in the

swollen state, it is important to realize that this could not explain the drastic increase in the induction period followed by a nearly identical slope of the relative absorbance as a function of time in the coated and uncoated systems. This, in fact, would indicate that another process is preventing CO reaching the detection layer in the in-situ ATR-IR experiments when the polymers are present. In this scenario, it is imperative to develop a mechanistic framework for the entangled transport and reaction processes occurring in such a system. In the following sections, we develop a multi-physics model aimed at testing two possible hypotheses, (1) diffusional resistances below p-NIPAM LCST temperature exclusively control the saturation curve, and (2) absorption of CO in the polymer in combination with diffusional resistance is responsible for the observed behavior. Finally, we will explore the possible conditions that could drive the process from a "negative" stimulus-responsive behavior (i.e. the diffusion is hindered below the polymer LCST) to a "positive" response one.
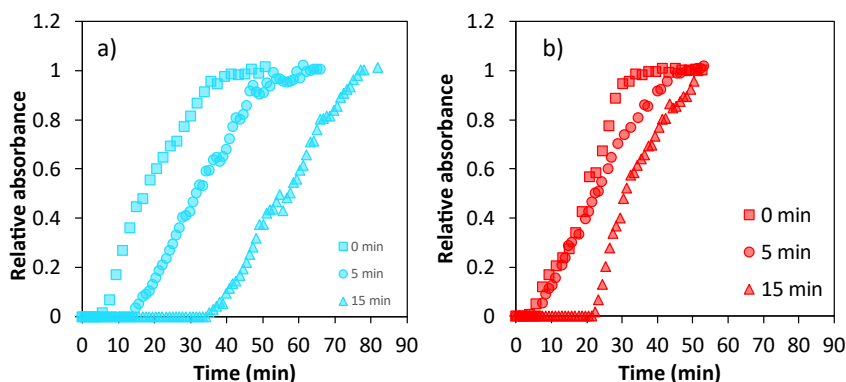

Figure 2.6: Relative absorbance (normalized integrated peak area of the three CO peaks) at the palladium surface at 25 °C (a) and 40 °C (b) for 0 (rectangle), 5 (circle) and 15 (triangle) minutes polymerization on Pd/Al$_2$O$_3$ catalyst containing 3.5 wt. % Pd coated on a ZnSe crystal containing c.a. 5 mg conducted on a flow of 10 % CO/Ar dissolved in water with a flow rate of 2 mL min^{-1}.

2.4   Methodology

2.4.1   Modelling *in-situ* ATR-IR CO-chemisorption on MCA

2.4.1.1 Diffusion processes

To further understand the transport on an ATR-IR cell, a one-dimensional diffusion model assuming Fick's second law was developed to describe the transport of dilute CO in water (see Eq. 2.2). Here c is the CO bulk concentration in the solvent (mol m^{-3}), x the vertical distance (m), t is the time (s), and Di is the diffusion coefficient of CO in water at infinite dilution (m^2 s^{-1}) at a given temperature.

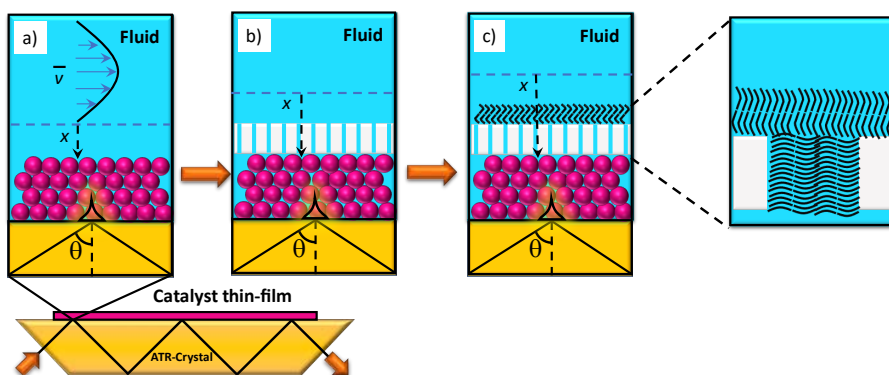$$\frac{\delta c(x,t)}{\delta t} = D_i \frac{\delta^2 c}{\delta x^2} \qquad\qquad \text{Eq.2.2}$$

Figure 2.7: Schematic representation of the different segmentation of the 1D model, which consisted of a boundary layer and Pd/Al$_2$O$_3$ catalyst layer (a); boundary layer, membrane and Pd/Al$_2$O$_3$ catalyst layer (b); and boundary layer, polymeric membrane and Pd/Al$_2$O$_3$ catalyst layer (c).

The ATR-IR cell was reduced to a one-dimensional model, where gradients across z (cell length) are negligible since the CO molar flow rate into the ATR-IR cell is 34 times higher than the adsorption rate at the palladium surface (see Section S2.8.12.1.). The model

calculates the transport of CO from the boundary layer (x=0) until the ATR crystal surface (x=L) over time, as shown in Figure 2.7a. Since no delay was detected on the saturation curves when the flow rate through the ATR cell was increased (1 and 2 mL min^{-1}) due to fast convection (Pe>>1) (see Section S2.8.12.1.), the initial CO concentration at the boundary layer (x=0) was assumed to be constant. This results in the two boundary conditions shown in Eq. 2.3 and 2.4.

$$x = 0; \ c = c_{co}^{initial} \hspace{3cm} \text{Eq. 2.3}$$

$$x = L; \ \frac{\delta c(x,t)}{\delta x} = 0 \hspace{3cm} \text{Eq. 2.4}$$

The CO concentration at the bulk was calculated using Henry's law, while the boundary layer thickness formed on top of the crystal layer was determined using the Sherwood's correlation (see Section S2.8.12.1). The CO diffusion coefficient was calculated by the Arrhenius equation (see Section S2.8.12.3.) to determine the transport in the diffusion layer. The saturation curve was obtained from the integration of the evanescent wave over time (see Section S2.8.12.2.).

2.4.1.2 CO chemisorption on palladium

The mass balance for CO in a porous bed catalyst was defined as shown on Eq. 2.5.

$$\frac{\delta c(x,t)}{\delta t} = D_{eff}^{Pd/Al_2O_3} \frac{\delta^2 c}{\delta x^2} - r_{CO}|_{x,t} \hspace{2cm} \text{Eq. 2.5}$$

Where $D_{eff}^{Pd/Al2O3}$ is the effective diffusion coefficient of CO in the porous bed (m^2 s^{-1}) and r_{CO} is the rate of CO chemisorption (mol m^{-3} s^{-1}). The stoichiometry of non-dissociative CO adsorption on the palladium active site was assumed to be 1:1 with Pd surface atoms (See Eq. 2.6). Here (*) represents an empty site on the palladium surface and CO* is the chemisorbed specie. The palladium active sites (*) at the catalyst layer were assumed to be equally distributed through the catalyst bed (z and x) and calculated as shown in Eq. 2.7.

Here the total moles of palladium available for chemisorption are calculated from the metal loading, dispersion, and catalyst weight on the crystal surface (see Table S2.1), where Θ_{pd} are the empty metal active sites, which are defined as a fraction between 0 and 1, n_{pd} is the moles of palladium available to chemisorb (mol) and n_{pd}^0 is the total palladium active sites (mol).

$$CO + * \leftrightarrow CO *$$

<div align="right">Eq. 2.6</div>

<div align="right">Eq. 2.7</div>

$$\left.\Theta_{pd}\right|_{x,t} = \frac{\left.n_{pd}\right|_{x,t}}{\left.n_{pd}^0\right|_{x,t}}$$

The CO chemisorption rate can be described as Eq. 2.8, assuming no desorption from the palladium active site. At temperatures below 60 °C, the rate of desorption can be neglected due to the strong interaction of CO with the palladium surface.[40] The CO saturation at the palladium site was reached when all the palladium active sites are fully covered (Eq. 2.7, $\Theta_{pd}=0$). While the activation barriers for CO adsorption are negligible on single crystals [40], the presence of water molecules in the liquid phase and residual hydrogen from the catalyst reduction will increase the energy penalty for the chemisorption. In this case, the apparent barrier will be coupled to the surface coverage of CO. Since, chemisorbed CO has a strong dipole moment the heat of adsorption will decrease with coverage.[24] Thus, the adsorption of CO on the metal site (k_{ads}) was assumed to have an activation energy barrier dependent on the surface coverage [41] (see Eq. 2.9). Here, k_{ads} is the adsorption rate constant (s^{-1}), c_{CO} is the CO concentration is the bulk (mol m^{-3}), k_{ads}^0 is adsorption rate at coverage zero (s^{-1}), Ea is the apparent activation energy barrier (J mol^{-1}), R is the universal gas constant (J mol^{-1} K^{-1}) and T is the absolute temperature (K).

<div align="right">Eq. 2.8</div>

$$r_{CO} = \left. k_{ads}c_{CO}\Theta_{pd}\right|_{x,t}$$

<div align="right">Eq. 2.9</div>

$$k_{ads} = k_{ads}^0 e^{(-\frac{(E_a)}{RT}(1-\Theta_{pd}))}$$

2.4.1.3 Diffusion through the porous membrane

The mass balance at the membrane was defined as shown in Eq. 2.10. In this domain, the membrane pore distribution is assumed to be homogenous throughout the entire surface with a regular pore size distribution (200 nm) and straight channels ($\tau = 1$). The schematic representation of the ATR-IR crystal, catalyst and PET membrane is shown in Figure 2.7b, which can be rationalized as a sequence of resistances in series for mass transfer, where ε_m is the membrane porosity used to calculate the effective diffusion coefficient in the porous membrane.

$$\frac{\delta c(x,t)}{\delta t} = D_i\ \varepsilon_m \frac{\delta^2 c}{\delta x^2}$$

Eq. 2.10

2.4.2   Modelling *in-situ* ATR-IR CO-chemisorption on PMCA

2.4.2.1 Diffusion processes in a polymeric membrane

The transport through a polymeric membrane was defined as a resistance in parallel (Eq. 2.11 and Figure S2.22), where the contribution from the polymer brushes was defined as Eq. 2.12 and the contribution from the membrane was defined as Eq. 2.13. The polymer distribution at the membrane surface and pores was considered homogeneous.

$$D_{i,eff}^{total,p} = D_{i,eff}^{p-nipam} + D_{i,eff}^{m}$$

Eq. 2.11

$$D_{i,eff}^{p-nipam,m} = D_i^{p-nipam}\ \varepsilon_m\ V_{x,p}(T)$$

Eq. 2.12

$$D_{i,eff}^{m,p-nipam} = D_i\ \varepsilon_m (1 - V_{x,p}(T))$$

Eq. 2.13

Here $D_{i,eff}^{total}$ is the total diffusion coefficient ($m^2\ s^{-1}$) of the specie i, $D_{i,eff}^{m}$ the effective diffusion coefficient of the membrane filled with water in the absence of polymer brushes ($m^2\ s^{-1}$), $D_{i,eff}^{p-nipam}$ is the effective diffusion coefficient in the polymer layer grown on the

membrane walls (m^2 s^{-1}), $D_i^{p\text{-}nipam}$ is the diffusion coefficient of the specie i through the polymeric brushes (m^2 s^{-1}), $V_{x,p}$ is the volume fraction of polymer in the membrane pore.

2.4.2.2 Effective diffusion in p-NIPAM polymer brushes

The diffusion of the solute in thermo-responsive polymeric brushes can be described by obstruction-hindered diffusion developed by Mackie and Mears [43], as shown in Eq. 2.14. This model assumes that the polymer chains impose an increase in the path length for the molecules in motion where the polymer blocks a fraction of the sites for transport. Although, this model is only valid for small sized solutes in semi dilute polymer solutions ($\varphi_{p\text{-}NIPAM} < \varphi_{LCST}$) without considering the intrinsic properties of the polymer or the solute, its validity has been confirmed experimentally in stimulus-responsive catalysts by several independent studies at moderate polymer densities. [4,43] More recently, Kanduc et al. [44] demonstrated using detailed molecular dynamic simulations that when the polymer is in the collapsed state, i.e. at the maximum density ($\varphi > \varphi_{LCST}$), the water distribution in the polymeric layer dominates the diffusion. In this state, solute molecules dissolved in water diffuse through the polymer matrix via a so-called "hopping" mechanism in which the dynamics of the soft polymer brushes controls the rate of transport.

To account for those effects, we developed a piecewise function that uses the Mackie and Mears model to describe the system below the maximum polymer density and the hopping mechanism developed by Kanduc et al. [44] above φ_{LCST}. Therefore, the diffusion of molecules in the collapsed state was defined as shown in Eq. 2.14, where the main contribution comes from the molecular size of the solute (See Section S2.8.12.5.). In this equation, $D_i^{p\text{-}NIPAM}$ is the effective diffusion coefficient of CO through the polymer brushes (m^2 s^{-1}), $\varphi_{p\text{-}NIPAM}$ is the p-NIPAM volume fraction, φ_{LCST} is the p-NIPAM volume fraction at the transition state, D_i the diffusion coefficient of CO in water at infinite dilution (m^2 s^{-1}), a_w is the Stokes hydrodynamic radii in pure water (nm) and λ the decay length constant (nm) (see results Section S2.8.12.6.).

Eq. 2.14

$$\frac{D_i^{p-NIPAM}}{D_i} = \begin{cases} \left[\dfrac{1 - \Phi_{p-NIPAM}}{1 + \Phi_{p-NIPAM}}\right]^2 , & \Phi_{p-NIPAM} < \Phi_{LCST} \\ e^{\frac{-a_w}{\lambda}} , & \Phi_{p-NIPAM} = \Phi_{LCST} \end{cases}$$

2.4.2.3 Polymer interaction with CO molecules

The mass balance at the polymeric layer (see Figure 2.7c) was defined as shown in Eq. 2.15. In this scenario, the absorption of CO inside the p-NIPAM domains were assumed to be non-activated. Given the fact that in our experiments the concentration of the CO in solution is constant, the desorption was neglected as the chemical potential difference in the saturation state vanishes (see Section S2.8.12.6.). In this case, the absorption capacity was defined as shown in Eq. 2.16. Here $D_i^{p\text{-NIPAM}}$ is the effective diffusion coefficient of a solute on the polymer brushes or on a polymeric membrane ($m^2\,s^{-1}$), kads is the absorption rate constant (s^{-1}) and $\theta_{p\text{-nipam}}$ is the free space on the polymer matrix for CO to absorb which is dependent on the polymer capacity (n_{CO}^{max}) and defined as a fraction between 0 and 1.

$$\frac{\delta c(x,t)}{\delta t} = D_i^{p-nipam}(T)\frac{\delta^2 c}{\delta x^2} - (k_{abs}c_{CO}\theta_{p-nipam}(T))_{x,t}$$

Eq. 2.15

$$\theta_{p-nipam} = \frac{n_{CO}|_{x,t}}{n_{CO}^{max}|_{x,t}}$$

Eq. 2.16

The strength of CO interaction with the polymer brushes was defined, as shown in Eq. 2.18, where it is a function of CO solubility in the p-NIPAM polymer brushes and the polymer volume (Eq. 2.17 and 2.18). While the volume of the polymer (V_p) is a function of the polymer thickness and surface area, the partitioning of solute, which is the ratio of CO chemical potential in the polymeric brushes ($S_{CO\text{-p-NIPAM}}$) to the bulk of the solvent ($S_{CO\text{-water}}$), is related to the solvation free energy of the polymeric brushes as proposed by Dzubiela and co-workers [46] (see Section S2.8.12.6.). Here nco are the CO moles absorbed (mol), V_p is the polymer volume (m^3) and S is the solubility (mol m^{-3}), ΔG is the difference in free enthalpy between CO interacting with solvent and CO interacting with polymeric brushes (J mol^{-1}), kb is the Boltzmann constant (J K^{-1}) and T the absolute temperature (K).

$$n_{CO} = V_p(T)\,S_{CO-p-NIPAM}(T)$$

Eq. 2.17

$$\frac{S_{CO-p-NIPAM}(T)}{S_{CO-water}(T)} = e^{\frac{-\Delta G}{k_b T}}$$

<div align="right">Eq. 2.18</div>

2.5 Modelling results and discussion

2.5.1 Diffusion on CA and MCA

As shown in Figure S2.25 (see Section S2.8.12.7.) the one-dimensional Fick's diffusion model coupled to CO-Pd surface reaction predicts well the CO chemisorption dynamics on a Pd/Al$_2$O$_3$ layer. The observed trends were in line with previous reports on oxidation chemistry in liquid-ATR-IR cells working in *operando mode*.[27,41] In particular the short induction period, herein observed, was also encountered when highly reactive probe species were employed, indicating the importance of favourable adsorption on the process dynamics. Notably, increasing the temperature in the case of catalyst assembly (CA) had negligible effect on the induction period and saturation time observed in (see Figure S2.26a), which is attributed to the low activation energy barriers for diffusion. As expected, addition of PET membrane (MCA) did not change the saturation curve, indicating unrestricted transport through these thin porous membranes with straight channels compared with the transport through the stagnant layer (see Figure S2.26b).

2.5.2 Interplay between effective diffusion coefficient and saturation curves on PMCA in the absence of CO absorption on p-NIPAM

To study the effect of polymer brushes on CO transport on a PMCA we employed the ellipsometry results corresponding to 15 minutes of polymerization with a thickness of 350 nm on the top surface of the membrane to design our 1D model. Considering that the PET membranes contain pores of 200 nm in diameter, the pores were assumed to be completely filled by p-NIPAM in the swollen state (at temperatures below the LCST). The rationale is that during ATRP polymerization mass transport limitations of fresh monomer will restrict the growth in the confined pores, leading to a maximum polymer content equal to the pore volume (i.e. $V_{x,p}$ is equal to 1). Figure 2.8a shows the normalized CO diffusion coefficient inside a p-NIPAM-water domain as a function on the polymer fraction ($\varphi_{p\text{-}nipam}$) at a fixed temperature (25 °C), where the increase of the polymer fraction retards CO diffusion in the polymeric matrix (Section 2.4.2.2.). The polymer fraction ($\varphi_{p\text{-}nipam}$) is coupled to the swelling state of the polymer, which can be obtained from the ellipsometry

experiments (see Section S2.8.4.3.). At 15 min polymerization the polymer fraction regressed from ellipsometry measurements on silicon was 0.2. Furthermore, we acknowledge that the swelling of the polymer brushes confined inside the PET could also behave differently from those on the surface, which could lead to overprediction of the polymer fraction inside the pores. Strikingly, our results indicate that even when large values of φ_{pNIPAM} (0.7), corresponding to reductions in the normalized $D_i^{p-NIPAM}$ of c.a. 90%, are employed, the saturation time remained nearly constant (Figure 2.8b). In addition, these changes in the effective diffusion coefficient could not explain the zero derivative with time (i.e. induction period) experimentally observed during the first 15-30 min of chemisorption for the PMCA (see Figure 2.6).
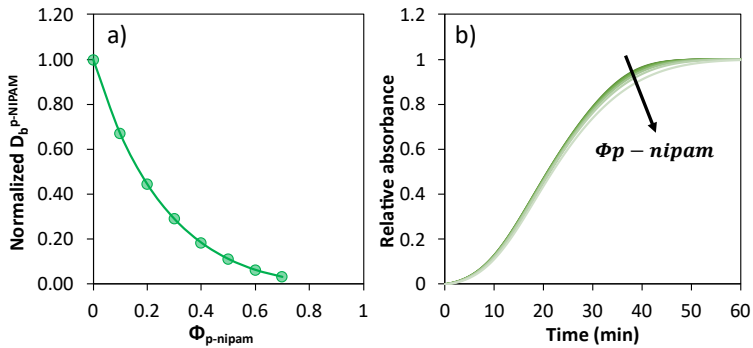

Figure 2.8: Normalized diffusion coefficient of CO in p-NIPAM brushes as a function of the polymer fraction ($\varphi_{p-NIPAM}$) at 25 °C (a) and Palladium saturation time obtained with different polymer fraction of p-NIPAM varied between 0.1 to 0.7 at 25 °C with no absorption assuming a $V_{x,p}$ of 1 and 350 nm thickness of p-NIPAM at the top of the membrane surface for 3.5 wt. % Pd/Al$_2$O$_3$ catalyst , a membrane with 200 nm pore diameter (b).

2.5.3   CO interaction with p-NIPAM brushes

The polymer thickness, volume fraction of polymer in the membrane pore, and polymer fraction were kept constant to study the effect of the CO interaction on the polymeric brushes. Figure 2.9 shows the modelling results for a polymeric membrane at temperature below LCST assuming that the pores become completely filled due to polymer swelling (15 min polymerization), as described in Section 2.5.2. In this case, the increase in the CO solubility in the polymeric brushes, at a low $k_{abs,p-NIPAM}$, led to shallower rates close to the

saturation, shifting the end of the breakthrough curve to the right (see Figure 2.9a). The higher solubility, however, did not explain the induction period observed in the presence of polymer brushes on the membrane surface, as shown in Figure 2.10a-b.
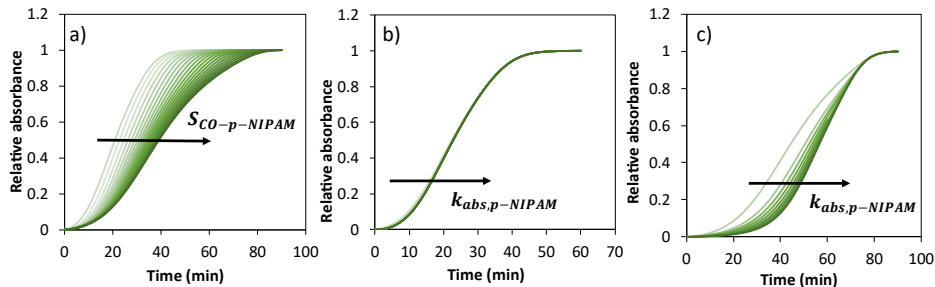

Figure 2.9: Palladium saturation curve at different CO solubility on the p-NIPAM brushes varied from 1 to 10 mol m^{-3} with a kads constant of 5 s^{-1} (a), CO absorption rate constant varied from 5 to 50 s^{-1} with a constant CO solubility of 1 mol m^{-3} (b), CO absorption rate constant varied from 5 to 50 s^{-1} with a constant CO solubility of 10 mol m^{-3} (c) at 25 °C assuming a $V_{x,p}$ of 1 and 350 nm thickness of p-NIPAM on the top of the membrane surface for 3.5 wt. % Pd/Al$_2$O$_3$ catalyst. The arrows indicate the increase of solubility (a) and kinetic constant (b and c).

Next, we studied the effect of increasing the $k_{abs,p-NIPAM}$, at low solubility (see Figure 2.9b). Here, it can be noted that regardless of the kinetics of the absorption process no induction period was observed and the saturation time was unaltered. Notably, increasing the $k_{abs,p-NIPAM}$ at a high solubility, an induction period was observed, followed by a sharp increase in relative absorbance of CO-Pd before approaching the regime (see Figure 2.9c). As shown in Figure 2.10a-b the combination of fast kinetics of absorption and high solubility results in good agreement between the results obtained from the ATR-IR cell model and experiment (relative error of 9% for 15 min polymerization) (see Section S2.8.12.8.).
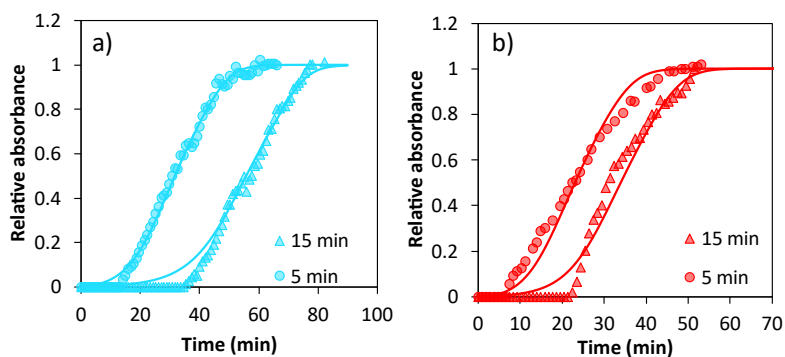
Figure 2.10: Normalized integrated peak area of the CO peaks at the palladium surface at 25 °C (c) and 40 °C (d) for 5 (circle) and 15 (triangle) minutes polymerization on Pd/Al_2O_3 catalyst containing 3.5 wt. % Pd coated on a ZnSe crystal containing c.a. 5 mg conducted on a flow of 10% CO/Ar dissolved in water with a flow rate of 2 mL min^{-1}, where the lines correspond to model based on Fick's 2nd law of diffusion for 15 (triangle) and 5 (circle) polymerization time assuming values from Table S2.5.

2.5.4   Polymer coverage dependency simulation

To demonstrate the sensitivity of a polymeric system to temperature, two different situations were considered using our validated 1D model of the ATR-IR saturation experiments, including; (1) a system containing polymeric brushes inside the pores of the membrane as well as on its surface following the experimentally tested membranes (Figure 2.11a) and (2) a hypothetical system containing only a dense layer of polymer on top of the membrane surface so-called "polymer blanket" (Figure 2.11b). The polymer was assumed to follow the temperature responsive behaviour obtained from independent in-situ ellipsometry measurements of p-NIPAM on Si-wafers (see Figure S2.23). Considering that the absorption of CO in the p-NIPAM domains was non-activated, we assumed constant absorption kinetics with respect to temperature (see Section S2.8.12.8.)
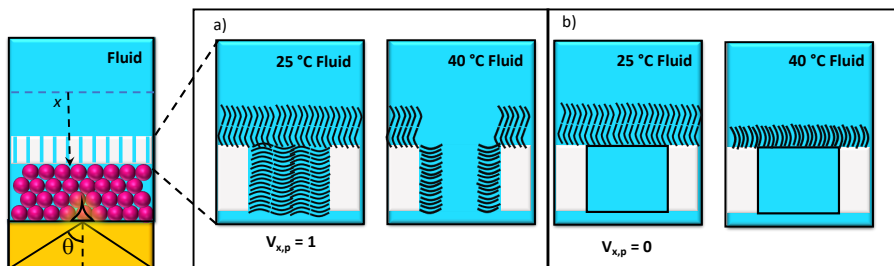
Figure 2.11: Schematic representation of the polymer growing in a polymeric membrane, where the polymer grows on the top surface and inside the pore (a) and a hypothetical situation as nano reactor where a dense layer grows only on top of the membrane (b).

Figure 2.12 shows the time needed to reach full saturation normalized by the saturation time of the non-coated membrane (at 25 °C), where (Pore) represents the polymers growing both on top as well as inside the membrane pores and (Top) relates to the model considering the "polymer blanket" (for further details see Section S2.8.12.9.). As can be noticed, when the polymers are located inside the membrane pores (see Figure 2.11a and Figure 2.12 designated as "Pore")) the time required to achieve full saturation of the Pd surface with CO decreases with temperature. This can be attributed to the lower fraction of pore volume occupied by the polymer as the p-NIPAM brushes collapse at temperatures above the LCST, essentially opening the pores for molecular diffusion, resembling the positive stimulus-responsive behaviour shown in Figure 2.1c across the entire temperature.

In stark contrast, when the polymer was located on top of the membrane as a blanket, the observed trends are more complex (see Figure 2.11b and Figure 2.12 designated as "Top"). At temperatures below the LCST the normalized time of saturation decreases as a function of temperature. Here, the diffusion of CO through the polymer layer is sufficiently fast to overcome the small changes in the polymer conformational structure. Above the LCST of p-NIPAM (32 °C), the polymer layer collapses leading to the formation of a dense layer that hinders diffusion leading to longer saturation times of CO-Pd. At this point, increasing further the temperature only causes a small reduction in the normalized saturation time,

which is due to the Arrhenius-like behaviour of the molecular diffusion with a small activation barrier of c.a. 18 kJ mol^{-1}. These observations resemble the negative stimulus-response behaviour (see Figure 2.1c). For further validation of this model future experiments need to be conducted to demonstrate the effect of polymer brushes on CO transport with respect to temperature and addition of a polymeric layer resembling a "polymer blanket".
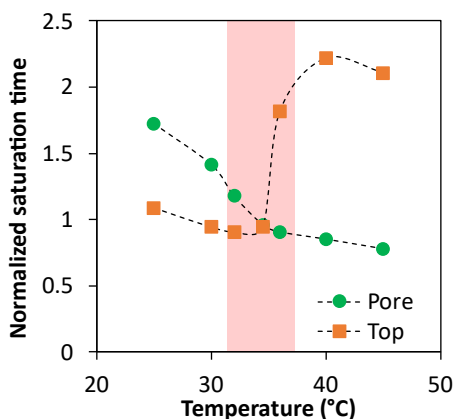

Figure 2.12: Normalized Palladium saturation time (normalized by the non-coated membrane (at 25 °C)) as a function of temperature for polymer brushes growing inside the pores (situation represented on Figure 2.11a) and polymer brushes growing on top to the membrane as a dense layer (situation represented on Figure 2.11b) where the demarked zone represents the temperatures near the LCST where the polymer has a transition from swell to collapse state.

2.6 Conclusion

This work provides direct evidence that on stimulus-responsive polymers a complex interplay between the swelling behaviour of the polymeric brushes, kinetics of absorption in the polymer matrix, polymer-absorbate energy of interaction (i.e. solubility) and molecular diffusivity determine the dynamic response of these layers towards reaction in core-shell nano reactors and membranes. Essentially, our experimental results using in-situ ATR-FTIR and theoretical calculations indicate that below the LCST (i.e. swollen state) the saturation time shifted to higher values due to the absorption of CO inside the

p-NIPAM domains which occupy the entire volume of the pores. Increasing the temperature collapsed the polymer to smaller volumes, thus opening the pores towards unrestricted diffusion after a short induction period caused by absorption. Contrary to previous theories on diffusion-absorption, we show that the rate of transport of solutes through these membranes is controlled by the kinetics of the absorption in the polymer, the strength of the solute-polymer interaction (i.e. solubility), the polymer fraction inside the pores, and the diffusion coefficient inside the polymer. These new insights on the behaviour of thermo-responsive membranes under dynamic operation will provide new opportunities for catalyst design rules, separation membranes, and drug-delivery systems with well-controlled kinetics of solute transport.

2.7   Acknowledgements

2.8   Annexes

2.8.1   Structure p-NIPAM
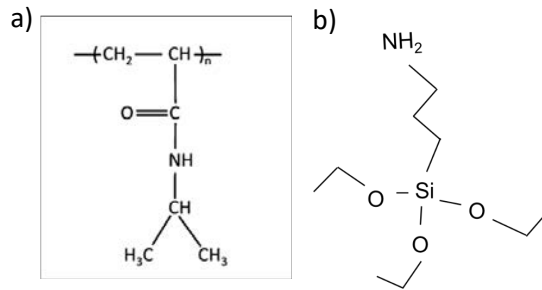
Figure S2.1: Poly(n-isopropylacrylamide) chemical structure[34] (a) and (3-aminopropyl) triethoxysilane (APTES) molecular structure (b).
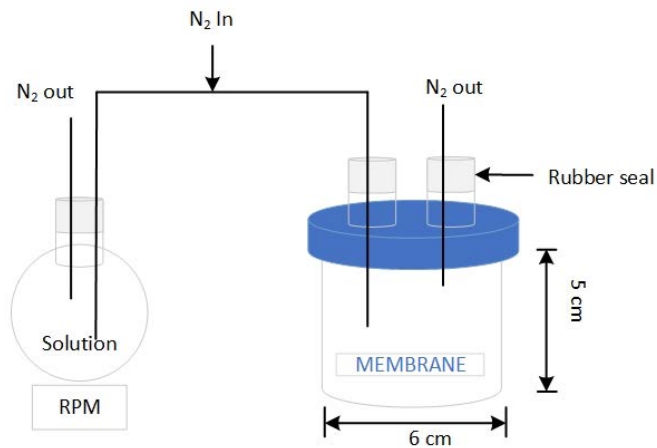
Figure S2.2: Schematic of the polymerization setup with a glass reactor where the membrane is added.

2.8.2 ATR-IR setup
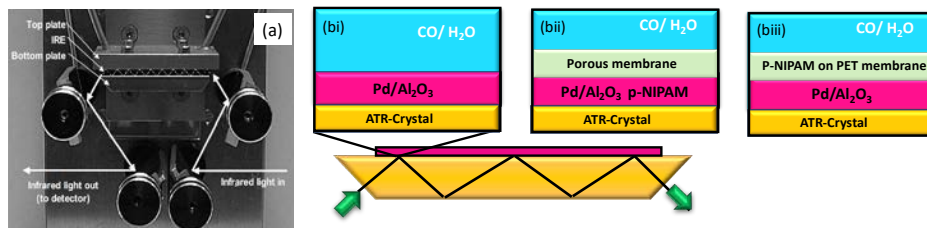
Figure S2.3: Home built in-situ ATR-IR flow through cell [47] (a) and schematic representation of the ATR-IR assembly in the case of Pd/Al$_2$O$_3$ containing 0 (bi) and 7 (bii) wt. % carbon, where a membrane was added to the top of the non-calcined catalyst layer and in the case of polymerized PET membranes where the polymer is decoupled on the palladium surface.
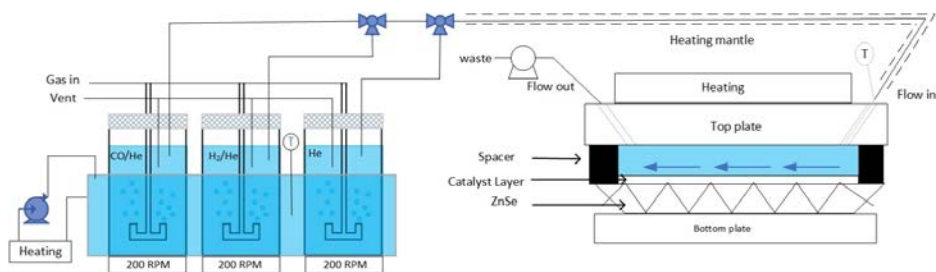
Figure S2.4: Schematic representation of the experimental setup and the customized flow through ATR-IR cell.

2.8.3 Characterization on Pd alumina

Table S2.1: Accessible metal on the Pd/Al$_2$O$_3$ calculated from the palladium metal loading and dispersion. Palladium particle size obtained from CO chemisorption and Specific surface area from Brunauer-Emmett-Teller (BET) method from N$_2$-physisorption at -196°C.

	Metal loading Pd wt. (%)	Dispersion CO chemisorption (%)	Pd diameter CO chemisorption (nm)	Accessible metal (mg)/mass catalyst (g)	BET surface area (m^2 g^{-1})
Pd/Al$_2$O$_3$ catalyst	0.9a	57	2	5.1	195
	3.3b	36	3	11.9	187

a – more details refer to [30], b – more details refer to **Chapter3**.

2.8.4 Polymer brushes characterization

2.8.4.1 TGA and Ea

Figure S2.5a shows the weight loss profile from TGA, where the polymer coated membrane did not reach 100 % weight loss due to possible contamination of the surface with Pd/Al$_2$O$_3$ after ATR-IR experiments. These p-NIPAM decomposition temperature is in agreement with previous results [47].
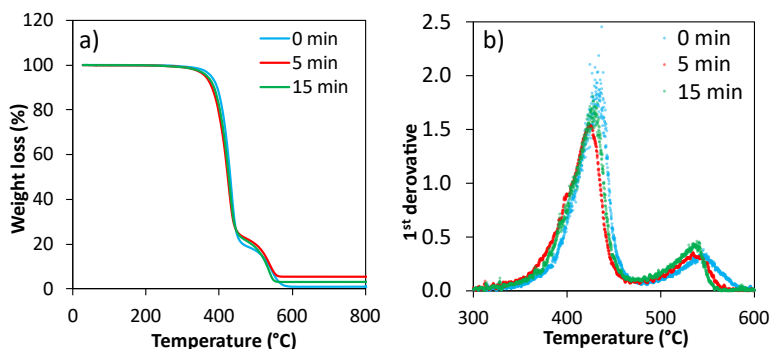
Figure S2.5: Thermal gravimetric analysis (TGA) from 25 to 800 °C (a) and 1st derivative (b) using synthetic air for the membrane containing 0 (blue), 5 (red) and 15 (green) min polymerization time, respectively.

Table S2.2: Carbon and Nitrogen content obtained from elemental analysis (EA). Where 5 min and 15 min represent the polymerization time used on the synthesis of the polymer brushes on the membrane surface and PET is a non-polymerized membrane.

	N %	C %
PET	0	62
5 min PET	0.6	60
15 min PET	0.8	58

2.8.4.2 EDS mapping

Figure S2.6biii shows the N presence inside the pore and the membrane pore, this could have been caused while cutting the membrane cross section.
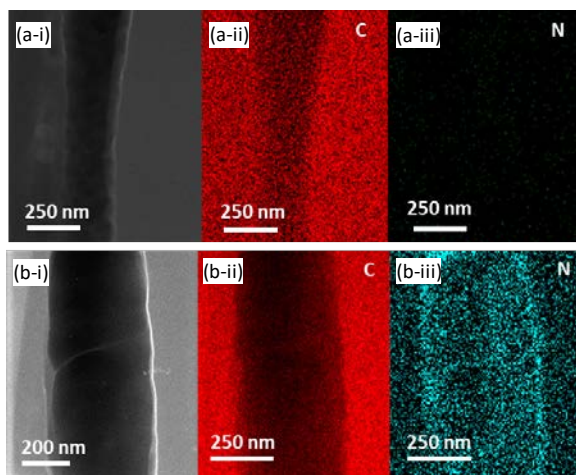
Figure S2.6: STEM-HAADF characterization (i) and EDS mapping for carbon (ii) and nitrogen (iii) inside the membrane pore containing 0 min and 15 min polymerization time (a-b, respectively).

2.8.4.3 Ellipsometry experiments

The polymerization growth time and temperature dependence on p-NIPAM polymer brushes was determined by ellipsometry. Ellipsometry experiments could not be conducted on the membrane used on the ATR-IR measurements, due to light absorption. Instead, a standard silicon wafers were used with a known refractive index. Dry thickness measurements were done under ambient conditions. To verify surface homogeneity six spots were measured at the Silicon wafer. Wet thickness and temperature responsiveness were measured by a 5 mL heated liquid cell filled with DI H_2O when polymer brush reached the steady state. The experiments were performed from low to high temperatures with an increment of 0.5 °C (20 to 40 °C). All the results were fitted using the CompleteEase software (J.A. Woollam Co). The polymer brush thickness and refractive index were determined from (Ψ, Δ) spectra. The substrate was modelled as a silicon wafer with 2nm native oxide. The optical dispersion (n) of the polymer was modelled with the Cauchy dispersion model, shown in Eq. S2.1.

$$n(\lambda) = A + \frac{B}{\lambda^2} + \frac{c}{\lambda^4}$$

Eq. S2.1

Where λ is the wavelength and A/B/C are Cauchy parameters obtained from fitting the data to the model. To have fewer fitting parameters c was considered zero. The polymer brush was considered a transparent material, with the assumption that the absorption coefficient was close to zero (k=0) which is related to the imaginary component of the refractive index. For the dry thickness, the p-NIPAM film was considered uniform and with a neglected roughness of the polymeric layer. For the swollen brush height, a gradual change in polymer density as a function of the distance from the surface was incorporated, for more details [48].

Figure S2.7 shows the brush thickness dependence on the polymerization time measured by Ellipsometry. A polymerization time of 15 min polymerization resulted on a homogeneous dry brush thickness of 60 ± 3 nm, increasing the polymerization time led to an increase on the polymer brush thickness (see Figure S2.7). Similar results were reported by Humpheys et al. [33]
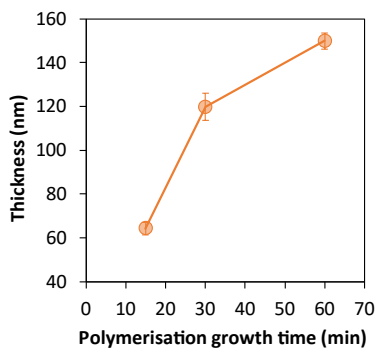
Figure S2.7: Average dry brush thickness with 15, 30, 60 min polymerization on a silicon wafer measured by ellipsometry.
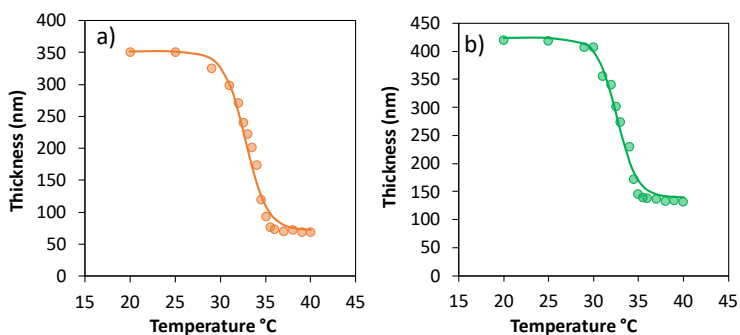
Figure S2.8: Polymer thickness at different temperatures on p-NIPAM polymer brushes with 15 min (a) and 30 min (b) polymerization on a silicon wafer measured by Ellipsometry in water.

The swelling ratio, the water fraction and polymer fraction of the polymer brush can be calculated from the thickness obtained on Figure S2.8, as shown on Eq. S2.(2-4).

$$r_{swelling} = \frac{d_{wet} - d_{dry}}{d_{dry}}$$

Eq. S2.2

$$\Phi_{water} = \frac{d_{wet} - d_{dry}}{d_{wet}}$$

Eq. S2.3

$$\Phi_{p-NIPAM} = 1 - \Phi_{water} \qquad \text{Eq. S2.4}$$

2.8.4.4 AFM experiments

The water and temperature effect on membrane pore coverage with polymer brushes was measured by AFM. Due to the fact of low resolution with 200 nm pore size diameter. Measurements were made using 2 μm pore diameter membrane with two hours polymerization. The polymer brush thickness cannot be extrapolated from the AFM measurements due to no reference to the membrane surface.

The effect of the polymer brushes at the membrane pores was measured by AFM images, as shown in Figure S2.9. At temperatures below LCST, the H-bonding with NH motive in the polymer chains and water molecules dominate resulting on the swollen state of the polymer brush. This resulted in a decrease of the effective pore diameter by the presence of the polymer brushes. Upon increasing temperature above the LCST, the hydrogen bonds are destabilized leading to the collapse of the polymer brushes, as demonstrated in Figure S2.9 b-c. Subsequently, the temperature was decreased to 20 °C, demonstrating reversible polymer conformation upon changing temperature (see Figure S2.9d).
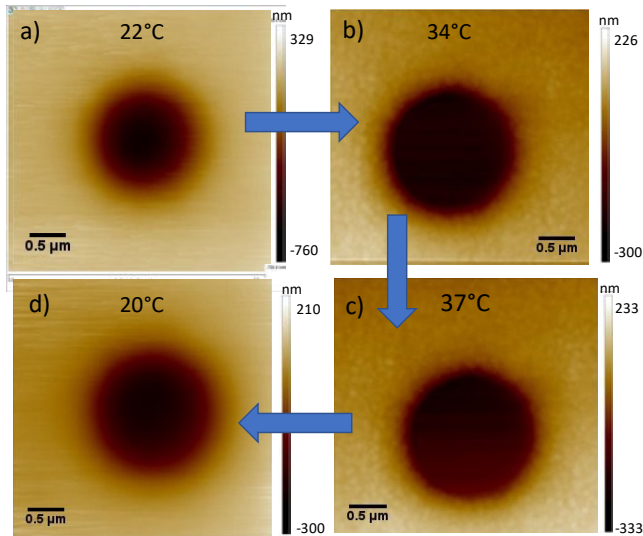
Figure S2.9: AFM images on 2 μm pore diameter PET membrane with 2 hours polymerization in water medium at 22 °C (a) then increased to 34 °C (b) and 37 °C (c). Then the polymer brush was measured again when 20 °C (d) reached again.

Figure S2.10 shows the effective pore diameter, although this is not the same representation as in 200 nm pore diameter size, shows the expected pore coverage behavior during our experimental results.
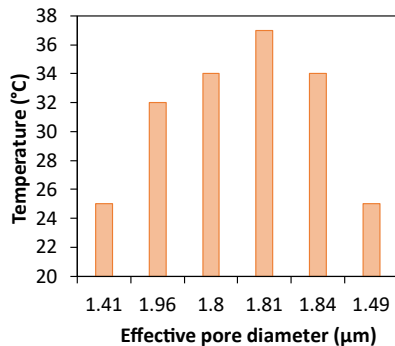
Figure S2.10: Effective pore diameter of PET (2μm) with 2h polymerization obtained from the AFM images, as shown in Figure S2.9.

2.8.5   Penetration depth and electric field decay

Table S2.3: Refractive index values for ZnSe crystal, alumina support, Pd metal and water [46].

	ZnSe	Al_2O_3	Pd	Water
Refractive index	2.43	1.67	3.10	1.33

The penetration depth of the evanescent wave was calculated using Eq.S2.5.[49]

$$d_p = \frac{\lambda}{2\pi n_1 \sqrt{(sin^2\theta - (\frac{n_2}{n_1})^2)}}$$

Eq. S2.5

Where n_2 and n_1 denote the refractive index of the crystal and sample, respectively, θ the angle of incidence (ZnSe, 45 °) and λ the wavelength. The refractive index of the samples (n_1) consisted dense material Pd/Al_2O_3 and the pores files with water.

The index of reflection of a dense material like Al_2O_3 and palladium significantly decreases with increasing porosity, therefore the refractive index of a porous material can be calculated with Eq. S2.6.[46]

$$n_{eff} = \sqrt{(1 - \Phi)n_c^2 + \Phi n_d^2}$$

Eq. S2.6

Where φ is the relative porosity and n are the refractive index of the phases c and d.

In this system the values are represented on Eq. S2.7 and S2.8.:

$$n_{eff,pd/Al2O3} = \sqrt{(0.9989(1.67)^2 + 0.00108(3.10)^2} = 1.67$$

Eq. S2.7

$$n_1(Pd / Al_2O_3, pores\ filled\ with\ water =$$
$$= \sqrt{(0.70(1.33)^2 + 0.3(1.67)^2} = 1.44$$

Eq. S2.8

Figure S2.11a shows the penetration depth as a function of wavenumber for catalysts with different palladium loading. We can conclude that the penetration depth increases with decreasing the wavenumber. No significant difference was obtained with different palladium loading on the alumina support.
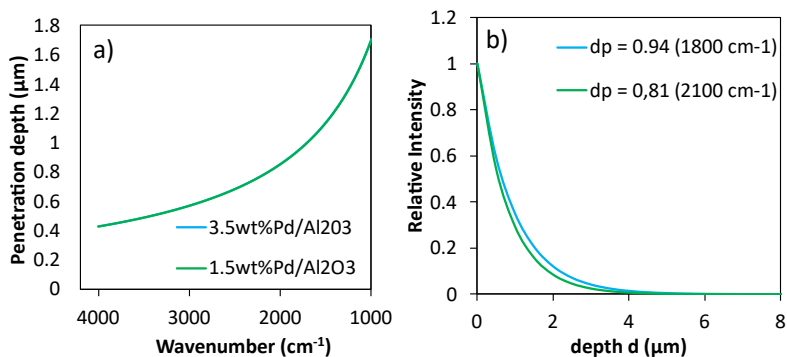
Figure S2.11: Penetration depth for 1 and 3.5 wt. % Pd/Al$_2$O$_3$ on ZnSe (a) and electric field decay on the ATR-IR evanescent wave (b).

Figure S2.11b shows the exponential decay of the evanescent field as a function of the distance from the surface of the crystal at 1800 and 2100 cm^{-1}. This was calculated by Eq. S2.9.[49]

$$\frac{I}{I_O} = e^{\left(-\frac{d}{d_p}\right)}$$

Eq. S2.9

Where I/I_O is the relative intensity of the electric field decay, d the distance from the surface of the crystal until the end of the catalyst layer (μm) and d_p is the penetration depth (μm).

2.8.6 CO moving front
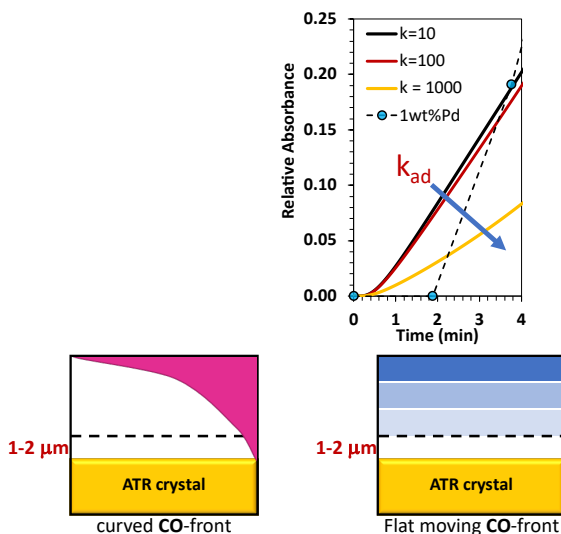
Figure S12: Schematic representation of CO transport on an ATR crystal.

2.8.7 Effect palladium surface area
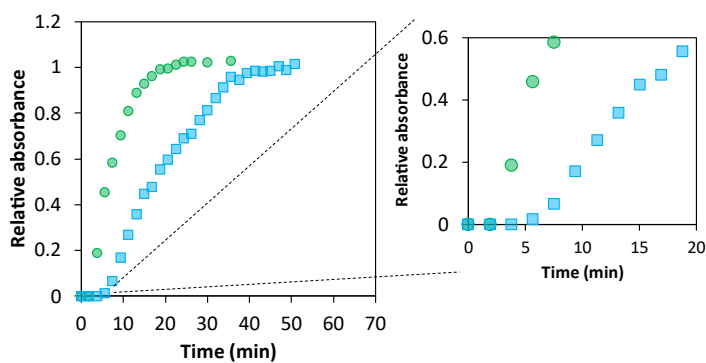
Figure S13: Normalized integrated area of the linear, bridge and multi peaks on Pd/Al$_2$O$_3$ catalyst containing 1 (green) and 3.5 (blue) wt. % at full palladium saturation on a ZnSe crystal containing c.a. 5 mg conducted at 25 °C on a flow of 10% CO/Ar dissolved in water with a flow rate of 2 mL min^{-1}. Based on the data in Figure 2.4b and Figure S2.14 respectively.
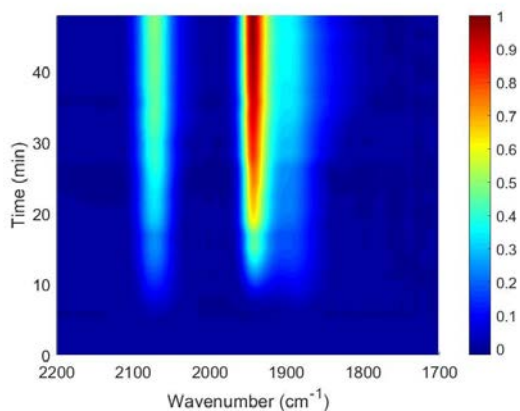
Figure S2.14: ATR-IR spectra as a function of time of CO adsorption on 3.5 wt. % Pd/Al$_2$O$_3$ catalyst on a ZnSe crystal containing c.a. 5 mg conducted at 25 °C on a flow of 10% CO/Ar dissolved in water with a flow rate of 2 mL min^{-1}.

2.8.8   Polymer coated catalyst

2.8.8.1 Polymer coated catalyst characterization

Table S2.4 shows the carbon percentage at the alumina surface and the weight loss from TGA obtained above 350 °C. For details related with characterization and synthesis of polymer coated catalyst [50].

Table S2.4: Carbon content from elemental analysis (EA) and weight loss from Thermal gravimetric analysis (TGA) obtained from 25 to 800 °C using synthetic air atmosphere.[50]

Pd/Al$_2$O$_3$ catalysts	Carbon (wt. %)	Weight loss (%)
0 wt. % C	0	
7 wt. % C	7	10

2.8.8.2 Polymer coated catalyst on ATR-IR

When designing the experiments, we realized that to properly understand the effect of mass transport of polymer coatings on working catalysts it essential to avoid so-called "ligand or solvation effects" that can convolute the dynamics of the diffusion and chemisorption. In fact, as shown in **Chapter 3** thermo-responsive polymer coatings on Pd/Al$_2$O$_3$ catalysts tune the reaction selectivity due to a change on the micro-solvation environment without altering the molecular transport next to the metal sites. Figure S2.15 shows the ATR-IR spectrum of CO chemisorption on pre-reduced Pd/Al$_2$O$_3$ containing 0 and 7 wt. % carbon as p-NIPAM. Where a red shift was observed of the CO bond on palladium by p-NIPAM brushes presence. This translates in the weaking of the CO bond to the palladium surface (see Figure S2.16 and Figure S2.17). Similar observations were encountered with the observations on NO$_2^-$ where a red shift was observed by the addition of polymer brushes indicating a change in the binding strength of chemisorbed species.
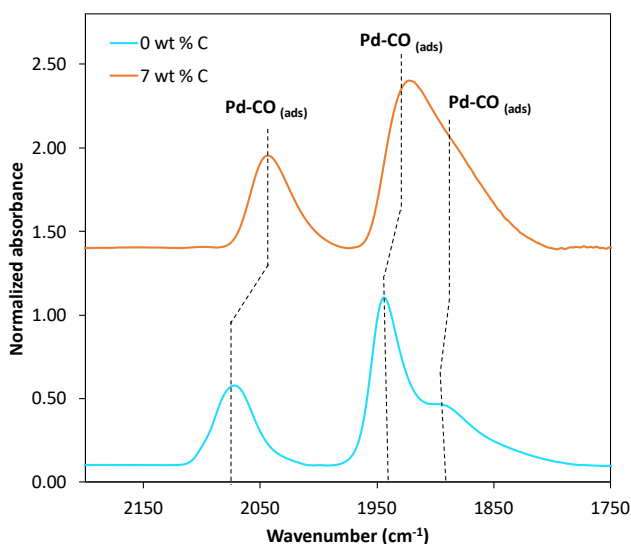
Figure S2.15: In situ ATR-IR spectra of CO chemisorption on Pd/Al$_2$O$_3$ catalyst containing 0 (blue) and 7 (orange) wt. % carbon in the form of p-NIPAM at full palladium saturation on a ZnSe crystal containing c.a. 5 mg conducted at 25 °C on a flow of 10 % CO/Ar dissolved in water with a flow rate of 2 mL min^{-1}.

Figure S2.16: Peak deconvolution at the saturation time for CO chemisorption on Pd/Al$_2$O$_3$ catalyst containing 0 (blue) and 7 (orange) wt. % carbon in the form of p-NIPAM at full palladium saturation on a ZnSe crystal containing c.a. 5 mg conducted at 25 °C on a flow of 10 % CO/Ar dissolved in water with a flow rate of 2 mL min^{-1}.

Figure S2.17: ATR-IR spectra as a function of time of CO adsorption on Pd/Al$_2$O$_3$ catalyst containing 7 wt. % carbon in the form of p-NIPAM on a ZnSe crystal containing c.a. 5 mg conducted at 25 °C on a flow of 10 % CO/Ar dissolved in water with a flow rate of 2 mL min^{-1}.

2.8.9   Effect of temperature and membrane
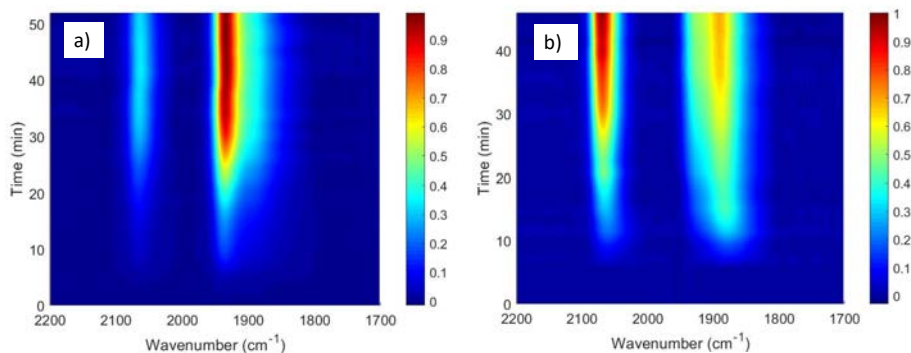
Figure S2.18: ATR-IR spectra as a function of time of CO adsorption on 3.5 wt. % Pd/Al$_2$O$_3$ catalyst at 40 °C (a) and containing a membrane with a 200 nm pore diameter at 25 °C (b) on a ZnSe crystal containing c.a. 5 mg conducted on a flow of 10 % CO/Ar dissolved in water with a flow rate of 2 mL min^{-1}.

2.8.9.1 CO distribution at the palladium surface

The spectrum of CO on the palladium surface shows some variability in the peak distribution of the CO linear, bridge and multi between different palladium samples. However, this distribution changes do not modify the total surface coverage. The CO molecules bonded to the surface is constant across the different analysed samples.

2.8.10 Effect of polymer
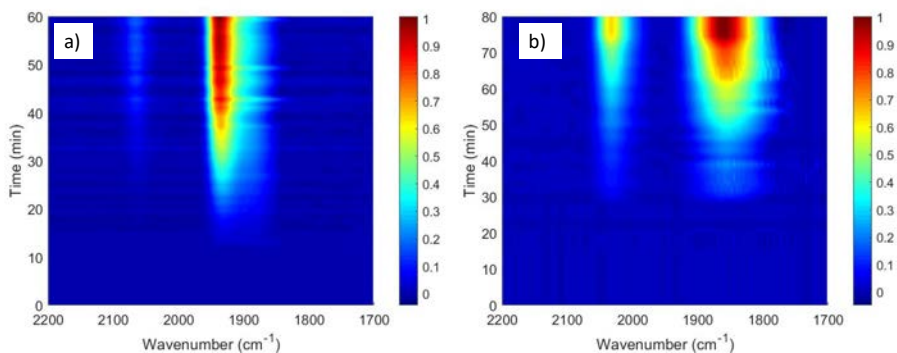
Figure S2.19: ATR-IR spectra as a function of time of CO adsorption on 3.5 wt. % Pd/Al$_2$O$_3$ catalyst containing a membrane with a 200 nm pore diameter with a polymerization time of 5 min (a) and 15 min (b) on a ZnSe crystal containing c.a. 5 mg conducted at 25 °C on a flow of 10 % CO/Ar dissolved in water with a flow rate of 2 mL min^{-1}.
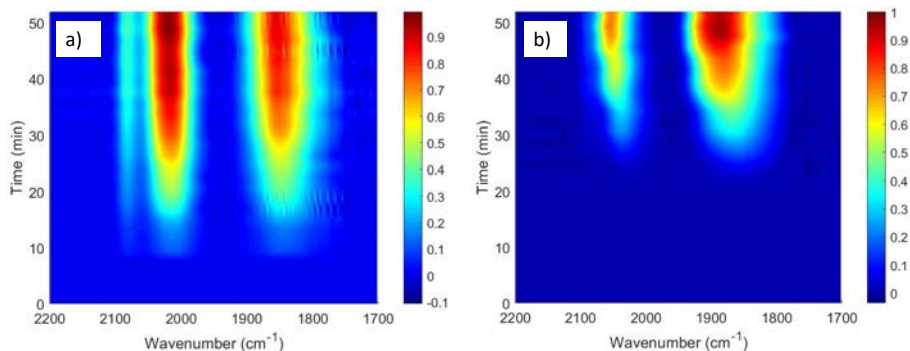
Figure S2.20: ATR-IR spectra as a function of time of CO adsorption on 3.5 wt. % Pd/Al$_2$O$_3$ catalyst containing a membrane with a 200 nm pore diameter with a polymerization time of 5 min (a) and 15 min (b) on a ZnSe crystal containing c.a. 5 mg conducted at 40 °C on a flow of 10 % CO/Ar dissolved in water with a flow rate of 2 mL min^{-1}.

2.8.11 Flow rate effect
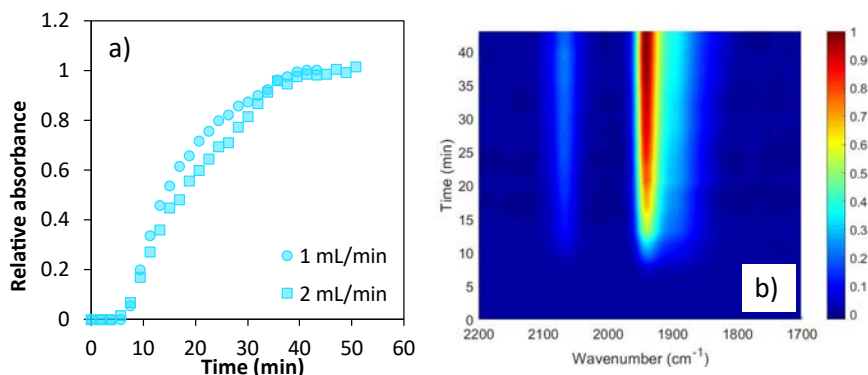
Figure S2.21: Normalized integrated area of the linear, bridge and multi peaks at different flow rates (a) and ATR-IR spectra as a function o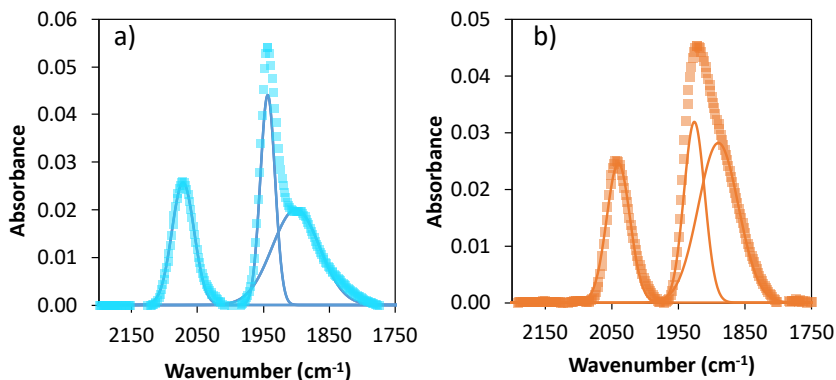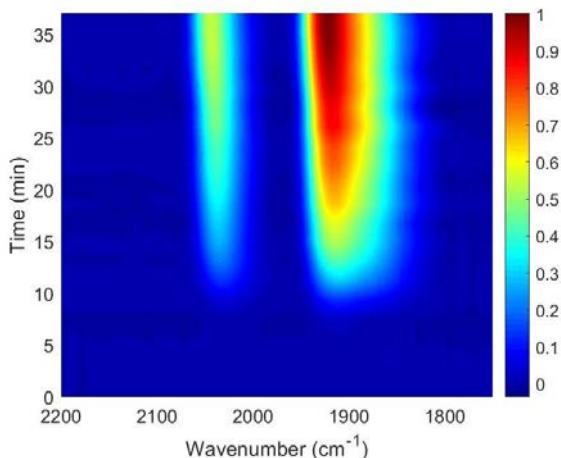f time with a 1mL min^{-1} flow rate (b) of CO adsorption on Pd/Al$_2$O$_3$ catalyst containing 3.5 wt. % Pd on a ZnSe crystal containing c.a. 5 mg conducted at 25 °C on a flow of 10 % CO/Ar dissolved in water.

2.8.12 Modelling

2.8.12.1 Boundary layer

Considering a flow rate into the ATR-IR cell of 2 mL min^{-1} with a CO concentration of 0.095 mol m^{-3}, this results on a CO molar flow rate of 3.2×10^{-9} mol s^{-1}. In addition, the adsorption rate for 3.5 wt. % Pd/Al$_2$O$_3$ was calculated based on the adsorption data with a saturation time of 40 min and assuming a stochiometric of 1:1 CO-Pd resulting on a CO molar flow rate of 9.4×10^{-11} mol s^{-1}. Since the flow rate of CO into the system is 34 times higher than the adsorption rate the gradients towards the ATR-IR cell can be considered negligible. From Peclet number (Pe) calculations (1.6×10^3), see Eq. S2.15, where Pe number was above 1 indicates that the ATR cell was under diffusion regime instead of convective regime. The boundary layer was 150 µm and calculated using the Sherwood's correlation (shown in Eq. S2.10-14). Re values were below 2100 indicating laminar flow in the reactor cell. Eq. 11 describes the Sherwood (Sh) correlation with respect to the length of the plate for a laminar boundary layer, which depends on the Reynolds (Re) and Schmidt (Sc) number.

$$v = \frac{Q}{A_{lateral}}$$

Eq. S2.10

$$Re = \frac{\rho\, v\, D}{\mu}$$

Eq. S2.11

$$Sc = \frac{\mu}{D_{CO/H_2O}\, \rho}$$

Eq. S2.12

$$Sh = \frac{k_c\, D}{D_{AB}} = 0.664 Re_D^{1/2} Sc^{1/3}$$

Eq. S2.13

$$d = \frac{Sh\; D_{AB}}{k_c}$$

Eq. S2.14

$$Pe = Re\, Sc$$

Eq. S2.15

Where v is the velocity of the fluid (m s^{-1}), Q is the flow (m^3 s^{-1}), A is the lateral area from the ATR cell (m^2), Re is the Reynold number, ρ water density (kg m^{-3}), v is the velocity of the fluid (m s^{-1}), D is the reactor height (m), μ dynamic fluid viscosity (Pa s), Sc is Schmidt number, D_{AB} diffusion coefficient CO in water (m^2 s^{-1}), Sh is the Sherwood number, k_c is the mass transfer coefficient (m s^{-1}), d the boundary layer thickness (m) and Pe is the Peclet number.

2.8.12.2   Saturation curve

From Beer-Lambert law, the absorbance (A) is directly proportional to the concentration (c), as shown in Eq. S2.16, where ε is the extinction coefficient of the attenuating specie and L is the optical path length. This is correlated with the integration of the evanescent field, where the evanescent wave follows an exponential decay as a function of the ATR-IR crystal surface distance shown on Section S2.8.5 (see Figure 2.7). By multiplying the total amount of palladium-CO bonds by the exponential decay function is assumed to

approximate the peak area obtained from ATR-IR spectroscopy. The modelled peak area is tracked over time to obtain a representation of the calculated saturation curve. Then, the normalized saturation curve can be determined, as shown on Eq. S2.17, where n_{pd} represent the total moles of the palladium, x the distance from the surface of the crystal until the end of the catalyst layer and d_p is the penetration depth.

$$A = -\log\left(\frac{I}{I_O}\right) = \varepsilon L c \qquad \text{Eq. S2.16}$$

$$\frac{A}{A_{total}} = \int_0^{t_{final}} \int_0^x \frac{1}{n_{pd(total)} \cdot e^{-\frac{x}{d_p}}} \, n_{pd}(t) \cdot e^{-\frac{x}{d_p}} \, dx \, dt \qquad \text{Eq. S2.17}$$

2.8.12.3   Diffusion coefficient CO

The diffusion coefficient of CO in water was calculated with Eq. S2.18.[38]

$$D_i = A e^{\frac{-E_a^d}{N_a k_b T}} \qquad \text{Eq. S2.18}$$

Where D_i is the CO diffusion in water (m^2 s^{-1}), A the pre- exponential factor (m^2 s^{-1}), E_{ad} the activation energy for diffusion (J mol^{-1}), N_a the Avogadro constant of value 6.023×10^{23} (mol^{-1}), k_b the Boltzmann constant of value 1.308×10^{-23} (J K^{-1}) and T the absolute temperature (K).

The E_{ad} has a value of 14.5 kJ mol^{-1} and a pre-exponential factor of 1839 m^2 s^{-1}. Giving a diffusion coefficient of 2.1 nm^2 s^{-1} and 2.8 nm^2 s^{-1} at 25°C and 40 °C.

2.8.12.4 Volume fraction at the polymeric membrane
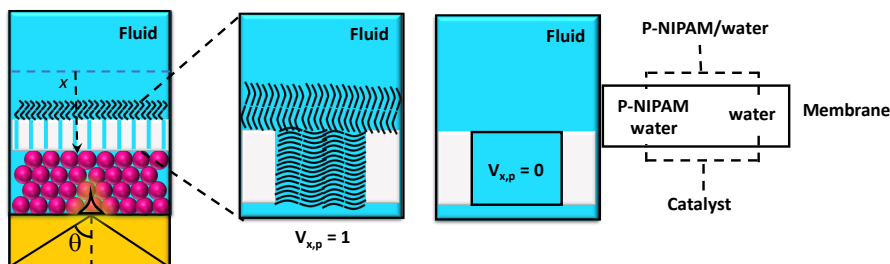
Figure S2.22: Schematic representation of the polymer volume fraction and the resultant resistance in parallel at the membrane pore due to the polymer brush presence at the membrane.

2.8.12.5 Stokes radii calculation

This model has the assumption that the dominant factor of the diffusion is the size of the particles, which is calculated by the stokes Einstein equation, as shown on Eq. S2.19.

$$a_w = \frac{k_b \, T}{6 \, \pi \, \eta \, D_i}$$

Eq. S2.19

Where k_b is the Boltzmann constant (J K^{-1}), T the absolute temperature (T), η the dynamic viscosity of water (Pa s^{-1}) and D_i the diffusion coefficient of CO in water (m^2 s^{-1}).

2.8.12.6 Diffusion coefficient on a polymeric membrane

First, we employed ellipsometry data to correlate the swelling and polymer volume fraction as function of time. As shown in Figure S2.23a, at temperatures where the polymer brushes are in the swollen state a lower fraction of p-NIPAM is obtained as the volume occupied is dominated by water molecules. At these conditions the diffusion coefficient is reduced by progressively decreases as the density of the polymer layer increases. However, at temperatures close to the LCST of the polymer the collapse of the p-NIPAM in a dense

polymer layer leads to large increase in the polymer density ($\varphi_{p\text{-NIPAM}} = \varphi_{LCST}$, see Figure S2.23a).

By coupling the evolution of the polymer conformational changes obtained from ellipsometry, with the diffusion coefficient model shown in Eq 2.14, one could obtain the relative change in the effective diffusion coefficient of CO inside the polymer. As shown in Figure S2.23b the normalized diffusion coefficient of CO on p-NIPAM brushes initially increases with temperature below the LCST. In this regime the polymer thickness and thus the polymer density are essentially constant. As a result, the coefficient is dominated by the exponential increase of the diffusion coefficient with temperature. As the temperature approaches the LCST the relative diffusion coefficient on the polymer decreases with temperature due to the collapse of the polymer. Essentially, the polymer fraction increases at the expense of and that of water leading to lower effective diffusion coefficients.
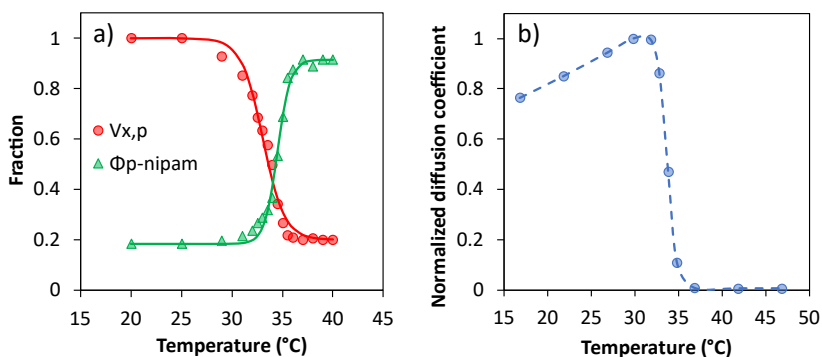
Figure S2.23: Swelling and polymer fraction calculated from Ellipsometry characterization (a), normalized diffusion coefficient for CO on p-NIPAM brushes from Eq. 2.14 (b) as a function of temperature.

CO solubility in p-NIPAM

The CO absorption rate can be described as Eq. S2.20, where k_{ads} is the absorption rate constant (s^{-1}) and k_{des} is the desorption rate constant (s^{-1}). The absorption is a reversible process with an equilibrium constant (K_{ads}) defined as Eq. S2.21. However, the desorption rate is assumed negligible due to the excess of CO in the liquid in comparison to the p-NIPAM matrix.

$$r_{CO}^{abs} = -k_{abs}c_{CO}\theta_{p-nipam}(T)_{x,t} + k_{des}(1 - \theta_{p-nipam}(T))_{x,t}$$

<div align="right">Eq. S2.20</div>

$$K_{abs} = \frac{k_{abs}}{k_{des}}, k_{abs} \gg k_{des}$$

<div align="right">Eq. S2.21</div>

The solubility of CO in the polymer brushes is closely related to the reactant-polymer-solvent interactions. In this case, the solubility of CO on the polymeric brush was assumed to be more favourable at lower temperatures due to the high dipole moment of CO, which most likely favours the formation of a hydration layer around the CO facilitating stabilization inside the polar p-NIPAM bushes at these conditions (spontaneous process, $\Delta G<0$). By increasing temperature, one expects that the relatively weak interactions between the water-CO-p-NIPAM is surpassed by the entropic contributions to the Gibbs Free energy of the system. Thus, decreasing its solubility in the p-NIPAM. To correlate this phenome a partitioning of the solute was used as defined on Eq. 2.18. The volume of polymer is dependent on temperature and independent of the solubility. In this case, the volume of polymer was defined as the total volume of polymer and water, which decreases with temperature due to the polymer collapse. Consequently, the volume available for CO to absorb decreases.

2.8.12.7 Transport in ATR-IR cells

Effect of the kinetic constant and palladium mol

The kinetic constant and β (equals to Ea/RT) were fitting parameters that define the curve shape. Figure S2.24 shows the effect of CO adsorption rate constant and coverage dependence constant (β) on CO chemisorption at the palladium alumina catalyst.
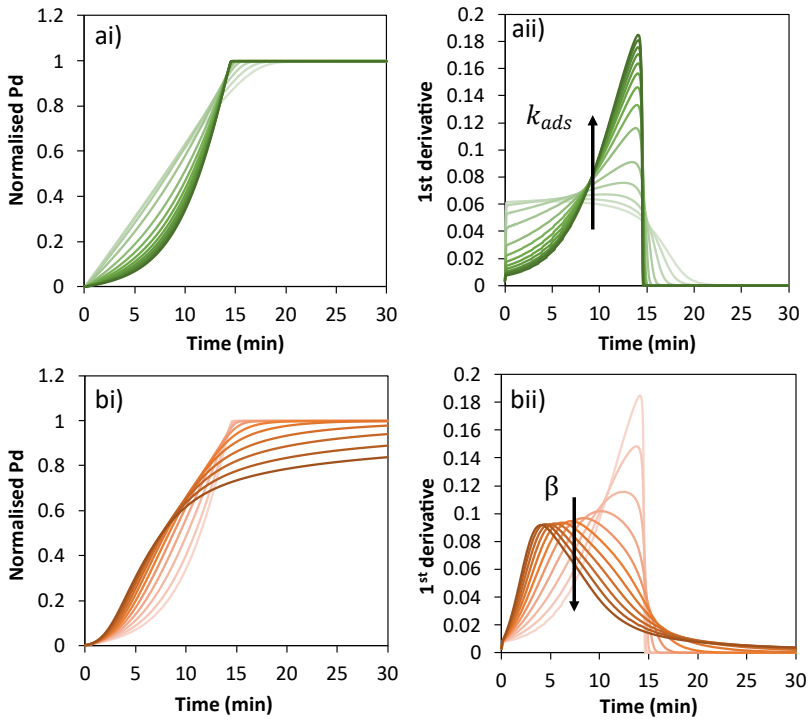
Figure S2.24: CO adsorption rate constant (a) varied between $10 - 1000$ s^{-1} with beta equals to zero and β (b) varied between 0 - 10 with rate constant equals to 1000 s^{-1} on 1 wt. % Pd/Al$_2$O$_3$ on the palladium chemisorption (ai-bi) and 1st derivative (aii-bii) at 25 °C with the diffusion coefficient calculated from Eq. S2.18.

The kinetic constant of adsorption used was 1000 s^{-1} due to the strong Pd-CO interaction. The beta which better describes the coverage effect on the CO rate was 5. Figure S2.25 shows the effect of accessible active metal surface on CO chemisorption. For these results the kinetic constant of adsorption and beta were kept constant, only the total moles of palladium were changed. The results show a good prediction from the 2nd Fick diffusion model, where higher palladium surface leads to longer time for the CO saturation.
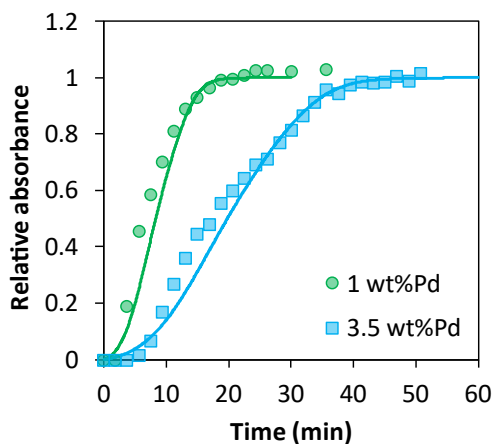
Figure S2.25: CO rate with 1 wt. % (green) and 3.5 wt. % (blue) Pd/Al$_2$O$_3$ at 25 °C 2 mL min^{-1} and 10 % CO/He dissolved in water and the respective results from 2nd Fick diffusion modelling, where the palladium moles were calculated from the values at Table S2.1.

Membrane and temperature effect on transport

Figure S2.26a shows the effect of temperature on the palladium saturation. The diffusion coefficient was calculated from Eq. S2.18. Since CO chemisorption on the palladium surface is not an activated process, the adsorption rate constant was considered constant. Adding the membrane on top of the catalyst layer effects the effective diffusion coefficient which is obtained by the porosity and tortuosity of the membrane, as shown on Eq. 2.10. Tortuosity is 1 due to the straight channels, porosity is 0.03 and the membrane thickness is 12 μm. It is assumed an equal pore distribution on the membrane surface from the SEM images (see Figure 2.2). Figure S2.26 shows that the model predicts well the ATR data.
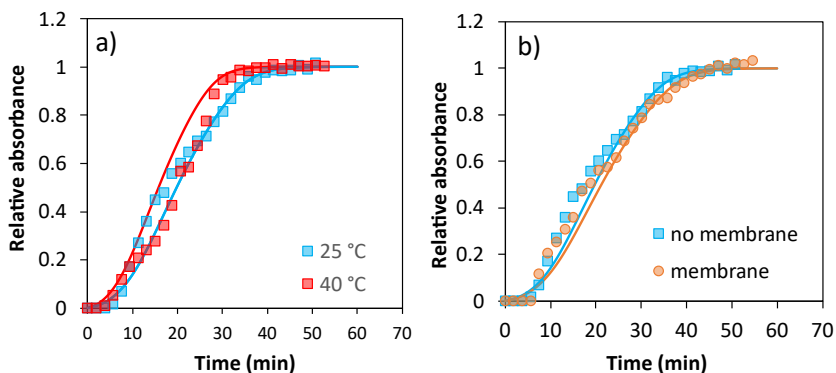
Figure S2.26: Pd saturation time with temperature (a) and membrane (b) results from 2nd Fick diffusion modelling with 10 % CO/He dissolved in water and 5 μm catalyst thickness of 3.5 wt. % Pd/Al$_2$O$_3$.

2.8.12.8 Transport on polymeric brushes

Figure 2.9 shows the fitting obtained from the one-dimensional model based on 2nd Fick diffusion model. Considering 15 minutes polymerization, the $\varphi_{p\text{-NIPAM}}$ and polymer thickness (on the top surface of the membrane) values were 0.2 and 350 nm, respectively, which were determined by ellipsometry. Consequently, this results on a $V_{x,p}$ equal to 1 (membrane pore full with polymer) at 25 °C. The polymer fraction ($\varphi_{p\text{-NIPAM}}$) is related with the ability of the polymer to swell, which is dependent on the surface density, polymer growth and temperature. In these simulations, the $\varphi_{p\text{-NIPAM}}$ was assumed to be constant at a fixed temperature, independent of the polymeric brush being located at the top surface or inside the membrane pores. The $k_{abs,p\text{-NIPAM}}$ obtained was 50 s^{-1} and the CO solubility at the polymeric brush obtained was equals to 10 mol m^{-3} (see Figure 2.9c and Table S2.5). The order of magnitude of the absorption rate constant ($k_{abs,p\text{-NIPAM}}$) is significantly lower than the adsorption rate constant of CO at the palladium surface, which is expected since the absorption process is based on a physisorption interaction instead of a chemical bond. Assuming an equal $\varphi_{p\text{-NIPAM}}$ at 5 min polymerization, the contribution of absorption is significantly higher at the pores compared to the top membrane surface due to the lower diffusion coefficient and long membrane thickness (12 μm). The $V_{x,p}$ had a decrease from 1 to 0.5 by the decrease of the polymerization time from 15 to 5 min, respectively (see

Figure 2.10a). This is in line with the experimental results, that the polymerization time has a correlation with the polymer thickness.

Upon an increase of temperature, the $V_{x,p}$, $S_{co,p\text{-NIPAM}}$ and polymer thickness decrease due to the polymer collapse. The $k_{abs,p\text{-NIPAM}}$ was considered constant, since absorption is a non-activated process and, therefore, less sensitive to temperature. Following Eq. 2.18, the $S_{co,p\text{-NIPAM}}$ at 40 °C was determined as 8 mol m^{-3}. Even though, the 5 minutes polymerization followed the ellipsometry behaviour in respect to the volume fraction decrease (Figure 2.10b and Table S2.5). In the case of 15 minutes polymerization at 40 °C the volume fraction decreased from 1 to 0.5 instead of 0.2 as determined by ellipsometry. This would indicate a higher polymer fraction inside the membrane pore, which could be a cause of the change in the shape of the surface from plane to round.

Table S2.5: Values of polymer thickness at the membrane surface (nm), polymer volume fraction ($V_{x,p}$) at the membrane pores, absorption rate constant (k_{abs}) and CO solubility at the p-NIPAM brush ($S_{co\text{-p-NIPAM}}$) obtained for the curves shown on Figure 2.10.

	Polymer thickness (nm)	Vx,p	kabs (s^{-1})	Sco-p-NIPAM (mol m^{-3})
15 min 25 °C	350	1	50	10
15 min 40 °C	70	0.6	50	8
5 min 25 °C	120	0.5	50	10
5 min 40 °C	70	0.2	50	8

2.8.12.9 Hypothetical situation to compare effect of polymer brushes on transport

Figure S2.27a shows the effect of the polymer in respect to temperature on the CO molecular transport, where the collapsing of the polymer causes the opening of the membrane pore leading to a faster saturation time. Although, Figure S2.27b shows the opposite behaviour when a polymer dense layer is on the top surface of the membrane. The polymer collapse causes the effective diffusion coefficient to decrease due to the lower water molecules following a hopping mechanism. Together with a high volume for CO to

absorb causes the palladium saturation time to decrease in comparison with the polymer in the swollen state.
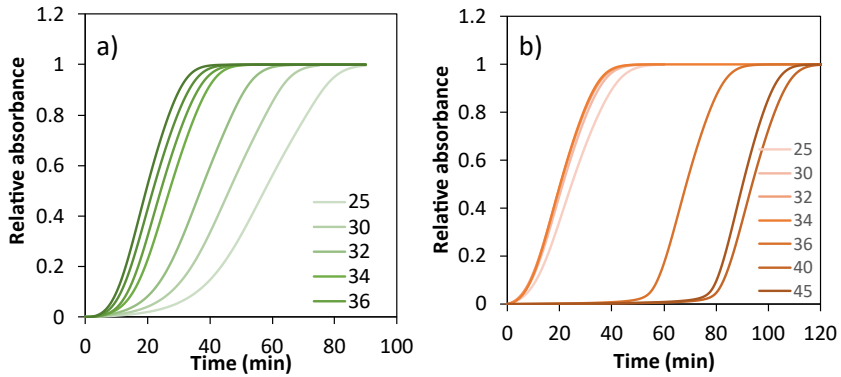
Figure S2.27: Palladium saturation time as a function of temperature for polymer brushes growing inside the pores (a) and polymer brushes growing on top of the membrane (b) where polymer thickness, $\varphi_{\text{p-NIPAM}}$ and $V_{x,p}$ was assumed to follow ellipsometry results with k_{abs} of 50 s^{-1} and $S_{\text{co-p-NIPAM}}$ following Eq. 2.18.

2.9   References

[1]   L.D. Zarzar, J. Aizenberg, Stimuli-responsive chemomechanical actuation: a hybrid materials approach., Acc. Chem. Res. 47 (2014) 530–539. https://doi.org/10.1021/ar4001923.

[2]   M. a C. Stuart, W.T.S. Huck, J. Genzer, M. Müller, C. Ober, M. Stamm, G.B. Sukhorukov, I. Szleifer, V. V Tsukruk, M. Urban, F. Winnik, S. Zauscher, I. Luzinov, S. Minko, Emerging applications of stimuli-responsive polymer materials., Nat. Mater. 9 (2010) 101–113. https://doi.org/10.1038/nmat2614.

[3]   A. Grinthal, J. Aizenberg, Adaptive all the way down: building responsive materials from hierarchies of chemomechanical feedback., Chem. Soc. Rev. 42 (2013) 7072–85. https://doi.org/10.1039/c3cs60045a.

[4]   R. Roa, W.K. Kim, M. Kanduč, J. Dzubiella, S. Angioletti-Uberti, Catalyzed Bimolecular Reactions in Responsive Nanoreactors, ACS Catal. 7 (2017) 5604–5611. https://doi.org/10.1021/acscatal.7b01701.

[5]   Y. Lu, Y. Mei, M. Drechsler, M. Ballauff, Thermosensitive core-shell particles as carriers for Ag nanoparticles: Modulating the catalytic activity by a phase transition in networks, Angew. Chemie - Int. Ed. 45 (2006) 813–816. https://doi.org/10.1002/anie.200502731.

[6]   R. Roa, S. Angioletti-Uberti, Y. Lu, J. Dzubiella, F. Piazza, M. Ballauff, Catalysis by Metallic Nanoparticles in Solution: Thermosensitive Microgels as Nanoreactors, Zeitschrift Für Phys. Chemie. 232 (2018) 773–803. https://doi.org/10.1515/zpch-2017-1078.

[7]   S. Angioletti-Uberti, Y. Lu, M. Ballauff, J. Dzubiella, Theory of Solvation-Controlled Reactions in Stimuli-Responsive Nanoreactors, J. Phys. Chem. C. 119 (2015) 15723–15730. https://doi.org/10.1021/acs.jpcc.5b03830.

[8]   H. Jia, R. Roa, S. Angioletti-Uberti, K. Henzler, A. Ott, X. Lin, J. Möser, Z. Kochovski, A. Schnegg, J. Dzubiella, M. Ballauff, Y. Lu, Thermosensitive Cu2O-PNIPAM core-shell nanoreactors with tunable photocatalytic activity, J. Mater. Chem. A. 4 (2016) 9677–9684. https://doi.org/10.1039/c6ta03528k.

[9]   S. Wu, J. Dzubiella, J. Kaiser, M. Drechsler, X. Guo, M. Ballauff, Y. Lu, Thermosensitive Au-PNIPA Yolk-Shell Nanoparticles with Tunable Selectivity for Catalysis, Angew. Chemie Int. Ed. 51 (2012) 2229–2233.

https://doi.org/10.1002/anie.201106515.

[10]   M. Shahid, Z.H. Farooqi, R. Begum, K. Naseem, M. Ajmal, A. Irfan, Designed synthesis of silver nanoparticles in responsive polymeric system for their thermally tailored catalytic activity towards hydrogenation reaction, Korean J. Chem. Eng. 35 (2018) 1099–1107. https://doi.org/10.1007/s11814-018-0016-x.

[11]   T. Lohaus, P. de Wit, M. Kather, D. Menne, N.E. Benes, A. Pich, M. Wessling, Tunable permeability and selectivity: Heatable inorganic porous hollow fiber membrane with a thermo-responsive microgel coating, J. Memb. Sci. 539 (2017) 451–457. https://doi.org/10.1016/j.memsci.2017.05.052.

[12]   N. Welsch, A.L. Becker, J. Dzubiella, M. Ballauff, Core-shell microgels as 'smart' carriers   for   enzymes,   Soft   Matter.   8   (2012)   1428–1436. https://doi.org/10.1039/c1sm06894f.

[13]   J.J. Keating, J. Imbrogno, G. Belfort, Polymer Brushes for Membrane Separations: A   Review,   ACS   Appl.   Mater.   Interfaces.   8   (2016)   28383–28399. https://doi.org/10.1021/acsami.6b09068.

[14]   G.W. De Groot, M.G. Santonicola, K. Sugihara, T. Zambelli, E. Reimhult, J. Vörös, G.J. Vancso, Switching transport through nanopores with pH-responsive polymer brushes for controlled ion permeability, ACS Appl. Mater. Interfaces. 5 (2013) 1400–1407. https://doi.org/10.1021/am302820y.

[15]   T. Chen, R. Ferris, J. Zhang, R. Ducker, S. Zauscher, Stimulus-responsive polymer brushes on surfaces: Transduction mechanisms and applications, Prog. Polym. Sci. 35 (2010) 94–112. https://doi.org/10.1016/j.progpolymsci.2009.11.004.

[16]   Y. Park, M.P. Gutierrez, L.P. Lee, Reversible Self-Actuated Thermo-Responsive Pore Membrane, Sci. Rep. 6 (2016) 1–10. https://doi.org/10.1038/srep39402.

[17]   Z.B. Zhang, X.L. Zhu, F.J. Xu, K.G. Neoh, E.T. Kang, Temperature- and pH-sensitive nylon membranes prepared via consecutive surface-initiated atom transfer radical graft polymerizations, J. Memb. Sci. 342 (2009) 300–306. https://doi.org/10.1016/j.memsci.2009.07.004.

[18]   H. Alem, A.S. Duwez, P. Lussis, P. Lipnik, A.M. Jonas, S. Demoustier-Champagne, Microstructure and thermo-responsive behavior of poly(N-isopropylacrylamide) brushes grafted in nanopores of track-etched membranes, J. Memb. Sci. 308 (2008) 75–86. https://doi.org/10.1016/j.memsci.2007.09.036.

[19]   G. Prieto, H. Tüysüz, N. Duyckaerts, J. Knossalla, G.H. Wang, F. Schüth, Hollow Nano- and Microstructures as Catalysts, Chem. Rev. 116 (2016) 14056–14119. https://doi.org/10.1021/acs.chemrev.6b00374.

[20]   X. He, M. Aizenberg, O. Kuksenok, L.D. Zarzar, A. Shastri, A.C. Balazs, J. Aizenberg, Synthetic homeostatic materials with chemo-mechano-chemical self-regulation, Nature. 487 (2012) 214–218. https://doi.org/10.1038/nature11223.

[21]   A. Aguirre, C.L.A. Berli, S.E. Collins, ATR-FTIR spectrokinetic analysis of the CO adsorption and oxidation at water/platinum interface, Catal. Today. 283 (2017) 127–133. https://doi.org/10.1016/j.cattod.2016.03.042.

[22]   B.L. Mojet, S.D. Ebbesen, L. Lefferts, Light at the interface: the potential of attenuated total reflection infrared spectroscopy for understanding heterogeneous catalysis in water, Chem. Soc. Rev. 39 (2010) 4643. https://doi.org/10.1039/c0cs00014k.

[23]   S.D. Ebbesen, B.L. Mojet, L. Lefferts, In situ ATR-IR study of nitrite hydrogenation over Pd/Al2O3, J. Catal. 256 (2008) 15–23. https://doi.org/10.1016/j.jcat.2008.02.013.

[24]   S.D. Ebbesen, B.L. Mojet, L. Lefferts, The influence of water and pH on adsorption and oxidation of CO on Pd/Al2O3--an investigation by attenuated total reflection infrared spectroscopy., Phys. Chem. Chem. Phys. 11 (2009) 641–649. https://doi.org/10.1039/b814605e.

[25]   X. Gao, Y. Zhang, Y. Liu, A kinetics study of the heterogeneous reaction of: N -butylamine with succinic acid using an ATR-FTIR flow reactor, Phys. Chem. Chem. Phys. 20 (2018) 15464–15472. https://doi.org/10.1039/c8cp01914b.

[26]   N.S. Gould, S. Li, H.J. Cho, H. Landfield, S. Caratzoulas, D. Vlachos, P. Bai, B. Xu, Understanding solvent effects on adsorption and protonation in porous catalysts, Nat. Commun. 11 (2020) 1–13. https://doi.org/10.1038/s41467-020-14860-6.

[27]   L. Rodríguez-García, R. Walker, E. Spier, K. Hungerbühler, F. Meemken, Mass transfer considerations for monitoring catalytic solid-liquid interfaces under operating conditions, React. Chem. Eng. 3 (2018) 55–67. https://doi.org/10.1039/c7re00179g.

[28]   L. Baij, J.J. Hermans, K. Keune, P.D. Iedema, Time-Dependent ATR-FTIR Spectroscopic Studies on Solvent Diffusion and Film Swelling in Oil Paint Model

Systems, Macromolecules. 51 (2018) 7134–7144. https://doi.org/10.1021/acs.macromol.8b00890.

[29] C.H. Mathis, M. Divandari, R. Simic, V. V. Naik, E.M. Benetti, L. Isa, N.D. Spencer, ATR-IR Investigation of Solvent Interactions with Surface-Bound Polymers, Langmuir. 32 (2016) 7588–7595. https://doi.org/10.1021/acs.langmuir.6b02086.

[30] P. Xu, S. Agarwal, L. Lefferts, Mechanism of nitrite hydrogenation over Pd/γ-Al2O3 according a rigorous kinetic study, J. Catal. 383 (2020) 124–134. https://doi.org/10.1016/j.jcat.2020.01.003.

[31] P. Xu, S. Agarwal, J.F. Albanese, L. Lefferts, Enhanced transport in Gas-Liquid-Solid catalytic reaction by structured wetting properties: Nitrite hydrogenation, Chem. Eng. Process. - Process Intensif. 148 (2020) 107802. https://doi.org/10.1016/j.cep.2020.107802.

[32] B.A. Humphreys, S.W. Prescott, T.J. Murdoch, A. Nelson, E.P. Gilbert, B. Webber, E.J. Wanless, Influence of molecular weight on PNIPAM brush modified colloidal silica particles †, Soft Matter. (2019) 55–64. https://doi.org/10.1039/c8sm01824c.

[33] B.A. Humphreys, J.D. Willott, T.J. Murdoch, G.B. Webber, E.J. Wanless, Specific ion modulated thermoresponse of poly(N-isopropylacrylamide) brushes, (2016) 6037–6046. https://doi.org/10.1039/C5CP07468A.

[34] S.D. Ebbesen, B.L. Mojet, L. Lefferts, In situ ATR-IR study of CO adsorption and oxidation over Pt/Al2O3 in gas and aqueous phase: Promotion effects by water and pH, J. Catal. 246 (2007) 66–73. https://doi.org/10.1016/j.jcat.2006.11.019.

[35] O. Corporation, Peak Fitting Module, 2002. www.OriginLab.com.

[36] Z. Liu, W. Wang, R. Xie, X.J. Ju, L.Y. Chu, Stimuli-responsive smart gating membranes, Chem. Soc. Rev. 45 (2016) 460–475. https://doi.org/10.1039/c5cs00692a.

[37] A. Tiwari, E. Sancaktar, Poly(N-isopropylacrylamide) grafting solution parameters for controlling temperature responsiveness in PET membranes fabricated using 248 nm KrF excimer laser, Eur. Polym. J. 103 (2018) 220–227. https://doi.org/10.1016/j.eurpolymj.2018.04.014.

[38] I. Poudyal, N.P. Adhikari, Temperature dependence of diffusion coefficient of

carbon monoxide in water: A molecular dynamics study, J. Mol. Liq. 194 (2014) 77–84. https://doi.org/10.1016/j.molliq.2014.01.004.

[39]   B. Geng, J. Cai, S. Liang, S.X. Liu, M.F. Li, Y.X. Chen, Temperature effects on CO adsorption/desorption at Pt film electrodes: An electrochemical in situ infrared spectroscopic study, Phys. Chem. Chem. Phys. 12 (2010) 10888–10895. https://doi.org/10.1039/c002665d.

[40]   H. Conrad, G. Ertl, J. Koch, E.E. Latta, Adsorption of CO on Pd single crystal surfaces, Surf. Sci. 43 (1974) 462–480. https://doi.org/10.1016/0039-6028(74)90270-2.

[41]   A. Aguirre, C.L.A. Berli, S.E. Collins, ATR-FTIR spectrokinetic analysis of the CO adsorption and oxidation at water/platinum interface, Catal. Today. 283 (2017) 127–133. https://doi.org/10.1016/j.cattod.2016.03.042.

[42]   L. Masaro, X.X. Zhu, Physical models of diffusion for polymer solutions, gels and solids, 1999. https://doi.org/10.1016/S0079-6700(99)00016-7.

[43]   P. Hervés, M. Pérez-Lorenzo, L.M. Liz-Marzán, J. Dzubiella, Y. Lub, M. Ballauff, Catalysis by metallic nanoparticles in aqueous solution: Model reactions, Chem. Soc. Rev. 41 (2012) 5577–5587. https://doi.org/10.1039/c2cs35029g.

[44]   M. Kanduč, W.K. Kim, R. Roa, J. Dzubiella, Selective Molecular Transport in Thermoresponsive Polymer Membranes: Role of Nanoscale Hydration and Fluctuations, Macromolecules. 51 (2018) 4853–4864. https://doi.org/10.1021/acs.macromol.8b00735.

[45]   R. Roa, W.K. Kim, M. Kanduč, J. Dzubiella, S. Angioletti-Uberti, Catalyzed Bimolecular Reactions in Responsive Nanoreactors, ACS Catal. 7 (2017) 5604–5611. https://doi.org/10.1021/acscatal.7b01701.

[46]   B.L. Mojet, S.D. Ebbesen, L. Lefferts, Light at the interface: The potential of attenuated total reflection infrared spectroscopy for understanding heterogeneous catalysis in water, Chem. Soc. Rev. 39 (2010) 4643–4655. https://doi.org/10.1039/c0cs00014k.

[47]   B.A. Humphreys, S.W. Prescott, T.J. Murdoch, A. Nelson, E.P. Gilbert, B. Webber, E.J. Wanless, Influence of molecular weight on PNIPAM brush modified colloidal silica particles †, Soft Matter. 15 (2019) 55–64. https://doi.org/10.1039/c8sm01824c.

[48] E.S. Kooij, X. Sui, M.A. Hempenius, H.J.W. Zandvliet, G.J. Vancso, Probing the thermal collapse of poly(n -isopropylacrylamide) grafts by quantitative in situ ellipsometry, J. Phys. Chem. B. 116 (2012) 9261–9268. https://doi.org/10.1021/jp304364m.

[49] A. Götz, R. Nikzad-Langerodi, Y. Staedler, A. Bellaire, J. Saukel, Apparent penetration depth in attenuated total reflection Fourier-transform infrared (ATR-FTIR) spectroscopy of Allium cepa L. epidermis and cuticle, Spectrochim. Acta - Part A Mol. Biomol. Spectrosc. 224 (2020) 1–6. https://doi.org/10.1016/j.saa.2019.117460.

Chapter 3

N-isopropylacrylamide polymer brushes alter the micro-solvation environment during aqueous nitrite hydrogenation on Pd/Al₂O₃ catalyst

Abstract

Nitrite contaminants in freshwater streams, resulting from run-off of fertilizers and livestock farming, are a major ecological challenge. Here, we have developed a new family of catalysts based on Pd/Al_2O_3 coated with N-isopropylacrylamide polymer (p-NIPAM) brushes that increase N-N bond formation over N-H bond formation, promoting nitrogen selectivity by 3-fold, reaching > 99 % for the Pd/Al_2O_3 containing 20 wt. % carbon in the form of p-NIPAM, without significant drops in catalytic activity (TOF of c.a. 6.8 ± 1.1 min^{-1}). Strikingly, rigorous mass transport studies revealed that the presence of p-NIPAM does not limit the transfer of molecules during the hydrogenation of nitrites in aqueous phase. These observations were corroborated by detailed reaction kinetics in which similar activation barriers for nitrites disappearance of 30-34 kJ mol^{-1} were obtained regardless the polymer content. The observed reaction orders for nitrites were similar on the coated and un-coated catalysts, indicating that the rate determining step, most likely NO_X-H bond formation, remained unaltered. The apparent barriers for ammonia formation, however, drastically increased from 41 ± 3 kJ mol^{-1} on Pd/Al_2O_3 to 63 ± 4 kJ mol^{-1} and 76 ± 5 kJ mol^{-1} on the 7 and 20 wt. % C counterparts, respectively. Contrary to the widely accepted operation mode of thermo-responsive catalysts containing p-NIPAM brushes, we demonstrated that these polymers modify the chemical environment near the active site as shown by in-situ ATR data, tunning the catalyst selectivity without altering the molecular transport. These results will facilitate the development of more selective catalysts for liquid phase reactions relevant for drinking water purification.

3.1   Introduction

Intensive usage of synthetic nitrogen-based fertilizers (i.e. nitrate salts and ammonia) has accelerated the adventitious release of nitrates to groundwater and surface water as only c.a. 20 % is absorbed by plants. This has led to major issues in drinking water supply as prolonged consumption of nitrites can lead to diabetes, liver damage, and methaemoglobinemia (blue baby syndrome).[1–3] Likewise, these nitrogen species can have detrimental impact on biodiversity due to the eutrophication of water bodies,[4] global warming as N_2O, released during natural denitrification, has a potent greenhouse effect,[5,6] and human health as NO and N_2O are responsible to the formation of harmful tropospheric ozone.[7] For these reasons, the World Health Organisation (WHO) stablished stringent guidelines for the maximum level of nitrate (50 mg L^{-1} NO_3^-), nitrite (3 mg L^{-1}) and ammonia (1.5 mg L^{-1}) in drinking water.[8] Here, biological denitrification plays a major role in reducing nitrites to nitrogen. However, the rates of natural denitrification reactions are insufficient to compete with the fast rates of anthropogenic nitrate release.[4] While other alternatives based on membrane separation technologies can remove nitrates from drinking water, the highly concentrated effluents generated must be treated prior disposal back to natural water bodies. In contrast, electro- and thermal-catalytic hydrogenation of nitrites to nitrogen offers fast reaction rates at room temperature, high selectivity to nitrogen, and stable operation in aqueous environments that facilitate practical implementation in a continuous process. The first step in the process is the reduction of nitrates (NO_3^-) to nitrite (NO_2^-), which is relatively slow compared to nitrite reduction. Activation of the relatively stable nitrate ion requires a bi-metallic catalyst, i.e. Cu/Pd.[9] The conversion of nitrite is faster and can be readily conducted on Pd, however, selective conversion to nitrogen is challenging due to the co-production of ammonia (Eq. 3.1 and 3.2 with free energy values at 25 °C (298 K) [10]).

$$NO_2^- + 2H^+ + 3H_2 \rightarrow NH_4^+ + 2H_2O \ \ \Delta G_{298\,K} = -508 \ kJ \ mol^{-1} \qquad \text{Eq. 3.1}$$

$$NO_2^- + H^+ + 1.5H_2 \rightarrow 0.5N_2 + 2H_2O \ \ \Delta G_{298\,K} = -428 \ kJ \ mol^{-1} \qquad \text{Eq. 3.2}$$
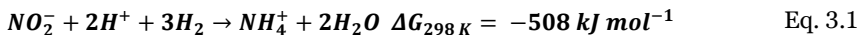
Conversion of nitrite to ammonium is not desirable as its toxicity is even higher than that of nitrites. Thus, quantitative conversion of nitrates to nitrogen is essential for practical

implementation of catalytic reduction strategies. Hörold at al.[11] reported that Ir and Rh have high ammonium selectivity while Pd is more selective to N_2 formation. While there is significant debate about the exact mechanism operating in this reaction it is generally accepted that NO_2^- quickly converts into NO^* on Pd surfaces, which can either form N_2 or fully hydrogenated NH_3^*. Recent kinetic studies on Pd showed that nitrite hydrogenation must involve multiple pre-equilibration steps of hydrogenation of surface species before the rate determining step (RDS).[12] This description matched previous in-situ and operando infrared spectroscopy that identified NO^* and $NO_xH_y^*$ species as relatively stable intermediates during nitrite reduction on Pd. [13] While the kinetics of this structure insensitivity reaction [14] are fast even at room temperature[15,16], the strong dependence of the selectivity to the local chemical environments[10,17–19] greatly complicates the control of the undesired ammonia formation reaction.

In an attempt to control the reaction micro-environment near the active site, so-called nano-reactors consisting in a catalyst metal cluster encapsulated in a small cage, have gained increasing attention due to the fine tunability of the nano-reactor shell and metal clusters.[20,21] When applying polymer shells as responsive hosts for metal catalysts,[22-26] it is possible to regulate the transport towards the catalyst according to the solvation state of the polymer shell, mimicking the exquisite selectivity and catalytic activity found in enzymes.[20,26,35,36,27–34] In stimulus-responsive nano-reactors the coating is composed of a polymer that can undergo reversible phase transitions. In the swollen state molecular transport through the membrane is unrestricted allowing the reaction to occur. Upon reaching a critical solubility point, the polymer collapses forming a dense polymer layer that strangles molecular diffusion to the active site.[37,38] The transition between swollen and de-swollen states can be tuned by modifying the chemistry of the polymer vesicle.[39–41] Here, poly-n-isopropyl acrylamide (p-NIPAM) is one of the most widely studied stimulus-responsive polymer employed in the fabrication of nano-reactors.[23] This temperature responsive polymer leverages the enthalpic H-bonding interaction between the -NH and C=O motives in the polymer chains and water molecules to stay solvated at low temperatures (low critical solubility point-LCST is 32 °C).[42,43] As temperature increases above the LCST, the hydrogen bonds are destabilized due to the increase in entropic contributions to the Gibbs free energy. In the absence of solvating water molecules the Van der Waals forces between polymer chains leads to the collapse of the polymer forming a globular-like structure.[44]

The theoretical description of stimulus-responsive nanoreactors with a so-called yolk-shell architecture was recently developed by Ballauff and Dzubiella.[25,45,46] In this description the authors argued that the experimentally measured reaction kinetics will be analogous to electrical transport through two resistances in series as long as the kinetics are first order. That is that the inverse of the apparent kinetic constant of the nano-reactor is the summation of the inverse of the rate constants of mass transport (k_d) and surface reaction (k_r) ($k_{app}^{-1} = k_d^{-1} + k_r^{-1}$). In essence, as the rate of diffusion decreases due to the conformational change of the polymer shell from the swollen to the collapsed states, the contribution of the mass transport to the observed reaction kinetics becomes more prominent. The intrinsic catalytic activity of the catalyst (k_r) is assumed to be the same as that observed on a non-coated catalyst, while the transport constant (k_d) was assumed to follow a Debye-Smoluchowski permeability-dependent diffusion.[45] However, in this description the authors did not consider the solvation effects that these complex polymeric environments can exert on the surface reaction intermediates and, consequently, transition state energetics of catalytic reactions. This is particularly relevant in the absence of mass transfer effects (i.e. $k_d >> k_r$). In this case, the authors argued that the reaction rates and product selectivity observed on the coated catalyst are essentially unaltered by the presence of the polymer. Furthermore, this description has been limited to model yolk-shell systems consisting of well-defined polymer gels containing catalytic metal nanoparticles. As a result, extrapolating this theory to more practical systems relevant for industrial catalysis, typically consisting of metal nanoclusters supported on porous metal oxides, remains highly unexplored.

In the present contribution, we explore the utilization of p-NIPAM brushes covalently attached to the surface of porous alumina supporting palladium clusters (Pd/Al$_2$O$_3$). Atom transfer radical polymerization (ATRP) synthesis strategies are used to create micro-solvation environments for tuning the selectivity of nitrite hydrogenation to nitrogen and ammonia. Our detailed mass transport studies, rigorous kinetics, and in-situ infrared spectroscopy demonstrate that polymer brushes can induce local changes on the surface adsorbed species during the reduction of nitrites on Pd that lead to increased nitrogen selectivity without altering the reaction kinetics. More importantly, these results suggest that polymer brushes do not affect the mass transport of reactive species when bonded to amorphous Al$_2$O$_3$ support. These observations pave the way towards the utilization of polymeric-catalyst modifiers on industrially scalable catalysts for precise tuning the

reaction selectivity of hydrogenation reactions relevant for pollution control and production of fine-chemicals.

3.2   Materials and methods

3.2.1   Materials

For the catalyst synthesis gamma alumina support (g-Al$_2$O$_3$) was obtained from BASF (Al 3992E 1/8"). Palladium precursor tetra-amine-palladium (II) nitrate solution (10 wt. % in H$_2$O, 1360-08-6), sodium nitrite (99.99 %, 7632-00-0), ammonium (25 % v/v water, 1336-21-6) were obtained from Sigma-Aldrich. For the polymerization N-isopropylacrylamide (NIPAM, 97 %, 2210-25-5), 3-aminopropyltriethoxysilane (APTES, 99 %, 919-30-2), trimethylamine (Eth3N, 99 %, 75-5-3), α-bromoisobutyrylbromide (BIBB, 98 %, 20769-85-1), copper (II) bromide (CuBr$_2$, 99 %, 7789-45-9), 1,1,4,7,10,10-Hexamethyltriethylenetetramine (HMTETA, 97%, 3083-10-1), L-ascorbic acid (99 %, 50-81-7) were also obtained from Sigma-Aldrich. The solvents n-hexane (99.4%, 110-54-3), Tetrahydrofuran (THF, 109-99-9), ethanol (64-17-5) and methanol (67-56-1) were obtained from Merck. The molecular sieves (4Å, 4-8 mesh, 70955-01-0) used to dry THF were procured from Honeywell. All the aqueous solutions were prepared using ultra purified water obtained from a water purification system (Millipore, Synergy).

3.2.2   Catalyst preparation

3.2.2.1 Palladium supported on alumina synthesis

Palladium on alumina catalyst was prepared by wet impregnation. First, γ-Al$_2$O$_3$ powder was sieved with a particle size of 0-38 μm (Figure S3.8 shows the γ-Al$_2$O$_3$ powder with a mean size of 27 μm) and calcined at 600 °C for 4 hours to remove any organic contaminants. For a typical synthesis of 3.5 wt. % Pd/Al$_2$O$_3$, 10 g of γ-Al$_2$O$_3$ were dispersed in 100 mL of DI H$_2$O and 4 ml ammonium hydroxide solution was added dropwise to adjust the pH to 9. Then, 12 g of tetra-amine-palladium (II) solution (10 wt. %) were added dropwise to the suspended solution and stirred for 1 hour at room temperature. Afterwards, the water was removed with a rotary evaporator in vacuum at 70 °C. Palladium supported on alumina was calcined in air for 3 hours at 400 °C (flow rate of 30 mL min^{-1}). After calcination, the system was purged with nitrogen for 30 min at 400 °C (30 mL min-

[1]) before conducting a reduction in a mixture of 50 % hydrogen in nitrogen at 400 °C for 3 hours.[12,47].

3.2.2.2 Polymer brushes growth on Pd/Al$_2$O$_3$

Poly(n-isopropylacrilamide) (p-NIPAM), shown in Figure S3.1a, was chemically bonded to Pd/Al$_2$O$_3$ catalyst surface via atom transfer radical polymerization (ATRP) method, which typically results in a well-defined structure and controlled molecular weight of the polymer chain.[48] The polymerization was made on a bromide functionalized Pd/Al$_2$O$_3$ catalyst, where the reactants NIPAM/CuBr$_2$/HMTETA/ ascorbic acid in the molar ratios 900/1.5/15/10 were dissolved in a solvent mixture of methanol/ water (4: 1 v/v).[49] The "grafted from" radical polymerization started with the N-isopropylacrylamide purification by recrystallization with hexane followed by storage below 4 °C. For the surface functionalization, the surface coverage of OH groups needed to be maximized. Therefore, the palladium alumina catalyst (5 g) was dispersed in water and the pH was adjusted to 10 by adding 0.1 M NaOH and stirred for 30 min. Then, the particles were rinsed three times with ethanol. 3-aminoprupyl)triethoxysilane (APTES), as shown in Figure S3.1b, was used as the coupling agent to bind the n-NIPAM monomer to the -OH at the alumina surface. For that, the Pd/Al$_2$O$_3$ particles were dispersed in 100 mL ethanol and submersed in a water bath at 40 °C with a condenser to avoid ethanol evaporation. The reaction started by adding 2.5 g APTES into the mixture and stirred for 3 hours. Then, particles were rinsed with ethanol followed by two sequential washings with THF. For the initiation, the APTES modified Pd/Al$_2$O$_3$ catalyst was dispersed on 60 mL of THF, where 2.5 mL of BIBB and 3 mL of Eth3N was added to start the reaction. The reaction was proceeded for 30 min under rigorous stirring. At the end, the bromide functionalized Pd/Al$_2$O$_3$ were rinsed with THF followed by four sequential washings with ethanol and methanol. For the polymerization, NIPAM/CuBr$_2$/HMTETA/ ascorbic acid in the molar ratios 900/1.5/15/10, dissolved in a solvent mixture of methanol/ water (4: 1 v/v) was used. The procedure consists of preparing two solutions under continuous stirring and N$_2$ atmosphere at room temperature. Solution (1) containing CuBr$_2$, HMTETA, methanol, and water. After 15 min under N$_2$ atmosphere L-ascorbic acid was added. Solution (2) containing NIPAM, bromide functionalized Pd/Al$_2$O$_3$ particles and the same water/methanol ratio as the other container. After 30 min, the solution (1) was added to the solution (2) starting the polymerization. After 6 hours, the polymerization was stopped by adding the mixture to a methanol and water solution (4:1 v/v) and rinse the particles four times with DI water. To

increase the polymer brush content, the polymerization was continued for 24h and the reactants concentrations were increased three times.

3.2.3 Catalyst characterization

3.2.3.1 Palladium alumina and polymer coated catalyst

The active metal surface area was measured by CO chemisorption at room temperature (Chemisorb 2750, Micrometrics, gas phase). After reduction in H_2 for 1 hour, the catalyst was flushed in He at room temperature during 20 min, followed by adsorption of CO in pulses. The palladium loading was measured by X-ray micro-fluorescence spectroscopy under helium atmosphere (Bruker S8 Tiger 4 kW wavelength dispersive μ-XRF spectrometer). The powder sample was measured as-received without any further pre-treatment and analysed using the Quantexpress program. N_2 physisorption at -196 °C was employed to determine the textural properties of the catalysts using a Micromeritics Tristar 3000 analyzer. Prior the N_2 adsorption experiments the palladium alumina catalyst was degassed at 300 °C for one day. In the case of the p-NIPAM polymer coated catalysts the degassing was conducted at 180 °C for one day. TEM (Tecnai F30) images were taken by Scanning Transmission Electron Microscope - High-Angle Annular Dark Field (STEM-HAADF) in a Cs-probe corrected Titan (ThermoFischer Scientific, formerly FEI) with 300KV and coupled with a HAADF detector (Fischione). The catalyst composition and distribution of carbon, alumina, oxygen and palladium was measured with X-Ray Energy Dispersive spectroscopy (EDS) topography with an Ultim Max detector (Oxford Instruments).

The atomic surface concentration and oxidation state of the different elements in the catalyst was determined using X-ray Photoelectron Spectroscopy (XPS). A Kratos AXIS Supra spectrometer using a monochromatized AlKa source at a power of 15 kV and 8mA (120 W) and a pressure of 1×10^{-9} Torr was employed to analyse the catalysts without any pre-treatment. High resolution narrow scans were performed at constant pass energy of 20 eV, while wide scans were performed at analyser pass energy of 160 eV. The C 1s (C-C) peak from the carbon-based contaminant with a literature value of 284.8 eV was used as a reference to calibrate the XPS spectra and eliminating charging effects.[50] Fitting has been carried out using Casa XPS software. The catalyst support particle size distribution was measured by Dynamic Light Scattering (DLS) using a Malvern Mastersizer 2000 with

hydro 2000s module. The polymer content on the catalyst surface was determined using elemental analysis (CHNS-0 Analyzer, Thermo Scientific) and thermo-gravimetrical analysis (TGA, Mettler Toledo). For the TGA experiments the sample was first purged in a mixture of 50 % synthetic air in Ar (total flow rate 50 mL min^{-1}) until the sample reached 25 °C (10 min). Then, the composition was changed to 100 % synthetic air with a 30 mL min^{-1} flow and heated up to 1000 °C at a ramp rate of 10 °C min^{-1}. The NO$_2^-$ adsorption on the palladium surface was measured with Attenuated Total Reflection Infrared spectroscopy, ATR-IR, in a home build setup (shown in Figure S3.2a). [51–54] The cell was mounted within the sample compartment of an infrared spectrometer (Bruker Tensor 27) equipped with a Mercury Cadmium Telluride (MCT) detector, cooled with liquid N$_2$. To stabilize the ATR equipment, two hours were needed before any experiment. Each spectrum was acquired by averaging 62 scans with a resolution of 4 cm^{-1}. The liquid flowing through the cell and over the catalyst layers were pumped by with a peristaltic pump downstream of the ATR-IR cell. All aqueous flow rates were 2 mL min^{-1}, resulting in a residence time of 12 s. The solutions were saturated with He (Praxair), or H$_2$ (Praxair) at 1 bar and 25 °C with gas flow rates of 50 mL min^{-1}. The temperature was kept constant by having the saturators in a water bath controlled via feed-back thermocouple placed in the water bath. For all experiments, after the flow-through-cell was assembled, the catalyst was firstly reduced by flushing with H$_2$/H$_2$O for 2 hours. Then, He/H$_2$O was flushed through the system for 30 min to remove hydrogen from the cell and the water background spectrum of the reduced catalyst exposed to water only was recorded. Subsequently, the solution containing 15 mM NO$_2^-$, which is purged in He overnight, was fed to the cell. At this point, IR spectra were recorded until the peak intensities reached steady state after typically 30 minutes. To prepare the catalyst layer at the crystal surface, 0.12 g of catalyst was dispersed in 20 mL 2-isopopanol and sonicated in an ultrasonic processor (Fischer Scientific – 705) for 45 min. Then, the solution was spray- coated on a zinc-selenide (ZnSe) crystal resulting in a thin catalyst film of c.a. 5 mm thickness at the crystal surface, containing typically 5 mg catalyst.[51–54] To obtain a stable layer at the crystal surface, the coated catalyst was calcined at 300 °C (1 °C min^{-1}) for 1 hour in N$_2$ at 20 mL min^{-1}. Because p-NIPAM is temperature sensitive, the polymer coated catalyst was not calcined. Instead, a membrane (Whatman Nuclepore track etched membrane filters with a pore size of 0.2 μm) was placed between the catalyst layer and the rubber from the cell chamber to guarantee the layer stability (see Figure S3.2b).

3.2.4 Catalytic test

The experiments were performed in a semi batch reactor (0.3 L) with continuous feed of gases (CO_2, H_2 and He) at atmospheric pressure. The pH was kept constant at 5.5 by continuous addition of 0.1 bar partial pressure of CO_2 in order to avoid both influence on the conformation of p-NIPAM polymer brushes [55] as well as on NH_4^+ formation [10,56]. In a typical experiment 15 mg of catalyst were mixed with 300 mL of DI water at a stirring speed of 500 rpm. The reduction of palladium consisted of flushing hydrogen for one hour at room temperature (0.5 bar H_2 in a gas mixture of 0.1 bar CO_2 and 0.4 bar He with a total flow rate of 100 mL min^{-1}). Then, 3 mL of a specific concentration of $NaNO_2^-$ was added to the reactor, starting the reaction time. Samples were taken and analyzed by Ion chromatography, as described in detail elsewhere. [12] Temperature was varied between 20 and 55 °C using a thermal bath controlled via feed-back thermocouple placed in the reaction solution. The initial NO_2^- concentration was varied between 1 and 4 mM and H_2 partial pressures between 0.1 to 0.7 bar.

The concentration of nitrite (NO_2^-) and ammonium (NH_4^+) ions were measured as a function of time. Figure S3.3 (see Section S3.7.3.) shows a typical experimental result for NO_2^- concentration (Figure S3a) and NH_4^+ concentration (Figure S3.3b) over time. From these plots the reaction rate was determined based on the initial activity at a low NO_2^- conversion to regress the instantaneous reaction rate at time zero. The rates were calculated as reaction rate per mass of palladium as well as the normalized rate per surface atoms of palladium as determined with CO chemisorption, resulting in a Turnover Frequency (TOF, min^{-1}). The NO_2^- conversion and the integral NH_4^+ selectivity was calculated with Eq. 3.3 and 3.4.

$$NO_2^- \; conversion = \frac{[NO_2^-]_0 - [NO_2^-]_t}{[NO_2^-]_0} \times 100 \qquad \text{Eq. 3.3}$$

Where $[NO_2^-]_0$ is the initial nitrite concentration, $[NO_2^-]_t$ concentration nitrite at time t. The initial concentration NO_2^- was measured immediately after addition of nitrite to the reactor.

In Figure S3.3 the NO_2^- concentration decreased from 3 mM to 0.5 mM resulting in 82% conversion after 120 minutes with an NH_4^+ selectivity of 7% as calculated according to Eq. 3.4 (Integral selectivity) when the bare Pd/Al_2O_3 catalyst was employed. It is well known

that N_2 and ammonia are the only two products formed under these conditions and the selectivity to N_2 is calculated based on the mass balance.

$$NH_4^+ = \frac{[NH_4^+]_t}{[NO_2^-]_0 - [NO_2^-]} \times 100$$

Eq. 3.4

Where $[NH_4^+]_t$ is the concentration of ammonium (mmol L^{-1}) at time t. The apparent activation barrier was calculated according to the Arrhenius Eq. 3.5.

$$ln(TOF) = -\frac{Ea}{R}\frac{1}{T} + ln(A)$$

Eq. 3.5

Where TOF (min^{-1}) is the normalized rate per mol surface-Pd, Ea (kJ mol^{-1}) the activation energy barrier, R (8.31 kJ mol^{-1} K^{-1}) the universal gas constant, T (K) absolute temperature and A the pre-exponential factor.

3.3 Results

3.3.1 Catalyst characterization

As shown in Table 3.1, BET analysis of the N_2-physisorption data indicated the addition of chemically bonded polymer brushes led to a decrease of the surface area and pore volume. This is not surprising as the polymer brushes are grown from the -OH moieties on γ-Al_2O_3 (see Section S3.7.4.1. and S3.7.4.2.). While no reports were found on p-NIPAM polymer brushes on heterogeneous porous metal oxides, similar observations have been reported by Xu et al.[47] when using a fluorinated carbon silane agent with hydrophobic character (perfluorinated-octyltrichlorosilane, FOTS) covalently bonded to the surface of γ-Al_2O_3. In that case, the drop in the surface area and pore volume upon hydrophobization even at low carbon-contents (few percent) was attributed to partial pore entrance blockage in the dry state.

Table 3.1: Specific surface area and pore volume from Brunauer-Emmett-Teller (BET) method from N_2-physisorption at -196 °C, carbon content from elemental analysis (EA) and weight loss from Thermal gravimetric analysis (TGA) obtained from 25 to 800 °C using N_2 as inert atmosphere.

Pd/Al$_2$O$_3$[a] catalysts	Carbon (wt. %)	Weight loss (%)	Specific surface area (m^2 g^{-1})	Pore volume (cm^3 g^{-1})
0 wt. % C 1 & 2	0		193	0.65
7 wt. % C	7	10	170	0.47
20 wt. % C	20	24	104	0.23

a-The surface area of bare γ-Al$_2$O$_3$ is around 196 m^2 g^{-1} indicating no decrease on support after palladium deposition.

The thermal stability of p-NIPAM brushes was studied via thermal gravimetric analysis (TGA), (see Section S3.7.4.3.). Above 350 °C a significant weight loss was observed on the polymer coated catalysts samples, both with 7 wt. % C and 20 wt. % C. This can be attributed to the decomposition of p-NIPAM brushes in air, which is in agreement with previous observations.[57] To determine the catalysts nanostructure and composition, STEM-HAADF and EDS mapping characterization were conducted on the Pd/Al$_2$O$_3$ with different p-NIPAM content (see Figure 3.1). As shown in Figure 3.1ai –ci, the Al$_2$O$_3$ support has an amorphous topology with the palladium nanoparticles well distributed on the surface, regardless of the polymer content. This is further confirmed by inspecting the Pd EDS mappings in Figure 3.1aii – cii. The distribution of polymer on the surface, however, was not possible to address by STEM-HAADF due to the low contrast between carbon in p-NIPAM and alumina. Similarly, EDS mappings of C and B were inconclusive. This is due to the overlap between Lacey carbon films present in the Cu-TEM grid and the low concentrations of B-terminated p-NIPAM present in the system (see Figure S3.6).
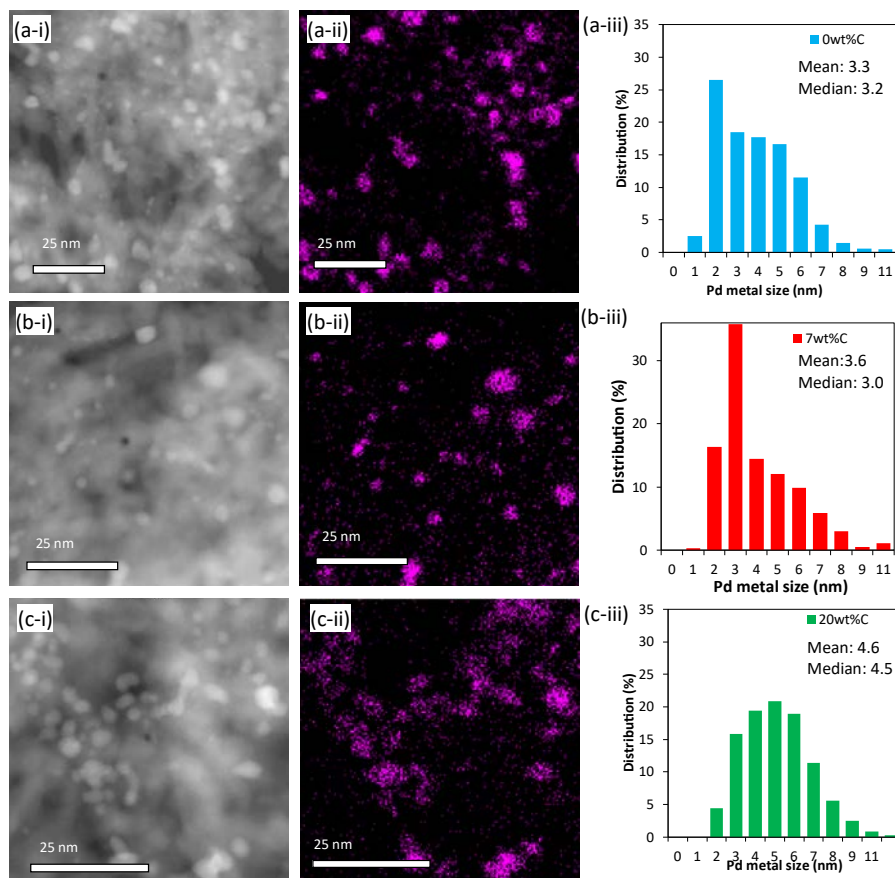
Figure 3.1: STEM-HAADF characterization (i), palladium EDS mapping, where the purple spots represent the palladium particles, (ii), and metal particle size distribution (iii) of the pre-reduced Pd/Al$_2$O$_3$ catalysts containing 0, 7, and 20 wt. % carbon (a-c, respectively).

As can be noted in Table S3.2, the polymer coated catalysts have lower metal loadings, decreased to 2.3 and 1.4 % for the catalyst containing 7 wt. % C and 20 wt. % C Pd/Al$_2$O$_3$, respectively, in comparison with uncoated catalyst. This drop could be caused by partial dissolution of small metal clusters during the p-NIPAM radical polymerization process. During the synthesis, ascorbic acid (pKa of 4.7) is employed as reducing agent to activate the copper catalyst. At this pH, Pd could partly lixiviate into the aqueous media.[58] This is consistent with the small shift of the Pd metal particle size distribution towards larger diameters with increasing polymer content (see Figure 3.1a-c-iii). Additionally, metal surface areas were measured using CO chemisorption, as presented in Table S3.2. This

information was used to estimate the mean metal particle size assuming uniform size distribution and a hemispherical shape. For the parent catalyst (Pd/Al$_2$O$_3$), the palladium metal particle size based on CO chemisorption and on STEM-HAADF have similar values, for both batches. In contrast, the metal particle sizes of the polymer coated catalysts obtained from CO chemisorption were different from those estimated from STEM-HAADF. These differences could be associated to partial coverage of the surface of metal nanoparticles as well as to pore-blockage in the dry state. These artifacts could mask CO-chemisorption underestimating the actual metal dispersion of the catalyst in comparison to STEM-HAADF.

Atomic composition analysis of the catalyst surface, obtained via XPS, indicated that nitrogen and carbon content monotonically increased with the concentration of polymer in the catalyst (see Table S3.3). Notably, no copper was detected on the polymer coated catalysts demonstrating that all the copper catalyst used during polymerization was efficiently removed. In all catalysts, palladium was detected on the surface. Detail analysis of the 3d peak of palladium was conducted to determine the metal oxidation state. Figure S3.7ai-ci shows the deconvolution of the Pd 3d peak into the corresponding 5/2 and 3/2 contributions obtained for Pd/Al$_2$O$_3$ containing 0, 7 and 20 wt. % carbon. Figure S3.7aii - cii and aiii – ciii shows the deconvolution of the C 1s and Al 2p peak as a reference for the calibration in energy[59] (see Table S3.4 and S3.5). Pd/Al$_2$O$_3$ catalyst had a binding energy of 335.7 (Pd 3d5/2) and 341.0 (Pd 3d3/2) corresponding to palladium in the metal form. On the polymer coated catalyst, the binding energy were 335.3 (Pd 3d5/2) and 340.6 (Pd 3d3/2). These results indicate that the electronic configuration of palladium was preserved regardless of the polymer content as no significant peak shifts were encountered (see Table S3.6).[50]

3.3.2 Catalytic performance of p-NIPAM coated Pd/Al$_2$O$_3$

Catalysts coated with thermo-responsive polymer brushes, such as p-NIPAM (LCST = 32 °C), are expected to display a stimulus-responsive behaviour during reaction (so-called nano-reactors). In this reasoning, the polymer is assumed to not tinker the energetics of surface reaction intermediates.[23] To challenge this concept, we conducted a detailed kinetic study on porous Pd/Al$_2$O$_3$ catalysts with increasing loadings of p-NIPAM at different initial concentrations of hydrogen and nitrites at temperatures above and below the LCST of the polymer.

As shown in Section S3.7.5., external and internal mass transfer limitations are negligible under the reaction conditions herein used. The fact that TOF rates are the same on the parent Pd/Al_2O_3 and polymer coated catalysts indicates that p-NIPAM brushes do not change the mass transport towards the active sites (see Table 3.2 and Section S3.7.6.). However, significant differences in the ammonium selectivity, measured at the same level of conversion (c.a. 10 %), were observed on the polymer coated catalysts (see Table 3.2 and Figure S3.11). Here, it can be noted that at temperatures below (25 °C) and above (45 °C) the LCST of p-NIPAM (32 °C) the NH_4^+ selectivity for Pd/Al_2O_3 was 2.8 ± 0.2 and 3.8 % ± 0.3, respectively. The higher selectivity to NH_4^+ with increasing temperature is in agreement with previous research on nitrite hydrogenation on supported Pd catalysts.[60,61] In stark contrast, on the catalysts containing polymer, the selectivity to ammonia was significantly lower regardless of the temperature used, suggesting that p-NIPAM polymer brushes hinder NH_4^+ formation.

Table 3.2: Nitrites (NO_2^-) reaction rate normalized per catalyst mass, palladium loading, and metal active surface area and ammonium selectivity (c.a. 10 % conversion level) at 500 rpm, 20 °C, 3 mM of NO_2^-, 0.5 bar of H_2, 0.1 bar of CO_2 as buffer.

Pd/Al_2O_3 catalysts	NO_2^- rate per catalyst mass (mmol min^{-1} g_{cat}^{-1})	NO_2^- rate per Pd mass (mmol min^{-1} g_{Pd}^{-1})	TOF (min^{-1})[a]	NH_4^+ Selectivity (%)
0 wt. % C (1)	0.81 ± 0.08	24 ± 2	6.9 ± 1.3	2.8 ± 0.2
0 wt. % C (2)	0.92 ± 0.08	32 ± 3	9.8 ± 2.3	2.5 ± 0.3
7 wt. % C[b]	0.35 ± 0.02	15 ± 1	5.2 ± 1.1	1.1 ± 0.1
20 wt. % C[c]	0.26 ± 0.02	15 ± 1	6.8 ± 1.1	0.8 ± 0.1

a: Calculated using TEM metal particle size data. b: 7 wt. % C was synthesized from Pd/Al_2O_3 0 wt. % C (1). c: 20 wt. % C was synthesized from Pd/Al_2O_3 0 wt. % C (2)."

3.3.3   Apparent activation energy

The Arrhenius plot in Figure S3.12 shows that both pre-exponential factors and activation energy barriers are essentially constant regardless of the polymer loading with an NO_2^- overall apparent activation barrier of 32 kJ mol^{-1}. This barrier is in line with previous reports on Pd-based catalysts.[60,61] Strikingly, the analysis of apparent activation barriers for NH_4^+ formation shows an increase from 41 ± 3 kJ mol^{-1} to 63 ± 4 and 76 ± 5 kJ mol^{-1} by the addition of 7 wt. % C and 20 wt. % C in the form of p-NIPAM brushes on the Pd/Al_2O_3 catalyst (Figure S3.12c). The increased apparent barriers are accompanied by a compensation on the pre-exponential factors when the polymer is present in the system, which explains the drastic differences in ammonia selectivity even at high temperatures (Table S3.12). While one would expect that the presence of the polymer should lead to partial blockage of active sites decreasing nitrites coverage, and thus reducing the rate of entropically demanding N-N coupling, these results indicate that p-NIPAM brushes favour nitrogen formation over ammonia. It also indicates that the dependence with temperature of NH_4^+ formation is much more pronounced for the p-NIPAM coated catalyst than for the parent Pd/Al_2O_3.

3.3.4   Apparent activation energy

The performance of Pd/Al_2O_3 catalysts containing 0 wt. % C and 7 wt. % C was measured at different NO_2^- and H_2 concentrations to further understand the NH_4^+ selectivity trends (Figure S3.13). Surprisingly, the NH_4^+ selectivity remained constant around 0.6 and 1 % independently of the reactant concentrations. In contrast, when the parent palladium alumina catalyst was employed NH_4^+ formation increased by two-fold from 1.5 to 3 % on increasing the concentration of either NO_2^- or H_2. The reaction orders obtained for the conversion of nitrites on the parent palladium alumina catalyst were -0.1 ± 0.1 for NO_2^- (m) and 0.5 ± 0.1 for H_2 (n) (see Table S3.13 and Figure 3.2a-b). These results are in agreement with the observations reported by Xu et al.[12] for hydrogenation of nitrite using 1 wt. % Pd/Al_2O_3 at the same reaction conditions. The reaction order for NO_2^- was unaffected by the addition of polymer brushes with a value of -0.07 ± 0.03 (zero order) (m) (Figure 3.2b), suggesting that the rate of nitrite is almost independent of NO_2^- concentration. However, the reaction order for H_2 decreased from 0.5 ± 0.1 to 0.1 ± 0.1 (n) for the p-NIPAM coated catalyst (Figure 3.2a). Notably, the apparent reaction orders in H_2 for NH_4^+ formation (see Figure 3.2c-d) are similar for both catalysts (n* c.a. 0.3-0.4), while the reaction orders in NO_2^- (m*) are 0.4 for the parent Pd/Al_2O_3 and slightly negative (-0.1) on the polymer coated counterpart.
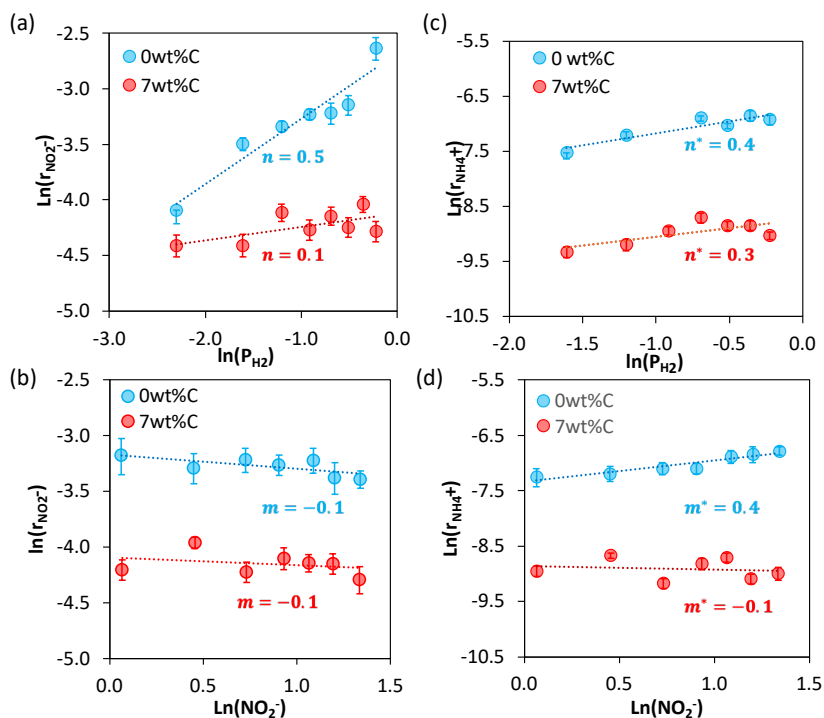
Figure 3.2. Apparent NO_2^- and H_2 reaction orders for nitrite hydrogenation (a-b) and ammonium formation (c-d) at 20 °C and 1 bar for Pd/Al_2O_3 containing 0 (blue) and 7 (red) wt. % carbon. The NO_2^- concentrations ranged from 1 to 4 mM at 0.5 bar of H_2 and 0.1 bar of CO_2, while H_2 partial pressures varied from 0.1 to 0.7 bar at 3 mM NO_2^- using 15 mg of catalyst and 500 rpm. Hydrogen, carbon dioxide, and helium (to balance) were added continuously to the system to ensure constant concentrations during the experiments.

3.3.5   *In-situ* Attenuated Total Reflectance Infrared (ATR-IR) Spectroscopy

In-situ ATR-IR spectroscopy was used to elucidate the role of p-NIPAM brushes in the hydrogenation of nitrates on palladium surface in aqueous environments. Figure 3.3 shows the ATR-IR spectrum of nitrites chemisorbed on Pd/Al_2O_3 containing 0 and 7 wt. % C as p-NIPAM. To improve the signal to noise ratio, these experiments were performed with a higher NO_2^- concentration (15 mM) than those employed in the kinetic experiments (3 mM). Here, the free nitrite ion [13,62,63] and HNO_2 [64] in solution have characteristic

IR adsorption bands located in the range of 1235 to 1286 cm^{-1} (see Section S3.7.9.). The peaks at c.a. 1350-1250 cm^{-1} correspond to NO stretching from NO_2^- (see Figure S3.14).[65] All these three peaks were detected on the blank experiment on bare ZnSe, confirming that these signals correspond to NO_2^- in the aqueous phase within the analysis volume of the ATR-IR with a penetration depth of 1-4 μm (see Figure S3.14b). As shown in Figure 3.3, a peak at 1235 cm^{-1} was observed for Pd/Al_2O_3. This band seems to shift to lower wavenumbers (c.a. 1231 cm^{-1}) in the p-NIPAM coated catalyst (7 wt. % C). Nitrite can adsorb at the palladium surface at frequencies of c.a. 1400 and 1330 cm^{-1}. For instance, Ebbesen et al. [13] reported that the frequencies at 1405 and 1325 cm^{-1} are associated to adsorption of NO_2^- palladium surfaces covered with chemisorbed oxygen. This agrees with the results where the formation of NO_x^- species (Pd-$NO_{x\ ads}^-$) are located at the frequencies of 1408 and 1319 cm^{-1}. Apparently, at high concentrations of NO_2^- the surface of the Pd catalyst seems to contain chemisorbed oxygen, as the reduced sample results in the formation of a IR spectrum resembling a partly oxidized Pd surface. [13]

Notably, when p-NIPAM brushes where present on the Pd/Al_2O_3 important changes were observed on the peak position of key adsorbed species. For instance, the Pd-$NO_{x\ ads}^-$ suffered a red shift from 1408 to 1402 cm^{-1} and from 1320 to 1310 cm^{-1} when covalently bonded p-NIPAM brushes were present (see Figure 3.3, Figure S3.14a-b and Figure S3.15). Zhao et al. reported similar results when conducting ATR-IR spectroscopy of CO on Pd in the presence of polymeric stabilizers.[66] The authors interpreted the lower wavenumbers of C-O vibration in chemisorbed CO as a result of interactions between the polymer and metal catalyst. This would suggest that p-NIPAM changes the properties of chemically bonded species (Figure 3.3b I-II).
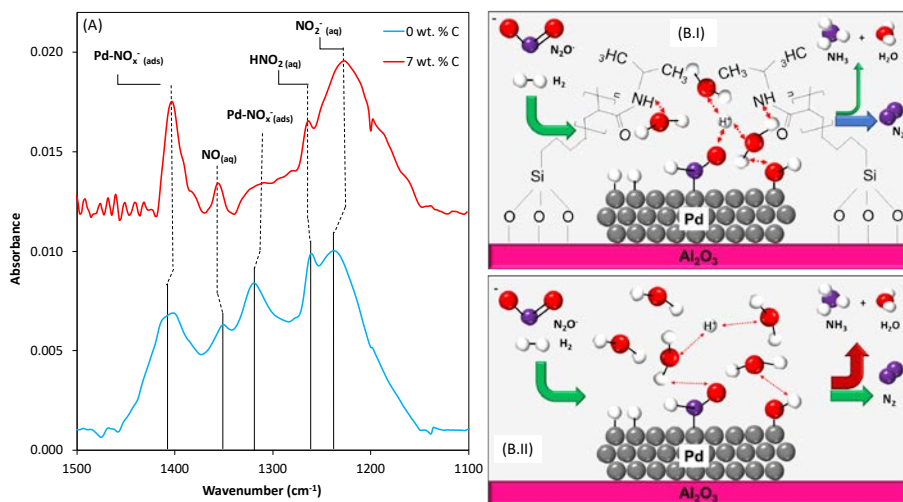
Figure 3.3: a) *In-situ* ATR-IR spectra of Pd/Al$_2$O$_3$ catalysts containing 0 and 7 wt. % carbon in the form of p-NIPAM conducted at 25 °C (pH=7) on a flow of 15 mM NO$_2^-$ and Ar over a spray coated silicon crystal containing c.a. 5 mg of catalyst thin film, b) schematic illustration of the binding strength effects on NH$_4^+$ selectivity during nitrite hydrogenation with 0 wt. % C (B.II) and 7wt. % C (B.I).

3.4   Discussion

P-NIPAM brushes covalently attached to the surface of porous alumina containing palladium nanoparticles (Pd/Al$_2$O$_3$) decreased by 3-fold the NH$_4^+$ selectivity compared with Pd/Al$_2$O$_3$ catalyst (Figure S3.10b). This indicates that the polymer coated catalyst favours nitrogen coupling over N-H bond formation. The reason for these differences could be explained by either (1) concentration profiles inside the catalyst particles of either NO$_2^-$, H$_2$ or H$^+$, (2) metal particle size effects, or (3) changes in the reaction energy landscape induced by the micro-solvation environment. In the next section, we will address each of these issues in detail.

3.4.1 Mass transport effects

Nitrite reduction is strongly sensitive to the surface coverage ratio of H_2/NO_2^- and the pH of the reaction media.[10,12,13] Recently, P. Xu et al.[47] studied the interplay of mass transport of hydrogen on Pd/Al_2O_3 catalysts rendered with compartmentalized wettabilities of the internal surface. That is that the internal as well as external surface of the support was partly hydrophobic and hydrophilic. The authors reported that the total rate of conversion is strongly influenced by internal mass transfer for catalyst support particles larger than 100 μm. Also, when 20 % hydrophobic support was introduced, the transport of hydrogen was enhanced, leading to faster nitrite conversion rates and concomitantly higher ammonia selectivity. Similar observations were reported by J. K. Chinthaginjala et al.[56] using Pd catalysts supported on carbon nanofibers, where high conversion rate as well as increasing selectivity to ammonia was attributed to improved mass transfer of H_2 in the catalyst support.

Although p-NIPAM polymer brushes are often used to modify the mass transport of reactive species in nano-reactors, the low selectivity towards ammonia that we observed is not easily rationalized in terms of mass transport effects as mass transport limitations on the bulky nitrite ions respect to molecular hydrogen would lead to higher ammonia formation rates, as the H/N would increase. Convincing confirmation of the absence of mass transfer limitations can be extracted from the apparent reaction orders. Here, one could argue that if concentration gradients were dominating the measured kinetics, then the observed reaction orders for hydrogen and nitrites should be equal to one, as molecular diffusion is a first order process. However, the reaction orders for NO2- and H2 on Pd/Al_2O_3 containing 7 wt. % C p-NIPAM were c.a. zero for both species (Figure 3.2). In the same line, Mears and Weisz-Prater (C_{wp}) criteria values suggest that there are no external and internal mass transfer limitations, respectively, on any of the catalysts studied. Finally, the regressed apparent activation energy barriers obtained for the overall nitrite conversion on Pd/Al_2O_3 containing 0 wt. % C, 7 wt. % C and 20 wt. % C (c.a. 30 kJ mol^{-1}) were similar to those reported on kinetically controlled systems at reaction conditions that are equivalent to those herein employed.[56] Hence, the effect of concentration profiles on the reaction selectivity can be discarded.

3.4.2　Metal particle size effects

The addition of p-NIPAM brushes to the catalyst surface reduced the metal loading, possibly due to dissolution of small palladium nanoparticles (<2 nm) (Table S3.2). This resulted in a shift to larger metal particle sizes, which could lead to a change on NH_4^+ selectivity without affecting the nitrite conversion rate. Shuai et al. [67] and Mendez et. al [68] reported that the ammonium selectivity increases with decreasing palladium particle size particularly below 10 nm. In contrast, Zhao et al. [66] and Yoshinaga et al. [69] observed that increasing palladium particle size favored the ammonium formation within the range between 2 to 3 nm. These differences in the effect of palladium particle size on the NH_4^+ selectivity could arise from the different levels of conversion employed to determine the NH_4^+ formation, experimental conditions and might also be influenced by mass transfer effects. In the case of Shuai et al. [67] and Zhao et al. [66] the differences on the experimental conditions and level of conversion make it difficult to fairly make a conclusion. In the case of Mendez et al. [68] and Yoshinaga et al. [69] the influence of mass transfer limitations was not addressed. As shown in Table S3.2, the particle size distribution of the Pd/Al_2O_3 catalyst with 0 and 7 wt. % carbon was the nearly unaltered. However, the NH_4^+ selectivity decreased from 3 % to 1 % (see Figure S3.10b), which would indicate that the palladium particle size cannot explain the changes in selectivity.

3.4.3　Solvation effects

Recently, Xu et al.[12] reported a nitrite hydrogenation mechanism in which the reaction rate was controlled by NO* hydrogenation reactions requiring multiple pre-equilibrated hydrogenation steps before the rate determining step (RDS). The authors concluded that N-N coupling could not be the RDS as the observed apparent reaction orders would not fit with the theoretically predicted orders at low surface coverages of nitrite and hydrogen. This proposed mechanism is in line with the work Clark et al. on Pd and Rh supported catalysts.[10] In these mechanisms, NO* is believed to quickly form from NO_2^- in the presence of chemisorbed hydrogen on Pd. This intermediate is then hydrogenated to NO_xH_y (NOH*, HNOH* and NH*), where NH_4^+ formation only proceeds via hydrogenation of NH*. In this context, both N_2 and NH_4^+ shared the same rate determining step. As a result, N_2 was speculated to be formed via either disproportionation of NO* and/or coupling of NO* with NOH_{ads}, $HNOH_{ads}$ and/or NH_{ads}. In this scenario, one would expect that NH_3 formation will be more favourable at increasing hydrogen coverages, as argued previously.[10,12,13] However, we observed that the addition of

p-NIPAM effectively leads to lower ammonia formation (see Table 3.2). In this context, the lower partial pressures required to reach saturation kinetics on the p-NIPAM coated catalyst could be associated to the stabilization of hydrogen on the surface. In turn, the stronger binding of hydrogen on the metal surface can lead to an increase in the activation barrier for ammonia formation (see Figure S3.12). This is assuming that the polymers do not change the number of active sites available for hydrogen chemisorption. If this would not be true and the number of active sites would be lowered, the consequence would be that the polymer increases the TOF on the remaining sites. These local interactions of p-NIPAM and chemisorbed species was demonstrated by our in-situ ATR experiments, in which a red shift of chemisorbed NOx was observed. One could imagine that the N-H and CO groups in the p-NIPAM can interact with other water molecules via hydrogen bonding near the chemisorbed hydrogen and nitrites, leading to changes energy of adsorbed species and consequently also the reactivity of those surface species.[70] This solvating effect can potentially explain the glaring differences on ammonia formation rate between the parent and polymer coated catalysts. More broadly, we envision that utilizing polymer-brushes like p-NIPAM as micro-solvation modifiers will play an essential role in developing highly selective catalysts for removal of pollutants in drinking water and specialty chemicals synthesis.

3.5   Conclusions

This contribution provides direct evidence that polymer brushes modify the selectivity of supported palladium catalysts during nitrite hydrogenation reaction, favouring the N_2 formation in wide range of operating conditions (i.e. $1 - 4$ mM NO_2^- and $0.1 - 0.8$ bar H_2). We demonstrated that mass transport limitations cannot be responsible for NH_4^+ selectivity as the observed reaction orders were below one for both nitrites and hydrogen and the estimated Weisz-Prater and Mears criteria indicated that internal and external transfer rates are negligible. Similarly, particle size effects could not explain the differences in selectivity as the differences in Pd particle sizes between the different catalysts was not significant. Instead, the observed changes in selectivity are attributed to the modification of the solvation environment around the active site induced by the p-NIPAM brushes as shown by in-situ ATR-IR spectroscopy measurements of NO_2^- on Pd. Contrary to previous research, arguing that polymer coatings only modify the transport of reactive species, we

showed that p-NIPAM brushes effectively induce solvation effects that modify the energy landscape of the catalytic reaction, mimicking the operation of enzymes.

3.6   Acknowledgements

3.7   Annexes

3.7.1   Structure p-NIPAM and polymerization

Figure S3.1: a) Poly(n-isopropylacrylamide) chemical structure. [44], b) (3-aminopropyl) triethoxysilane (APTES) molecular structure.

3.7.2 ATR-IR setup
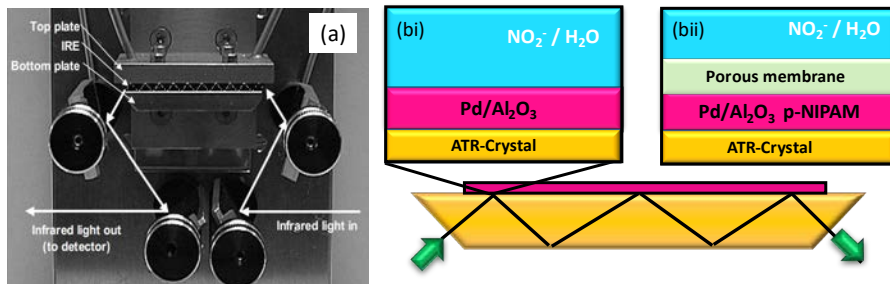
Figure S3.2: Home built in-situ ATR-IR flow through cell [52] (a) and schematic representation of the ATR-IR assembly in the case of Pd/Al$_2$O$_3$ containing 0 (bi) and 7 (bii) wt. % carbon, where a membrane was added to the top of the non-calcined catalyst layer.

3.7.3 Palladium alumina experiment

In the presence of protons, the NO$_2^-$ can be protonated to form the weak acid HNO$_2$. The acid dissociation constant (Ka) is 4.5×10^{-4} at 25 °C, resulting on a pKa of 3.3. At pH values higher than the pKa, the equilibrium shifts to the deprotonated form. The addition of CO$_2$ to the reaction medium resulted on a pH equal to c.a. 5.6. The HNO$_2$ concentration obtained was 2.18×10^{-6} mol L^{-1} for an initial concentration of NO$_2^-$ of c.a. 3×10^{-3} mol L^{-1}. Therefore, only the NO$_2^-$ concentration was considered (see Figure S3.2).
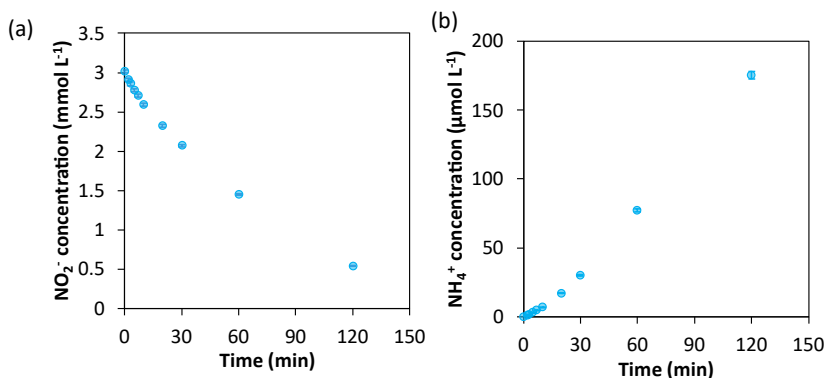
Figure S3.3: a) Nitrite concentration over time on palladium alumina at 20 °C, 500 RPM, 3mM NO$_2^-$ and 0.5bar H$_2$, b) ammonia concentration over time under the same condition initial rates are calculated from these plots with 13 % conversion level.

3.7.4   Catalyst characterization

3.7.4.1 Estimation of the p-NIPAM volume occupied in the catalyst

To estimate the volume of the polymer p-NIPAM brushes in the catalyst we employed the carbon content obtained from elemental analysis (see Table 3.1) and the p-NIPAM bulk density (1.1 g cm^{-3}) at 20 °C. Then, we employed the MW of P-NIPAM's monomer (N-isopropyl acrylamide) of 113.16 g mol^{-1} to obtain the final volumes per unit mass of catalyst using Eq. S3.1.

$$V_{P_{NIPAM_{Cat}}}(\frac{cm^3}{g_{cat}}) = \frac{\%_{Carbon_{cat}} * MW_{N-IPA}}{MW_C * 6} * \frac{1}{D_{P-NIPAM}} \qquad \text{Eq. S3.1}$$

The results of the calculations are summarized in Table S3.1. Here, it can be noted that the pore volume reduction observed on the samples containing 7 and 20 percentage of carbon was slightly higher than that of the polymer brushes. The volume fraction of polymer equivalent per pore volume loss in the different catalysts was estimated as the ratio of N-IPA volume to pore volume reduction. As shown in Table S3.1, the equivalent volume of polymer brushes per unit mass of catalyst was 0.1 and 0.35 cm^3 g^{-1} for Pd/Al$_2$O$_3$ containing 7 and 20 wt. % of carbon, respectively. These volumes are slightly smaller than the observed decrease in pore volume for these samples by N$_2$-physisorption (Table 3.1). This could indicate that in the dry state pore mouth blockage occurs upon growing the p-NIPAM polymeric brushes.

Table S3.1: Mass and volume fractions of equivalent polymer on the Pd/Al$_2$O$_3$ catalysts estimated based on the carbon content obtained by elemental analysis.

Catalyst	Mass fraction of N-IPA	Volume of N-IPA (ml gcat^{-1})	Vol. Fraction of N-IPA per cat. Pore vol. (%)
0wt. %C	0	0	0
7wt. %Ca	0.1	0.12	67
20wt. %C	0.3	0.35	84

3.7.4.2 N$_2$ physisorption

As shown in Table 3.1, BET analysis of the N$_2$-physisorption data indicated that he addition of chemically bonded polymer brushes decreased the surface area by 12 % and pore volume by 27 %, reaching values of 170 m^2 g^{-1} and 0.47 m^2 g^{-1}, respectively, for the sample containing 7 wt. % C. Increasing further the carbon content led to even lower surface area (103 m^2 g^{-1}) and pore volumes (0.23 m^2 g^{-1}). Figure S3.4a shows the N$_2$ adsorption-desorption isotherms of Pd/Al$_2$O$_3$ catalysts containing 0, 7 and 20 wt. % C in the form of p-NIPAM. The shape of the adsorption isotherm is a type IV corresponding to a mesoporous structure. Here, it can be noted that the polymer decreases the quantity of nitrogen adsorbed via capillary condensation, as discussed above. Typically, γ-Al$_2$O$_3$ supports are meso-porous with pore diameters smaller than 20 nm.[12] According to Figure S3.4b, the presence of polymer decreases the pore sizes for both 7 wt. % C and 20 wt. % C, resulting from polymer growth inside the pores. These results show a significant change in the textural properties of the catalysts in gas phase and low temperature used for N$_2$-physisorption -196 °C, possibly causing under-estimation of the pore volume as collapsed polymer brushes may effectively block pore openings. In contrast, under reaction conditions in aqueous solutions, the available pore volume for molecular diffusion is potentially larger if polymers are in the swollen state.[71]
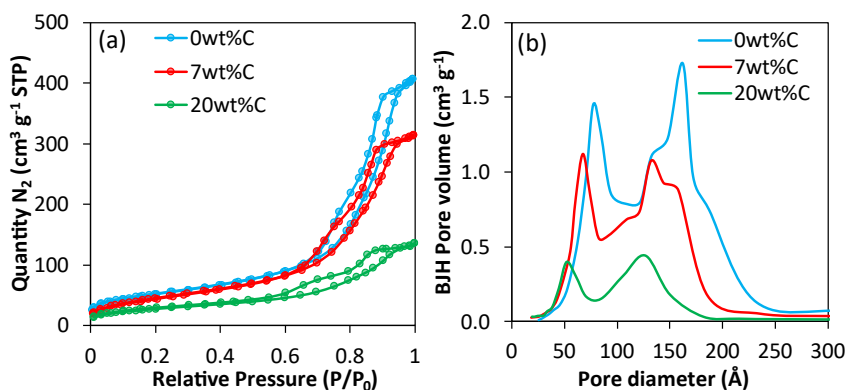
Figure S3.4: N$_2$-Physisorption curves obtained at -196 °C (a) and pore size distribution obtained from N$_2$-physisorption data using the Barrett-Joyner-Halenda (BJH) method (b) for the Pd/Al$_2$O$_3$ catalyst containing three different p-NIPAM polymer contents including 0 (blue), 7 (red), and 20 (green) wt. % carbon, respectively.

3.7.4.3 TGA

Figure S3.5 shows the weight loss profile using TGA for palladium alumina catalyst and polymer coated catalyst with different polymer content. The weight loss on palladium alumina catalyst is caused by desorption of water, because alumina is a hygroscopic material containing OH groups at the surface. This initial weight loss decreases in presence of polymer. This is probably caused by less available OH groups at the alumina surface, because APTES reacts with the alumina surface OH groups. This shows that under reaction conditions (20 to 55 °C) all catalysts are thermally stable.

The resulting weight loss, at 350 °C, is comparable to the carbon content, obtained from elemental analysis (Table 3.1). The aforementioned carbon content is equivalent to a polymer mass fraction of 10 and 32 wt. %, respectively, which is in good agreement with the mass losses herein observed above 350 °C (see Table S3.1).
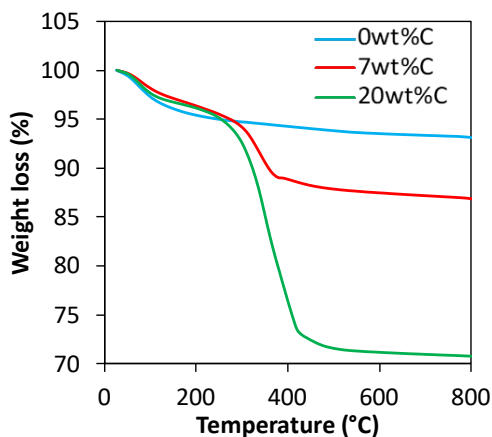
Figure S3.5: Thermal gravimetric analysis (TGA) from 25 to 800 °C using synthetic air for the Pd/Al_2O_3 catalyst containing three different p-NIPAM polymer contents including 0 (blue), 7 (red), and 20 (green) wt. % carbon, respectively.

3.7.4.4 STEM-HAADF characterization
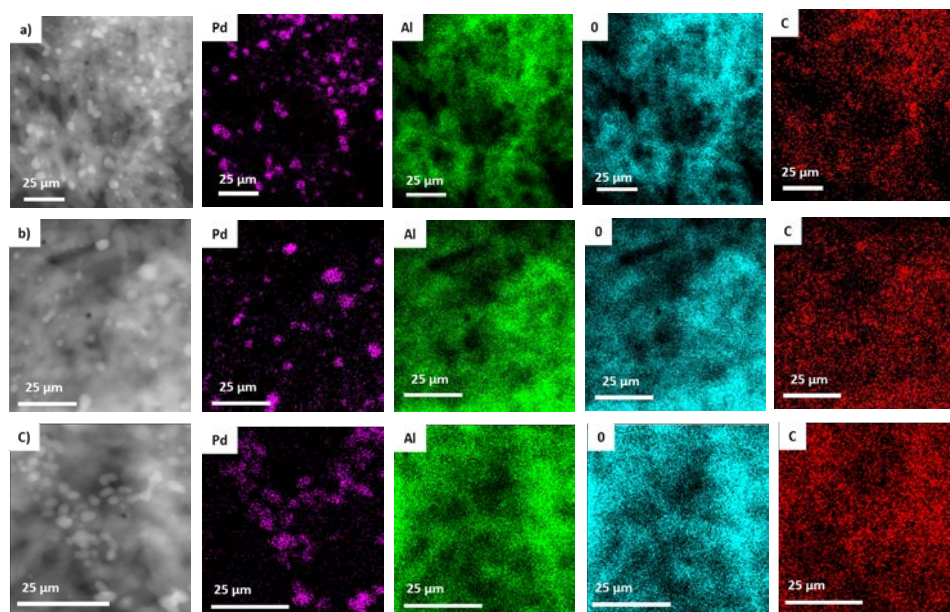
Figure S3.6: STEM-HAADF images for Palladium (Pd), Alumina (Al), Oxygen (O) and Carbon (C) distribution of the pre-reduced Pd/Al_2O_3 catalysts containing 0, 7, and 20 wt. % carbon (a-c, respectively).

3.7.4.5 Pd particle size

Table S3.2: Palladium particle size and dispersion obtained from CO chemisorption and STEM-HAADF and palladium loading obtained from XRF characterization.

Pd/Al_2O_3 catalysts	Pd loading (%)	Dispersion CO-chem. (%)	Dispersion TEM (%)	Pd diameter CO-chem. (nm)	Pd diameter TEM (nm)c
0 wt. % C 1	3.3	37	37	3.0	3.1 ± 1.7
0 wt. % C 2	2.9	40	34	2.8	3.3 ± 1.6
7 wt. % C[a]	2.3	14	31	7.9	3.6 ± 2
20 wt. % C[b]	1.4	12	24	11.8	4.2 ± 1.7

a: 7 wt. % C synthesized from Pd/Al_2O_3 0 wt. % C (1). b: 20 wt. % C was synthesized from Pd/Al_2O_3 0 wt. % C (2). c: Presented values correspond to the average Pd particle size and the width of distribution as shown in Figure 3.3a-c iii.

3.7.4.6 XPS results

Table S3.3: Detected elements (in atomic %) by XPS on the Pd/Al_2O_3 catalysts containing 0, 7 and 20 wt. % carbon.

Catalyst	C 1s % at.	O 1s % at.	Al 2p % at.	N 1s % at.	Pd3d %at.
0 wt. % C	13.5	54.5	30.8	0.5	0.3
7 wt. % C	24.3	46.9	25.6	2.9	0.3
20 wt. % C	29.3	42.5	24.0	4.0	0.2
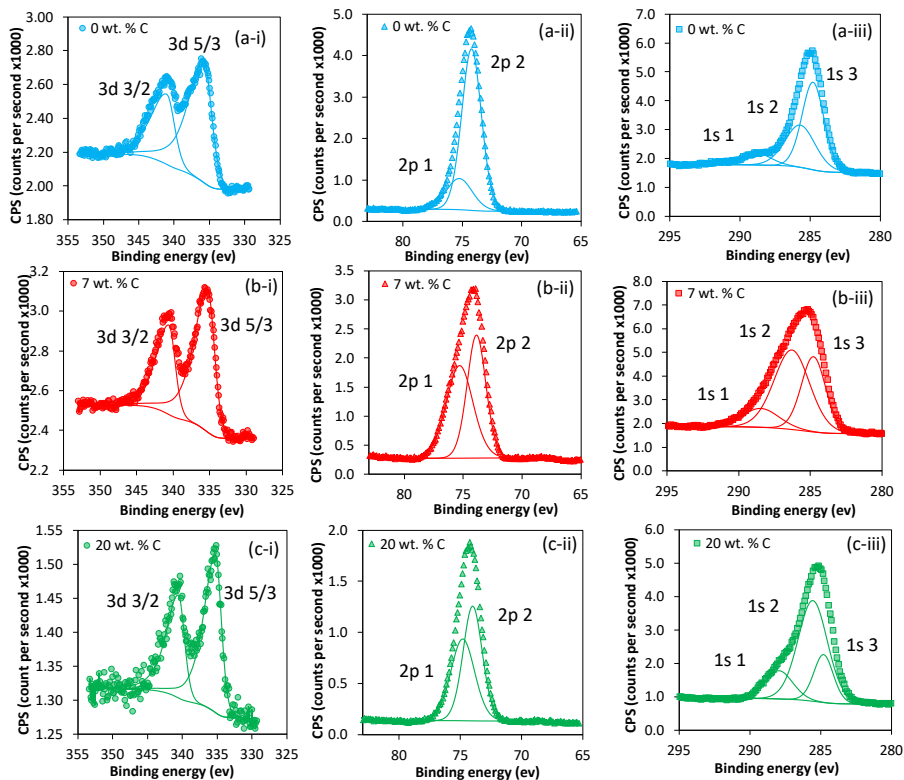
Figure S3.7: XPS spectra of obtained for Pd/Al$_2$O$_3$ containing 0 (blue), 7 (red) and 20 (green) wt. % carbon. All spectra have been calibrated using C 1s (C-C) equals to 284.8 eV as reference.

Table S3.4: XPS deconvolution and binding energy of alumina support, where the integrated peak areas were determined by applying a gaussian function.

	Al 2p 1		Al 2p 2	
Catalyst	Peak area (%)	B.E. (eV)	Peak area (%)	B.E. (eV)
0 wt. % C	79.4	74.2	20.5	75.2
7 wt. % C	48.4	73.9	51.6	75.3
20 wt. % C	53.1	74.0	46.9	74.8

Table S3.5: XPS deconvolution and binding energy of carbon, where the integrated peak areas were determined by applying a gaussian function.

	C 1s 1		C 1s 2		C 1s 3	
Catalyst	Peak area (%)	B.E. (eV)	Peak area (%)	B.E. (eV)	Peak area (%)	B.E. (eV)
0 wt. % C	54.3	284.8	36.2	285.7	9.5	288.8
7 wt. % C	34.4	284.8	52.7	286.3	12.9	288.5
20 wt. % C	20.0	284.8	63.5	285.6	16.5	287.9

Table S3.6: XPS deconvolution and binding energy of palladium nanoparticles, where the integrated peak areas were determined by applying a gaussian function.

	Pd 3d 5/3		Pd 3d 3/2	
	Peak area (%)	B.E. (eV)	Peak area (%)	B.E. (eV)
0 wt. % C	63.5	335.7	36.5	341.0
7 wt. % C	63.2	335.3	36.8	340.6
20 wt. % C	59.8	335.2	40.2	340.5

3.7.4.7 DLS characterization

The γ-Al_2O_3 support particles were sieved to a particle size < 38 μm. Figure S8 shows the catalyst particle size distribution obtained from DLS, where a broad particle size distribution was encountered. The observed average particle size of 27 μm is in line with the sieving conducted before the catalyst synthesis. The larger particles herein detected are the result of the strong particle-particle interactions that lead to agglomerates of larger sizes.
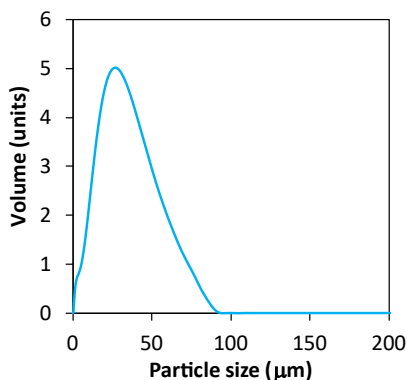
Figure S3.8: catalyst particle size distribution determined by dynamic light scattering (DLS) on the palladium alumina catalyst.

3.7.5   Mass transfer limitations

The influence of gas-liquid mass transport of hydrogen in the reaction rate was determined using the dimensionless Maers criteria within the operational window employed to conduct the catalytic studies. The results indicated that there are no interfacial limitations for hydrogen transport from the gas to the liquid phase (c.a. 0.08 see Table S3.7). To exclude the external transport limitations for nitrites and hydrogen we conducted catalytic experiments at agitation rates varying from 0 to 625 rpm (see Figure S3.9). The results indicated that above 500 rpm the rate of nitrite hydrogenation is constant. Because all kinetic experiments were conducted at 500 rpm, external mass transfer limitations can be discarded. Possible influence of internal diffusional limitations was evaluated using the Weisz-Prater criteria for both nitrogen and hydrogen. The results for Pd/Al_2O_3 containing 0, 7, and 20 wt. % C showed values in the range of 0.03 -0.8 (i.e. <1) at the reaction conditions applied (i.e. temperature ranging from 25 to 50 °C, hydrogen partial pressures varying from 0.2 to 0.7 bar, and nitrite concentrations within 1 to 4 mM, shown Table S3.8, S3.9 and S3.10). While these calculations suggest that internal mass transfer limitations are negligible for Pd/Al_2O_3, the possible effects of the polymer brushes on the molecular diffusion of hydrogen and nitrites were not considered. Instead, only the effect of the polymer on the catalyst volume, as obtained from N_2-physisorption, was considered in the calculation of the effective diffusion coefficients. Notably, previous data on molecular transport of large organic molecules in p-NIPAM gels for drug delivery applications, have shown that the ratio between diffusion coefficients of the molecule inside p-NIPAM matrix

and the diffusion coefficients of bulk water vary from 0.6 to 0.8 at low and high temperatures, respectively.[72] Extrapolating these results to hydrogen and nitrite is not trivial as the molecular size and charge of these species is different from that of the substrates previously reported. Nevertheless, a sensitivity analysis of the diffusion coefficient of hydrogen and nitrites within a ± 50 % variation, indicates that the WP criteria remains below unity.

3.7.5.1 External mass transfer G-L and L-S

Calculations

Mears criteria is used to determine if under the reaction conditions there is no external mass transfer limitations determined by Eq. S3.2.

$$ME = \frac{-r_{obs} \times \rho_c \times R_p \times n}{k_i^{mtl} \times C_i^s} < 0.15 \qquad \text{Eq. S3.2}$$

Which $-r_{obs}$ is catalyst rate observed (mol kg^{-1} s^{-1}), ρ_c is the catalyst density (kg m^{-3}), R_p catalyst radius average particle (m), n the reaction order, k_i^{mtl} mass transfer coefficient (m s^{-1}) and C_i^s the reactant concentration in the bulk (mol m^{-3}).

Particle velocity is determined by applying stokes law which is valid for a laminar flow (Re<1). It was assumed all spheres move with a constant velocity called terminal velocity, u_t which can be calculated with Eq. S3.3.

$$u_t = \frac{g \times d_p^2 \times (\rho_c - \rho_L)}{18\mu} \qquad \text{Eq. S3.3}$$

Which g is the standard gravity (9.81 m s^{-2}), ρ_c is the catalyst density (kg m^{-3}), ρ_l is the water density (kg m^{-3}) and μ is the dynamic water viscosity (Pa s).

Mass transfer coefficient was obtained using the Sherwood correlation which depends on Reynold, Schmidt and Sherwood number (Eq. S3.4-7).

$$Re = \frac{d_p \times u_t \times \rho_l}{\mu} \qquad \text{Eq. S3.4}$$

Where Re is Reynolds number, dp average diameter particle size (m), u_t the terminal velocity (m s^{-1}), ρ_l is the water density (kg m^{-3}) and μ is the dynamic water viscosity (Pa s).

$$Sc_i = \frac{\mu}{D_{i,water}\,\rho_l} \qquad \text{Eq. S3.5}$$

Which Sci is the Schmidt number, μ is the dynamic water viscosity (Pa s) and $D_{i,water}$ is the diffusivity of the reactant in water (m^2 s^{-1}).

$$Sh_i = 2 + 0.552\,Re^{1/2}Sc_i^{1/3} \qquad \text{Eq. S3.6}$$

Where Shi is the Sherwood number.

From Eq. S3.7, mass transfer coefficient was calculated.

$$k_i^{mtl} = \frac{D_{i,water}\,Sh_i}{d_p} \qquad \text{Eq. S3.7}$$

Table S3.7: Parameters for the calculations of Mears criteria for H_2 at 3mM NO_2^- and 0.5bar H_2 at 20°C.

	0wt. %C	7wt. %C
$r_{ob}s(H_2)$ (mol s^{-1}kg^{-1})	0.0205	0.008
PC (kg m^{-3})	1082	1326
n_{H2}	0.4	0.4
Rp (m)	13.5x10^{-6}	13.5x10^{-6}
Cis (H_2) (mol m^{-3})	0.4	0.4
$k_i^{mtl}(H_2)$ (m s^{-1})	5.81x10^{-4}	7.82x10^{-4}
ME (H_2)	0.08	0.03

For all the experiments ME was below 0.15 which concludes that there are no external mass transfer limitations on H_2. NO_2^- has zero order on the range measured on this paper which will never be a limiting factor.

Experimental results
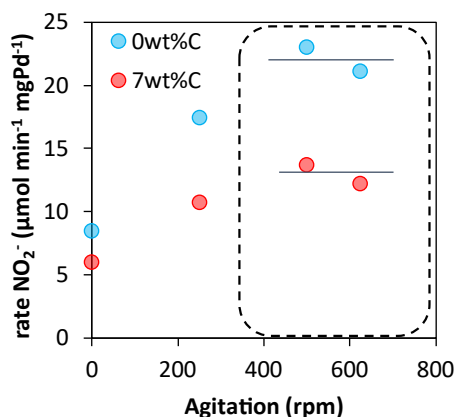
Figure S3.9: NO_2^- Rate based on palladium amount over the rotation speed of the stirring device for 0 wt. % C and 7 wt. % C at 3mM NO_2^- and 0.5bar H_2 at 20°C.

3.7.5.2 Internal mass transfer: Weisz-Prater criterion

Weisz-Prater criterion was used to calculate how efficient the reactant diffuses into the pellet before reacting, which can be calculated from Eq. S3.8. C_{wp} values higher than one indicates several mass transfer limitations.

$$C_{WP} = \frac{r_{obs}L^2\rho_{cat}}{C_s D_{eff}} < 1 \qquad \text{Eq. S3.8}$$

Where r_{obs} is the reaction per mass catalyst (mol s^{-1} kg^{-1}), L is the slab geometry (m), ρ_{cat} is the density of the catalyst particles (kg m^{-3}), C_s is the concentration at the catalyst surface (mol m^{-3}) and D_{eff} the effective diffusion coefficient (m^2 s^{-1}). In the presence of sphere catalyst, the distance L was defined as Eq. S3.9

$$L = \frac{r_p}{3}$$ <div align="right">Eq. S3.9</div>

where r_p is the average radius particles (m).

On a catalyst particle the effective diffusion coefficient was defined as Eq. S3.10.

$$D_{eff} = \frac{D_{AB}\ \varepsilon}{\tau}$$ <div align="right">Eq. S3.10</div>

In which D_{AB} is the species diffusion coefficient in water ($m^2\ s^{-1}$), ε is the catalyst porosity and τ is the catalyst tortuosity. Tortuosity was defined as a function dependent of porosity (Eq. S3.11).

$$\tau = 1 - \ln(\varepsilon)$$ <div align="right">Eq. S3.11</div>

Table S3.8: Weisz-Prater numbers for NO_2^- reaction orders with a fixed H_2 pressure of 0.5 bar with average diameter particle size of 27 μm, porosity of 0.7, D_{AB}^{NO2} 1.99X10^{-9} $m^2\ s^{-1}$ and D_{AB}^{H2} 5.11X10^{-9} $m^2\ s^{-1}$ at 20 °C.

	$C_{wp}\ H_2$		$C_{wp}\ NO_2^-$	
NO_2^- (mM)	0wt. %C	7wt. %C	0wt. %C	7wt. %C
1.5	0.421	0.38	0.17	0.12
2.5	0.39	0.25	0.11	0.07
4	0.35	0.21	0.065	0.039

Table S3.9: Weisz-Prater numbers for H_2 reaction orders with a fixed NO_2^- concentration of 3 mM with average diameter particle size of 27 μm, porosity of 0.7, D_{AB}^{NO2} 1.99×10^{-9} m^2 s^{-1} and D_{AB}^{H2} 5.11×10^{-9} m^2 s^{-1} at 20°C.

H2 (bar)	C_{wp} H_2			C_{wp} NO_2^-		
	0wt. %C	7wt. %C	20wt. %C	0wt. %C	7wt. %C	20wt. %C
0.2	0.85	0.6		0.08	0.045	
0.5	0.2	0.24	0.5	0.049	0.059	0.12
0.7	0.28	0.189		0.097	0.065	

Table S3.10: Weisz-Prater numbers for NH_4^+ and NO_2^- at different temperatures with a fixed NO_2^- concentration of 3 mM and H_2 pressure of 0.5 bar with average diameter particle size of 27 μm, porosity of 0.7, D_{AB}^{NO2} 1.99×10^{-9} m^2 s^{-1} and D_{AB}^{H2} 5.11×10^{-9} m^2 s^{-1}.

Temperature (°C)	C_{wp} H_2			C_{wp} NO_2^-		
	0wt. %C	7wt. %C	20wt. %C	0wt. %C	7wt. %C	20wt. %C
25	0.42	0.36	0.58	0.1	0.065	0.13
30	0.45	0.3	0.55	0.14	0.2	0.12
50	0.56	0.37	0.72	0.25	0.17	0.13

All the experiments C_{wp} is lower than 1 indicating no internal mass transfer.

3.7.6 Conversion, selectivity and catalytic rate

Figure S3.10a shows the nitrite conversion using the same catalyst mass for the parent Pd/Al_2O_3 and the polymer coated catalysts (c.a. 15 mg). The results indicate that on Pd/Al_2O_3 (samples 1 and 2) reaction rates of c.a. 0.86 mmol min^{-1} g_{cat}^{-1} can be obtained, while on the Pd/Al_2O_3-NIPAM catalysts containing 7 and 20 wt. % C the rates decreased to c.a. 0.35 and 0.26 mmol min^{-1} g_{cat}^{-1}, respectively. The low activities per mass of catalyst on the p-NIPAM rendered catalysts can be attributed to the lower Pd content (see Table S3.2) in comparison to the parent Pd/Al_2O_3. Notably, normalizing the activity using the metal dispersion obtained from HAADF-STEM indicates that on bare Pd/Al_2O_3 (1) and

(2) the TOF values were 6.9 ± 1.3 and 9.8 ± 2.3 min^{-1}, respectively. Incorporation of p-NIPAM in the catalyst led to TOF values of 5.2 ± 1.1 and 6.8 ± 1.1 min^{-1} for 7 wt.% C and 20 wt. % C (see Table 3.2). While it is tempting to ascribe this reduction to the presence of the polymer, it is important to consider that these values are statistically undistinguishable as all of them are within the 3σ region (shown in Table S3.11). Furthermore, the herein reported rates for coated and uncoated catalysts are also in line with previous nitrite hydrogenation studies conducted using conventional Pd/Al$_2$O$_3$ at similar reaction conditions.[12,47] In short, p-NIPAM does not affect the reaction rates significantly.
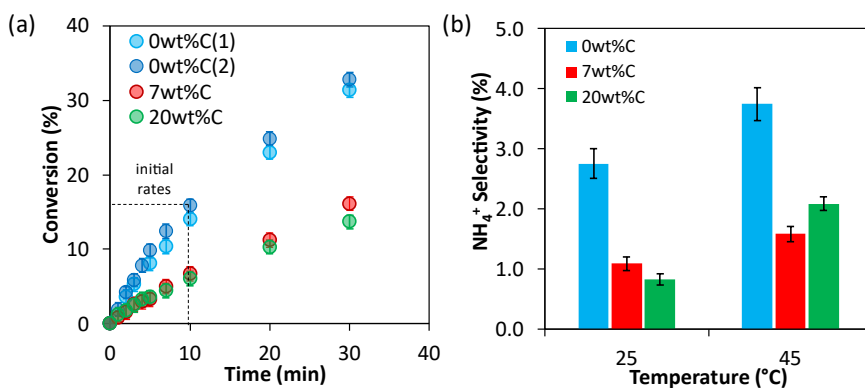
Figure S3.10: Conversion of nitrites as a function of time (a) and ammonium selectivity (at 13% conversion) obtained the parent catalysts Pd/Al$_2$O$_3$ 0 wt. % C (1) and 0 wt. % C (2) in blue, and 7 wt. % C (red) and 20 wt. % C (green) at 500 rpm, 20 °C, 3 mM of NO$_2^-$, 0.5 bar of H$_2$, 0.1 bar of CO$_2$ as buffer in the presence of 15 mg of catalyst. Error bars correspond to 95 % confidence.

Table S3.11: Comparison between NO$_2^-$ rate normalized as catalyst amount, palladium amount and metal active surface area from TEM dispersion images at 45°C.

	NO$_2^-$ rate (mmol min^{-1} g$_{cat}$)	NO$_2^-$ rate (mmol min^{-1} g$_{Pd}$)	TOF (min^{-1}) from TEM images
0wt. %C (1)	1.71 ± 0.1	52 ± 3	14.9 ± 2.6
7wt. %C	0.85 ± 0.04	37 ± 1	12.6 ± 1.9
20wt. %C	0.65 ± 0.04	39 ± 2	17.0 ± 2.1

Figure S3.11a shows the NH_4^+ concentration over time from where the integral NH_4^+ selectivity was calculated (Eq. 3.4). Figure S3.11b shows the NH_4^+ selectivity as a function of NO_2^- conversion. A fixed value of 13 % NO_2^- conversion value was fixed to compare the different NH_4^+ selectivity between the different catalysts.
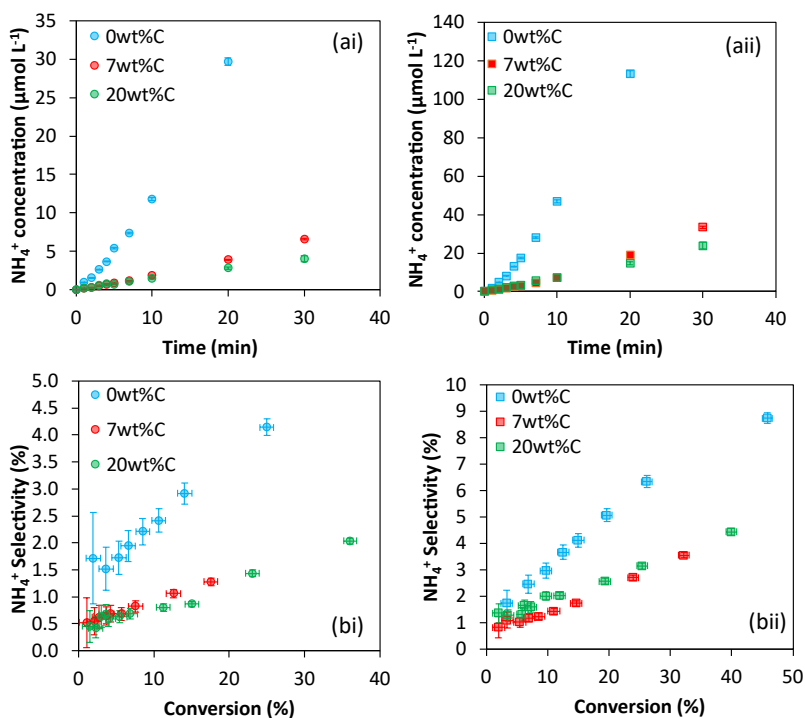

Figure S3.11: NH_4^+ concentration over time (a) and NH_4^+ selectivity as a function of NO_2^- conversion (b) (calculated from Eq. 3.5 and Eq. 3.6) for Pd/Al_2O_3 containing 0 (blue), 7 (red) and 20 (green) wt. % of carbon obtained at 3 mM NO_2^-, 0.5 bar H_2, 0.1 bar of CO_2, 0.4 bar of He, at agitation rates of 500 rpm at 25 °C (i) and 45 °C (i).

3.7.7 Apparent activation energies and pre-exponential factors
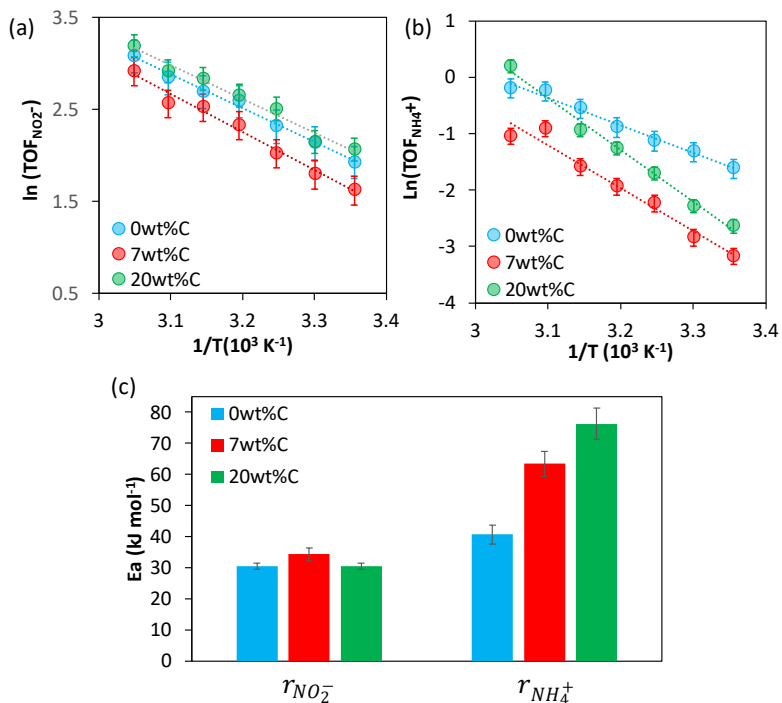
Figure S3.12. Arrhenius plots for NO_2^- (a) reaction and NH_4^+ formation rates (b) and the resulting apparent activation energy barriers for Pd/Al$_2$O$_3$ containing 0 (blue), 7 (red) and 20 (green) wt. % of carbon obtained at 3 mM NO_2^-, 0.5 bar H_2, 0.1 bar of CO_2, 0.4 bar of He, at agitation rates of 500 rpm from 25 to 55 °C.

Table S3.12: Apparent activation energy barriers (Ea) of NH_4^+ formation and overall NO_2^- consumption (kJ mol^{-1}) and pre-exponential factors (A) (min^{-1}) of 0, 7 and 20wt. % C catalyst. From 25 to 55 °C temperature, 500 rpm, 0.1 bar CO_2, 3mM NO_2^- and 0.5 bar H_2.

	Ea NH$_4^+$ (kJ mol^{-1})	A NH$_4^+$ (min^{-1})	Ea NO$_2^-$ (kJ mol^{-1})	A NO$_2^-$ (min^{-1})
0 wt. % C	41±3	14.9	31±1	14.3
7 wt. % C	63±4	22.4	34±2	15.4
20 wt. % C	76±5	28.1	30±1	14.3

3.7.8 Apparent reaction orders
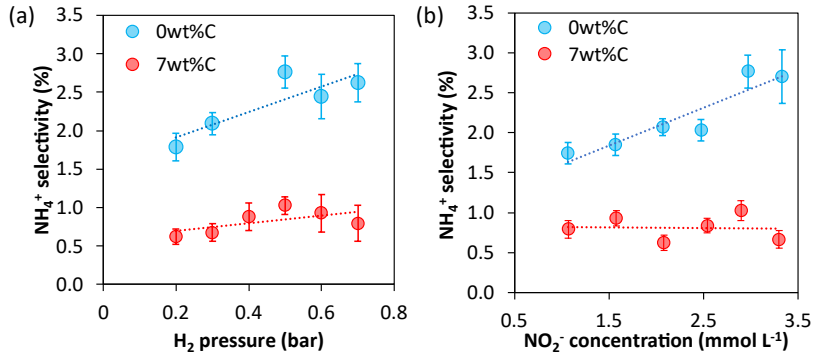
Figure S3.13: a) NO_2^- concentration effect on NH_4^+ selectivity at 20 °C with 0.5 bar H_2, 500 rpm for 0 and 7wt. % C (at 13% conversion level), b) H_2 concentration effect on NH_4^+ selectivity at 20 °C with 3mM NO_2^-, 500 rpm for 0 wt. % C and 7wt. % C (13% conversion level).

The rate expressions for NO_2^- overall consumption and NH_4^+ formation can be defined (Eq. S3.12-13), where "n" represents the reaction order for H_2 and "m" the reaction order for NO_2^-.

$$r_{NO_2^-} = k_{NO_2^-} [H_2]^n [NO_2^-]^m \qquad \text{Eq. S3.12}$$

$$r_{NH_4^+} = k_{NH_4^+} [H_2]^{n^*} [NO_2^-]^{m^*} \qquad \text{Eq. S3.13}$$

Table S3.13: Apparent NO_2^- and H_2 reaction orders for nitrite hydrogenation and ammonium formation at 20 °C and 1 bar for Pd/Al_2O_3 containing 0 (blue) and 7 (red) wt. % carbon. The NO_2^- concentrations ranged from 1 to 4 mM at 0.5 bar of H_2 and 0.1 bar of CO_2, while H_2 partial pressures varied from 0.1 to 0.7 bar at 3 mM NO_2^- using 15 mg of catalyst and 500 rpm. Hydrogen, carbon dioxide, and helium (to balance) were added continuously to the system to ensure constant concentrations during the experiments

	NO2- reaction orders		NH4+ reaction orders	
	$m_{NO_2^-}$	n_{H_2}	$m^*_{NO_2^-}$	$n^*_{H_2}$
0 wt. % C	-0.1 ± 0.1	0.5 ± 0.1	0.4 ± 0.2	0.4 ± 0.2
7 wt. % C	-0.07 ± 0.03	0.1 ± 0.1	-0.1 ± 0.1	0.3 ± 0.2

3.7.9 ATR-IR spectrum

In the presence of protons, the NO_2^- can be protonated to form the weak acid HNO_2. The acid dissociation constant (Ka) is $4.5x10^{-4}$ at 25 °C, resulting on a pKa of 3.3. At a pH of 7, The HNO_2 concentration obtained was 9.71×10^{-8} mol L^{-1} for an initial concentration of NO_2^- of c.a. $15x10^{-3}$ mol L^{-1}. Therefore, on the blank experiment the peak on 1260 cm^{-1} is assigned to HNO_2 in solution (see Figure S3.9b). The peak at 1235 cm^{-1} corresponds to NO_2^- in solution. The peak at 1350 cm^{-1} was observed in all the experiments, which indicates a NO stretch from NO_2^- in solution. The other peaks observed in the blank experiment which were not detect at Pd/Al_2O_3 containing 0 and 7 wt. % carbon was attributed to water.
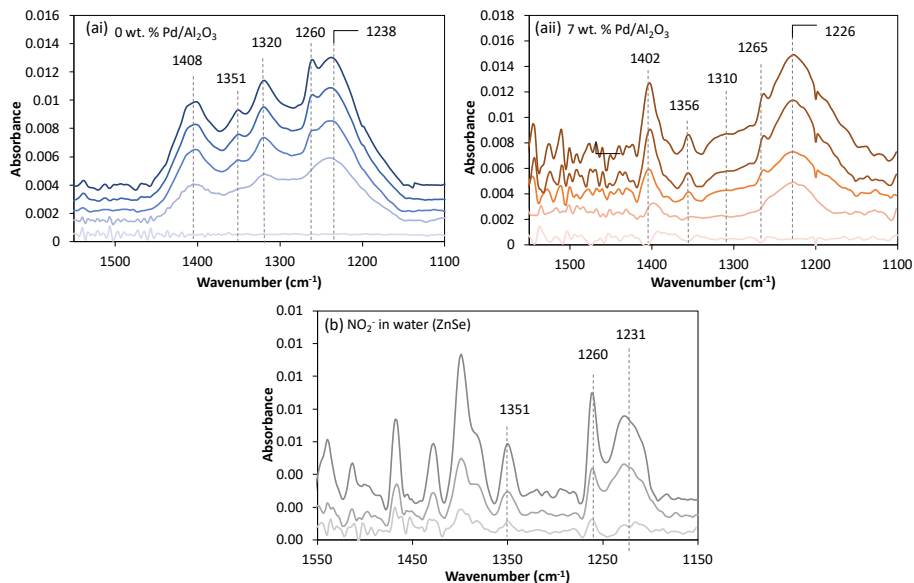
Figure S3.14: Water correct in situ ATR-IR spectrum over time on 0 wt. % C (blue) (ai) and 7 wt. % C (orange) (aii) Pd/Al$_2$O$_3$ catalyst and NO$_2^-$ solution in water (grey) (b) obtained from a flow of 15 mM NO$_2^-$ at pH 7 and 25 °C.
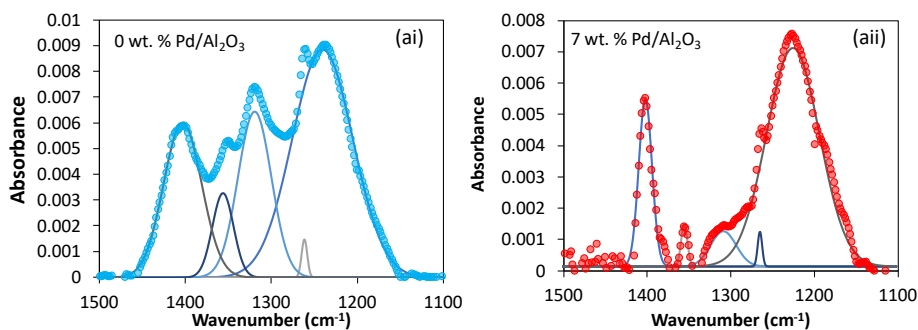

Figure S3.15: Peak deconvolution at the saturation time for 0 wt. % C (blue) (ai) and 7 wt. % C (red) (aii) Pd/Al$_2$O$_3$ catalyst from a flow of 15 mM NO$_2^-$ at pH 7 and 25 °C.

3.8   References

[1]   J. Brightling, Ammonia and the fertiliser industry: The development of ammonia at Billingham, Johnson Matthey Technol. Rev. 62 (2018) 32–47. https://doi.org/10.1595/205651318X696341.

[2]   S. Tyagi, D. Rawtani, N. Khatri, M. Tharmavaram, Strategies for Nitrate removal from aqueous environment using Nanotechnology: A Review, J. Water Process Eng. 21 (2018) 84–95. https://doi.org/10.1016/j.jwpe.2017.12.005.

[3]   J.N. Galloway, A.R. Townsend, J.W. Erisman, M. Bekunda, Z. Cai, J.R. Freney, L.A. Martinelli, S.P. Seitzinger, M.A. Sutton, Transformation of the Nitrogen Cycle :, Science (80-.). 320 (2008) 889–892. https://doi.org/10.1126/science.1136674.

[4]   D.E. Canfield, A.N. Glazer, P.G. Falkowski, The evolution and future of earth's nitrogen cycle, Science (80-.). 330 (2010) 192–196. https://doi.org/10.1126/science.1186120.

[5]   J.W. Erisman, M.A. Sutton, J. Galloway, Z. Klimont, W. Winiwarter, How a century of ammonia synthesis changed the world, Nat. Geosci. 1 (2008) 636–639. https://doi.org/10.1038/ngeo325.

[6]   J.W. Erisman, J.N. Galloway, S. Seitzinger, A. Bleeker, N.B. Dise, A.M. Roxana Petrescu, A.M. Leach, W. de Vries, Consequences of human modification of the global nitrogen cycle, Philos. Trans. R. Soc. B Biol. Sci. 368 (2013). https://doi.org/10.1098/rstb.2013.0116.

[7]   P.J. Crutzen, A.R. Mosier, K.A. Smith, W. Winiwarter, N2O release from agro-biofuel production negates global warming reduction by replacing fossil fuels, Atmos. Chem. Phys. 8 (2008) 389–395. https://doi.org/10.5194/acp-8-389-2008.

[8]   WHO, Nitrate and nitrite in drinking water: background document for development of WHO guidelines for drinking water quality, Geneva World Heal. Organ. (2016) 31. http://www.who.int/publications/guidelines/%0Ahttp://www.who.int/water_sanitation_health/dwq/chemicals/nitratenitrite2ndadd.pdf.

[9]   Y. Sakamoto, Y. Kamiya, T. Okuhara, Selective hydrogenation of nitrate to nitrite in water over Cu-Pd bimetallic clusters supported on active carbon, J. Mol. Catal.

A Chem. 250 (2006) 80–86. https://doi.org/10.1016/j.molcata.2006.01.041.

[10]   C.A. Clark, C.P. Reddy, H. Xu, K.N. Heck, G. Luo, T.P. Senftle, M.S. Wong, Mechanistic insights into ph-controlled nitrite reduction to ammonia and hydrazine over rhodium, ACS Catal. 10 (2020) 494–509. https://doi.org/10.1021/acscatal.9b03239.

[11]   S. Hörold, K.D. Vorlop, T. Tacke, M. Sell, Development of catalysts for a selective nitrate and nitrite removal from drinking water, Catal. Today. 17 (1993) 21–30. https://doi.org/10.1016/0920-5861(93)80004-K.

[12]   P. Xu, S. Agarwal, L. Lefferts, Mechanism of nitrite hydrogenation over Pd/γ-Al2O3 according a rigorous kinetic study, J. Catal. 383 (2020) 124–134. https://doi.org/10.1016/j.jcat.2020.01.003.

[13]   S.D. Ebbesen, B.L. Mojet, L. Lefferts, Effect of pH on the Nitrite Hydrogenation Mechanism over Pd/Al2O3 and Pt/Al2O3: Details Obtained with ATR-IR Spectroscopy, J. Phys. Chem. C. (2011) 1186–1194. https://doi.org/10.1021/jp106521t.

[14]   D. Shuai, D.C. McCalman, J.K. Choe, J.R. Shapley, W.F. Schneider, C.J. Werth, Structure sensitivity study of waterborne contaminant hydrogenation using shape- and size-controlled Pd nanoparticles, ACS Catal. 3 (2013) 453–463. https://doi.org/10.1021/cs300616d.

[15]   R. Brunet Espinosa, D. Rafieian, R.S. Postma, R.G.H. Lammertink, L. Lefferts, Egg-shell membrane reactors for nitrite hydrogenation: Manipulating kinetics and selectivity, Appl. Catal. B Environ. 224 (2018) 276–282. https://doi.org/10.1016/j.apcatb.2017.10.058.

[16]   R.S. Postma, B. Espinosa, L. Lefferts, Competitive Adsorption of Nitrite and Hydrogen on Palladium during Nitrite Hydrogenation, (2018) 3770–3776. https://doi.org/10.1002/cctc.201800523.

[17]   J.K. Chinthaginjala, L. Lefferts, Support effect on selectivity of nitrite reduction in water, Appl. Catal. B Environ. 101 (2010) 144–149. https://doi.org/http://dx.doi.org/10.1016/j.apcatb.2010.09.023.

[18]   S. Hôrold, T. Tacke, K.D. Vorlop, Catalytical removal of nitrate and nitrite from drinking water: 1. screening for hydrogenation catalysts and influence of reaction conditions on activity and selectivity, Environ. Technol. (United Kingdom). 14

(1993) 931–939. https://doi.org/10.1080/09593339309385367.

[19]   K. Daub, G. Emig, M.J. Chollier, M. Callant, R. Dittmeyer, Studies on the use of catalytic membranes for reduction of nitrate in drinking water, Chem. Eng. Sci. 54 (1999) 1577–1582. https://doi.org/10.1016/S0009-2509(99)00049-4.

[20]   G. Prieto, H. Tüysüz, N. Duyckaerts, J. Knossalla, G.H. Wang, F. Schüth, Hollow Nano- and Microstructures as Catalysts, Chem. Rev. 116 (2016) 14056–14119. https://doi.org/10.1021/acs.chemrev.6b00374.

[21]   M.B. Gawande, A. Goswami, T. Asefa, H. Guo, A. V Biradar, D.-L. Peng, R. Zboril, R.S. Varma, Core-shell nanoparticles: synthesis and applications in catalysis and electrocatalysis, Chem. Soc. Rev. 44 (2015) 7540–7590. https://doi.org/10.1039/c5cs00343a.

[22]   M. Shakeri, L. Roiban, V. Yazerski, G. Prieto, R.J.M. Klein Gebbink, P.E. de Jongh, K.P. de Jong, Engineering and Sizing Nanoreactors to Confine Metal Complexes for Enhanced Catalytic Performance, ACS Catal. 4 (2014) 3791–3796.

[23]   J. Zhang, M. Zhang, K. Tang, F. Verpoort, T. Sun, Polymer-based stimuli-responsive recyclable catalytic systems for organic synthesis, Small. 10 (2014) 32–46. https://doi.org/10.1002/smll.201300287.

[24]   D. Díaz Díaz, D. Kühbeck, R.J. Koopmans, Stimuli-responsive gels as reaction vessels and reusable catalysts, Chem. Soc. Rev. 40 (2011) 427–448. https://doi.org/10.1039/C005401C.

[25]   R. Roa, W.K. Kim, M. Kanduč, J. Dzubiella, S. Angioletti-Uberti, Catalyzed Bimolecular Reactions in Responsive Nanoreactors, ACS Catal. 7 (2017) 5604–5611. https://doi.org/10.1021/acscatal.7b01701.

[26]   Z. Chen, Z.M. Cui, C.Y. Cao, W.D. He, L. Jiang, W.G. Song, Temperature-responsive smart nanoreactors: Poly(N-isopropylacrylamide)- coated Au@mesoporous-SiO2 hollow nanospheres, Langmuir. 28 (2012) 13452–13458. https://doi.org/10.1021/la3022535.

[27]   F. Xia, L. Jiang, Bio-inspired, smart, multiscale interfacial materials, Adv. Mater. 20 (2008) 2842–2858. https://doi.org/10.1002/adma.200800836.

[28]   X. Liu, Y. Yang, M.W. Urban, Stimuli-Responsive Polymeric Nanoparticles, Macromol. Rapid Commun. 201700030 (2017) 1–20. https://doi.org/10.1002/marc.201700030.

[29] X. He, R.S. Friedlander, L.D. Zarzar, J. Aizenberg, Chemo-mechanically regulated oscillation of an enzymatic reaction, Chem. Mater. 25 (2013) 521–523. https://doi.org/10.1021/cm303313a.

[30] M. Motornov, Y. Roiter, I. Tokarev, S. Minko, Stimuli-responsive nanoparticles, nanogels and capsules for integrated multifunctional intelligent systems, Prog. Polym. Sci. 35 (2010) 174–211. https://doi.org/10.1016/j.progpolymsci.2009.10.004.

[31] S.S. Nagarkar, A. V. Desai, S.K. Ghosh, Stimulus-responsive metal-organic frameworks, Chem. - An Asian J. 9 (2014) 2358–2376. https://doi.org/10.1002/asia.201402004.

[32] X. He, M. Aizenberg, O. Kuksenok, L.D. Zarzar, A. Shastri, A.C. Balazs, J. Aizenberg, Synthetic homeostatic materials with chemo-mechano-chemical self-regulation, Nature. 487 (2012) 214–218. https://doi.org/10.1038/nature11223.

[33] L.D. Zarzar, J. Aizenberg, Stimuli-responsive chemomechanical actuation: a hybrid materials approach., Acc. Chem. Res. 47 (2014) 530–539. https://doi.org/10.1021/ar4001923.

[34] P. Kim, L.D. Zarzar, X. He, A. Grinthal, J. Aizenberg, Hydrogel-actuated integrated responsive systems (HAIRS): Moving towards adaptive materials, Curr. Opin. Solid State Mater. Sci. 15 (2011) 236–245. https://doi.org/10.1016/j.cossms.2011.05.004.

[35] T. Chen, R. Ferris, J. Zhang, R. Ducker, S. Zauscher, Stimulus-responsive polymer brushes on surfaces: Transduction mechanisms and applications, Prog. Polym. Sci. 35 (2010) 94–112. https://doi.org/10.1016/j.progpolymsci.2009.11.004.

[36] D. Zhao, T.M. Neubauer, B.L. Feringa, Dynamic control of chirality in phosphine ligands for enantioselective catalysis, Nat. Commun. 6 (2015) 1–7. https://doi.org/10.1038/ncomms7652.

[37] Y. Lu, Y. Mei, M. Drechsler, M. Ballauff, Thermosensitive core-shell particles as carriers for Ag nanoparticles: Modulating the catalytic activity by a phase transition in networks, Angew. Chemie - Int. Ed. 45 (2006) 813–816. https://doi.org/10.1002/anie.200502731.

[38] S. Carregal-Romero, N.J. Buurma, J. Pérez-Juste, L.M. Liz-Marzán, P. Hervés, Catalysis by Au@pNIPAM nanocomposites: Effect of the cross-linking density,

Chem. Mater. 22 (2010) 3051–3059. https://doi.org/10.1021/cm903261b.

[39]   R. Roa, S. Angioletti-Uberti, Y. Lu, J. Dzubiella, F. Piazza, M. Ballauff, Catalysis by metallic nanoparticles in solution: Thermosensitive microgels as nanoreactors, ArXiv. (2018).

[40]   M. Galanti, D. Fanelli, S. Angioletti-Uberti, M. Ballauff, J. Dzubiella, F. Piazza, Reaction rate of a composite core-shell nanoreactor with multiple nanocatalysts, Phys. Chem. Chem. Phys. 18 (2016) 20758–20767. https://doi.org/10.1039/c6cp01179a.

[41]   N. Welsch, A.L. Becker, J. Dzubiella, M. Ballauff, Core-shell microgels as 'smart' carriers for enzymes, Soft Matter. 8 (2012) 1428–1436. https://doi.org/10.1039/c1sm06894f.

[42]   H. il Lee, J. Pietrasik, S.S. Sheiko, K. Matyjaszewski, Stimuli-responsive molecular brushes, Prog. Polym. Sci. 35 (2010) 24–44. https://doi.org/10.1016/j.progpolymsci.2009.11.002.

[43]   M. Wei, Y. Gao, X. Li, M.J. Serpe, Stimuli-responsive polymers and their applications, Polym. Chem. (2017) 127–143. https://doi.org/10.1039/c6py01585a.

[44]   B.A. Humphreys, J.D. Willott, T.J. Murdoch, G.B. Webber, E.J. Wanless, Specific ion modulated thermoresponse of poly(N-isopropylacrylamide) brushes, Phys. Chem. Chem. Phys. 18 (2016) 6037–6046. https://doi.org/10.1039/C5CP07468A.

[45]   S. Angioletti-Uberti, Y. Lu, M. Ballauff, J. Dzubiella, Theory of Solvation-Controlled Reactions in Stimuli-Responsive Nanoreactors, J. Phys. Chem. C. 119 (2015) 15723–15730. https://doi.org/10.1021/acs.jpcc.5b03830.

[46]   S. Wu, J. Dzubiella, J. Kaiser, M. Drechsler, X. Guo, M. Ballauff, Y. Lu, Thermosensitive Au-PNIPA yolk-shell nanoparticles with tunable selectivity for catalysis, Angew. Chemie - Int. Ed. 51 (2012) 2229–2233. https://doi.org/10.1002/anie.201106515.

[47]   P. Xu, S. Agarwal, J.F. Albanese, L. Lefferts, Enhanced transport in Gas-Liquid-Solid catalytic reaction by structured wetting properties: Nitrite hydrogenation, Chem. Eng. Process. - Process Intensif. 148 (2020) 107802. https://doi.org/10.1016/j.cep.2020.107802.

[48]   K. Matyjaszewski, Atom Transfer Radical Polymerization (ATRP): Current Status and Future Perspectives, Macromolecules. 45 (2012) 4015–4039. https://doi.org/10.1021/ma3001719.

[49]   B.A. Humphreys, S.W. Prescott, T.J. Murdoch, A. Nelson, E.P. Gilbert, B. Webber, E.J. Wanless, Influence of molecular weight on PNIPAM brush modified colloidal silica particles †, Soft Matter. 15 (2019) 55–64. https://doi.org/10.1039/c8sm01824c.

[50]   G. Greczynski, L. Hultman, X-ray photoelectron spectroscopy: Towards reliable binding energy referencing, Prog. Mater. Sci. 107 (2020) 100591. https://doi.org/10.1016/j.pmatsci.2019.100591.

[51]   S.D. Ebbesen, B.L. Mojet, L. Lefferts, In situ ATR-IR study of CO adsorption and oxidation over Pt/Al2O3 in gas and aqueous phase: Promotion effects by water and pH, J. Catal. 246 (2007) 66–73. https://doi.org/10.1016/j.jcat.2006.11.019.

[52]   B.L. Mojet, S.D. Ebbesen, L. Lefferts, Light at the interface: the potential of attenuated total reflection infrared spectroscopy for understanding heterogeneous catalysis in water, Chem. Soc. Rev. 39 (2010) 4643. https://doi.org/10.1039/c0cs00014k.

[53]   S.D. Ebbesen, B.L. Mojet, L. Lefferts, In situ ATR-IR study of nitrite hydrogenation over Pd/Al2O3, J. Catal. 256 (2008) 15–23. https://doi.org/10.1016/j.jcat.2008.02.013.

[54]   S.D. Ebbesen, B.L. Mojet, L. Lefferts, The influence of water and pH on adsorption and oxidation of CO on Pd/Al2O3--an investigation by attenuated total reflection infrared spectroscopy., Phys. Chem. Chem. Phys. 11 (2009) 641–649. https://doi.org/10.1039/b814605e.

[55]   Y. Pei, J. Chen, L. Yang, L. Shi, Q. Tao, B. Hui, J. Li, The effect of pH on the LCST of poly(N-isopropylacrylamide) and poly(N-isopropylacrylamide-co-acrylic acid), J. Biomater. Sci. Polym. Ed. 15 (2004) 585–594. https://doi.org/10.1163/156856204323046852.

[56]   J.K. Chinthaginjala, L. Lefferts, Support effect on selectivity of nitrite reduction in water, Appl. Catal. B Environ. 101 (2010) 144–149. https://doi.org/10.1016/j.apcatb.2010.09.023.

[57]   B.A. Humphreys, S.W. Prescott, T.J. Murdoch, A. Nelson, E.P. Gilbert, B. Webber,

E.J. Wanless, Influence of molecular weight on PNIPAM brush modified colloidal silica particles †, Soft Matter. (2019) 55–64. https://doi.org/10.1039/c8sm01824c.

[58]   H.B. Schlegel, A theoretical study of ascorbic acid oxidation and HOO/O2- Radical scavenging, Org. Biomol. Chem. 15 (2017) 4417–4431. https://doi.org/10.1039/c7ob00791d.

[59]   G. Greczynski, L. Hultman, X-ray photoelectron spectroscopy: Towards reliable binding energy referencing, Prog. Mater. Sci. 107 (2020) 100591. https://doi.org/10.1016/j.pmatsci.2019.100591.

[60]   V. Höller, K. Rådevik, I. Yuranov, L. Kiwi-Minsker, A. Renken, Reduction of nitrite-ions in water over Pd-supported on structured fibrous materials, Appl. Catal. B Environ. 32 (2001) 143–150. https://doi.org/10.1016/S0926-3373(01)00139-4.

[61]   A. Pintar, G. Berčič, J. Levec, Catalytic liquid-phase nitrite reduction: Kinetics and catalyst deactivation, AIChE J. 44 (1998) 2280–2292. https://doi.org/10.1002/aic.690441017.

[62]   S.D. Ebbesen, B.L. Mojet, L. Lefferts, A. No, N.H. Oh, P. Al, P. Al O, In Situ Attenuated Total Reflection Infrared (ATR-IR) Study of the Adsorption of NO , NH OH , and NH on Pd / Al O and Pt / Al O In Situ Attenuated Total Reflection Infrared (ATR-IR) Study of the, (2008) 869–879.

[63]   S.D. Ebbesen, B.L. Mojet, L. Lefferts, Mechanistic Investigation of the Heterogeneous Hydrogenation of Nitrite over Pt/Al 2 O 3 by Attenuated Total Reflection Infrared Spectroscopy, J. Phys. Chem. C. 113 (2009) 2503–2511. https://doi.org/10.1021/jp8081886.

[64]   A. V. Pipa, J. Ropcke, Analysis of the mid-infrared spectrum of the exhaust gas from an atmospheric pressure plasma jet (APPJ) working with an argon-air mixture, IEEE Trans. Plasma Sci. 37 (2009) 1000–1003. https://doi.org/10.1109/TPS.2009.2013865.

[65]   K.I. Hadjiivanov, Identification of neutral and charged NxOy surface species by IR spectroscopy, Catal. Rev. - Sci. Eng. 42 (2000) 71–144. https://doi.org/10.1081/CR-100100260.

[66]   Y. Zhao, J.A. Baeza, N. Koteswara Rao, L. Calvo, M.A. Gilarranz, Y.D. Li, L.

Lefferts, Unsupported PVA- and PVP-stabilized Pd nanoparticles as catalyst for nitrite hydrogenation in aqueous phase, J. Catal. 318 (2014) 162–169. https://doi.org/http://dx.doi.org/10.1016/j.jcat.2014.07.011.

[67] D. Shuai, J.K. Choe, J.R. Shapley, C.J. Werth, Enhanced activity and selectivity of carbon nanofiber supported Pd catalysts for nitrite reduction, Environ. Sci. Technol. 46 (2012) 2847–2855. https://doi.org/10.1021/es203200d.

[68] C.M. Mendez, H. Olivero, D.E. Damiani, M.A. Volpe, On the role of Pd β-hydride in the reduction of nitrate over Pd based catalyst, Appl. Catal. B Environ. 84 (2008) 156–161. https://doi.org/10.1016/j.apcatb.2008.03.019.

[69] Y. Yoshinaga, T. Akita, I. Mikami, T. Okuhara, Hydrogenation of nitrate in water to nitrogen over Pd-Cu supported on active carbon, J. Catal. 207 (2002) 37–45. https://doi.org/10.1006/jcat.2002.3529.

[70] G. Li, B. Wang, D.E. Resasco, Water-Mediated Heterogeneously Catalyzed Reactions, ACS Catal. 10 (2020) 1294–1309. https://doi.org/10.1021/acscatal.9b04637.

[71] B.P. Adrados, I.Y. Galaev, K. Nilsson, B. Mattiasson, Size exclusion behavior of hydroxypropylcellulose beads with temperature-dependent porosity, J. Chromatogr. A. 930 (2001) 73–78. https://doi.org/10.1016/S0021-9673(01)01142-6.

[72] S. Wang, B. Jing, Y. Zhu, Molecule motion at polymer brush interfaces from single-molecule experimental perspectives, J. Polym. Sci. Part B Polym. Phys. 52 (2014) 85–103. https://doi.org/10.1002/polb.23414.

Chapter 4

The onset of mass transport limitations triggers the stimulus responsiveness of polymer coated catalysts

Abstract

A series of Pd/Al$_2$O$_3$ catalysts coated with N-isopropylacrylamide polymer (p-NIPAM) brushes with increasing particle size of the support were prepared to study the interplay between mass transport limitations and the ability of the thermo-responsive catalysts to modify reactivity during reaction. Nitrite hydrogenation in water was chosen as probe reaction, which is a key step in the reduction of nitrites and nitrates from drinking water. The results show that the apparent activation energy decreases on increasing temperature above the LCST, i.e. the temperature where the polymer undergoes a phase change, for catalyst with particle sizes between 38 and 100 μm, alluding to a significant increase in mass transfer limitations. In sharp contrast, both p-NIPAM modified catalysts with smaller particle size and uncoated catalysts do not show this change in activation energy with temperature. Detailed multi-physics mass transport and reaction modelling indicated that the transport of the limiting reagent, hydrogen in this case, is severely reduced when the p-NIPAM collapses at temperatures above its LCST. It is concluded that effective reaction control using stimulus-responsive polymers requires the system to be close to the mass transport limitation regime, to maximize the effect of the conformation change of the polymer on the catalyst performance and achieve sharp and reversible transitions from active to inactive.

4.1   Introduction

Combining catalytic materials with stimulus-responsive polymers has led to the development of hybrid organic-inorganic catalysts with temperature, pH, magnetic, and light responsiveness.[1–5] These so-called "bio-inspired" polymers can reversibly change their conformation from swollen to collapsed states as a response from an external stimulus. The most widely studied thermo-responsive polymer is poly-n-isopropyl acrylamide (p-NIPAM), which is soluble in aqueous environments below 32 °C (low critical solubility point, LCST).[6,7] At low temperatures the Gibbs free energy of the polymer in liquid water is primarily dominated by the H-bonding between the -NH motive in the polymer chains and water molecules, facilitating the stabilization of large quantities of water inside the polymer matrix with the concomitant entropy loss upon transfer. As temperature increases above the LCST the hydrogen bonds are destabilized and the Van der Waals forces between polymer-chains start to dominate the Gibbs free energy of the system, leading to the collapse of the polymer into a globular-like structure. [8]

This conformational change of the polymer can be used to alter the molecular transport of reactive species, when these brushes are coated on a catalyst metal nanoparticle creating so-called "stimulus-responsive nano-reactors". That is that the catalyst activity is altered depending on the polymer conformational state.[9–14] Here, it has been shown that at temperatures above the LCST lower reaction rates are obtained. This was attributed to lower effective diffusion coefficient of the reactants through the collapsed p-NIPAM layer. This behavior has been described by M. Ballauff and J. Dzubiella as two resistances in series that included the reaction kinetics and mass transfer.[13,15–18] Here, the authors argued that the observed kinetics are dominated by mass transfer at temperatures above the LCST, while the measured activity was assumed to be the same as that of the uncoated catalyst at temperatures below the LCST. Extrapolating this concept to a porous heterogeneous catalyst, however, is not straight forward. Recently, we demonstrated that even at low temperatures the polymer can influence the catalyst selectivity by inducing changes in the binding energy of surface reaction intermediates. This indicated that when the polymer is in close proximity to the active site the surface chemical activity is modified, leading to changes in the reaction kinetics. (see **Chapter 3**) Furthermore, the transport of molecules through polymer coated pores is strongly linked to the solubility of the diffusing species in the p-NIPAM, pore geometry, and available volume for diffusion. In fact, detailed transport studies using in-situ ATR-IR spectroscopy of CO in model polymer-

membrane-catalyst assemblies (PCMA), based on p-NIPAM, revealed that at low temperatures a long induction time is observed in the transport of CO through the polymer, due to the absorption of the probe molecule in the polymer brush. (see **Chapter 2**) This led to long saturation times, when compared to the experiments conducted at temperatures above the LCST (> 32 °C). Here, the interplay between solubility of CO in p-NIPAM and effective diffusion was key to rationalize these results.

In this context, one can envision that the measured reaction kinetics in a polymer-coated porous catalyst will be the result of entangled transport and reaction kinetics, especially if the polymer brushes are grown on both the external and internal surfaces. Here, one can anticipate two extreme cases. In one scenario, the size of the support catalyst particle could be sufficiently small to allow fast molecular diffusion inside the particle at temperatures below and above the LCST of p-NIPAM (32 °C), resulting in a non-stimulus-responsive polymer-coated catalyst. That is that the responsive behavior of the catalyst at low and high temperatures is absent. On the other extreme, at large enough support particle sizes the onset of mass transfer limitations could accentuate the impact of the polymer transition from swollen to collapsed state on the observed molecular diffusion, leading to the responsive behavior reported in the literature for stimulus-responsive nanoreactors.

To challenge this concept, we have studied the interplay between the support particle size of Pd-Al_2O_3 catalyst rendered with p-NIPAM polymer brushes and the nitrite hydrogenation reaction kinetics as a function of temperature. This reaction is characterized by fast kinetics even at low temperatures, making this system ideal to study the effect of thermo-responsive polymeric brushes on the catalytic performance of supported Pd clusters. In this reaction, nitrite reacts with hydrogen to form either dinitrogen or ammonia. Finding catalysts that can conduct this reaction in a selective manner is key for the purification of drinking water polluted with nitrite and nitrate as ammonia toxicity is higher than that of the nitrites.[19,20] Our results show that polymer-coated catalysts with small (0-38 μm) particle size do not display stimulus-responsive behavior. Strikingly, when the catalyst particle size was moderately large (38-100 μm) it was possible to observe a thermo-switchable response. Here, an inflexion point in the Arrhenius plot was observed at the LCST of p-NIPAM, where at low temperatures the apparent activation barrier was higher than that obtained above the LCST. By combining experimental reaction rates with multi-physics modelling, we demonstrate that in

polymer-coated porous catalysts the onset of moderate internal mass transport limitations is a pre-requisite for the polymers to induce thermo-responsive behavior on the catalyst.

4.2   Materials and methods

4.2.1   Materials

For the catalyst synthesis gamma alumina support (γ-Al_2O_3) was obtained from BASF (Al 3992E 1/8"). Palladium precursor tetra-amine-palladium (II) nitrate solution (10 wt. % in H2O, 1360-08-6), sodium nitrite (99.99 %, 7632-00-0), ammonium (25 % v/v water, 1336-21-6) were obtained from Sigma-Aldrich. For the polymerization N-isopropylacrylamide (NIPAM, 97 %, 2210-25-5), 3-aminopropyltriethoxysilane (APTES, 99 %, 919-30-2), trimethylamine (Eth3N, 99 %, 75-5-3), α-bromoisobutyrylbromide (BIBB, 98 %, 20769-85-1), copper (II) bromide ($CuBr_2$, 99 %, 7789-45-9), 1,1,4,7,10,10-hexamethyltriethylenetetramine (HMTETA, 97 %, 3083-10-1), L-ascorbic acid (99 %, 50-81-7) were also obtained from Sigma-Aldrich. The solvents n-hexane (99.4 %, 110-54-3), tetrahydrofuran (THF, 109-99-9), ethanol (64-17-5) and methanol (67-56-1) were obtained by Merck. The molecular sieves (4Å, 4-8 mesh, 70955-01-0) used to dry THF were procured from Honeywell. All the aqueous solutions were prepared using ultra purified water obtained from a water purification system (Millipore, Synergy).

4.2.2   Catalyst preparation

4.2.2.1 Palladium supported on alumna synthesis

Palladium on alumina catalyst was prepared by wet impregnation, the method was described in **Chapter 3**. After synthesizing the Pd/Al_2O_3 with a particle size of 0-38 µm, part of the Pd/Al_2O_3 powder was pressurized at 400 bar for 2 min in a cold isostatic press. The pressurized pellet was broken and sieved to obtain samples with particles 38-100 µm. The catalyst with particle size in the range of 0-38 µm was labelled S (small) and particles in the range of 38-100 µm were labelled L (large).

4.2.2.2 Polymer brushes growth on Pd/Al_2O_3

Poly(n-isopropylacrilamide) (p-NIPAM) was chemically bonded to Pd/Al_2O_3 catalyst surface via atom transfer radical polymerization (ATRP) method, where the two different

particle sizes (0-38 and 38-100 μm) were polymerized in different batches. The polymerization was made on a bromide functionalized Pd/Al_2O_3 catalyst, where the reactants NIPAM/$CuBr_2$/HMTETA/ ascorbic acid in the molar ratios 900/1.5/15/10 were dissolved in a solvent mixture of methanol/ water (4: 1 v/v). For more details see **Chapter 3**.

4.2.3 Catalyst characterization

For the details regarding characterization see **Chapter 3**.

4.2.4 Catalytic test

The experiments were performed in a semi-batch reactor (0.3 L) with continuous feed of gases (CO_2, H_2 and He) at atmospheric pressure. The pH was kept constant at 5.5 by continuous addition of 0.1 bar partial pressure of CO_2. The Pd/Al_2O_3 catalyst was reduced for 1 hour with hydrogen. Then, 3 mL of a specific concentration of $NaNO_2$ was added to the reactor, starting the reaction time. Samples were taken and analyzed by ion chromatography (IC). For more details regarding experimental procedure and reactor design refer to **Chapter 3**.

A typical experiment consisted of using a hydrogen concentration of 0.4 mol m^{-3} and NO_2^- concentration of 3 mol m^{-3}. Temperature was varied between 20 and 50 °C using a thermal bath controlled via feedback thermocouple placed in the reaction solution. The concentration of nitrite (NO_2^-) and ammonium (NH_4^+) ions were measured as a function of time. Figure S4.1 shows a typical experimental result for NO_2^- concentration (Figure S4.1a) and NH_4^+ concentration (Figure S4.1b) over time. By applying integral kinetics at several reaction temperatures and concentration of both reactants, it was possible to estimate the reaction orders, pre-exponential factors and activation barriers (Eq. 4.1).

$$c_{i,final} = nAe^{\frac{\pm E_{a,i}}{RT}}[c_{NO2}^t]^x[c_{H2}^t]^Y \Delta t + C_{i,initial} \qquad \text{Eq. 4.1}$$

Where $c_{i,final}$ is the final concentration of the specie i in the bulk, A the pre-exponential factor, $E_{a,i}$ is the activation energy barrier, R is the universal gas constant, T is the absolute

temperature, c_{NO2}^t is the bulk concentration of NO_2^- at time t, and c_{H2}^t is the bulk concentration of H_2 at time t, x the reaction order in NO_2^- and y the reaction order in H_2, Δt is the time interval, $c_{i,initial}$ is the initial concentration of the specie i in the bulk and n is 1 for the product ammonia, while n=-1 for the reactant NO_2^-. Here, the i species are NO_2^- and NH_4^+. Since The H_2 was continuously added to the system, $[c_{H2}^t]^Y$ was assumed to be constant. From the concentration profile of NO_2^- the reaction rate was determined using initial activity at 10 % NO_2^- conversion to regress the instantaneous reaction rate at time zero. To correctly compare the rates between different catalyst, the rates were normalized per surface atoms of palladium, resulting in a Turnover Frequency (TOF, min^{-1}), shown in Eq. 4.2. Here, the metal active sites were obtained by the metal particle size distribution measured by TEM characterization assuming that no polymeric brushes block the accessibility of the palladium active sites (see Section S4.7.2.3.).

$$TOF = \frac{[conversion\ rate\ NO_2^-]_t}{moles\ of\ Pd\ available} \qquad \text{Eq. 4.2}$$

The NO_2^- conversion and the integral NH_4^+ selectivity was calculated with Eq. 4.3 and 4.4, respectively.

$$NO_2^-\ conversion = \frac{[NO_2^-]_0 - [NO_2^-]_t}{[NO_2^-]_0} \times 100 \qquad \text{Eq. 4.3}$$

$$NH_4^+ = \frac{[NH_4^+]_t}{[NO_2^-]_0 - [NO_2^-]} \times 100 \qquad \text{Eq. 4.4}$$

Where $[NO_2^-]0$ is the initial nitrite concentration, $[NO_2^-]t$ concentration nitrite at time t, $[NH_4^+]t$ is the concentration of ammonium (mmol L^{-1}) at time t. Here, it is assumed that N_2 and ammonia are the only two products formed under these conditions. Thus, the selectivity to N_2 was calculated based on the mass balance.

The apparent activation barrier was calculated according to the Arrhenius equation (see Eq. 4.5).

$$ln(TOF) = -\frac{Ea}{R}\frac{1}{T} + ln(A)$$

Eq. 4.5

Where TOF (min⁻¹) is the normalized rate per mol surface-Pd, Ea (kJ mol⁻¹) the activation energy barrier, R (8.31 kJ mol⁻¹ K⁻¹) the universal gas constant, T (K) absolute temperature, and A the pre-exponential factor.

4.2.5 Modelling

The catalyst was described using a one-dimensional model based on electroneutral Nernst-Planck diffusion to understand the effect of the catalyst particle size and polymeric brushes on the transport of reactants and products inside. The mass balance inside of one porous catalyst particle assuming a spherical shape, where the concentration only varies in the radial direction, can be defined as shown in Eq. 4.6 (see Figure 4.1).

$$r^2 \frac{\delta c_i \varepsilon}{\delta t} = -\frac{\delta}{\delta r}\left(J_{r,i} r^2\right) + r^2 (\xi v)_i$$

Eq. 4.6

Where c_i (mol m⁻³) is the bulk concentration of the specie i, t (s) is the time, J (mol m⁻² s⁻¹) is the flux of the specie i, r (m) is the radius of the particle, ε is the porosity of the catalyst, ξ is the stoichiometric factor of the reaction and v (mol m⁻³ s⁻¹) is the reaction rate per catalyst particle volume of the specie i. [22]
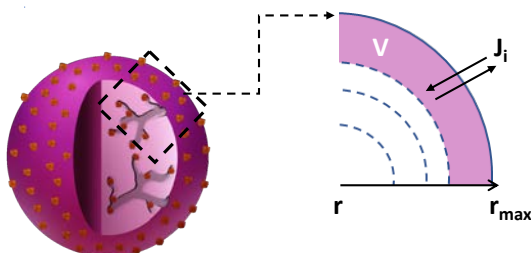

Figure 1: Schematic representation from the 3D particle to the 1D model where the catalyst particle is discretized in volumes (ΔV), r represents the planar direction from the

center of the particle (r=0) until the maximum radius of the particle (r=r_{max}) and J_i is the flux of species.

The model calculates the transport of the reactants and products of the nitrite hydrogenation reaction from the surface of the particle (r_{max}) until the centre of the particle (r=0) over time. As reported previously in **Chapter 3**, no external mass transfer limitations were encountered when performing reaction experiments at a agitation rate of 500 RPM. Consequently, the bulk concentration (c_b) inside the batch reactor was assumed to be the same as that of the catalyst surface (C_S). This results in the two boundary conditions shown in Eq. 4.7-8.
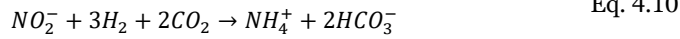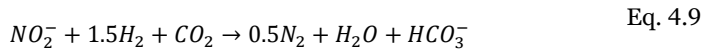
$$r = 0; \qquad \frac{\delta c}{\delta r} = 0$$

Eq. 4.7

$$r = r_{max}; \qquad \left\{ \begin{array}{ll} \frac{\delta c_b}{\delta t} = J_{n,i}, & c_b = c_s \\ c_b = c_{i,initial}, & c_b = c_s \end{array} \right.$$

Eq. 4.8

Here, the c_b was defined as the initial concentration of specie i when reactants were continuously feed to the reactor, such as H_2 and CO_2. Meanwhile, for those species whose concentration changes over time, the bulk concentration is normalized by the flux of the total number of particles present in the reactor, $J_{n,i}$ (see Section S4.7.5.1.).

4.2.5.1 Reaction rate

The two parallel reactions of nitrite hydrogenation were identified as shown in Eq. 4.9-10 (see Section S4.7.5.2.). Changes in the concentration of protons were negligible due to the continuous addition of CO_2. Since the CO_2 hydrolysis reaction to carbonic acid and the subsequent deprotonation rates were c.a. 23 times faster than the conversion of NO_2^-, while diffusion coefficients are similar (see Section S4.7.5.4.), one can consider that reaction of CO_2 with water is not a limiting factor as a sufficiently high flux of protons can be generated as the reaction evolves (see Section S4.7.5.3.). In addition, the H_2CO_3/HCO_3^- buffer is preventing internal pH gradients.

$$NO_2^- + 1.5H_2 + CO_2 \rightarrow 0.5N_2 + H_2O + HCO_3^-$$

<div align="right">Eq. 4.9</div>

$$NO_2^- + 3H_2 + 2CO_2 \rightarrow NH_4^+ + 2HCO_3^-$$

<div align="right">Eq. 4.10</div>

The rate of nitrite hydrogenation was defined as shown in Eq. 4.11 (mol m^{-3} s^{-1}). Here, f is the reaction factor used to convert the units from rate per reactor volume to rate per catalyst particle volume, as defined in Eq. 4.6 (see Section S.4.7.5.2.), k_i is the kinetic constant, c_{NO2} is the bulk concentration of NO$_2^-$, c_{H2} is the bulk concentration of H$_2$, x is the reaction order of NO$_2^-$ and y the reaction order of H$_2$. Here, one must be aware that this reaction kinetics can only be used to interpolate the reaction rates within the reaction operational window herein studied.

$$v_i = fk_i[c_{NO2}]^x[c_{H2}]^y$$

<div align="right">Eq. 4.11</div>

4.2.5.2 Transport in the catalyst particle

The diffusion of molecules inside the catalyst particle was assumed to follow Fick's law. Here, it is key to consider the mobility of ions in solution to ensure electroneutrality since the reduction of nitrite is dominated by charged species (e.g. H$^+$, NO$_2^-$, and NH$_4^+$) and no electrical potential is externally applied over the system. To account for the effect of the electric field arising from the charged species on the diffusion, the Fick's law was expanded into the Nernst Planck equation, as shown in Eq. 4.12 (see Section S4.7.5.4.). [23,24]

$$J_i = -D_{i,eff}\left(\frac{\delta c_i}{\delta r} + z_i c_i \frac{\sum_1^j z_j D_{i,eff} \frac{\delta c_i}{\delta r}}{\sum_1^j (z_j^2 c_j D_{j,eff})}\right)$$

<div align="right">Eq. 4.12</div>

Where J is the flux of the specie i (mol m^{-2} s^{-1}), c is the bulk concentration (mol m^{-3}), r is the particle radius (m), $D_{i,eff}$ is the effective diffusion coefficient in the catalyst particle (m^2 s^{-1}) and z_i is the elementary charge.

Pd/Al$_2$O$_3$ catalyst

The effective diffusion coefficient of a molecule in the porous bed was defined as Eq. 4.13. Here, D$_i$ is the diffusion coefficient of the specie i in water at infinite dilution (m^2 s^{-1}), ε is the catalyst porosity obtained from N$_2$ physisorption. The tortuosity (τ) was calculated by the empirical correlation between τ and ε (τ = 1-ln(ε)). In this domain, the porosity and tortuosity were assumed to be constant throughout the catalyst particle with the values of 0.70 and 1.40, respectively.

$$D_{i,eff} = D_i \frac{\varepsilon}{\tau}$$

Eq. 4.13

The molecular diffusion (D$_i$) of the different reaction species was obtained using the Stokes-Einstein relation [25,26], see Eq. 4.14, assuming the molecule as a spherical suspended particle and neglecting any influence of the solvation effects between water and ions [27–29]. Here, k$_b$ is the Boltzmann's constant (1.38x10^{-23} kg m^2 s^{-2} K^{-1}), T is the absolute temperature (K), η is the dynamic viscosity (kg m^{-1} s^{-1}) and R is the radius of the particle (see Section S4.7.5.4.).

$$D_i = \frac{k_b T}{6 \pi \eta R}$$

Eq. 4.14

P-NIPAM Pd/Al$_2$O$_3$ catalyst

The transport through a catalyst with polymeric brushes inside the pores was defined as a summation of resistances either in parallel (Eq. 4.15) or series (Eq. 4.16), where the contribution from the polymer brushes was defined as Eq. 4.18 and the contribution from the catalyst was defined as Eq. 4.19. Since the polymer distribution at the catalyst surface and pores was considered to be homogeneous one could imagine two possible scenarios. In the first one, the polymer occupies the volume close to the pore walls, leaving water-filled volume completely available for diffusion. This would lead to resistances in parallel, where the molecules can take the path with least resistance. In the second one, the effective diffusion coefficient will be the result of resistances in series in which the molecules have to penetrate a polymer layer at pore constrictions, completely filled with polymer, before

entering a pore where resistances in series are then dominant as only the pore walls are coated with the polymer. This would lead to a combination of resistances in series and parallel (see Eq. 4.17).

$$D_{i,eff}^{total,p} = D_{i,eff}^{p-nipam} + D_{i,eff}^{m}$$

Eq. 4.15

$$\frac{1}{D_{i,eff}^{total,s}} = \frac{1}{D_{i,eff}^{p-nipam}} + \frac{1}{D_{i,eff}^{m}}$$

Eq. 4.16

$$D_{i,eff}^{total,c} = x\, D_{i,eff}^{total,p} + (1-x)\, D_{i,eff}^{total,s}$$

Eq. 4.17

$$D_{i,eff}^{p-nipam} = D_{i}^{p-nipam}\, \frac{\varepsilon}{\tau} V_{x,p}(T)$$

Eq. 4.18

$$D_{i,eff}^{m} = D_{i}\frac{\varepsilon}{\tau}(1 - V_{x,p}(T))$$

Eq. 4.19

Here $D_{i,eff}^{total}$ is the total diffusion coefficient ($m^2\ s^{-1}$) of the specie i for the resistance in parallel (p), series (s) and combined (c), $D_{i,eff}^{m}$ is the effective diffusion coefficient of the catalyst filled with water in the absence of polymer brushes ($m^2\ s^{-1}$), $D_{i,eff}^{p-nipam}$ the effective diffusion coefficient in the polymer layer grown on the support surface ($m^2\ s^{-1}$), $D_{i}^{p-nipam}$ is the diffusion of CO through the polymeric brushes ($m^2\ s^{-1}$), $V_{x,p(T)}$ is the volume fraction of polymer in the catalyst pore and x fraction of pores defined as parallel.

The diffusion of the solute in thermo-responsive polymeric brushes was defined as a piecewise function, as shown on Eq. 4.20. Here, $\varphi_{p-NIPAM}$ is the p-NIPAM volume fraction, φ_{LCST} is the p-NIPAM volume fraction at the transition temperature (~32 °C), aw is the Stokes hydrodynamic radii in pure water (nm) and λ the decay length constant (nm). The Mackie and Mears [30] model was used to describe the system below the transition polymer density and the hopping mechanism developed by Kanduc et al.[31] above φ_{LCST} (see Section S4.7.5.5.) For more details see **Chapter 2**.

Eq. 4.20

$$\frac{D_i^{p-NIPAM}}{D_i} = \begin{cases} \left[\dfrac{1 - \Phi_{p-NIPAM}}{1 + \Phi_{p-NIPAM}}\right]^2 , & \Phi_{p-NIPAM} < \Phi_{LCST} \\ e^{\frac{-a_w}{\lambda}} , & \Phi_{p-NIPAM} = \Phi_{LCST} \end{cases}$$

Bulk concentration and rate

The obtained bulk concentration of NO_2^- and NH_4^+ were used to estimate the initial reaction rate. To correctly compare the rates between different catalyst, the rates were normalized per surface atoms of palladium (TOF).

4.3 Experimental results and discussion

4.3.1 Catalyst characterization

As reported previously in **Chapter 3**, BET analysis of the N_2-physisorption data showed that the addition of chemically bonded polymer brushes reduces the support surface area and pore volume. This observed trend was attributed to the partial pore entrance blockage in the dry state. As shown in Table 4.1, the same result was observed upon the increase of catalyst particles from 0-38 μm, designated small ("S"), to 38-100 μm, designated large ("L") (see Section 4.7.2.1.). The thermal stability of p-NIPAM brushes was studied via thermal gravimetric analysis (see Section S4.7.2.2.). Above 350 °C a significant weight loss was observed on the polymer coated catalysts samples for both small and large particles. This can be attributed to the decomposition of p-NIPAM brushes in air.

Table 4.1: Specific surface area and pore volume from Brunauer-Emmett-Teller (BET) method from N_2-physisorption at -196 °C, carbon content from elemental analysis (EA), palladium loading obtained from XRF characterization, palladium particle size and dispersion obtained from STEM-HAADF. The catalyst with particle size 0-38 μm and 38-100 μm was assigned S and L, respectively. Dispersion calculated based on TEM as shown in Section S4.7.2.3.

Pd/Al_2O_3 catalysts	Carbon (wt. %)	Specific surface area ($m^2\,g^{-1}$)	Pore volume ($cm^3\,g^{-1}$)	Pd loading (%)	Pd diameter TEM[c] (nm)	Dispersion (%)
S&L 0 wt. % Ca	0	193	0.65	2.9	3.3 ± 1.6	34
S 20 wt. % Ca	20	104	0.23	1.6	4.6 ± 1.7	24
L 20 wt. % C	21	95.7	0.18	1.4	4.2 ± 2	26

a: For more details refer to **Chapter 3**. c: Presented values correspond to the average Pd particle size and the width distribution as shown in Figure S4.3a-c iii.

As it can be noted in Table 4.1, the polymer coated catalysts have lower metal loadings independent of the catalyst particle size. In comparison with the uncoated catalyst, the loading decreased to 1.6 and 1.4 % for 20 wt. % C Pd/Al_2O_3 catalyst with small and large particle size, respectively. Note that the characteristics of the uncoated catalyst will remain constant regardless of the particle size, because the support was loaded with palladium before pelletizing followed by crushing and sieving into the desired support particle size. However, Pd loading was influenced upon addition of polymeric brushes, as explained in our earlier publication in **Chapter 3**. The p-NIPAM radical polymerization process caused a drop in the metal loading due to the partial dissolution of small metal clusters (see **Chapter 3**).

STEM-HAADF and EDS mapping characterization were conducted to determine the palladium nanoparticles distribution. As shown in Figure S4.3, the Al_2O_3 support has palladium nanoparticles well distributed on the surface, regardless of the polymer addition. The average particle size obtained was 3.3 nm for the uncoated catalyst. The coated catalyst shifted towards larger palladium particles to 4.6 and 4.2 nm for 20 wt.% C Pd/Al_2O_3 catalyst for small and large particles, respectively. Consequently, polymer coated

catalysts have lower catalyst dispersion compared to uncoated catalyst due to the partial dissolution of small metal clusters (see Table 4.1).

Elemental composition of the catalyst surface according XPS indicated that nitrogen and carbon were present on the catalyst surface for both small and large particle sizes (see Table S4.2). In addition, the palladium binding energies obtained from XPS show that palladium electronic configuration is in the metal form regardless the presence of polymer at the support surface (see Section S.4.7.2.4.).

4.3.2   Arrhenius plot

In this section, the effect of catalyst particle size on nitrite hydrogenation was investigated for both uncoated and p-NIPAM coated Pd/Al$_2$O$_3$ catalysts (Figure 4.2). Particles smaller than 38 μm (S) operate in the kinetic regime based on our previous work on **Chapter 3** (see Section S4.7.3.). As a result, there is no effect on the NO$_2^-$ rate by the addition of polymeric brushes into the catalyst surface (see Figure S4.8). In sharp contrast, when large particles (38-100 μm) are employed the mass transfer limitations start to control the reaction rate, as shown by the lower reaction rate per quantify of actives sites. In this case, an inflexion point is observed in the in the Arrhenius plot for the catalyst with polymer. This change in the temperature dependence of the rate was absent in the uncoated catalyst. Notably, this inflexion point was located just at the Low Critical Solubility Temperature (LCST) of the p-NIPAM.
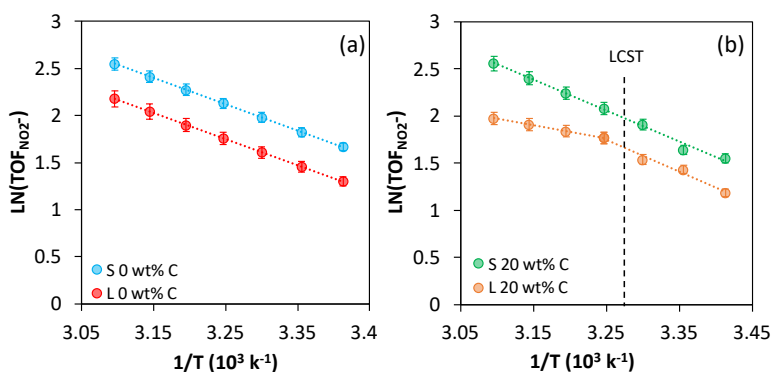

Figure 4.2: Arrhenius plots for NO$_2^-$ for uncoated Pd/Al$_2$O$_3$ catalyst with small and large particles (a) and p-NIPAM coated Pd/Al$_2$O$_3$ catalyst with small (0-38 μm) and large

(38-100 µm) particles (b) at 3 mM NO_2^-, 0.5 bar H_2, 0.1 bar of CO_2, at agitation rates of 500 rpm from 20 to 50 °C. Data shown at small particle size for both coated and uncoated Pd/Al_2O_3 was published previously in **Chapter 3.**

In contrast to results reported for nano-reactors [14,32–34], the observed rate was not lower at temperatures above the LCST. Instead, increasing the temperature simply caused a decrease of the apparent activation energy barrier indicating the presence of more severe mass transfer limitations in comparison with uncoated catalyst. Since the polymer swelling occurs at lower temperatures, one could envision that this would lead to lower apparent activation energy barriers due to the higher degree of filling of the pores by the polymeric brushes compared to higher temperatures. However, it was observed the opposite, an alternative explanation for the observed trend would be that the polymer collapse causes blockage of catalyst pores, hindering molecular diffusion (see Figure 4.2b).

4.4   Modelling results and discussion

In the following section, we detail the results from a multi-physics model aimed at providing new insights on the observed trends of reaction rates for both uncoated and p-NIPAM coated catalysts with increasing particle size. Here, the kinetic data was regressed using the integral method considering the complete reaction time, more details considering the regression can be found in Section 4.2.4. The parity plots showing the goodness of the regression can be found in Section S4.7.4. The parity plots show the quality of the fit of the concentrations over time of NO_2^- and NH_4^+ (Figure S4.1 shows an example of one single experiment) obtained from the experimental and model data. Here, the different colors represent different experimental conditions.

4.4.1   Uncoated Pd/Al$_2$O$_3$ catalyst

First, intrinsic kinetics of the catalyst, such as kinetic constant and reaction orders for nitrite and ammonia, were determined using the results for the uncoated catalyst with particle size of 0-38 µm. The obtained reaction orders of NO_2^- and H_2 for nitrite hydrogenation are 0.1 and 0.5, respectively (see Section S4.7.4.4), which are in good

agreement with previous work in **Chapter 3**. As reported by P. Xu [35], the reaction orders are constant in the concentration window used and therefore integral kinetics based on these reaction orders can be safely applied. On the other hand, the reaction rate based on the integral description is somewhat lower than the initial activity at a low NO_2^- conversion (see Table S4.7). This suggest that the products formed or protons consumed influence the reaction rate. The obtained kinetic values were used as an input in the electroneutral Nernst-Planck reaction-diffusion model, details can be found in Section S4.7.4.4.

To study the effect of mass transfer limitations on the reaction, the catalyst particle size was increased from 0-38 μm to 38-100 μm. The change of particle size was incorporated to the calculation of the reaction kinetics, assuming a Gaussian distribution of the particle size resulting in an average particle size of 69 μm for the larger particles.

The quality of the fit from both kinetics and mass transfer limitation regime can be found in Figure S4.13a. As it can be noticed, the one-dimensional model predicts the NO_2^- concentrations well, independent of the catalyst particle size. At the same time, NH_4^+ concentrations were more dispersed. This larger discrepancy between the experimental and predicted values for ammonia was attributed to the larger error associated to the small values of the experimentally measured concentrations (see Figure S4.13b).

The concentration profiles inside the catalyst particle are calculated with the one-dimensional model of the coated catalyst. As can be noticed in Figure 4.3a, the concentration of NO_2^- and H_2 slightly decreased as a function of the radius when the catalyst with the small particles were employed (0-38 μm). As expected, the concentration profile inside the larger particles (38-100 μm) was rather pronounced (Figure 4.3b). In particular, the H_2 profile was more pronounced than that of NO_2^-. While the diffusion coefficient of H_2 is significantly larger than that of NO_2^- (see Figure S4.10), the H_2 concentration is 7.5 times lower than the NO_2^- concentration and the stoichiometry of the reaction (NO_2^-/H_2) is between 2/3 and 1/3, depending on the selectivity to ammonia. Consequently, a stronger H_2 concentration gradient develops. As a result, only part of the catalyst particle was actively contributing to the reduction of NO_2^- (see Figure 4.3bii) for the large particles (38-100 μm). Similar observations on mass transfer limitations upon increasing the particle size haves been previously reported by P.Xu et al. [36]. Notably, increasing temperature led to very minor changes in the nitrite concentration profiles (see

Figure 4.3i), while in the case of hydrogen a more significant drop in the concentration was observed (see Figure 4.3ii). The concentration profile of the other species involved in the reaction can be seen in Section S4.7.5.7, indicating that hydrogen mass transfer rates are affected in a greater extent than those of the CO_2, NH_4^+, N_2, and HCO_3^-.
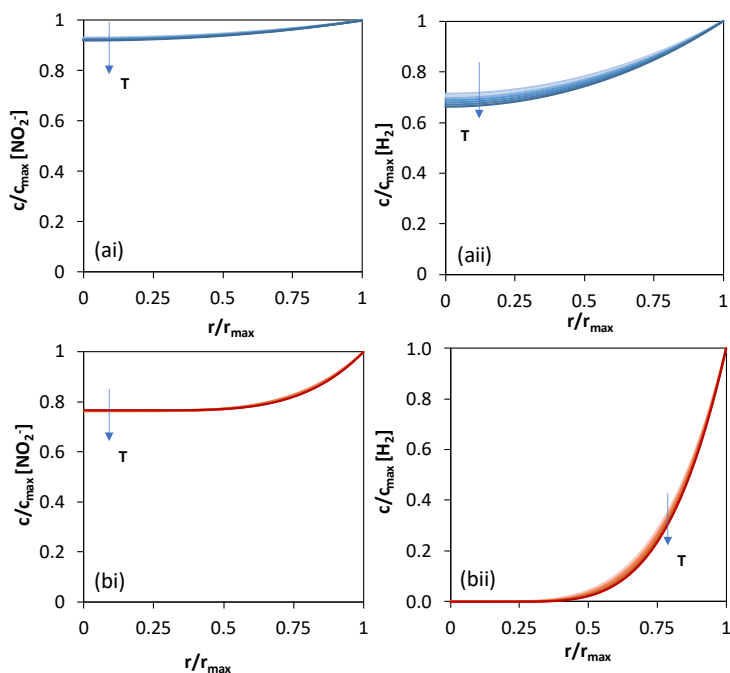

Figure 4.3: Concentration profile inside the catalyst particles for NO_2^- (i) and H_2 (ii) for uncoated Pd/Al_2O_3 catalyst with 0-38 μm (a) and 38-100 μm (b) particle size at 10 % NO_2^- conversion level at 3 mM NO_2^-, 0.5 bar H_2, 0.1 bar of CO_2 at agitation rates of 500 rpm from 20 to 50 °C for light to darker colour, respectively. The arrow indicates the direction in which temperature increased.

4.4.2   P-NIPAM coated Pd/Al₂O₃ catalyst

Next, we extended the model to the p-NIPAM coated Pd/Al_2O_3 catalyst. The details regarding the regression of kinetic parameters can be found in Section S4.7.4.4. Here, the pores were assumed to be completely filled with p-NIPAM brushes in the swollen state (i.e. at temperatures below LCST). This assumption was supported by the large drop in the pore

volume when adding p-NIPAM according N_2-physisorption measurements (see Table 4.1), suggesting that the polymer filled a large fraction of the pores. Ellipsometry measurements of p-NIPAM polymer-grafted silicon wafers at low and high temperatures were employed to include the thermo-responsive behaviour of the polymer on the model the (see Section S4.7.5.5)[37], which allowed the introduction of thermo-responsive behaviour in the pore-volume at different temperatures.

As mentioned in section 4.2.5.2., the transport inside the p-NIPAM coated catalyst could be described as either (1) a system of resistances in parallel, where molecules can diffuse via the pathway of minimum resistance, or (2) a system with resistances in series at the pore-constrictions followed by resistances in parallel in the pores (see Eq. 4.17). A priori it is difficult to anticipate which of the two systems are dominant in the p-NIPAM coated catalyst. For this reason, a model was employed to interrogate the system and stablish the interplay resistances in series and parallel on the reaction rate.

4.4.2.1 Resistances in parallel

The transport inside the catalyst particle was assumed to be described by resistances in parallel, where the molecules can choose the pathway with the lowest resistance. As shown in Parity plots in Figure 4.4a-b, the one-dimensional model predicts the NO_2^- concentrations and NH_4^+ concentrations well for the small particle sizes on the p-NIPAM coated Pd/Al_2O_3 catalyst. Here, the concentration profile of NO_2^- and H_2 are similar to the concentration profiles for the uncoated catalyst (see Figure 4.3a and Figure 4.4c). Here, one could notice that already in the small particles (0-38 μm) the concentration profile for hydrogen was slightly more pronounced than that observed on the uncoated catalyst. This indicates that the presence of the polymer induced small changes on the mass transfer already in the small particles. Likewise, significant concentration profiles were obtained for CO_2, NH_4^+, N_2, and HCO_3^- (see Section S4.7.5.8.).
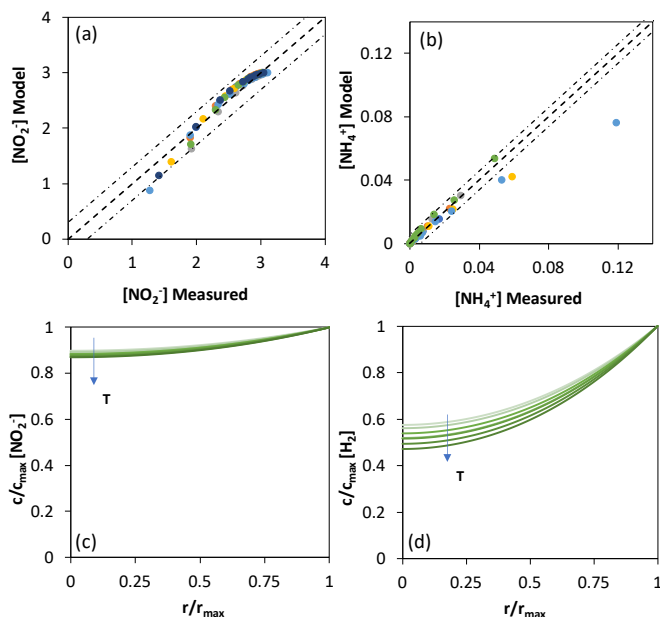
Figure 4.4: Parity plot of model results compared to experimental results obtained on the 0-38 μm p-NIPAM coated Pd/Al_2O_3 containing 100 % parallel resistance in the particle for NO_2^- concentrations (a), NH_4^+ concentrations (b), concentration profile inside the catalyst particles for NO_2^- (c) and H_2 (d) at 10 % NO_2^- conversion level using 3 mM NO_2^-, 0.5 bar H_2, 0.1 bar of CO_2 at agitation rates of 500 rpm. The arrow indicates the direction in which temperature increased. The different colours on (a) and (b) represent the different experiments (temperature and concentration)

Extrapolating this model to the large particles of p-NIPAM coated Pd/Al_2O_3 led to significant deviations. As shown in Figure S4.18, the inflexion point in the Arrhenius plot experimentally observed at c.a. 32 °C was absent when the model was employed. This suggests that the initial model considering exclusively resistances in parallel is insufficient to predict the impact of the p-NIPAM on the reaction kinetics above and below the LCST.

4.4.2.2 Combination of resistances in parallel and series

As schematically shown in Figure 4.5, the presence of a polymeric brush at pore constrictions could cause a blockage in the collapsed state of the polymers. In this case, the reactive species would have to diffuse through the polymers and/or the empty volume inside the pores in the collapse state of the polymer. To model such mechanism, one must consider resistances in series and parallel. Since it is difficult to experimentally measure the extent of pore constrictions it was decided to explore the impact of increasing the contribution of parallel resistances using a linear combination approach.
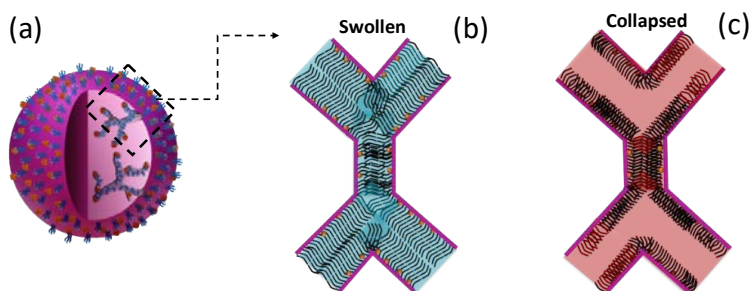

Figure 4.5: Schematic representation of the polymer growing inside the pores of a catalyst particle (a) in the swollen (b) and collapsed state (c), where in the presence of a constriction the collapse of the polymer creates a blockage of the catalyst pore.

Figure 4.6a shows the effect of increasing the contribution of the resistances in parallel on the Arrhenius plot for p-NIPAM coated catalyst with small particles. As can be noticed, the reaction rate significantly decreased while the change in the slope of the apparent activation energy barriers at 32 °C was rather moderate even when 30 % of resistance in parallel was employed (Figure 4.2). This indicates the transport rate in the coated catalysts with small particle size is not limiting.

Upon increasing the catalyst particle size, a more drastic drop in the reaction rate was observed with the increasing contribution of the resistance in series (see Figure 4.6b). Here, the reaction rate decreased substantially near the transition temperature of the p-NIPAM with at least 70:30 ratio series:parallel. This led to lower apparent activation

barriers at temperatures above the LCST of the polymer, suggesting that upon collapse of the polymer the TOF decreases to a lower value due to the changes in the mass transfer rates. These trends are qualitatively in line with the experimental apparent barriers as shown in Figure 4.7 (see Section S4.7.5.9. and 4.7.5.10.), indicating that larger particles and higher percentage of resistance in series are the cause for mass transfer limitations.
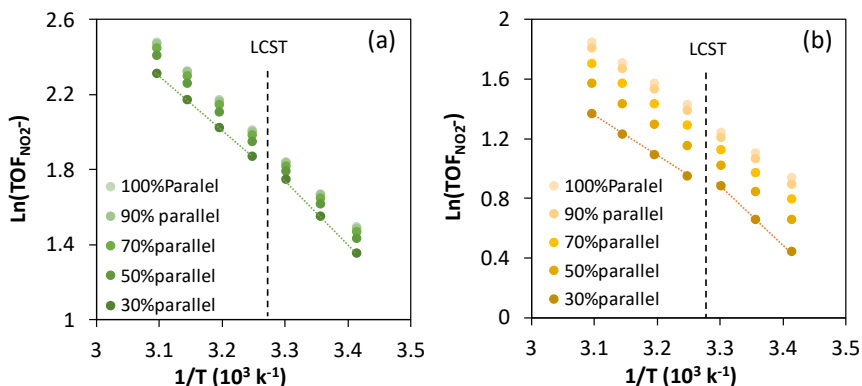
Figure 4.6: Arrhenius plots for NO_2^- for p-NIPAM coated Pd/Al$_2$O$_3$ catalyst with small (a) and large particles (b) obtained with different contributions between resistance in parallel and series, varied between 100% to 30 % parallel, at 3 mM NO_2^-, 0.5 bar H_2 and 0.1 bar of CO_2 from 20 to 50 °C.
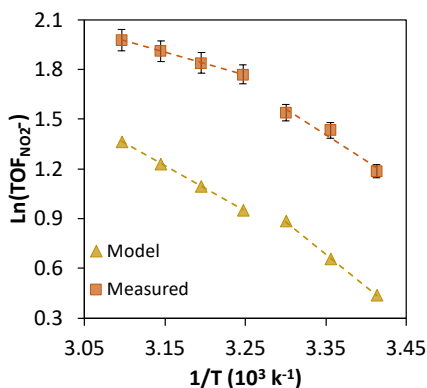

Figure 4.7: Arrhenius plots for NO_2^- for p-NIPAM coated Pd/Al$_2$O$_3$ catalyst with large particles assuming 30 % parallel at 3 mM NO_2^-, 0.5 bar H_2, 0.1 bar of CO_2, at agitation rates of 500 rpm from 20 to 50 °C.

At the same time, the shift of the Arrhenius curve to lower values suggests that the model underpredicts the reaction rates. This difference could arise from the use of initial rates to experimentally determine the reaction kinetics at different temperatures. At these conditions the absorption of nitrites in the polymer could lead to an overestimation of the nitrite disappearance, and thus the activity. Despite the simplifications implemented in our model, we have shown that the conceptual description of mass transport resistances in series and parallel is a reasonable approximation to the observed inflexion point on the activity of the polymer-coated catalysts at the LCST of p-NIPAM (see Figure S4.17). This suggests that the role of pore-topologies outcompetes that of the polymer-reactant interactions. More importantly, the fact that the difference in apparent barriers above and below the LCST becomes more pronounced as the particle size increases, indicating that partial internal mass transport limitations is a prerequisite for the induction of stimulus-responsive behaviour of the catalysts.

4.5 Conclusion

This contribution shows that the addition of thermo-responsive polymer brushes onto the surface of a porous heterogeneous catalysts can induce important changes in the observed reaction rates. We demonstrate that the reaction rate remained constant on coating p-NIPAM on Pd/Al_2O_3 catalysts, provided that mass transfer limitations are negligible by using small support particles. In contrast, when larger particles are employed, the p-NIPAM coating of the catalyst decreases the activity, resulting in a decreased apparent activation energy at temperatures above the LCST. This was attributed to the thermo-responsive character of the polymer. To describe the results, those changes were attributed to the polymer collapse at elevated temperatures causing a tandem effect on the molecular transport. On one hand, transport is enhanced due to the opening of the pore as the volume occupied by the polymer decreased in the collapsed state. And on the other, the molecular diffusion is hindered by the blockage of the pore constrictions. The reaction-diffusion model is able to describe the behaviour of the coated and uncoated catalysts when mass transfer limitations are not present. When using larger particle sizes, it was necessary to include the impact of pore constrictions in order to describe the occurrence of the inflexion point in the Arrhenius plot at the LCST of the p-NIPAM. Increasing the contribution of resistances in series, at the same time, led to the overprediction of the reaction rates, which is potentially due to the fast absorption of molecules on the polymer. The results suggest that the pore topology and the extent of pore constrains are key descriptors for the

development of switchable porous catalysts that are relevant for industrial applications. This knowledge will be key in the development of scalable catalysts with high surface area, functionalized with polymers that can rapidly switch ON/OFF in response to external stimuli, mimicking the self-regulating behaviour of living organisms.

4.6 Acknowledgments

Keywords: Nitrite reduction · Polymer-coated catalyst · Poly-n-isopropylacrylamide brushes · Mass transport, particle size effects, stimulus-responsive catalysts

4.7 Annexes
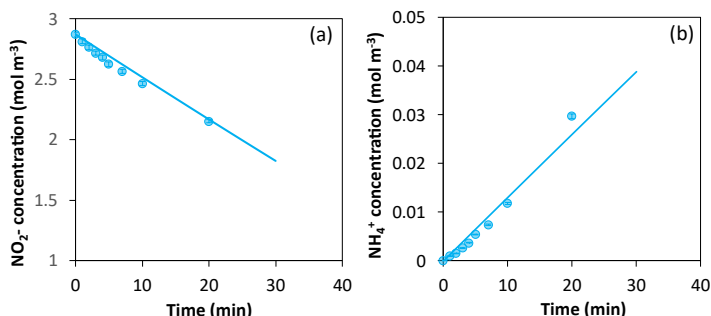
4.7.1 Palladium alumina experiment

Figure S4.1: Nitrite concentration over time on palladium alumina at 25 °C, 500 RPM, 3mM NO_2^-, 0.5 bar H_2 and 0.1 bar CO_2 (a) and ammonia concentration over time under the same conditions (b). The Line observed in the graph is obtained from the Eq. 4.1 based on integral kinetics.

4.7.2   Characterization

4.7.2.1 Estimation of p-NIPAM volume occupied in the catalyst

As reported previously in **Chapter 3** to estimate the volume of the polymer p-NIPAM brushes in the catalyst we employed the carbon content obtained from elemental analysis (see Table 4.1) and the p-NIPAM bulk density (1.1 g cm^{-3}) at 20 °C. Then, we employed the MW of P-NIPAM's monomer (N-isopropyl acrylamide) of 113.16 g mol^{-1} to obtain the final volumes per unit mass of catalyst using Eq. S4.1.

$$V_{P_{NIPAM\,Cat}}(\frac{cm^3}{g_{cat}}) = \frac{\%_{Carbon_{cat}} * MW_{N-IPA}}{MW_C * 6} * \frac{1}{D_{P-NIPAM}} \qquad \text{Eq. S4.1}$$

As shown in Table S4.1, the equivalent volume of polymer brushes per unit mass of catalyst was 0.3 cm^3 g^{-1} for Pd/Al$_2$O$_3$ containing 20 wt. % of carbon for both particle sizes S and L.

Table S4.1: Mass and volume fractions of equivalent polymer on the Pd/Al$_2$O$_3$ catalysts estimated based on the carbon content obtained by elemental analysis. Small particles data published previously **Chapter 3**.

Catalyst	Mass fraction of N-IPA	Volume of N-IPA (ml g$_{cat}$$^{-1}$)
S 0wt. %C	0	0
S 20wt. %C	0.3	0.3
L 20wt. %C	0.3	0.3

4.7.2.2 TGA

The resulting weight loss using TGA is comparable to the carbon content, obtained from elemental analysis. The aforementioned carbon content is equivalent to a polymer mass fraction of 32 and 34 wt.% for a Pd/Al$_2$O$_3$ catalyst coated with p-NIPAM with particle size

of 0-38 μm (S) and 38-100 μm (L), respectively, which is in good agreement with the mass losses herein observed above 350 °C.

Figure S4.2: Thermal gravimetric analysis (TGA) from 25 to 800 °C using synthetic air for the Pd/Al$_2$O$_3$ catalyst with 0-38 μm (S) containing 0 wt.% C (blue) and 20 wt.% C (green) and with 38-100 μm (L) containing 20 wt.% C (red). Blue and green data published previously **Chapter 3.**

4.7.2.3 STEM-HAADF characterization and Pd particle size

Figure S4.3(a-c)iii shows the metal particle size distribution obtained for STEM-HAADF characterization, where the sample with 0 wt. % carbon, 20 wt. % carbon for the small particles and 20 wt. % carbon for large particles obtained a metal particle size of 3.3, 4.6 and 4.2 nm, respectively. The mean metal particle size can be also obtained from CO chemisorption assuming uniform size distribution and a hemispherical shape (see Eq. S4.2-4). As reported previously **Chapter 3**, the palladium metal particle size based on CO chemisorption and on STEM-HAADF have similar values for the uncoated catalyst (Pd/Al$_2$O$_3$). In contrast, the metal particle sizes of the polymer coated catalysts (p-NIPAM-Pd/Al$_2$O$_3$) estimated from CO chemisorption had a higher metal particle size compared to the estimated from STEM-HAADF. These differences could be associated to partial coverage of the surface of metal nanoparticles as well as to pore-blockage in the dry state. These artifacts could mask CO-chemisorption underestimating the actual metal dispersion

of the catalyst in comparison to STEM-HAADF. For this reason, the turn of frequency will be based on the results from STEM-HAADF characterization.

Figure S4.3: STEM-HAADF characterization (i), palladium EDS mapping, where the purple plots represent the palladium particles (ii), and the metal particle size distribution (iii) of the pre-reduced Pd/Al$_2$O$_3$ catalyst containing 0 and 20 wt. % C with S and 20 wt. % C with L particle size distribution (a-c, respectively) based on 700 measured particles. Blue and green data published previously **Chapter 3**.

$$D = S_f \frac{V_{ads}}{V_g} \frac{Mw_{pd}}{\%M} \, 100\% \, 100\% \qquad \text{Eq. S4.2}$$

$$MSA = S_f \frac{V_{ads}}{V_g} \frac{100\%}{\%M} N_A \sigma_m \frac{1}{10^{18}} \qquad \text{Eq. S4.3}$$

$$d_{mean} = \frac{F_g}{\rho_{pd} MSA} \frac{1}{10^6} \frac{10^9}{1} \qquad \text{Eq. S4.4}$$

Here, D is the metal dispersion (%), S_f is the stoichiometric factor between CO and the metal (CO:Pd is 1:1), V_{ads} is the volume of CO adsorbed ($cm^3 g^{-1}$), Vg is the molar volume gas at STP equals to 22414 ($cm^3 mol^{-1}$), Mw_{pd} is the molecular weight of palladium equals to 106.4 ($g\ mol^{-1}$), %M is the metal loading (%), MSA is the active metal surface area ($m^2 g^{-1}$), NA is the Avogadro's number equals to 6.023×10^{23} (mol^{-1}), σ_m is the cross-sectional area of the palladium equals to 0.0787 (nm^2), d_{mean} is the mean metal particle size (nm), Fg is the crystallite geometry factor equals to 6 for an hemisphere and ρ_{pd} is the specific gravity of the palladium equals to 12 $g\ cm^{-3}$.

4.7.2.4 XPS characterization

Detail analysis of the 3d peak of palladium was conducted to determine the metal oxidation state. Figure S4.4ai-ci shows the deconvolution of the Pd 3d peak into the corresponding 5/2 and 3/2 contributions obtained for uncoated Pd/Al_2O_3 with small particles and p-NIPAM coated Pd/Al_2O_3 catalyst with small and large particles. Figure S4.4aii - cii and aiii – ciii shows the deconvolution of the C 1s and Al 2p peak as a reference for the calibration in energy (see Table S4.3 and S4.4). Pd/Al_2O_3 catalyst had a binding energy of 335.7 (Pd 3d5/2) and 341.0 (Pd 3d3/2) corresponding to palladium in the metal form. On the polymer coated catalyst for small particles, the binding energy were 335.2 (Pd 3d5/2) and 340.5 (Pd 3d3/2). On the polymer coated catalyst for big particles, the binding energy were 335.3 (Pd 3d5/2) and 340.6 (Pd 3d3/2).

Table S4.2: Detected elements (in atomic %) by XPS on the Pd/Al_2O_3 catalysts containing 0 and 20 wt.% C with S and L particle size distribution. Small particles data published previously **Chapter 3.**

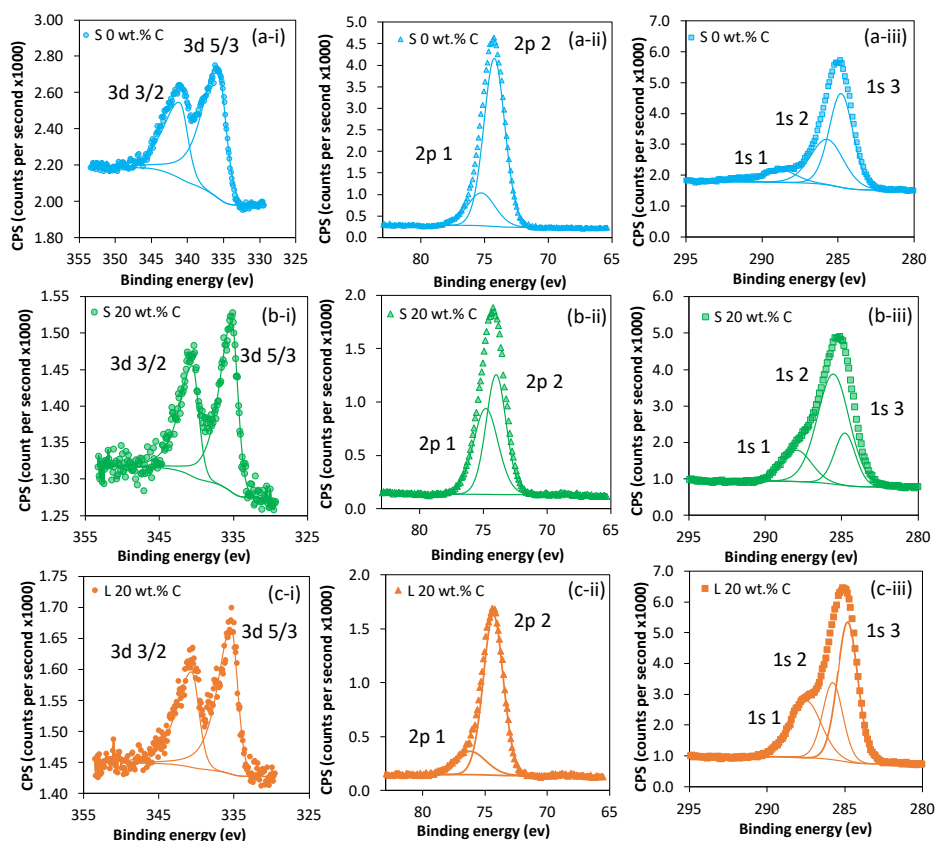| Catalyst	C 1s % at.	O 1s % at.	Al 2p % at.	N 1s % at.	Pd 3d % at.
S 0 wt. % C	13.5	54.5	30.8	0.5	0.3
S 20 wt. % C	29.3	42.5	24.0	4.0	0.2
L 20 wt. % C	38.2	36.29	19.89	4.76	0.2

Figure S4.4: XPS spectra of palladium (i), alumina (ii) and carbon (iii) obtained for Pd/Al_2O_3 catalysts containing 0 (a) and 20 wt.% C with S (b) and L (c) particle size distribution. All spectra have been calibrated using C 1s (C-C) equals to 284.8 eV as reference. Blue and green data published previously chapter 3

Table S4.3: XPS deconvolution and binding energy of alumina support, where the integrated peak areas were determined by applying a gaussian function. Small particles data published previously **Chapter 3.**

Catalyst	Al 2p 1		Al 2p 2	
	Peak area (%)	B.E. (eV)	Peak area (%)	B.E. (eV)
S 0 wt. % C	79.4	74.2	20.5	75.2
S 20 wt. % C	53.1	74.0	46.9	74.8
L 20 wt. % C	81.5	74.3	18.5	76.2

Table S4.4: XPS deconvolution and binding energy of carbon, where the integrated peak areas were determined by applying a gaussian function. Small particles data published previously **Chapter 3**

Catalyst	C 1s 1		C 1s 2		C 1s 3	
	Peak area (%)	B.E. (eV)	Peak area (%)	B.E. (eV)	Peak area (%)	B.E. (eV)
S 0 wt. % C	54.3	284.8	36.2	285.7	9.5	288.8
S 20 wt. % C	20.0	284.8	63.5	285.6	16.5	287.9
L 20 wt. % C	46.2	284.8	25.1	285.78	28.6	287.5

Table S4.5: XPS deconvolution and binding energy of palladium nanoparticles, where the integrated peak areas were determined by applying a gaussian function. Small particles data published previously **Chapter 3**

Catalyst	Pd 3d 5/3		Pd 3d 3/2	
	Peak area (%)	B.E. (eV)	Peak area (%)	B.E. (eV)
S 0 wt. % C	63.5	335.7	36.5	341.0
S 20 wt. % C	59.8	335.2	40.2	340.5
L 20 wt. % C	58.2	335.3	41.8	340.6

4.7.3 Conversion and selectivity

Our previous publication **Chapter 3** demonstrated that the addition of p-NIPAM brushes on small catalyst particles suppressed the formation of NH_4^+ (see Figure S4.5). External and internal mass transport limitations could not be responsible for the NH_4^+ selectivity changes due to the lower values of Weisz-Prater and Mears criteria for the internal and external mass transfer, respectively. In addition, similar apparent activation energy values for uncoated and p-NIPAM coated Pd/Al_2O_3 catalysts indicated that mass transfer limitations can be neglected. In turn, the observed changes in selectivity were attributed to solvation effects induced p-NIPAM polymeric brushes that modified the electronic environment of the metal nanoparticle. Notably, a similar trend on the NH_4^+ selectivity was observed upon an increase on the catalyst particle size (Figure S4.5), suggesting that the observed changes in selectivity are independent of the temperature and particle size.

Figure S4.5: NH_4^+ selectivity as a function of NO_2^- conversion (calculated from Eq. 4.3 and 4.4) at 25 °C (a) and 45 °C (b) for Pd/Al_2O_3 with particle size S containing 0 wt. % C (blue) and 20 wt.% C (green) and with particle size L containing 0 wt.% C (red) and 10 wt.% C (orange) obtained at 3 mM NO_2^-, 0.5 bar H_2, 0.1 bar of CO_2, 0.4 bar of He, at agitation rates of 500 rpm. The catalyst with particle size 0-38 μm and 38-100 μm was assigned S and L, respectively. Blue and green data published previously **chapter 3.**

4.7.4 Integral kinetics regression

Figure S4.6 and Figure S7 show the parity plot for NO_2^- and NH_4^+ concentrations upon the regression of the pre-exponential factor, apparent activation energy barriers and reaction orders for NO_2^- and H_2. Considering the small particle regime, particles in the range 0-38 μm, the kinetic parameters can be obtained. The results are shown in Section 4.7.4.4. Note that the reaction orders used for the catalyst with 20 wt.% C were assumed to be the same as a catalyst with 7 wt.% C.

4.7.4.1 Pd/Al₂O₃ catalyst

Figure S4.6: Parity plot of integral kinetics results compared to experimental results for NO_2^- concentrations (a) and NH_4^+ concentrations (b) at 3 mM NO_2^-, 0.5 bar H_2, 0.1 bar of CO_2 at agitation rates of 500 rpm from 20 to 50 °C with small (0-38 μm) and large (38-100 μm) particles on uncoated Pd/Al₂O₃ catalyst, NO_2^- concentrations ranged from 1 to 4 mM at 0.5 bar of H_2 and 20 °C to obtain the reaction order for NO_2^- with small particles, H_2 partial pressures varied from 0.1 to 0.7 bar at 3 mM NO_2^- and 20 °C to obtain the reaction order for NO_2^- with small particles. Experimental data for small particles was previously published **Chapter 3.** The different colours on (a) and (b) represent the different experiments (temperature and concentration).

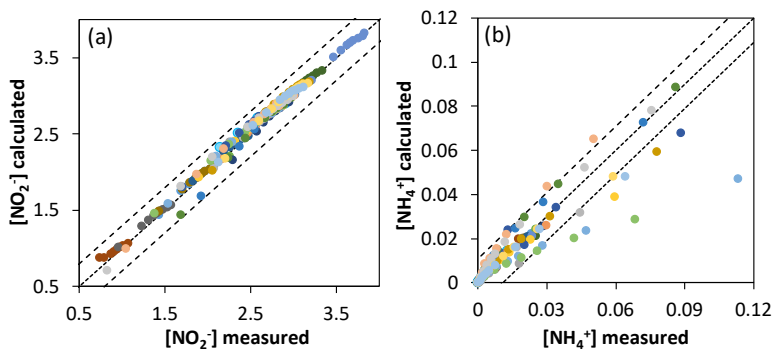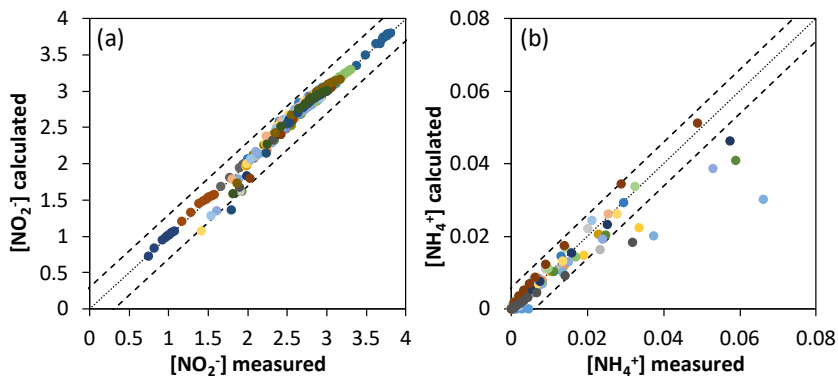### 4.7.4.2 P-NIPAM coated Pd/Al$_2$O$_3$ catalyst

Figure S4.7: Parity plot of integral kinetics results compared to experimental results for NO$_2^-$ concentrations (a) and NH$_4^+$ concentrations (b) at 3 mM NO$_2^-$, 0.5 bar H$_2$, 0.1 bar of CO$_2$ at agitation rates of 500 rpm from 20 to 50 °C with small and large particles on p-NIPAM coated Pd/Al$_2$O$_3$ catalyst containing 20 wt.% carbon, NO$_2^-$ concentrations ranged from 1 to 4 mM at 0.5 bar of H$_2$ and 20 °C to obtain the reaction order for NO$_2^-$ with small particles measured with 7 wt.% carbon, H$_2$ partial pressures varied from 0.1 to 0.7 bar at 3 mM NO$_2^-$ and 20 °C to obtain the reaction order for NO$_2^-$ with small particles measured with 7 wt.% carbon. It was assumed that 7 wt.% carbon and 20 wt.% carbon catalyst had the same reaction orders. Experimental data for small particles with 7 wt.% and 20 wt.% carbon contents on Pd/Al$_2$O$_3$ catalyst was previously published **Chapter 3**. The different colours on (a) and (b) represent the different experiments (temperature and concentration)

4.7.4.3 Comparison of the TOF

As it can be noticed in Figure S4.8a, for the samples in the kinetic regime, the TOF rates are the same on both the uncoated and p-NIPAM coated catalysts. As reported previously, p-NIPAM brushes do not change the mass transport towards the metal active site for small catalyst particles. In the case of the uncoated catalyst, increasing the catalyst particles caused a decrease on the observed reaction rate (see Figure S4.8a-b), which followed a linear behaviour upon increasing temperature (Figure 4.2a). In the case of polymer coated catalyst, a different behaviour was observed. Essentially, at temperatures below the LCST similar TOF rates were obtained for both uncoated and polymer coated catalysts, while at

temperatures above the polymer transition temperature, the observed rate had a higher decrease in the presence of the polymer.

Figure S4.8: Turnover frequency (TOF) (a) with small particles (0-38 μm) and (b) large particles (38-100 μm) for uncoated Pd/Al_2O_3 and Pd/Al_2O_3 catalyst coated with p-NIPAM brushes at 3 mM NO_2^-, 0.5 bar H_2, 0.1 bar of CO_2, 0.4 bar of He, at agitation rates of 500 rpm, at 20 °C and 50 °C.

4.7.4.4 Kinetic parameters

Table S4.6: Apparent activation energy barriers (Ea) of NH_4^+ formation and overall NO_2^- consumption (kJ mol^{-1}) and pre-exponential factors (A) of 0 and 20 wt. % C catalyst for the small particles. From 20 to 50 °C temperature, 500 rpm, 0.1 bar CO_2, 3mM NO_2^- and 0.5 bar H_2. This reaction orders were obtained from the integral kinetics regression.

	Ea NH_4^+ (kJ mol^{-1})	A NH_4^+	Ea NO2- (kJ mol^{-1})	A NO2-
0 wt. % C	31	503	23	584
20 wt. % C	52	3700	26	480

Table S4.7: Apparent activation energy barriers (Ea) of NO_2^- consumption (kJ mol^{-1}) calculated based on the initial activity and integral method of 0 and 20wt. % C catalyst for the small particles. From 20 to 50 °C temperature, 500 rpm, 0.1 bar CO2, 3mM NO_2^- and 0.5 bar H$_2$. This reaction orders were obtained from the integral kinetics regression.

	Initial activity method Ea NO_2^- (kJ mol^{-1})	Integral method Ea NO_2^- (kJ mol^{-1})
0 wt. % C	31	23
20 wt. % C	30	26

The rate expressions for NO_2^- overall consumption and NH_4^+ formation can be defined as shown in Eq. S4.5-6, where "n" represents the reaction order for H$_2$ and "m" the reaction order for NO_2^-.

$$r_{NO_2^-} = k_{NO_2^-}[H_2]^n[NO_2^-]^m \qquad \text{Eq. S4.5}$$

$$r_{NH_4^+} = k_{NH_4^+}[H_2]^{n^*}[NO_2^-]^{m^*} \qquad \text{Eq. S4.6}$$

Table S4.8: Apparent NO_2^- and H$_2$ reaction orders for nitrite hydrogenation and ammonium formation at 20 °C and 1 bar for Pd/Al$_2$O$_3$ containing 0 and 7 wt. % carbon for the small particles. The NO_2^- concentrations ranged from 1 to 4 mM at 0.5 bar of H$_2$ and 0.1 bar of CO$_2$, while H$_2$ partial pressures varied from 0.1 to 0.7 bar at 3 mM NO_2^- using 15 mg of catalyst and 500 rpm. Hydrogen, carbon dioxide, and helium (to balance) were added continuously to the system to ensure constant concentrations during the experiments. This reaction orders were obtained from the integral kinetics regression. The reaction order obtained from 7 wt.% C were assumed to be the same as 20 wt.% C.

	NO_2^- reaction orders		NH_4^+ reaction orders	
	$m_{NO_2^-}$	n_{H_2}	$m^*_{NO_2^-}$	$n^*_{H_2}$
0 wt. % C	0.1	0.5	0.1	0.4
20 wt. % C	0.2	0.2	0.1	0.5

4.7.5 Modelling

4.7.5.1 Number of particles

In this model it was assumed that all the particles have the same size. The surface area of one particle ($A_{p,1}$) was defined as the surface of one sphere with radius r (see Eq. S4.7). The volume of one particle ($V_{p,1}$) was defined as the volume of one sphere with radius r (see Eq. S4.8).

$$A_{p,1} = 4\pi r^2 \qquad \text{Eq. S4.7}$$

$$V_{p,1} = \frac{4}{3}\pi r^2 \qquad \text{Eq. S4.8}$$

The weight of one catalyst particle can be obtained by multiplying the $V_{p,1}$ with the density of the catalyst ($\rho_{catalyst}$) obtained from N_2 physisorption analysis, as shown in Eq. S4.9.

$$w_{p,1} = V_{p,1}\rho_{catalyst} \qquad \text{Eq. S4.9}$$

The total number of catalyst particles (n) can be obtained by dividing the weight of catalyst used in one experiment, e.g. 15 mg, with $w_{p,1}$ (see Eq. S4.10).

$$n = \frac{w_{catalyst}}{w_{p,1}} \qquad \text{Eq. S4.10}$$

The total volumetric flux of the specie i ($J_{n,i}$) entering/leaving the bulk can be calculated by multiplying the surface flux across one particle (J_i) by the surface area of one particle and total number of particles (n) and then dividing by the volume of the reactor ($V_{reactor}$), as shown on Eq. S4.11.

$$J_{n,i} = J_i \frac{A_{p,1}n}{V_{reactor}} \qquad \text{Eq. S4.11}$$

4.7.5.2 Reaction rate

Reaction equation

The equations used on the proposed model were obtained from the Eq. S4.12-13. (1) and (2) refer to nitrite hydrogenation reactions [19,35], while the CO_2 hydration reaction and water formation, due to H^+ and OH^- recombination were lumped in the same reaction balance as nitrite hydrogenation, due to their fast reaction rates compared to nitrite hydrogenation. In this way significantly improving the models speed as well as stability.

$$NO_2^- + 1.5H_2 \rightarrow 0.5N_2 + H_2O + OH^- (1)$$

$$H^+ + OH^- \rightarrow H_2O$$

$$CO_2 + H_2O \rightarrow H^+ + HCO_3^-$$

Eq. S4.12

$$NO_2^- + 3H_2 \rightarrow NH_4^+ + 2OH^- (2)$$

$$2H^+ + 2OH^- \rightarrow 2H_2O$$

$$2CO_2 + 2H_2O \rightarrow 2H^+ + 2HCO_3^-$$

Eq. S4.13

Reaction rate expression

For the reaction rate expression since the kinetic constant is obtained experimentally, it is necessary to convert the units from rate per volume reactor (mol $m^{-3}_{reactor}$ s^{-1}) to rate per catalyst particle volume (mol $m^{-3}_{catalyst}$ s^{-1}), as shown in Eq. S4.14.
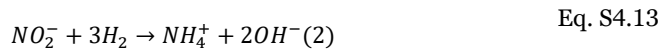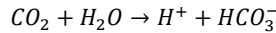
$$f = V_R \times \frac{1}{S_{Pd}} \times \frac{S_{Pd}}{n} \times \frac{n}{[\rho_{cat}w_{cat}]}$$

Eq. S4.14

Where V_R (m^3) is the volume of the reactor, S_{Pd} is the palladium surface area, n is the number of particles, ρ_{cat} (kg m^{-3}) is the density of the catalyst and w_{cat} (kg) is the weight of catalyst inside the reactor.

4.7.5.3 CO₂ kinetics

Hydration rate of CO_2 depends on the pH of the solution. Under neutral or acidic conditions, the CO_2 reacts with water to form carbonic acid (H_2CO_3) and bicarbonate (HCO_3^-) (see Eq. S4.15-16). Whereas at pH above 8, the reaction of CO_2 with hydroxide (OH^-) dominates and the main products are HCO_3^- and CO_3^{2-} (Eq. S4.17-18). [38–41] In this system, the partial pressure of CO_2 was 0.1 bar resulting in a CO_2 concentration of 3.4 mol m^{-3} based on Henry law. At 25 °C with an equilibrium constant of 1.49×10^{-3} for CO_2 to form H_2CO_3 (K1,eq) and equilibrium constant of 4.45×10^{-7} for H_2CO_3 to form proton (H^+) and HCO_3^- (K2,eq) results in a solution with a pH of 5.8 ([H^+] equals to 1.5×10^{-6} mol L^{-1}). Therefore, the reactions shown in Eq. S4.17-18 can be neglected.

$$CO_2 + H_2O \overset{K_{1,eq}}{\Longleftrightarrow} H_2CO_3 \qquad \text{Eq. S4.15}$$

$$H_2CO_3 \overset{K_{2,eq}}{\Longleftrightarrow} H^+ + HCO_3^- \qquad \text{Eq. S4.16}$$

$$HCO_3^- \overset{K_{3,eq}}{\Longleftrightarrow} H^+ + CO_3^{2-} \qquad \text{Eq. S4.17}$$

$$CO_2 + OH^- \overset{K_{4,eq}}{\Longleftrightarrow} HCO_3^- \qquad \text{Eq. S4.18}$$

$$K_{i,eq} = \frac{k_i}{k_{-i}} \qquad \text{Eq. S4.19}$$

The ratio of the kinetic rate constants for forward (i) and backward reaction (-i) gives us the equilibrium constant ($K_{i,eq}$), as shown in Eq. S4.19. Proton concentration gradients inside the particle and reactor can be neglected if the reaction of CO_2 with water is much faster than NO_2^- conversion. The hydration of CO_2 in Eq. S4.15 is slow compared to the dissociation of H_2CO_3 so that H_2CO_3, H^+ and HCO_3^- are in equilibrium. As shown in Figure S4.9, the forward reaction is slower than the backwards reaction of Eq. S4.15. At 25 °C the kinetic constant of CO_2 hydrolysis is 0.0034 s^{-1}, with a CO_2 concentration of 3.4×10^{-3} mol

l^{-1} resulting in a reaction rate of 1.14×10^{-5} mol L^{-1} s^{-1}. The rate of NO_2^- consumption is much slower with 5×10^{-7} mol L^{-1} s^{-1}, based on the initial activity (conversion level 13%) for a NO_2^- concentration of 3×10^{-3} mol L^{-1} and H_2 partial pressure of 0.5 bar at 25 °C. Furthermore, the amount of protons consumed is always smaller than the concentration of HCO_3^- and therefore, the buffer capacity of the H_2CO_3/HCO_3^- buffer is also preventing the pH gradients in the catalyst particles.

Figure S4.9: Arrhenius plots for the forward (k_1) and backwards (k_{-1}) kinetic constant for the CO_2 reaction with water shown in Eq. S4.15.[42]

In summary, the proton concentration gradients inside the catalyst particle are less pronounced than NO_2^- and H_2 because:

- CO_2 is dissolved before adding the NO_2^- to the solution
- CO_2 is continuously added to the reactor, keeping the concentration constant
- Similar diffusion coefficients of CO_2 and NO_2^- indicates similar flux
- Higher rate of CO_2 conversion towards H^+ and HCO_3^- compared to NO_2^- reaction
- Buffering in the H_2CO_3/HCO_3^- buffer

4.7.5.4 Molecular diffusion

Electroneutrality

Fick diffusion is defined as shown in Eq. S4.20. To account for the effect of electric fields the Nernst Plank equation was used as shown in Eq. S4.21.

$$J_a = -D_{i,eff}\frac{\delta c_i}{\delta r} \qquad\qquad \text{Eq. S4.20}$$

$$J_a = -D_{i,eff}\left(\frac{\delta c_i}{\delta r} + \frac{Fz_i c_i}{R_G T}(\nabla\phi)\right) \qquad\qquad \text{Eq. S4.21}$$

Where F is the Faraday constant (96485 C mol^{-1}), RG is the gas constant (8.314 J K^{-1} mol^{-1}), z is the elementary charge, T is the absolute temperature (K) and $\nabla\phi$ is the electric field (kg m s^{-2} C^{-1}).

To account for the electroneutrality the summation of all the charged species were defined as equal to zero, as shown in Eq. S4.22.

$$\sum Z_j * J_j = 0 \qquad\qquad \text{Eq. S4. 22}$$

Since $\frac{F}{R_G T}(\nabla\phi)$ is fixed and independent of species, it will be defined as a constant called $\varUpsilon$.

$$\sum_{1}^{j} z_j D_{j,eff}\frac{\delta c_j}{\delta r} + \sum_{1}^{j}(z_j^2\, c_j\, D_{j,eff})\varUpsilon = 0 \qquad\qquad \text{Eq. S4.23}$$

$$\varUpsilon = \frac{F}{R_G T}(\nabla\phi) = -\frac{\sum_1^j z_j D_{j,eff}\frac{\delta c_j}{\delta r}}{\sum_1^j (z_j^2 c_j D_{j,eff})} \qquad\qquad \text{Eq. S4.24}$$

Diffusion coefficient in water

Figure S4.10 shows the values of the diffusion coefficients used in the model.

Figure S4.10: Arrhenius plot for the diffusion coefficient (m^2 s^{-1}) for H_2, N_2, NO_2^-, Na^+, NH_4^+, HCO_3^- and CO_2 in water at infinite dilation. CO_2 results is published elsewhere [43,44].

4.7.5.5 Volume and polymer fraction

The polymer equilibrium hydration transition function ($f_{p\text{-nipam}}$) describes the changes of the thickness of the polymer layer with temperature following a silica sphere coated with p-NIPAM polymeric brushes [37] (see Figure S4.11).

$$f_{p-nipam}(T) = \left[\frac{B}{1 + e^{k(T_o - T)}}\right] + A$$

Figure S4.11: Normalised equilibrium hydration transition function ($f_{p\text{-nipam}}$) obtained for on a silica sphere coated with p-NIPAM polymeric brushes, adapted from [37].

The volume fraction of polymer in the catalyst pore (v x,p) was calculated according to Eq. S4.25. Where, $r_{sweling}$, represents the swelling ratio and v dry the volume fraction of polymer in the dry state. The v dry was obtained from BET results with a value of 0.3 (see Table S4.1).

$$v_{x,p} = r_{swelling} \times f_{p-nipam} \times v_{dry}$$ Eq. S4.25

Usually, the swelling ratio, the water fraction (Φ_{water}) and polymer fraction ($\Phi_{p-NIPAM}$) of the polymeric brushes can be calculated from the polymer hy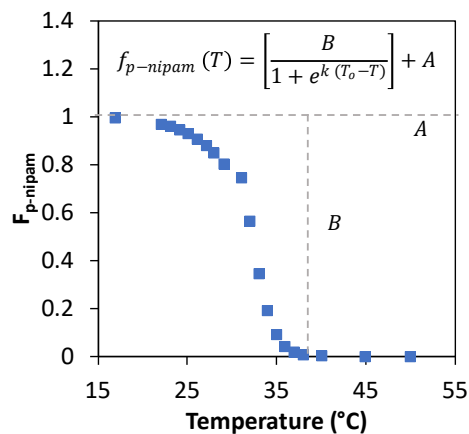dration equilibrium function (Figure S4.11), as shown in Eq. S4.26-28. Here, d_{wet} represents the thickness of the polymer is the presence of water and d_{dry} the thickness obtained in the collapsed state. However, we could not determine the thickness of polymer in the porous catalyst in the dry state from TEM images. Therefore, it was assumed to be equal to the polymer fraction obtained from BET results (see Section S4.7.2.1.).

$$r_{swelling} = \frac{d_{wet} - d_{dry}}{d_{dry}}$$ Eq. S4.26

$$\Phi_{water} = \frac{d_{wet} - d_{dry}}{d_{wet}}$$ Eq. S4.27

$$\Phi_{p-NIPAM} = 1 - \Phi_{water}$$ Eq. S4.28

Figure S4.12a shows the volume fraction and polymer fraction assumed for these experiments. We acknowledge that the swelling ratio was assumed to follow the behaviour published by B. A. Humphreys et al. [37] on a silica sphere coated with p-NIPAM polymeric brushes. However, depending on the surface density of polymer at the surface the swelling ratio could vary as demonstrated in Figure S4.12b.
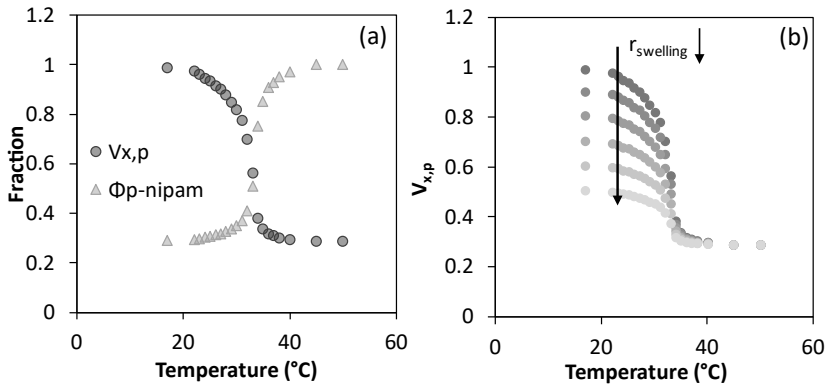
Figure S4.12: Swelling and polymer fraction as a function of temperature (a) effect of the swelling ratio in the hydration equilibrium temperature profile (b).

4.7.5.6 Parity plot of uncoated Pd/Al$_2$O$_3$
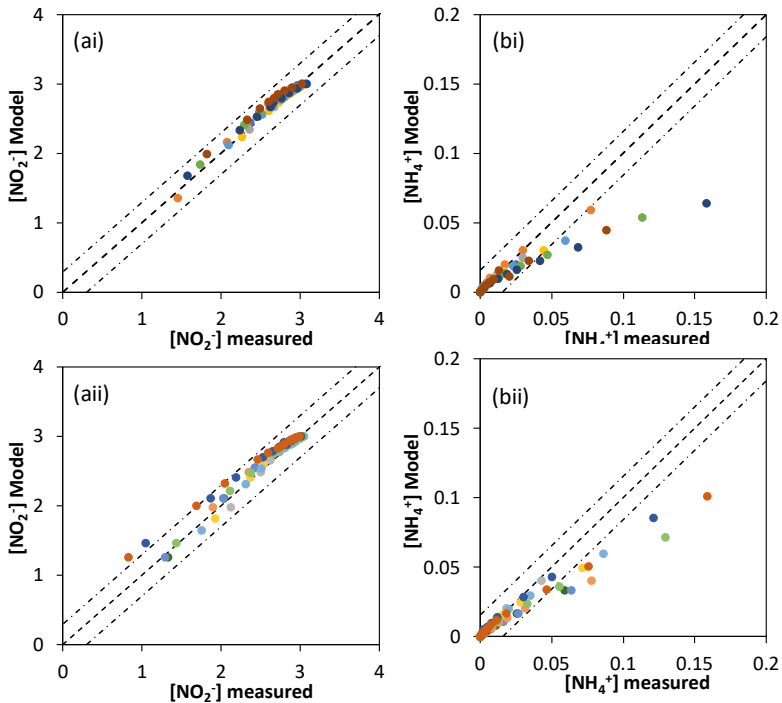
Figure S4.13: Parity plot of model results compared to experimental results for NO$_2^-$ concentrations (a) and NH$_4^+$ concentrations (b) at 3 mM NO$_2^-$, 0.5 bar H$_2$, 0.1 bar of CO$_2$

at agitation rates of 500 rpm from 20 to 50 °C with 0-38 μm (i) and 38-100 μm (ii) particles on uncoated Pd/Al_2O_3 catalyst.

4.7.5.7 Concentration profiles uncoated Pd/Al_2O_3
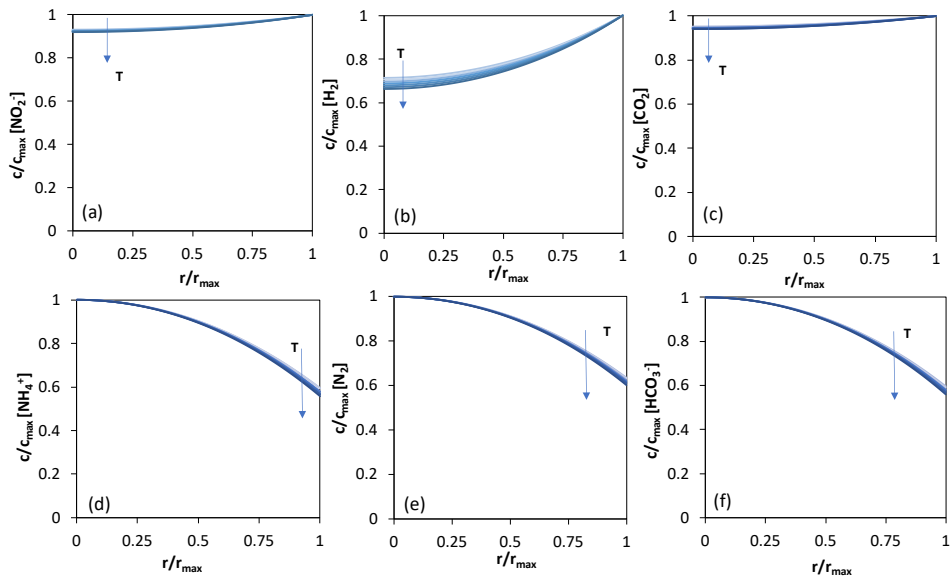
Figure S4.14: Normalized concentration profile inside the catalyst particles for NO_2^- (a), H_2 (b), CO_2 (c), NH_4^+ (d), N_2 (e) and HCO_3^- (f) at 10 % NO_2^- conversion level for the uncoated Pd/Al_2O_3 catalyst with a particle size of 0-38 μm at 3 mM NO_2^-, 0.5 bar H_2, 0.1 bar of CO_2 at agitation rates of 500 rpm from 20 to 50 °C.
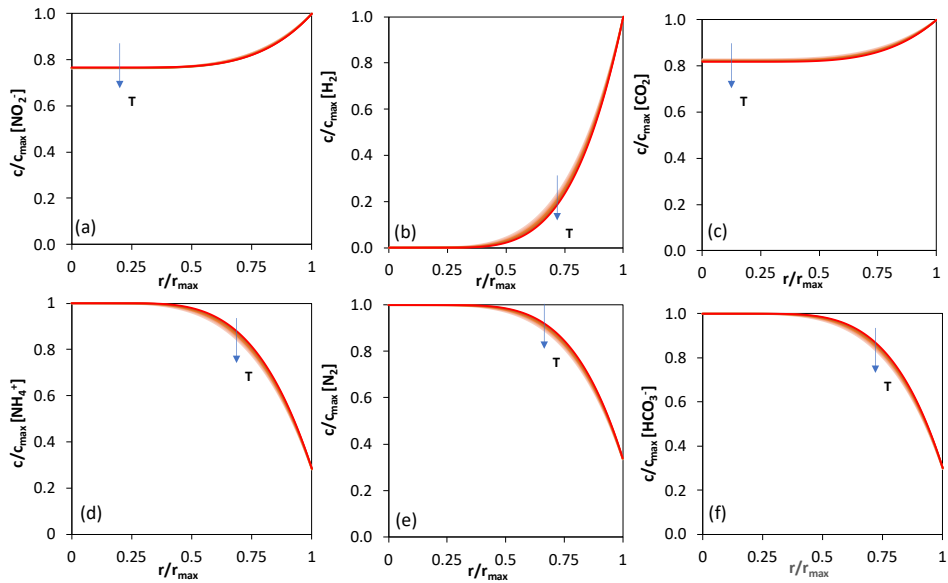
Figure S4.15: Normalized concentration profile inside the catalyst particles for NO_2^- (a), H_2 (b), CO_2 (c), NH_4^+ (d), N_2 (e) and HCO_3^- (f) at 10 % NO_2^- conversion level for the uncoated Pd/Al_2O_3 catalyst with a particle size of 38-100 μm at 3 mM NO_2^-, 0.5 bar H_2, 0.1 bar of CO_2 at agitation rates of 500 rpm from 20 to 50 °C.

4.7.5.8 Concentration profile P-NIPAM coated Pd/Al$_2$O$_3$ catalyst
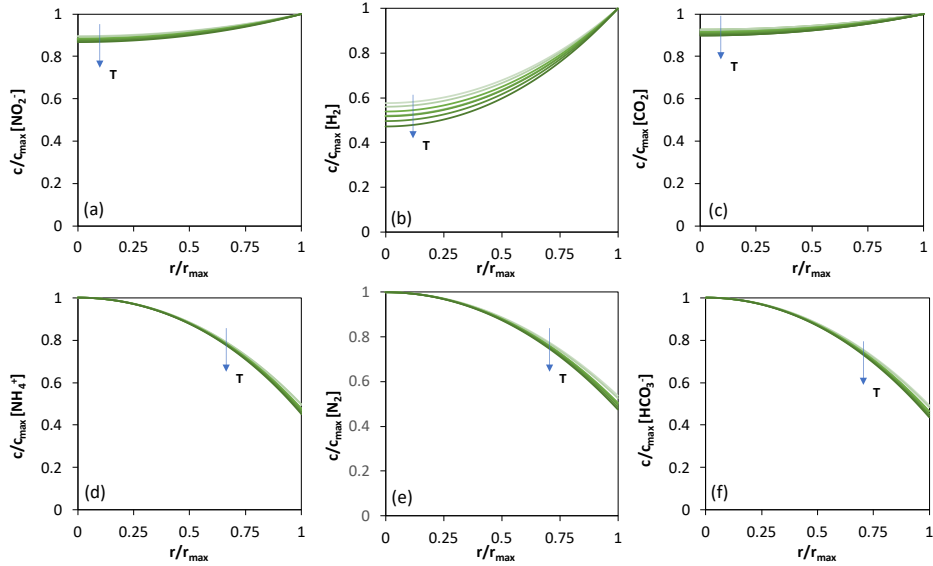
Figure S4.16: Concentration profile inside the catalyst particles for NO$_2^-$ (a), H$_2$ (b), CO$_2$ (c), NH$_4^+$ (d), N$_2$ (e) and HCO$_3^-$ (f) at 10 % NO$_2^-$ conversion level for p-NIPAM coated Pd/Al$_2$O$_3$ catalyst with 0-38 μm particle size at 3 mM NO$_2^-$, 0.5 bar H$_2$, 0.1 bar of CO$_2$ at agitation rates of 500 rpm from 20 to 50°C assuming 100 % parallel.
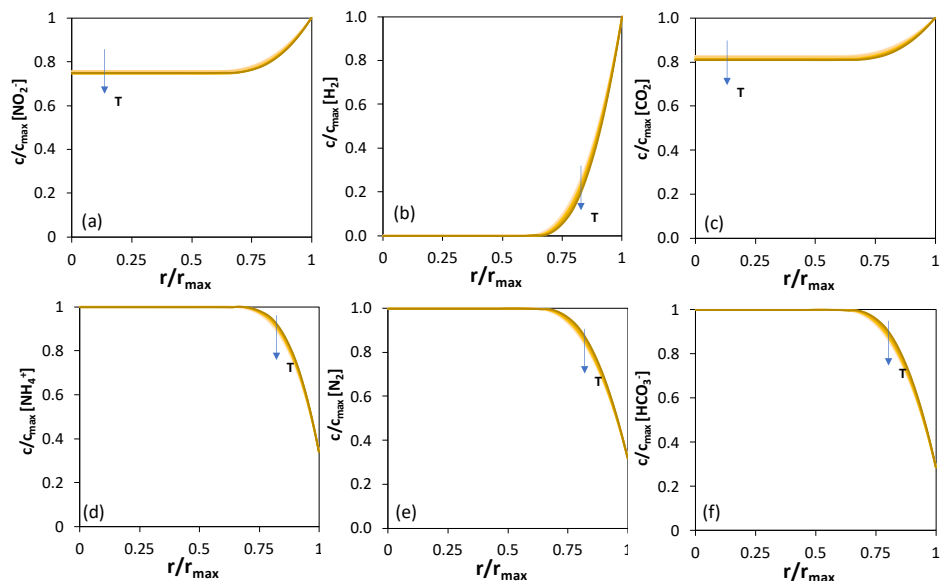
Figure S4.17: Concentration profile inside the catalyst particles for NO_2^- (a), H_2 (b), CO_2 (c), NH_4^+ (d), N_2 (e) and HCO_3^- (f) at 10 % NO_2^- conversion level for p-NIPAM coated Pd/Al_2O_3 catalyst with 38-100 μm particle size at 3 mM NO_2^-, 0.5 bar H_2, 0.1 bar of CO_2 at agitation rates of 500 rpm from 20 to 50°C assuming 100% parallel.

4.7.5.9 Comparison model and experimental data
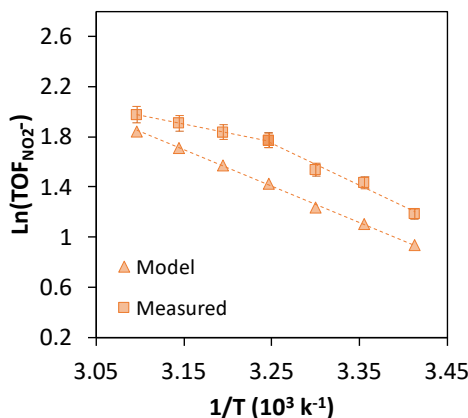
Figure S4.18: Arrhenius plots for NO_2^- for p-NIPAM coated Pd/Al_2O_3 catalyst with 38-100 μm particles assuming 100 % parallel at 3 mM NO_2^-, 0.5 bar H_2, 0.1 bar of CO_2, at agitation rates of 500 rpm from 20 to 50 °C.

Table S4.9: Activation energy barrier of NO_2^- for for p-NIPAM coated Pd/Al_2O_3 catalyst with big particles assuming 30 % parallel at 3 mM NO_2^-, 0.5 bar H_2, 0.1 bar of CO_2, at agitation rates of 500 rpm from 20 to 50 °C. Ea^{low} is measured in the regime 20-30 °C and Ea^{high} is measured in the regime 35-50 °C. Experimental data can be found Figure 4.7.

	Ea^{low} (kJ mol^{-1})	Ea^{high} (kJ mol^{-1})
Model	30	23
Measured	28	11

4.7.5.10 Outside Shell addition

Since in this porous catalyst is not easy to determine if either the polymer grows only in the inside of the particle or also on the outside surface of the catalyst, it was considered to define the polymeric brushes as an external resistance to the molecular diffusion as a so called "core-shell". As shown in Figure S4.19 only a significant polymer thickness will cause a change in the observed apparent activation energy barriers. However, it did not induce a significant drop in the apparent barrier at higher temperatures (see Figure 4.2). In addition, this shows that the main contribution to the effects on the observed reaction rate originate from the polymers grown inside the catalyst particle. This is not surprising as in the presence of a catalyst with high internal surface area, the percentage of polymer in the outside surface is almost negligible compared with the internal surface area, this assuming the particle is a defined sphere.
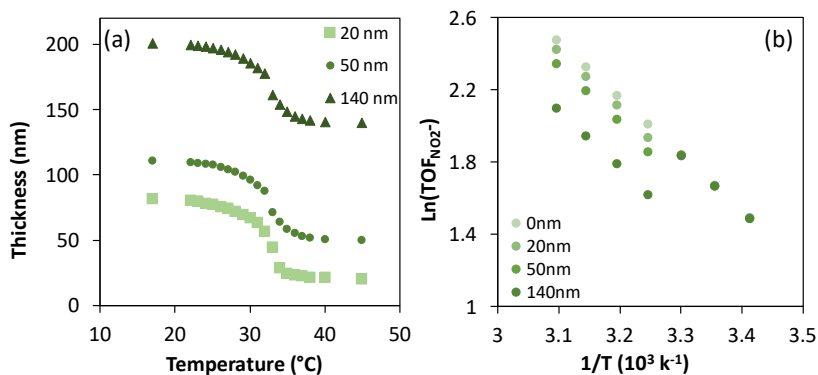
Figure S4.19: Temperature effect on the polymer thickness (a) and Arrhenius plots for NO_2^- at different polymer thickness for p-NIPAM coated Pd/Al_2O_3 catalyst with small particles assuming 100 % parallel at 3 mM NO_2^-, 0.5 bar H_2, 0.1 bar of CO_2, at agitation rates of 500 rpm from 20 to 50 °C (b). The thickness 20, 50 and 140 nm represent the thickness obtained in the collapsed state. Equilibrium hydration transition at a thickness designated as "20 nm" was obtained from [37].

4.8   References

[1]   F. Hapiot, S. Menuel, E. Monflier, Thermoresponsive hydrogels in catalysis, ACS Catal. 3 (2013) 1006–1010. https://doi.org/10.1021/cs400118c.

[2]   L. Tzounis, M. Doña, J.M. Lopez-Romero, A. Fery, R. Contreras-Caceres, Temperature-Controlled Catalysis by Core-Shell-Satellite AuAg@pNIPAM@Ag Hybrid Microgels: A Highly Efficient Catalytic Thermoresponsive Nanoreactor, ACS Appl. Mater. Interfaces. 11 (2019) 29360–29372. https://doi.org/10.1021/acsami.9b10773.

[3]   L. Tzounis, M. Don, J.M. Lopez-romero, A. Fery, R. Contreras-caceres, Temperature-Controlled Catalysis by Core – Shell – Satellite AuAg@pNIPAM@Ag Hybrid Microgels: A Highly Efficient Catalytic Thermoresponsive Nanoreactor, ACS Appl. Mater. Interfaces. 11 (2019) 29360–29372. https://doi.org/10.1021/acsami.9b10773.

[4]   Y. You, K.K. Kalebaila, S.L. Brock, D. Oupicky, Temperature-Controlled Uptake and Release in PNIPAM-Modified Porous Silica Nanoparticles, Chem. Mater. (2008) 3354–3359. https://doi.org/10.1021/cm703363w.

[5]   Z. Chen, Z. Cui, C. Cao, W. He, L. Jiang, W. Song, Temperature-responsive smart nanoreactors: Poly(N-isopropylacrylamide)- coated Au@mesoporous-SiO2 hollow nanospheres, Langmuir. 28 (2012) 13452–13458. https://doi.org/10.1021/la3022535.

[6]   H. il Lee, J. Pietrasik, S.S. Sheiko, K. Matyjaszewski, Stimuli-responsive molecular brushes, Prog. Polym. Sci. 35 (2010) 24–44. https://doi.org/10.1016/j.progpolymsci.2009.11.002.

[7]   M. Wei, Y. Gao, X. Li, M.J. Serpe, Stimuli-responsive polymers and their applications, Polym. Chem. (2017) 127–143. https://doi.org/10.1039/c6py01585a.

[8]   B.A. Humphreys, J.D. Willott, T.J. Murdoch, G.B. Webber, E.J. Wanless, Specific ion modulated thermoresponse of poly(N-isopropylacrylamide) brushes, Phys. Chem. Chem. Phys. 18 (2016) 6037–6046. https://doi.org/10.1039/C5CP07468A.

[9]   H.C. Lee, T. Heil, J.K. Sun, B.V.K.J. Schmidt, Dispersed nano-MOFs via a stimuli-responsive biohybrid-system with enhanced photocatalytic performance, Mater.

Horizons. 6 (2019) 802–809. https://doi.org/10.1039/c8mh01342j.

[10]   X. Mao, W. Tian, J. Wu, G.C. Rutledge, T.A. Hatton, Electrochemically responsive heterogeneous catalysis for controlling reaction kinetics, J. Am. Chem. Soc. 137 (2015) 1348–1355. https://doi.org/10.1021/ja512224g.

[11]   Y. You, K.K. Kalebaila, S.L. Brock, D. Oupicky, Temperature-Controlled Uptake and Release in PNIPAM-Modified Porous Silica Nanoparticles, (2008) 3354–3359. https://doi.org/10.1021/cm703363w.

[12]   Z. Chen, Z. Cui, C. Cao, W. He, L. Jiang, W. Song, Temperature-Responsive Smart Nanoreactors : Poly(N-isopropylacrylamide)-Coated Au@Mesoporous-SiO2 Hollow Nanospheres, Langmuir. 28 (2012) 13452–13458. https://doi.org/10.1021/la3022535.

[13]   S. Wu, J. Dzubiella, J. Kaiser, M. Drechsler, X. Guo, M. Ballauff, Y. Lu, Thermosensitive Au-PNIPA Yolk-Shell Nanoparticles with Tunable Selectivity for Catalysis, Angew. Chemie Int. Ed. 51 (2012) 2229–2233. https://doi.org/10.1002/anie.201106515.

[14]   H. Jia, R. Roa, S. Angioletti-Uberti, K. Henzler, A. Ott, X. Lin, J. Möser, Z. Kochovski, A. Schnegg, J. Dzubiella, M. Ballauff, Y. Lu, Thermosensitive Cu2O-PNIPAM core-shell nanoreactors with tunable photocatalytic activity, J. Mater. Chem. A. 4 (2016) 9677–9684. https://doi.org/10.1039/c6ta03528k.

[15]   R. Roa, W.K. Kim, M. Kanduč, J. Dzubiella, S. Angioletti-Uberti, Catalyzed Bimolecular Reactions in Responsive Nanoreactors, ACS Catal. 7 (2017) 5604–5611. https://doi.org/10.1021/acscatal.7b01701.

[16]   Y. Lu, Y. Mei, M. Drechsler, M. Ballauff, Thermosensitive core-shell particles as carriers for Ag nanoparticles: Modulating the catalytic activity by a phase transition in networks, Angew. Chemie - Int. Ed. 45 (2006) 813–816. https://doi.org/10.1002/anie.200502731.

[17]   M. Kanduč, W.K. Kim, R. Roa, J. Dzubiella, Modeling of stimuli-responsive nanoreactors: Rational rate control towards the design of colloidal enzymes, Mol. Syst. Des. Eng. 5 (2020) 602–619. https://doi.org/10.1039/c9me00106a.

[18]   S. Angioletti-Uberti, Y. Lu, M. Ballauff, J. Dzubiella, Theory of Solvation-Controlled Reactions in Stimuli-Responsive Nanoreactors, J. Phys. Chem. C. 119 (2015) 15723–15730. https://doi.org/10.1021/acs.jpcc.5b03830.

[19]   C.A. Clark, C.P. Reddy, H. Xu, K.N. Heck, G. Luo, T.P. Senftle, M.S. Wong, Mechanistic insights into ph-controlled nitrite reduction to ammonia and hydrazine over rhodium, ACS Catal. 10 (2020) 494–509. https://doi.org/10.1021/acscatal.9b03239.

[20]   K.N. Heck, S. Garcia-Segura, P. Westerhoff, M.S. Wong, Catalytic Converters for Water Treatment, Acc. Chem. Res. 52 (2019) 906–915. https://doi.org/10.1021/acs.accounts.8b00642.

[21]   B.A. Humphreys, S.W. Prescott, T.J. Murdoch, A. Nelson, E.P. Gilbert, B. Webber, E.J. Wanless, Influence of molecular weight on PNIPAM brush modified colloidal silica particles †, Soft Matter. (2019) 55–64. https://doi.org/10.1039/c8sm01824c.

[22]   M.E. Davis, R.J. Davis, Fundamentals of Chemical Reaction Engineering, 2013.

[23]   K. Krabbenhøft, J. Krabbenhøft, Application of the Poisson-Nernst-Planck equations to the migration test, Cem. Concr. Res. 38 (2008) 77–88. https://doi.org/10.1016/j.cemconres.2007.08.006.

[24]   C. Tournassat, C.I. Steefel, T. Gimmi, Solving the Nernst-Planck Equation in Heterogeneous Porous Media With Finite Volume Methods: Averaging Approaches at Interfaces, Water Resour. Res. 56 (2020) 1–10. https://doi.org/10.1029/2019WR026832.

[25]   J.T. Edward, Molecular volumes and the Stokes-Einstein equation, J. Chem. Educ. 47 (1970) 261–270. https://doi.org/10.1021/ed047p261.

[26]   S. Berkowicz, F. Perakis, Exploring the validity of the Stokes-Einstein relation in supercooled water using nanomolecular probes, Phys. Chem. Chem. Phys. 23 (2021) 25490–25499. https://doi.org/10.1039/d1cp02866a.

[27]   D.W. McCall, D.C. Douglass, The effect of ions on the self-diffusion of water. I. Concentration dependence, J. Phys. Chem. 69 (1965) 2001–2011. https://doi.org/10.1021/j100890a034.

[28]   R.E. Zeebe, On the molecular diffusion coefficients of dissolved CO_2, HCO_3^-, and CO_3^{2-} and their dependence on isotopic mass, Geochim. Cosmochim. Acta. 75 (2011) 2483–2498. https://doi.org/10.1016/j.gca.2011.02.010.

[29]   P. Banerjee, B. Bagchi, Ions' motion in water, J. Chem. Phys. 150 (2019). https://doi.org/10.1063/1.5090765.

[30] L. Masaro, X.X. Zhu, Physical models of diffusion for polymer solutions, gels and solids, 1999. https://doi.org/10.1016/S0079-6700(99)00016-7.

[31] M. Kanduč, W.K. Kim, R. Roa, J. Dzubiella, Selective Molecular Transport in Thermoresponsive Polymer Membranes: Role of Nanoscale Hydration and Fluctuations, Macromolecules. 51 (2018) 4853–4864. https://doi.org/10.1021/acs.macromol.8b00735.

[32] Z. Chen, Z.M. Cui, C.Y. Cao, W.D. He, L. Jiang, W.G. Song, Temperature-responsive smart nanoreactors: Poly(N-isopropylacrylamide)- coated Au@mesoporous-SiO2 hollow nanospheres, Langmuir. 28 (2012) 13452–13458. https://doi.org/10.1021/la3022535.

[33] P. Hervés, M. Pérez-Lorenzo, L.M. Liz-Marzán, J. Dzubiella, Y. Lub, M. Ballauff, Catalysis by metallic nanoparticles in aqueous solution: Model reactions, Chem. Soc. Rev. 41 (2012) 5577–5587. https://doi.org/10.1039/c2cs35029g.

[34] S. Carregal-Romero, N.J. Buurma, J. Pérez-Juste, L.M. Liz-Marzán, P. Hervés, Catalysis by Au@pNIPAM nanocomposites: Effect of the cross-linking density, Chem. Mater. 22 (2010) 3051–3059. https://doi.org/10.1021/cm903261b.

[35] P. Xu, S. Agarwal, L. Lefferts, Mechanism of nitrite hydrogenation over Pd/γ-Al2O3 according a rigorous kinetic study, J. Catal. 383 (2020) 124–134. https://doi.org/10.1016/j.jcat.2020.01.003.

[36] P. Xu, S. Agarwal, J.F. Albanese, L. Lefferts, Enhanced transport in Gas-Liquid-Solid catalytic reaction by structured wetting properties: Nitrite hydrogenation, Chem. Eng. Process. - Process Intensif. 148 (2020) 107802. https://doi.org/10.1016/j.cep.2020.107802.

[37] B.A. Humphreys, S.W. Prescott, T.J. Murdoch, A. Nelson, E.P. Gilbert, B. Webber, E.J. Wanless, Influence of molecular weight on PNIPAM brush modified colloidal silica particles †, Soft Matter. 15 (2019) 55–64. https://doi.org/10.1039/c8sm01824c.

[38] A.H.G. Cents, D.W.F. Brilman, G.F. Versteeg, CO2 absorption in carbonate/bicarbonate solutions: The Danckwerts-criterion revisited, Chem. Eng. Sci. 60 (2005) 5830–5835. https://doi.org/10.1016/j.ces.2005.05.020.

[39] M.J. Mitchell, O.E. Jensen, K.A. Cliffe, M.M. Maroto-Valer, A model of carbon dioxide dissolution and mineral carbonation kinetics, Proc. R. Soc. A Math. Phys.

Eng. Sci. 466 (2010) 1265–1290. https://doi.org/10.1098/rspa.2009.0349.

[40]   A. Stirling, I. Papai, H2CO3 forms via HCO3- water, J. Phys. Chem. C. (2010) 16854–16859. https://doi.org/https://doi.org/10.1021/jp1099909.

[41]   Q. Xiang, M. Fang, H. Yu, M. Maeder, Kinetics of the reversible reaction of CO2(aq) and HCO3- with sarcosine salt in aqueous solution, J. Phys. Chem. A. 116 (2012) 10276–10284. https://doi.org/10.1021/jp305715q.

[42]   X. Wang, W. Conway, R. Burns, N. McCann, M. Maeder, Comprehensive study of the hydration and dehydration reactions of carbon dioxide in aqueous solution, J. Phys. Chem. A. 114 (2010) 1734–1740. https://doi.org/10.1021/jp909019u.

[43]   W.J. Thomas, M.J. Adams, Measurement of the diffusion coefficients of carbon dioxide and nitrous oxide in water and aqueous solutions of glycerol, Trans. Faraday Soc. 61 (1965) 668–673. https://doi.org/10.1039/tf9656100668.

[44]   A. Tamimi, E.B. Rinker, O.C. Sandall, Diffusion Coefficients for Hydrogen Sulfide, Carbon Dioxide, and Nitrous Oxide in Water over the Temperature Range 293–368 K, J. Chem. Eng. Data. 39 (1994) 330–332. https://doi.org/10.1021/je00014a031.

Chapter 5

Conclusion and Outlook

5.1   Conclusions

Chapter 1 of this thesis introduced the concept of a self-regulating mechanism applied to heterogeneous catalysis. The most common example involves stimulus-responsive polymers added to the surface of a heterogeneous catalyst, to manipulate the catalytic performance upon an external stimulus (i.e. temperature, pH, light intensity). These bio-inspired materials have been previously studied in idealised systems, where the thermo-responsive polymeric brushes were coated on a nanocluster. A decrease in the reaction rate was observed upon the collapse of the polymeric brushes in these so-called "thermo-responsive nano-reactors" when reaching the threshold temperature of solubility or low critical solubility temperature (LCST). However, there is a significant gap in research regarding the development of more practical catalysts that can have this hybrid behaviour under industrially relevant conditions. In this context, this thesis focusses on understanding the interplay between polymeric brushes and the catalytic performance of thermo-responsive nano-reactors to pave the way to industrial applications such as water purification where variability of the feedstock and operating conditions can generate important challenges in the composition of the effluent. Next, the main advantages and practical challenges of using *in-situ* attenuated total reflection infrared (ATR-IR) spectroscopy are revised for studying liquid-solid interfaces of thermo-responsive nano-reactors. First, different operational modes were discussed in the context of liquid phase catalysis. Next, the main issues related to mass transfer effects in the design of reaction cells were addressed with the aim of developing kinetically relevant information about the underlaying reaction mechanisms.

Chapter 2 demonstrated that the molecular transport through a thermo responsive polymeric matrix under dynamic operation is strongly coupled to the polymer-probe interaction and the polymer content. This was proven by combining experimental measurements of CO chemisorption on Pd/Al_2O_3 coated on the ATR-IR crystal with diffusion-reaction numerical modelling. Notably, the saturation time and induction period of the saturation curve decreased when the temperature was above the LCST of p-NIPAM (40 °C). This was attributed to the collapse of the polymeric brushes, thus increasing the effective pore diameter for diffusion in comparison with the swollen state. An accurate fit of the *In-situ* ATR experimental data with the developed model could only be obtained by including the absorption of CO into the polymeric matrix. Hence, it was concluded that the rate of molecular transport of solutes through these polymeric membranes depends on the

strength of the interaction between the solute and the polymer, where the solute will absorb rapidly into the polymeric matrix before reaching the catalyst layer covering the ATR-IR crystal. Clearly, it is essential to know the kinetics of the absorption in the polymer matrix, the maximum absorption capacity, and the diffusion coefficient inside the polymer at temperatures above and below the LCST to disentangle the effect of the thermos-responsive polymer on the molecular transport under dynamic operations.

In **Chapter 3**, the polymeric brushes were coated near the metal active sites directly on the surface of an industrially relevant catalyst, i.e. porous Pd/Al$_2$O$_3$ catalyst. Firstly, the mass transfer limitations were mitigated to evaluate the impact of the polymeric brushes in the kinetics of nitrite hydrogenation reaction. Consequently, the p-NIPAM coated catalyst had a lower NH$_4^+$ selectivity in comparison with the uncoated catalyst. To disentangle this observation, ATR-IR spectroscopy measurements were performed showing a red peak shift on the NO$_2^-$ adsorption on palladium. Similar observations were reported on **Chapter 2**, where the polymers addition caused a red shift on the CO-Pd bond peaks. The observed changes in selectivity were attributed to solvation effects, where the functional groups in the p-NIPAM brushes modified the energy landscape of the catalytic reaction. This implies that the reaction kinetics as well as the operating mechanism can be significantly influenced by the presence of polymers near the metal active site. Therefore, it is demonstrated that these polymer-coated catalysts cannot only be used to modify the transport of reactive species, but also to tune catalyst selectivity.

Chapter 4 builds further on the work from **Chapter 3** by studying the effect of the particle size of the Pd/Al$_2$O$_3$ catalyst to induce mass transfer limitations. In this way, we could evaluate the impact of the polymeric brushes on the observed reaction rate of nitrite hydrogenation at temperatures above and below the LCST of p-NIPAM. Here, it was observed a linear increase of the reaction rate with the temperature when smaller particles (0-38 µm) were employed regardless of the presence of p-NIPAM brushes. Strikingly, a decrease in the apparent activation energy barrier was observed at temperatures above the LCST in the presence of p-NIPAM coated catalyst with larger particles. Since the polymeric brushes were grown throughout the catalyst particle, the polymer upon collapse could either increase the effective pore diameter for diffusion, as discussed in **Chapter 2**, or block pore junctions. Therefore, the inflexion point in the Arrhenius plot was attributed to the partial blockage of the catalyst pores by the polymer collapse in the large particles.

While the observed reaction rates at temperatures above the LCST were lower than those measured below the 32 °C threshold, the changes in the apparent barriers suggest that the process becomes transfer limited. A detailed diffusion model was developed to shed light into the effect of polymeric brushes on the surface of a highly porous catalyst. This model could accurately predict the experimental results of the uncoated catalyst. The modelling efforts on the polymer-coated catalyst for the large particles suggested that the polymer transition from swollen to collapse at high temperatures is only relevant for the catalyst particles that are already mass transport controlled (i.e. 38-100 μm). As discussed in **Chapter 4,** the model accuracy could be significantly improved by including the absorption kinetics and capacity of the p-NIPAM.

5.2   Outlook

The series of ATR measurements performed for this thesis can be expanded by measuring a system with p-NIPAM brushes only on the top of the surface of the membrane, mimicking a polymer "blanket" configuration, by protecting the membrane channels during the polymerization step. This strategy could help us to demonstrate the simulated results presented in **Chapter 2**, showing a decrease in the reaction rates at temperatures above LCST. As reported by M. Cirelli [1], the polymer surface coverage can be manipulated by changing the ratio between an active and inactive initiator, such as BIBB (bromo isobutyrilbromide) and BMA (1-bromo-carbonyl-1-methylethyl), respectively. Leveraging this concept, one could prevent the growth inside the pores by protecting the membrane pores with BMA following a sequential process. The membrane is firstly exposed to the coupling agent, e.g. APTES ((3-aminopropyl)triethoxysilane), followed by exposure to the inactive initiator, e.g. BMA. Afterwards, plasma cleaning could be applied to remove the APTES-BMA from the top surface of the membrane leaving the pores filled with the inactive initiator. Finally, the membrane surface can be exposed to the coupling agent followed by the active initiator, e.g. BIBB. In this way, only the active initiators placed on the top surface will contribute to the growth of the polymeric brushes. Consequently, the molecular transport can be studied by manipulating the membrane pore size and polymer thickness. Note that the polymer thickness obtained by this procedure must be carefully controlled to maximize its effect on the molecular transport.

The model developed in **Chapter 2** describing the ATR-IR system assumed a constant concentration across the length of the IRE. As explained in **Chapter 1**, concentration gradients can be formed in the presence of multi-bounced IRE. Therefore, changing from 1D to 2D would make the model more versatile. In addition, the model calculations revealed that there is a complex interplay between the kinetics of absorption in the polymer matrix and polymer-absorbate energy of interaction (i.e. solubility). However, in the current simulations the kinetic constant and absorption capacity were regressed from the available experimental data. The absorption capacity could be obtained by measuring the CO concentration as a function of time upon exposure to the p-NIPMA polymer at different temperatures and initial concentration, allowing the estimation of the absorption kinetics and solubility. This information will improve the accuracy of the modelling of PMCA. Another interesting line of research using *in-situ* ATR-IR spectroscopy would be

to study the polymer-molecule interactions with other species that are relevant for industrial applications, such as organic molecules or ionic species, e.g. nitrites/nitrates.

To further investigate the induced solvation effects, a suggestion would be to perform *in situ* ATR-IR experiments of nitrite hydrogenation on Pd/Al_2O_3 coated with p-NIPAM brushes. As shown in **Chapter 1**, ATR-IR can be used to help deducing the reaction mechanism by detecting interactions of reactants and reaction intermediates with catalytic surfaces in liquid phase. This approach could demonstrate if the adsorption strength of the intermediate species or/and the reaction mechanism changes upon the addition of polymeric brushes. The results could be afterwards compared with the previously reported work of S. Ebbesen et al. [2] on Pd/Al_2O_3 (see **Chapter 1**). While *in-situ* ATR-IR spectroscopy detects changes on molecular vibrations, which are key to detect the polymer-surface reaction intermediates interaction, the influence of the polymer on the electronic configuration of the metal remains hidden. For our catalyst with a polymer content of 20 wt.% carbon, the oxidation state of the palladium remained constant in comparison with the uncoated catalyst (see **Chapter 3**). Notably, it was previously reported by A. R. Riscoe et al. [5] that polymers (not stimulus-responsive) can influence the oxidation state of the metal. An interesting line of research would be to verify if increasing the polymer content at the catalyst surface leads to stronger interactions between the polymeric brushes and the metal surface. Next to experimental studies, the theoretical understanding of these materials on catalytic reaction remains elusive. This is primarily due to the high computational cost of conducting quantum chemical calculations (e.g. Density Functional Theory - DFT) in these large systems. For this reason, performing Molecular Dynamics Simulations (MDS) could be employed to determine the interactions between nitrites-polymer-metal. [3,4]

In addition, the mass transport model developed based on electroneutral Fick's diffusion can be further improved to study the effect of unevenly distributed polymer throughout the catalyst particle on the observed rate and concentration profile (see **Chapter 4**). The catalyst mapping of the polymeric brushes could be obtained by X-ray absorption spectroscopy. Here, a 3D scan of a single particle could allow us to better determine where the polymeric brushes have grown during polymerization. This information can help us to validate our model system with homogenous distribution. Another important revision to the model would be to include the of carbon dioxide (CO_2) kinetics instead of assuming the

proton concentration constant. This condition will be even more important considering that polymeric brushes interact with charged species. Consequently, this could induce a concentration gradient of protons inside the particle which would not be observed in the uncoated catalyst.

From the research performed in this thesis, it is clear that a well-defined structured catalyst is needed to develop a catalyst with self-regulating capabilities. The ability to control where the polymer growth is crucial because the observed effect on the reaction rate depends on whether the polymer grows inside or outside the pores, polymer content, and pore sizes. In addition, polymer chemistry and the ability of the polymer to interact with the diffusing species cannot be discarded as it equally affects the observed reaction performance. Then, depending on the desired application to either tune reaction selectivity or control the observed reaction rate, the polymer can either be near the metal active site or physically separated from the metal active site, respectively. This demonstrates that developing a self-regulating catalyst is rather challenging. On one hand, to prove the concept on a laboratory scale, a possible reaction would be hydrogen peroxide decomposition, for a thermo-responsive polymer, because this is an exothermic reaction that can lead to an adiabatic temperature rise of the system. In a similar matter one could image that a pH sensitive polymers could be employed for the nitrite hydrogenation reaction. In this is reaction the formation of NH_4^+ is favored at high pH, which leads to a positive feedback loop. Consequently, this affects the reaction selectivity and activity after reaching a certain pH threshold after which the reaction is out of control. Thus, this reaction could be suitable to demonstrate the concept of self-regulating catalysis. On the other hand, a theoretical evaluation of the self-regulation mechanism would be rather interesting. First, one could create a model system (agnostic of the chemistry of the polymer) that can indicate the boundary conditions in which it is possible to observe oscillating or self-regulating catalytic behavior. Then, this in-silico study could be used to provide the designing rules for self-regulating catalysts.

5.3   References

[1]   M. Cirelli, Multifunctional, complex polymers for functional and stimuli-responsive coatings, Chapter 3, 2013.

[2]   S.D. Ebbesen, B.L. Mojet, L. Lefferts, In situ ATR-IR study of nitrite hydrogenation over Pd/Al2O3, J. Catal. 256 (2008) 15–23. https://doi.org/10.1016/j.jcat.2008.02.013.

[3]   K.H. Shen, M. Fan, L.M. Hall, Molecular Dynamics Simulations of Ion-Containing Polymers Using Generic Coarse-Grained Models, Macromolecules. 54 (2021) 2031–2052. https://doi.org/10.1021/acs.macromol.0c02557.

[4]   T.E. Gartner, A. Jayaraman, Modeling and Simulations of Polymers: A Roadmap, Macromolecules. 52 (2019) 755–786. https://doi.org/10.1021/acs.macromol.8b01836.

[5]   A.R. Riscoe, C.J. Wrasman, A.A. Herzing, A.S. Hoffman, A. Menon, A. Boubnov, M. Vargas, S.R. Bare, M. Cargnello, Transition state and product diffusion control by polymer–nanocrystal hybrid catalysts, Nat. Catal. 2 (2019) 852–863. https://doi.org/10.1038/s41929-019-0322-7.

Summary

This thesis presents a proof of concept of self-regulating mechanism by a heterogeneous catalyst in combination with stimuli responsive polymer. These polymers have the unique ability to reversibly change conformation from a swollen to a collapsed state in response to an environmental stimulus (e.g. temperature or pH). The conformation change of the polymer could allow to locally adjust the molecular diffusion of reactants, thereby changing the catalytic activity autonomously. Since the reaction will be intrinsically manipulated, implementing this concept to industrial processes will potentially alleviate the need for using external measures to control the reaction rate, such as passive cooling or using inert dilutants.

Thus far, the self-regulating mechanism using stimuli responsive polymers has never been demonstrated for heterogeneous catalysis. Instead, an external stimulus is applied to alter the catalyst activity depending on the polymer conformational state when polymeric brushes are coated on a nano cluster. In the presence of a thermo-responsive polymer, such as poly(n-isopropylacrylamide) (p-NIPAM), the increase of temperature causes the polymeric brushes to collapse after surpassing a certain temperature, the so called Lower Critical Solution Temperature (LCST). Consequently, the change in conformation resulted in a decrease on the reaction rate, due to the partial blockage of the diffusion path of the reactants. These idealized systems demonstrate that thermo-responsive materials can be used to control molecular transport of reactants. However, there is still a significant research gap concerning the development of more practical catalysts that can have this stimulus-responsive behaviour under industrially relevant condition. More details regarding the underlining topics can be found in **Chapter 1**.

This thesis provides significant insights on the interplay between polymeric brushes, using a thermo-responsive polymer (p-NIPAM), and catalytic performance of a palladium alumina porous catalyst (Pd/Al_2O_3) by combining diffusion studies and rigorous reaction kinetics measurements. **Chapter 2** discusses transport studies of CO in model catalysts consisting of a porous Pd/Al_2O_3 layer and a polymeric membrane coated with p-NIPAM brushes using *in-situ* ATR-IR spectroscopy. In this model, the polymer is physically segregated from the metal active sites, thus avoiding any influence on the CO-Pd interaction. It is shown that the polymeric brushes drastically change the CO diffusion through the membrane. Here, the collapse of the polymeric brushes caused an increase of

the CO transport through the polymeric membrane. This was attributed to the increase of the pore diameter for CO diffusion in comparison to the swollen state. The experimental results were used to create a detailed molecular transport modelling based on Fick's 2nd law of diffusion. The model suggests significant interaction between CO and the polymeric brushes, where CO absorption on the polymeric matrix plays a key role on the mass transport towards the catalyst.

Nitrite hydrogenation was selected as model reaction to study the effect of polymeric brushes on catalyst performance. Here, p-NIPAM brushes were coated near the metal active sites on a palladium alumina porous catalyst (Pd/Al_2O_3). The activity and selectivity towards nitrogen and ammonia of this reaction is strongly affected by the temperature and concentration profile inside the catalyst particles, making this chemistry ideal for probing these polymer-coated catalysts. **Chapter 3** demonstrates the effect of polymeric brushes on the reaction kinetics, where a decrease in ammonia selectivity was observed by the p-NIPAM/Pd/Al_2O_3 catalyst in comparison with the bare Pd/Al_2O_3 catalyst. This observation was attributed to solvation effects caused by the proximity of the metal nanoparticles to the functional groups present on the polymeric chain and independent of the polymer conformation. *In-situ* ATR-IR spectroscopy demonstrated the induced solvation effects as the addition of polymeric brushes caused a red-shift of the NO_2^- adsorption peaks on palladium at low temperatures (25 °C). *In-situ* ATR-IR spectroscopy showed these effects by a red shift of the NO_2^- adsorption peaks for palladium catalyst with polymer-brushes-coating relative to the palladium catalyst without coating, at low temperatures (25 °C).

The effect of the polymeric conformational changes on the reaction performance was investigated by inducing mass transfer limitations on increasingly large catalyst particles (i.e. 0-38 μm to 38-100 μm), as shown in **Chapter 4**. The uncoated Pd/Al_2O_3 catalyst follows Arrhenius behaviour upon increasing temperature, independent of the catalyst particle size fraction (0-38 μm and 38-100 μm). The same trend was obtained for the catalyst in the presence of the p-NIPAM/Pd/Al_2O_3, but only for smaller particles (0-38 μm). Increasing the catalyst particle size fraction to 38-100 μm caused a decrease in the apparent activation energy barrier at temperatures where the polymer is in the collapsed state, i.e. above the LCST of 32 °C. A detailed reaction-diffusion model was developed to elucidate the interplay between the polymer conformation and catalyst pore structure. In the presence of a highly porous catalysts with undefined pore structure, the collapse of the polymeric brushes can either cause the blockage of pore constrictions and/or increase the effective pore diameter, as discussed in **Chapter 2**. In order to obtain the inflexion point

in the model with the Arrhenius plot, the polymer collapsing must lead to partial blockage of the catalyst pores. Increasing the contribution of pore blockage, however, led to overestimation of the reaction rate. This strongly suggests that polymeric brushes do not only create a barrier for molecular diffusion but also interact with the reactive species, as discussed in **Chapter 2**.

Based on the results of this thesis, it is proposed in **Chapter 5**, to launch a research study on the effect of varying the membrane pore size on molecular transport of CO and/or growing the polymeric brushes only on the top of the membrane. The study should continue to experimentally obtain the absorption capacity of CO in the polymeric matrix by measuring the CO concentration as a function of time upon exposure to p-NIPAM polymeric brushes. The research should include *in-situ* ATR-IR spectroscopy experiments following nitrite hydrogenation reaction, to elucidate the effect of polymeric brushes on the reaction mechanism and intermediates adsorption strength. X-ray absorption spectroscopy can be added to map the distribution of the polymeric brushes inside the catalyst pores, which can help to improve our model predictions of the catalytic performance.

Samenvatting

Dit proefschrift beschrijft een proof-of-concept van een zelfregulatie mechanisme in een heterogene katalysator, in combinatie met een stimulus gevoelige polymeer. Deze polymeren hebben het unieke vermogen om reversibel van vorm, van een gezwollen naar een samengetrokken staat te veranderen, als gevolg van een omgevingsstimulus (bijv. temperatuur of pH). De vormverandering van het polymeer zou de moleculaire diffusie van de reactanten plaatselijk kunnen beïnvloeden en daarmee de katalytische activiteit onafhankelijk van een externe stimulus kunnen veranderen. Omdat de reactie intrinsiek beïnvloed zal worden, zal de implementatie van dit concept in industriële processen potentieel het gebruik verminderen van externe maatregelen, zoals passief koelen of verdunnen met een inerte oplosmiddelen.

Tot nu toe is het zelfregulerende mechanisme, gebruikmakende van stimulus gevoelige polymeren, nooit aangetoond in heterogene katalyse. Over het algemeen wordt een externe stimulus gebruikt om de katalysator-activiteit te beïnvloeden, waarbij de verandering afhankelijk is van de vorm/conformatie van de stimulus gevoelige polymeer borsteltjes die zijn gecoat op een nano cluster. In een thermisch gevoelige polymeer, zoals poly(n-isopropylacrylamide) (p-NIPAM) zullen, bij het overschrijden van een bepaalde temperatuur (de zogenaamde 'Lower Critical Solution Temperature :LCST), de polymeer-borstels slinken. Deze verandering in vorm/conformatie leidt, door de resulterende, gedeeltelijke blokkering van het diffusie-pad van de reactanten, tot een afname van de reactiesnelheid. Dit geïdealiseerde model toont aan dat thermisch gevoelige materialen gebruikt kunnen worden om moleculair transport van reactanten te beïnvloeden. Er is echter nog een aanzienlijk tekort aan onderzoek aan de ontwikkeling van meer praktisch toepasbare katalysatoren met deze stimulus-gevoelige eigenschappen onder industrieel relevante omstandigheden. Meer details over deze onderwerpen zijn te vinden in **hoofdstuk 1**.

Dit proefschrift geeft een duidelijk inzicht in de interactie tussen polymeer-borstels (van het thermisch gevoelige polymeer (p-NIPAM)) en de katalytische activiteit van een palladium-aluminium poreuze katalysator (Pd/Al_2O_3), door diffusie-studies en precieze reactie-kinetiek-metingen te combineren. **Hoofdstuk 2** behandelt transportstudies van koolmonoxide (CO) in model katalysatoren bestaande uit een poreuze Pd/Al_2O_3-laag en een polymeer-membraan gecoat met p-NIPAM-borstels en gebruik makende van *in-situ*

ATR-IR-spectroscopie. In dit geïdealiseerd systeem wordt het polymeer fysiek gescheiden van het katalytisch actieve metaal, waardoor de invloed van het polymeer op de CO-Pd-interactie wordt vermeden. Het is aangetoond dat de polymeer borstels de CO-diffusie door het membraan sterk veranderen. Het slinken van de polymeer-borstels geeft hier een toename van het CO-transport door het polymeer-membraan. Dit wordt toegeschreven aan de vergrootte porie-diameter voor CO-diffusie in vergelijking met de gezwollen toestand van het polymeer. De resultaten van de experimenten zijn gebruikt om het moleculair transport gedetailleerd en gebaseerd op Fick's 2de diffusie wet te modelleren. Het model geeft een significante interactie tussen CO moleculen en de polymeer borstels weer, waarbij CO-absorptie op de polymeren een belangrijke rol speelt in het massatransport naar de katalysator toe.

Nitriet-hydrogenering is gekozen als referentie reactie voor het meten van het effect van polymeer-borstels op de activiteit van de katalysator. Hiertoe werden p-NIPAM-borstels gecoat naast de actieve palladium deeltjes op enen poreuze aluminiumoxide drager (Pd/Al$_2$O$_3$). De nitriet hydrogenerings activiteit en selectiviteit richting stikstof of ammonia van deze reactie wordt sterk beïnvloed door de temperatuur en het concentratie profielen in de katalysator deeltjes, wat deze reactie uitermate geschikt maakt voor onderzoek naar deze polymeer-gecoate katalysatoren. **Hoofdstuk 3** toont het effect van polymeer-borstels op de reactiekinetiek. De ammoniakselectiviteit nam af in de p-NIPAM/Pd/Al$_2$O$_3$ katalysator in vergelijking met de Pd/Al$_2$O$_3$ katalysator zonder polymeer. Deze waarneming kan toegeschreven worden aan solvatatie-effecten, veroorzaakt door de korte nabijheid tussen het actieve metaal en de functionele groepen in de polymere keten en die onafhankelijk zijn van de polymeer conformatie. *In-situ* ATR-IR-spectroscopie toonde deze effecten door een roodverschuiving van de NO$_2^-$ adsorptie-pieken bij de palladium katalysator met polymeer-borstel-coating ten opzichte van de palladium katalysator zonder coating, bij lage temperaturen (25 °C).

Het effect van de vormverandering van de polymeren op de reactiesnelheid werd onderzocht door massatransport te limiteren door middel van oplopend grotere katalysator korrelgrootte (d.w.z. 0-38 μm tot 38-100 μm), zoals beschreven in **hoofdstuk 4**. De niet gecoate Pd/Al$_2$O$_3$-katalysator volgt de wet van Arrhenius bij stijgende temperatuur, onafhankelijk van de korrelgrootte van de katalysator (0-38 μm en 38-100 μm). Een vergelijkbare trend werd waargenomen in de aanwezigheid van p-NIPAM/Pd/Al$_2$O$_3$ maar slechts met de kleine korrelfractie (0-38 μm). Het vergroten van de korrelfractie van de katalysator tot 38-100 μm veroorzaakte echter een afname van de activeringsenergie-barrière bij temperaturen waarbij het polymeer zich in de geslonken

toestand bevindt, d.w.z. boven een LCST van 32 °C. Een gedetailleerd reactie-diffusiemodel werd ontwikkeld om de interactie tussen de polymere conformatie en de poriestructuur van de katalysator op te helderen. Bij zeer poreuze katalysatoren met een niet definieerde poriestructuur, kan het slinken van de polymeerborstels ofwel verstopping van de porie veroorzaken en/of de effectieve poriediameter vergroten, zoals besproken in **hoofdstuk 2**. Om het experimenteel geobserveerde buigpunt in het model met de Arrhenius vergelijking te verkrijgen, moet het slinken van het polymeer leiden tot gedeeltelijke verstopping van de katalysator-poriën. Het verhogen van de bijdrage van deze verstopping in het model leidde echter tot een overschatting van de reactiesnelheid. Dit duidt er sterk op dat polymeerborstels niet alleen een barrière vormen voor moleculaire diffusie, maar dat ze ook een interactie hebben met de reactieve moleculen, zoals besproken in **hoofdstuk 2**.

Gebaseerd op de resultaten van dit proefschrift wordt in **hoofdstuk 5** voorgesteld om een nieuwe studie uit te voeren op het effect van de membraan porie-grootte op het moleculaire transport van CO en/of het effect te onderzoeken van de polymeer-borstels alleen op de bovenkant van het membraan te laten groeien. In het onderzoek moeten vervolgmetingen gedaan worden aan de CO concentratie als functie van de tijd van blootstelling aan de p-NIPAM polymeer borstels om zo de absorptiecapaciteit van de polymeermatrix te achterhalen. Ook moeten *in-situ* ATR-IR spectroscopie metingen aan de nitriet-hydrogenatie reactie worden gedaan, ter opheldering van de invloed van de polymeerborstels op het reactiemechanisme en de adsorptie sterkte van de tussenproducten. Röntgenabsorptiespectroscopie metingen zullen toegevoegde waarde hebben om de verdeling van de polymeerborstels in de katalysatorporiën in kaart te brengen, wat behulpzaam is ter verbeteringen van het katalytische vermogen.

Acknowledgements

I would like to show my gratitude to everyone who contributed to this booklet, scientifically, as well as who supported me during this period. The outcome would not have been the same without all those influences.

I started in CPM as a master student under the supervision of Shilpa. I am grateful for your supervision, you taught me how to structure my research, you really try to get the best out of people. Your care goes beyond work, I would like to show my appreciation when you took care of me after I got ill, you drove me home and you made sure I was going to recover. Now, you live in the UK, I wish you all the best with James and the new baby.

After my master, I could continue in the research group to do my PhD research. Jimmy, you were my supervisor for 4+ years and I cannot thank you enough for giving me this opportunity. You are a dreamer with endless ideas. From your optimist, you really taught me that for every challenge there is a solution. We had a long journey and your contribution turned me into a better scientist. I cannot forget to highlight your contribution, teaching me how to explain complex concepts presenting them in an understandable manner. I wish you a lot of success in the new steps of your career and happiness with Pilar, the girls and the new member, the well-behaved puppy.

I would like to show my gratitude to Leon, you were involved in my progress from my master until the end of my PhD. You have always made relevant questions and helped me structure my PhD research. Even though the writing journey is endless, your precision makes the process of publishing articles smoother. I would like to emphasise your contribution in keeping the research group together by organizing barbecues, promoting trips and free rounds at the borrels.

During my PhD, another professor joined the group. Aayan, your arrival to the group could not have been handier for me. I owe you for big part of my knowledge in computational modelling. Your commitment was really appreciated, it was impressive how quickly I would receive feedback from you in case of modelling related questions. It was nice having you around in the borrels and dinners.

Furthermore, I want to thank Bert. You really think two or three steps ahead when it comes to building setups and experiments. I cannot thank you enough for all your contributions in my master and PhD, I learned a lot from you. You care about the students and your contribution to keep the borrels going is really appreciated. Karin, thank you for all the

help regarding analysis and also advice. You keep our laboratory in high standards, that is really appreciated. It was always nice to have someone to talk to in the laboratory designated to IR, Raman and CO chemisorption instead of only listening to the radio. I wish you lot of success building more beautiful cakes and enjoying the nice holidays in the fields of Germany. Tom, thank you for performing characterization analysis and often passing by my setup, I had really nice talks with you. Ties, it was really nice to have you during the borrel, having good discussions including some dark humour. I wish you a lot of success in your new job developing new inks for children's toys. Anne, thank you for all the help regarding the organization of the group trip to Munich. You care for the group and you promote social activities, I hope you are having a good experience living in Hengelo.

PhD times would not be the same without the colleagues, especially Friday's afternoon after the bell at 5 o'clock. This is a real opportunity to gather the group and I would like to thank everyone who joined creating all the unforgettable memories. Pengyu, you have always been extremely kind. One of my researches ended up related with your PhD topic, nitrite hydrogenation reaction, all the discussions we had were helpful. Apart from work, it was nice to see you becoming less shy in the borrels. You showed interest in exploring the areas around, even biking from Enschede to Münster. Even though, I would never do that, it was nice to bike around Hengelo and Enschede together. I hope to see you around in the Netherlands in the coming times. Then, I would like to thank the *guapa* Nuria. You bring light and energy around you, I could just pass by your office and talk whenever I needed it. Before we used to walk around Enschede, now you are back to Spain, I wish you a lot of success building up a new setup at your current job. Pengcheng, we have significant differences in opinion which made discussions interesting. You are a true hard worker, not wasting any time from the laboratory. I wish you a lot of success in your career while buying one or (perhaps) two houses. I could not forget the other officemate I had for a short time, Pepe, it was nice to share with you the unhealthy snacks in the office. You, Nuria and Guido really made the all show happening. Guido, the Italian of the group, making always statements for thought. Funny enough, even though Rolf used your dirty Italian phrases, you were the one ending up slapped. There are no dull moments with you around. I wish you a lot of happiness in your new home with the lovely Michaela and Alessandro.

Fernando, it was really nice having you as an officemate. I would like to thank you for making sure the IC would continue to work properly after Rolf delegated the maintenance to you. I am amazed that after you arrived in the Netherlands you switched directly the

lunch tradition into sandwiches, well-done. Lola, I enjoyed having you in the group, especially in the borrels, you felt like another partner in crime. I am glad that now you have the freedom to bike home and the borrel can go on for longer than the last bus to Enschede. The three of us had the opportunity to make a small trip to Deventer, where we saw interesting dolls dressed up like angels, I guess that's what art is, it was a lot of fun. I hope we continue to see each other in the future.

Kevin, it was nice having in the group, you are a networker and well gifted scientist who thrills for new challenges, I wish you a lot of success preaching the gospel of green ammonia. Jord, you are always willing to help everyone regarding either research or group activities, it was a relief that you could take over the organization of the group trip to Munich. I wish you a lot of success in the next marathons and finishing your PhD. Shahab, you always kept appearing in the research group borrels even after your graduation. A lot of times you are the responsible person who remembers that drinking with an empty stomach is not a good combo. Madi and Azam, your time in the group was short, but I really enjoyed meeting you.

While doing my research, I got the opportunity to supervise several students: Angela, Jorn, Joanne, Anusha, Max, Thomas and Sanjay. I would like to thank each one of you, I learned a lot from our interactions. I wish you all a bright career. My PhD also benefitted from interactions with other research groups. Joshua, I appreciate your availability, helping me to build the setup for polymerization and explain me the synthesis process. To characterize these materials, I needed to learn how to use an ellipsometer. For this, I would like to show my gratitude to Kristianne. You explained me the fundaments on how to model and use an ellipsometer. Fortunately, I got the opportunity to further learn the technique by following a course in Germany together with Farzaneh, I had a pleasant time with you. I would like to thank Sissi and Marco for helping me and my student Anusha on how to use the AFM. Margot, you are kind, it was a pleasure to organize the Munich group trip together, not only once but twice. I could not forget to thank Yang, even though the research did not come to light, I really appreciate your help in trying to get homogenous coatings of palladium particles in a ATR-IR crystal.

My journey in the Netherlands started in the last year of my master. Even though I had always planned to have an international experience, this trip would not have happened if my friend Magda did not help me with the final push. I would like to thank her for joining me in the Erasmus+ programme in the University of Twente. You were a true roommate, I had a lot of fun exploring Europe with you and getting used to bike everywhere. I will not forget the time spent in 399, where the only seasoning was salt and pepper. I got the

opportunity to make new friends, Pedro and João, whom luckily decided to remain in the Netherlands until now and they have been true companions. Pedro, thank you for all the support and patience during the start of my PhD. I had a lovely time living together with you (in a house that is better not to mention), despite our differences, we could always come to an agreement after a good talk and a bottle of wine. At that time, for Pedro, it was not an option to have a meal without warm food (perhaps, this is still the case). João, you have always been there for me even to answer modelling questions. In our gatherings, I enjoy making Portuguese dishes with you, funny enough, we always end up calling our mothers for advice. I still remember one night after party that we could not stop eating toasts, for some reason bread and butter tasted amazing. Later on, I also met Tony. We both lived in Matenweg for a while, listening to the loud neighbour from room 16. Thank you for keeping up the spirit, making us wake up around 6:30 and bike through the rain and snow, to keep us fit in the gym. Carolina, what an adventure for two students to find a non-student house in Enschede. My apologies for waking you up every morning before going to the university, your schedules were completely different from mine. Still, I had a great time living together with you and I wish you a lot of success in Switzerland.

From the friends at the university time, I would like to highlight Walgode and Ruben (Mimo). Walgode, you are a talent, not everyone could be an artistic roller skater and do a PhD in chemical engineering at same time. I want to congratulate you on your incredible performance until this year, World champion in artistic roller skates, I am proud of you. Even though your schedules are always full, you always can find time for your friends. I really enjoyed our Thursday night outs and lunch in the "delicious" food of the university canteen. Ruben, I am thankful for all your help, friendship and all the rides to Covelo. Many hours we spent in the library or in the student rooms at the University. You really have a passion for Porto city and I owe all my discovers to you. If someone travels to Porto, they should look for you as a guide. Furthermore, I could not forget the group "amigos dos copos", my friends from youth specially: Rik, Dani, Simão, Hugo, Catrina, Tiago and Bordalo. Time flies when I am spending time with all of you. Even though I am living abroad for a while, when I see you feels like old times. I would like to highlight the help from Hugo, this thesis would not be the same without your drawings. The last (but not least), I want to thank the friends that I have gained via my boyfriend, namely: Lionel, Dion, Vahideh, Raoul, Dennis, David, Edo, Finn and Devi. It was always nice to make reunions at the TBS or other activites. I want to specially thank Lionel for the good times during the dancing classes, I might have stepped on your toes a couple of times.

Now I would like to move on to my family that I am grateful for their support. This next section will be written in Portuguese. Gostaria de agradecer a toda a minha família pelo apoio nesta etapa da minha vida, em especial aos meus pais, sem eles não tinha concretizado este desafio. Mãe, obrigada por tudo, tu és capaz de mover o mundo por mim. Sei que quando preciso estás sempre lá para me apoiar e me ouvir. Desejo-te tudo de bom nesta nova etapa, tu mereces. Infelizmente, vais ter de esperar pelo teu anexo na Holanda. Pai, obrigada pelo positivismo, as tuas influências de engenheiro deram fruto. É sempre bom desfrutar de um churrasco em Cardielos. Agora, estás numa nova etapa, ser político, espero que continues a lutar por um país mais sustentável. Gostaria de agradecer as minhas avós, em especial a minha avó Idalina. Ela que, com quase 90 anos, ainda nos (eu e o Rolf) visitou na Holanda. Ela era a pura definição de ser "dura como o aço", para além de ser a melhor cozinheira do mundo. Agora temos o tio Jorge, que faz uns petiscos muito jeitosos, obrigada por ajudares a matar saudades das comidinhas portuguesas quando chego a "casa".

Now I have also gained a Dutch family, for this reason this section will be in Dutch. Ik wil graag mijn waardering uitspreken voor Rolfs familie, zij hebben mij altijd goed ontvangen. Erik en Carla, jullie zijn een voorbeeld voor hoe een relatie hoort te zijn, jullie hebben mij vanaf het begin omarmt als een deel van het gezin. Jullie hebben mij ook veel geholpen bij het tot stand brengen van dit proefschrift, waar ik jullie erg dankbaar voor ben. Erik, jij hebt mij geleerd dat er geen problemen zijn, maar alleen uitdagingen, ik wil je heel erg bedanken voor alle hulp die je hebt geven als ik moeite had met mijn promotie. Carla, jij hebt in mij een smaak voor discussies ontwikkelt, welke ik niet wist dat ik had. Ik wil je bedanken voor het hebben van een luisterend oor en goed advies. Sjoerd en Anne, ik heb altijd genoten van de weekenden die Rolf en ik bij jullie thuis gespendeerd hebben, jullie geven veel om onze vreugde en welzijn. Eline en Wessel, het is altijd leuk om jullie op visite te hebben, ik geniet ook erg van onze gezamenlijke skivakanties, ik hoop dat ik in de toekomst jullie ski vaardigheden kan bijbenen. Ik wens jullie heel veel geluk in jullie nieuwe huis, met jullie kat Monster. Laura en Wilko, ik wil jullie ook bedanken voor de gezellige avonden bij jullie thuis, samen met Alex en Lars.

Tot slot wil ik Rolf graag in het bijzonder bedanken. Ik ben jou enorm dankbaar voor jouw geduld en bijdragen aan dit proefschrift, wat zelfs geleid heeft tot een gezamenlijk artikel. De universiteit heeft ons samen gebracht en, dankzij jou, is Nederland inmiddels mijn thuis geworden. Je hebt een bijzonder talent om snel nieuwe dingen te leren, waar de Portugese taal er één van is. Daarmee maak je altijd indruk op me. Toch is Duolingo als leermiddel wellicht niet altijd de beste optie, want ik vraag me af wanneer je de zin "Ik heb

vliegen op mijn laarzen" ooit in het dagelijks leven zult gebruiken. We hebben samen al een lange weg afgelegd en ik ben elke dag blij om terug te keren in ons nieuwe, prachtige huis, om daar samen te zijn met jou en onze katten Julius en Lilly. Ik hou ontzettend veel van jou en ik ben jou zeer dankbaar voor al jouw steun tijdens mijn PhD.

List of Publications

Until August 2022

Journal articles:
To be submitted as: Enes da Silva, M.J., Postma, R.S., Banerjee, A., Lefferts, L., Albanese, J.A.F., The onset of mass transport limitations triggers the stimulus responsiveness of polymer coated catalysts; M.J. Enes da Silva, R. Postma, A. Banarjee, L. Lefferts, J.A.F. Albanese.

Enes da Silva, M.J., Banerjee, A., Lefferts, L., Albanese, J.A.F., *In-situ ATR-IR spectroscopy reveals complex absorption-diffusion dynamics in model polymer-membrane-catalyst assemblies (PCMA), Chemcatchem 2022, https://doi.org/10.1002/cctc.202101835*.

Enes da Silva, M.J., Lefferts, L., Albanese, J.A.F., *N-isopropylacrylamide polymer brushes alter the micro-solvation environment during aqueous nitrite hydrogenation on Pd/Al$_2$O$_3$ catalyst, J. Catal. 2021, 402, https://doi.org/10.1016/j.jcat.2021.08.003*

Book Chapter:
Enes da Silva, M.J., Albanese, J.A.F., Lefferts, L., *Elucidating transport and reaction processes in solid-liquid interfaces using attenuated total reflectance infrared spectroscopy (ATR-IR)*, Encyclopedia of Solid-Liquid interfaces, editors-in-chief Klaus Wandelt and Gianlorenzo Bussetti, to be published by Elsevier 2022.

Conference presentations:
Enes da Silva, M.J., Banerjee, A., Lefferts, L. & Albanese, J.A.F., *In situ ATR-IR spectroscopy of CO chemisorption on bio inspired catalyst in liquid environment.* 2022, Oral presentation at NCCC conference in Noordwijkerhout, the Netherlands

Enes da Silva, M.J., Banerjee, A., Lefferts, L. & Albanese, J.A.F., *In situ ATR-IR spectroscopy of CO chemisorption on bio inspired catalyst in liquid environment.* 2021, Oral presentation at ACS online conference

Enes da Silva, M.J., Lefferts, L. & Albanese, J.A.F., *Leveraging polymer over-coatings to tune selectivity of metal supported catalyst for liquid phase hydrogenation.* 2020, Oral presentation at ICEC online conference

Conference poster presentations:
Enes da Silva, M.J. & Albanese, J.A.F., Polymer over-coatings on metal supported catalysts for liquid-phase hydrogenation: mass transport and macro-kinetics studies. 2019, poster presentation at NCCC conference in Noordwijkerhout, the Netherlands

Enes da Silva, M.J. & Albanese, J.A.F., In-situ ATR-IR spectroscopy of CO chemisorption on bio-inspired catalysts in liquid environments. 2019, poster presentation at Europacat conference

Maria João Enes da Silva was born on the 30th of January 1994 in Viana do Castelo, Portugal. For university studies Maria went to Universidade do Porto to study chemical engineering. During her studies she did volunteering work by cleaning up the human waste from the oceanic coast and assisting elderly people. Her engagement to sustainability has been largely stimulated by these activities and directed her to pursue research associated to the development of more efficient processes. She obtained a master degree specializing in process and products. For the final part of her master program, Maria moved to the Netherlands on an Erasmus+ program. She performed her master thesis within the Catalytic Process and Material group at the University of Twente, developing a prototype analysis machine for liquid phase CO chemisorption measurements, which triggered an interest in liquid phase catalysis. Maria continued in the research group with her PhD, under the supervision of Jimmy A. Faria Albanese, the findings of which are described in this thesis.